

HZDR-026

Quantitative dopant profiling in semiconductors: A new approach to Kelvin probe force microscopy

Christine Baumgart

Wissenschaftlich-Technische Berichte
HZDR-026 · ISSN 2191-8708

WISSENSCHAFTLICH-
TECHNISCHE BERICHTE

HZDR



HELMHOLTZ
| ZENTRUM DRESDEN
| ROSSENDORF

Wissenschaftlich-Technische Berichte
HZDR-026

Christine Baumgart

**Quantitative dopant profiling in semiconductors:
A new approach to Kelvin probe force microscopy**

HZDR

 **HELMHOLTZ**
ZENTRUM DRESDEN
ROSSENDORF

Institut für Ionenstrahlphysik und Materialforschung
Helmholtz-Zentrum Dresden-Rossendorf e.V.

**Quantitative dopant profiling in semiconductors:
A new approach to Kelvin probe force microscopy**

von der
Fakultät Mathematik und Naturwissenschaften
der Technischen Universität Dresden
genehmigte

Dissertation

zur Erlangung des akademischen Grades
Doctor rerum naturalium
(Dr. rer. nat.)

vorgelegt von
Dipl.-Phys. Christine Baumgart

geboren am 18.07.1982
in Berlin, Deutschland

Dresden 2011

Eingereicht am 23.11.2011

1. Gutachter: Prof. Dr. Manfred Helm

2. Gutachter: Prof. Dr. Dr. h. c. Dietrich R. T. Zahn

Verteidigt am 19.07.2012

Abstract

Failure analysis and optimization of semiconducting devices request knowledge of their electrical properties. To meet the demands of today's semiconductor industry, an electrical nanometrology technique is required which provides quantitative information about the doping profile and which enables scans with a lateral resolution in the sub-10 nm range. In the presented work it is shown that Kelvin probe force microscopy (KPFM) is a very promising electrical nanometrology technique to face this challenge. The technical and physical aspects of KPFM measurements on semiconductors required for the correct interpretation of the detected KPFM bias are discussed. A new KPFM model is developed which enables the quantitative correlation between the probed KPFM bias and the dopant concentration in the investigated semiconducting sample. Quantitative dopant profiling by means of the new KPFM model is demonstrated by the example of differently structured, n - and p -type doped silicon. Additionally, the transport of charge carriers during KPFM measurements, in particular in the presence of intrinsic electric fields due to vertical and horizontal pn junctions as well as due to surface space charge regions, is discussed. Detailed investigations show that transport of charge carriers in the semiconducting sample is a crucial aspect and has to be taken into account when aiming for a quantitative evaluation of the probed KPFM bias.

Kurzfassung

Die Fehleranalyse und Optimierung von Halbleiter-Bauelementen erfordert genaue Kenntnis über deren elektrische Eigenschaften. Um dem heutigen Anspruch der Halbleiter-Industrie zu genügen, wird eine elektrische Nanometrologie-Methode benötigt, die sowohl eine quantitative Bestimmung von Dotierprofilen als auch Messungen mit einer lateralen Auflösung unter 10 nm ermöglicht.

Im Hinblick auf diese Anforderungen wird in der vorgelegten Arbeit gezeigt, dass die Raster-Kelvin-Mikroskopie (KPFM) eine Erfolg versprechende elektrische Nanometrologie-Methode ist. Auf Basis einer grundlegenden Auseinandersetzung mit den technischen und physikalischen Aspekten der Raster-Kelvin-Mikroskopie an Halbleitern wird ein neues KPFM-Modell entwickelt, das den quantitativen Zusammenhang zwischen der gemessenen KPFM-Spannung und der Dotierkonzentration in der untersuchten Probe liefert. Am Beispiel von unterschiedlich strukturiertem, n - und p -Typ dotiertem Silizium wird die quantitative Bestimmung des Dotierprofils mit Hilfe des neuen Modells demonstriert. Mit besonderem Augenmerk auf intrinsische elektrische Felder an horizontalen und vertikalen pn -Übergängen und in Oberflächen-Raumladungszonen wird des Weiteren der Transport von Ladungsträgern während der KPFM-Messung diskutiert. Ausführliche Untersuchungen zeigen, dass der Transport von Ladungsträgern in der halbleitenden Probe von entscheidender Bedeutung ist und für eine quantitative Auswertung der gemessenen KPFM-Spannung berücksichtigt werden muss.

Contents

List of Abbreviations	VII
1 Introduction	1
1.1 Motivation	1
1.2 State of the art in electrical nanometrology techniques	1
1.3 The great potential of Kelvin probe force microscopy	2
2 Electrical nanometrology techniques	4
2.1 Scanning spreading resistance microscopy	4
2.2 Conductive atomic force microscopy	5
2.3 Scanning capacitance microscopy	7
2.4 Scanning microwave microscopy	11
2.5 Electrostatic force microscopy	13
3 Experimental details	16
3.1 Semiconducting samples	16
3.1.1 Silicon static and dynamic random access memory cells	16
3.1.2 Cross-sectionally prepared silicon epilayer samples	19
3.1.3 Horizontal silicon nanowires	21
3.2 Kelvin probe force microscopy setup	25
3.2.1 Ambient KPFM	25
3.2.2 Ultrahigh vacuum KPFM	27
3.3 Complementary characterization methods	28
3.3.1 Secondary ion mass spectrometry	28
3.3.2 Stopping and range of ions in matter calculations	28
4 Silicon surface in ambient environment	29
4.1 Native oxide	29
4.2 Adsorption of water	29
5 Quantitative dopant profiling by KPFM	32
5.1 Traditional KPFM model: Contact potential difference	32
5.2 New KPFM model: Charge carrier accumulation	35
5.2.1 Surface space charge region	35
5.2.1.1 Surface states	35
5.2.1.2 Charge balance	37
5.2.2 Definition of the KPFM bias	40
5.2.2.1 Compensation of the electrostatic forces	40
5.2.2.2 Reclassification of CPD model results	43
5.2.3 Calculation of the Fermi energy	45
5.2.4 Potential shielding and KPFM bias offset	48
5.2.5 Bias-induced band bending	50

5.2.6	Lateral resolution of KPFM	51
5.2.7	Intrinsic electric fields in locally doped semiconductors	53
5.2.7.1	Investigation of pn junctions	53
5.2.7.2	Frequency dependent KPFM	56
5.2.8	Electrostatic force and higher harmonics	59
6	Results	61
6.1	Silicon static and dynamic random access memory cells	61
6.1.1	Static random access memory cell	61
6.1.1.1	Quantitative dopant profiling	61
6.1.1.2	Frequency dependent KPFM measurements	64
6.1.1.3	AC-bias dependent KPFM measurements	72
6.1.1.4	Comparison between UHV and ambient KPFM	75
6.1.2	Dynamic random access memory cell	78
6.1.2.1	Quantitative dopant profiling	78
6.1.2.2	Frequency dependent KPFM measurements	80
6.2	Cross-sectionally prepared silicon epilayer samples	84
6.2.1	Si:B epilayer sample	84
6.2.1.1	Quantitative dopant profiling	84
6.2.1.2	Independence of the cantilever potential	86
6.2.1.3	Frequency dependent KPFM measurements	88
6.2.1.4	AC-bias dependent KPFM measurements	97
6.2.2	Si:P epilayer sample	101
6.2.2.1	Quantitative dopant profiling	101
6.2.2.2	Frequency dependent KPFM measurements	103
6.2.2.3	AC-bias dependent KPFM measurements	105
6.3	Horizontal silicon nanowires	108
6.3.1	Dopant distribution	108
6.3.1.1	Implanted silicon nanowires	108
6.3.1.2	Unimplanted silicon nanowires	112
6.3.2	Shape of the silicon nanowires	117
7	Conclusions	121
7.1	Quantitative dopant profiling	121
7.2	Lateral resolution	122
7.3	Future challenges	123
	List of Figures	125
	List of Tables	130
	References	131
	Publications	145

List of Abbreviations

AFM	Atomic force microscopy
AM	Amplitude-modulated
BOX	Buried oxide
CAFM	Conductive atomic force microscopy
CPD	Contact potential difference
CVD	Chemical vapour deposition
DPMM	Doping profile measurement module
DRAM	Dynamic random access memory
EBL	Electron beam lithography
EFM	Electrostatic force microscopy
FM	Frequency-modulated
FWHM	Full width half maximum
GAA	Gate-all-around
HD	Highly doped
HF	Hydrofluoric
HOPG	Highly oriented pyrolytic graphite
KPFM	Kelvin probe force microscopy
LDD	Lightly doped drain
MOS	Metal-oxide-semiconductor
MOSFET	Metal-oxide-semiconductor field-effect-transistor
Nano-SRP	Nanometer spreading resistance profiling
NP	Nitric/phosphoric
NW	Nanowire
PNA	Performance network analyzer
RAM	Random access memory
RMS	Root mean squared
RTA	Rapid thermal annealing
SCM	Scanning capacitance microscopy
SIMS	Secondary ion mass spectrometry
SMM	Scanning microwave microscopy
SOI	Silicon-on-insulator
SPM	Scanning probe microscopy
SRAM	Static random access memory
SRIM	Stopping and range of ions in matter
SRP	Spreading resistance profiling
SSRM	Scanning spreading resistance microscopy
TRIM	Transport of ions in matter
UHV	Ultrahigh vacuum

1 Introduction

1.1 Motivation

Electrical nanometrology techniques have become more and more important during the last decades. This is mostly due to the semiconductor industry where failure analysis and optimization of semiconductor devices demand knowledge of their electrical properties. A focus of investigations lies on the dopant concentration and distribution which mainly determine the transport properties of semiconductor devices. Therefore, characterization techniques are required that provide quantitative information about the doping profile in semiconductors. Another important issue regarding electrical nanometrology is the lateral resolution of the applied techniques. Since the invention of the first transistor in 1948 [1] semiconductor devices have been fabricated smaller and smaller in order to increase implementation density and operating speed. Nowadays, conventional metal-oxide-semiconductor field-effect-transistors (MOSFETs) are working in the sub-100 nm range [2]. Moreover, devices in the sub-10 nm range have been fabricated and investigated [3–5]. A new concept of nanoscale MOSFET devices is the development of gate-all-around Si nanowire structures [6–13].

In addition to experimental studies there have been theoretical approaches to understand device physics on the nm length scale where effects like quantum confinement, and non-equilibrium, near-ballistic carrier transport have to be taken into account [14–16].

In summary, for the characterization of semiconductor devices an electrical nanometrology technique is required which provides quantitative information about the doping profile and which enables precise measurements on the nm length scale. In the presented work it is shown that Kelvin probe force microscopy is a very promising electrical nanometrology technique to address this challenge.

1.2 State of the art in electrical nanometrology techniques

Nowadays, various electrical nanometrology techniques are applied for the characterization of semiconductors. The conventional scanning probe microscopy (SPM) techniques for electrical characterization of semiconductors on the nm length scale are divided into contact mode methods, i.e. scanning capacitance microscopy (SCM), scanning spreading resistance microscopy (SSRM), scanning microwave microscopy (SMM), and conductive atomic force microscopy (CAFM), and non-contact mode methods, i.e. electrostatic force microscopy (EFM) and Kelvin probe force microscopy (KPFM). For SCM [17–19], SSRM [20–22], or CAFM [23–25], very sensitive capacitance, resistance, or conductivity sensors, respectively, have been developed. The corresponding sensor has to be attached onto the scanner head frame of the atomic force microscope (AFM).

In SCM, which was developed by Matey *et al.* in 1985 [26], the change of capacitance in dependence on an applied alternating bias is measured. Quantitative dopant profiling is only achieved by using special setups, as for example ultrahigh-precision, calibrated capacitance bridges [27]. However, for conversion of the measured SCM data into dopant concentra-

tions extended calculations of the SCM capacitance between tip and sample are required [28]. SSRM was developed in 1995 by W. Vandervorst *et al.* [29] who combined conventional spreading resistance profiling (SRP) [30] with the AFM technique. The measured resistance values have to be transformed into carrier-concentration values by performing *n*-type and *p*-type SSRM calibration measurements [22, 31]. In CAFM a current flowing through the sample is detected, which is a measure for the local conductivity. CAFM is commonly applied in the field of dielectric film characterization [32]. A new and promising electrical nanometrology technique is SMM which has been developed in 2008 by Agilent Technologies [33]. Here, the impedance is measured in dependence on an applied dc-bias by means of a frequency-tunable, high-quality GHz resonator circuit. A calibration procedure is required for the quantitative interpretation of the probed SMM data [34].

These electrical nanometrology techniques only yield the quantitative doping profile in semiconductors if they are used complementary and if calibration measurements have been performed on well-described reference samples. The technical and physical aspects of the introduced contact-mode electrical nanometrology techniques are discussed in Sect. 2.

A more straightforward electrical nanometrology technique is the non-contact KPFM method.

1.3 The great potential of Kelvin probe force microscopy

KPFM is derived from a method developed by Lord Kelvin in 1898 [35]. The Kelvin method was primarily combined with the AFM technique by Nonnenmacher *et al.* in 1991 to investigate electrostatic forces between the probe and metals [36] and in 1992 between the probe and a semimetal, i.e. highly oriented pyrolytic graphite (HOPG) [37]. After this, KPFM has been used to investigate various physical aspects like the interface dipole layer formed between a metal surface and alkali chloride thin films [38, 39], surface defects in chalcopyrite solar cell devices [40] and semiconductors [41, 42], minority charge carrier diffusion lengths [43], doping profiles in semiconductors [44, 45] even with atomic resolution [46], *pn* junctions in semiconductors without [47, 48] and under applied bias [49, 50], the tip-sample interaction [51, 52], the frequency dependence of the KPFM signal [53], or the electrostatic forces between the conductive probe and bulk insulating materials, e.g. correlated with the Madelung surface potential [54].

An interesting new field of application is the investigation of organic materials by means of KPFM. The broad field of biotechnology also comprises the research on organic solar cells. For the development of efficient organic solar cells the doping and nanostructure processing of organic materials has to be studied and understood. In Ref. [55] KPFM is used for example to investigate the nanoscale phase segregation of a C₁₃₂-C₁₆-perylene heterojunction, where C₁₃₂-C₁₆ fibers with donor-type character and with a constant cross-section form on the acceptor-type perylene layer. A mere biological application of KPFM is for example the study of biomolecules. Single biomolecules exhibit well-defined charge centers. At the formation of highly specific binding complexes the charge density locally changes [56]. Therefore, by means of KPFM different interactions between biomolecules and the resulting binding complexes can be qualitatively distinguished. This allows for example

to probe protein-DNA interactions on the nm length scale [57]. Also double-stranded DNA and transcription complexes on an insulating mica substrate have been investigated successfully with molecular resolution by means of an electrostatic force microscope [58]. For biological applications KPFM provides many advantages as for example its non-destructive measurement principle. However, the quantitative evaluation of KPFM data probed on organic materials remains an open issue.

For a quantitative interpretation of the probed KPFM bias, the electrostatic interaction between the cantilever and the sample as well as the KPFM measurement technique itself have to be understood. In this work, a physical model is developed which enables the quantitative correlation of the probed KPFM bias with the dopant concentration in semiconductors. The investigated semiconducting samples are introduced in Sect. 3.1. In Sect. 5 it is explained in detail how the developed KPFM model combines the physical properties of the semiconductor surface and bulk with the unique measurement principle of KPFM. Additionally, major aspects of KPFM measurements on semiconductors as for example the influence of intrinsic electric fields due to vertical and horizontal pn junctions are discussed within the new KPFM model in Sect. 5. Complementary characterization methods have been applied for validation of the developed KPFM model. These methods are introduced in Sect. 3.3. In Sect. 6 the main results of the presented work are discussed. Quantitative dopant profiling is successfully demonstrated on conventional Si static random access memory (SRAM) and Si dynamic random access memory (DRAM) cells (Sect. 6.1), and on cross-sectionally prepared Si epilayers (Sect. 6.2). The transport of charge carriers during KPFM measurements, in particular in the presence of intrinsic electric fields due to vertical and horizontal pn junctions as well as due to surface space charge regions, is investigated. It is shown that the transport of charge carriers in the semiconducting sample is a crucial aspect which has to be understood when aiming for a quantitative evaluation of the probed KPFM bias. Finally, in Sect. 6.3 KPFM is applied to investigate the dopant distribution and shape of horizontal Si nanowires which are the basic unit in gate-all-around MOSFETs. In Sect. 7 the results are summarized and a proposal for future work is given.

2 Electrical nanometrology techniques

For the aim of electrical characterization on the nm length scale various scanning probe microscopy methods have been developed. The main SPM techniques can be divided into contact mode methods, i.e. scanning spreading resistance microscopy, conductive atomic force microscopy, scanning capacitance microscopy, and scanning microwave microscopy, and non-contact mode methods, i.e. electrostatic force microscopy and Kelvin probe force microscopy. In this section an overview regarding these SPM techniques is given and their advantages and disadvantages are discussed.

2.1 Scanning spreading resistance microscopy

Scanning spreading resistance microscopy, also referred to as nanometer spreading resistance profiling (nano-SRP) [31, p. 3], has been developed for 2D carrier profiling in semiconductors [29, 59]. The basic measurement principle of SSRM is shown in Fig. 2.1. During the SSRM measurement a dc-bias is applied between the sample and the conductive cantilever. The probe is scanned over the sample surface in contact mode and the current flow through the sample is detected. Typical detected currents are in the range of 10^{-12} A to 10^{-4} A [60]. Finally, the local spreading resistance is mapped. Series resistances occurring for example at the back contact of the sample or between the conductive probe and the sample surface have to be avoided because they might influence the SSRM measurement [61, p. 18].

For providing the necessary good electrical contact between the probe and the semiconducting sample, the probe has to be pushed with high forces for penetrating the thin oxide layer on top of the semiconductor [61, p. 18]. Therefore, SSRM measurements require special probes. The tip radius has to be small, and the probe has to be electrically conductive and wear resistant [32]. Pyramidal diamond tips are commonly applied nowadays [32, 62]. In general, hard probes have to be used for the SSRM measurement because only at high forces the spreading resistance dominates over the contact resistance [31, p. 34].

In a simple model, the spreading resistance occurring during the SSRM measurement is described by means of a flat circular ohmic contact and a hemispherical ohmic contact [61, p. 20]. In reality, more phenomena have to be taken into account for the correct correlation of the spreading resistance with the local carrier concentration. The probe, for example, is not flat and may be deformed during the SSRM measurement due to the high contact forces. Additionally, a phase change of the underlying semiconductor may occur at high probe contact pressures [61, p. 22]. These effects result in a non-linear resistance-resistivity response [61, p. 26] and complicate quantitative SSRM measurements. Normally, it is assumed that the measured spreading resistance is proportional to the local sample resistivity. Even with this assumption the SSRM data can be converted into the local carrier concentration only by carrying out highly accurate and complicated SSRM calibration measurements [22, 63].

In general, SSRM damages the sample surface and after several scans at the same sample position the surface may even change structure and electric properties. Nevertheless, the

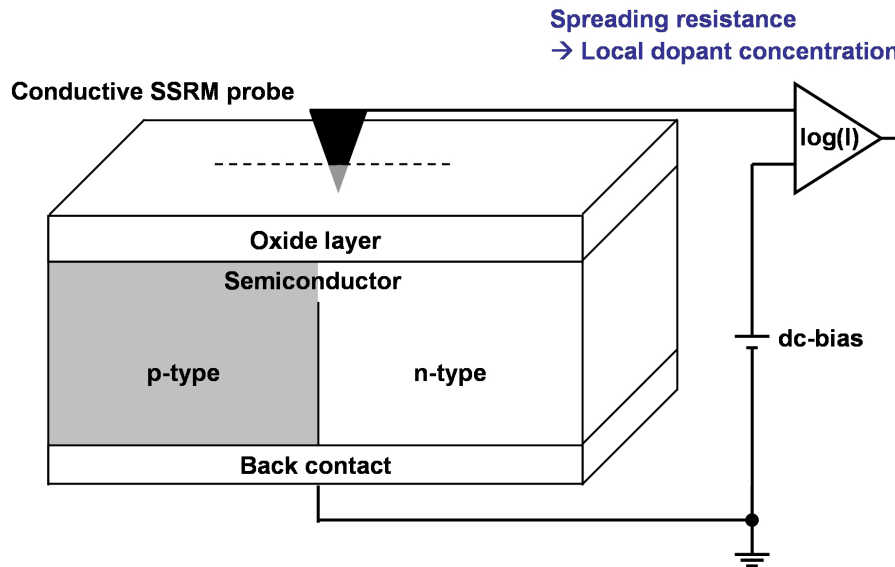


Figure 2.1: Measurement principle of scanning spreading resistance microscopy (SSRM). A dc-bias is applied between the conductive cantilever and the back contact of the sample. By means of a logarithmic amplifier $[\log(I)]$ the current flow through the sample is detected. The thin oxide layer on top of the semiconductor has to be locally penetrated by the hard SSRM probe. SSRM provides a two-dimensional map of the local spreading resistance. Adapted from Ref. [60].

lateral resolution of SSRM is unique and values below 10 nm are achieved. Eyben *et al.* [64] for example investigated the doping profile in MOSFET structures and observed a lateral resolution below 3 nm. Only recently a lateral resolution of 4 nm was reported by X. Ou *et al.* who examined individual Si nanowires and used the abrasive SSRM technique for depth-resolved dopant profiling [65].

2.2 Conductive atomic force microscopy

Conductive atomic force microscopy is used to measure variations in the electrical conductivity of materials with medium conductivity, i.e. currents of 10^{-12} A to 10^{-6} A [66]. The measurement principle of CAFM is illustrated in Fig. 2.2. While the conductive probe is scanned over the sample surface in contact mode, a dc-bias is applied between the probe and the sample. The current passing through the sample is detected which is a measure for the local conductivity. Note that the oxide layer on top of the semiconductor is not penetrated during the CAFM measurement in contrast to SSRM measurements. This major difference between the CAFM and SSRM technique results in different fields of application. CAFM has been originally developed to investigate degradation and dielectric breakdown effects in SiO_2 gate dielectrics [68] and is nowadays the preferred electrical nanometrology technique in the field of dielectric film characterization [32]. CAFM is extremely sensitive to the oxide thickness and can detect thickness variations with an accuracy in the Å-regime [69]. By modeling the probed current to the Fowler-Nordheim law it is possible

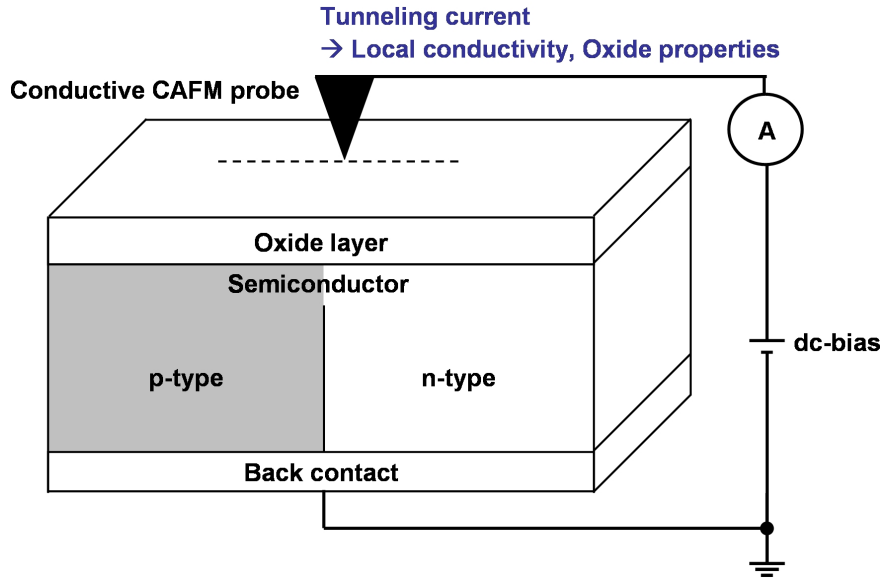


Figure 2.2: Measurement principle of conductive atomic force microscopy (CAFM). A dc-bias is applied between the conductive probe and the back contact of the sample. The tunneling current passing through the sample is detected. Note that the conductive probe does not penetrate the thin oxide layer on top of the semiconductor. CAFM provides a two-dimensional map of the tunneling current. Adapted from Ref. [67].

to determine the absolute layer thickness as successfully demonstrated by the example of CAFM measurements on SiO_2 [24, 68–70].

The field of applications of the CAFM technique is permanently increasing. Various materials like high-k dielectrics [71, 72], diamond and diamond-like carbon films [73, 74], semiconducting films [75], organic light-emitting diodes [76], and electroluminescent polymers [77] have been investigated with respect to morphology and electrical properties such as the local conductivity [75], charge transport [76–78], localized charges [79], and quantum confinement on the nm length scale [80].

CAFM has also been proved to be a reliable tool for the detection of electrical defects in semiconductor storage devices. For example, Si nanocrystals are embedded in the SiO_2 gate oxide of MOS structures for the development of advanced highly integrated nonvolatile memory devices [24, 25]. Porti *et al.* investigated the charge storage in such MOS memory devices by means of CAFM and found that the Si nanocrystals locally enhance the conductivity of the gate oxide [24, 25]. This is explained with the phenomenon of trap-assisted tunneling. The charge that can be stored in the Si nanocrystals was estimated from the I-V characteristics by means of fitting the data to the Fowler-Nordheim tunneling law. It was found that approximately 20 % of the Si nanocrystals are charged [24, 25].

A new field of application for the CAFM technique is found in material research and failure analysis in the solar cell industry. CAFM is useful to investigate the local electrical properties of solar cells, as was shown for example by Moutinho *et al.* on CdTe/CdS films [81]. A surface non-uniformity, e.g. due to grains with different electrical properties, has

been observed which is the reason for the poorer conductivity of untreated CdTe/CdS films. For improving the electrical conductivity of thin film solar cells different surface treatments have been carried out by Moutinho *et al.* [81]. They found that only a nitric/phosphoric (NP) etching increases the conductivity of the CdTe/CdS film due to the formation of a conductive Te-rich layer on the surface of the solar cell which significantly improves the ohmic contact.

2.3 Scanning capacitance microscopy

Scanning capacitance microscopy is a well established tool for qualitative 2D imaging of doped semiconductors [17, 28, 82, 83] with dopant concentrations in the range of 10^{15} cm^{-3} to 10^{20} cm^{-3} [84]. The measurement principle of SCM is illustrated schematically in Fig. 2.3. SCM is based on the detection of the local free carrier concentration by measuring the local depletion/accumulation capacitance that is formed below a conductive cantilever. When the conductive probe is in contact, a metal-oxide-semiconductor (MOS) capacitor is formed between the probe and the semiconducting sample which has a thin oxide layer on top. The extension of the accumulation/depletion region in the formed MOS capacitor changes when applying a dc-bias and an ac-bias to the sample backside. Charge carriers in the surface region of the semiconductor alternatively accumulate and deplete, thus

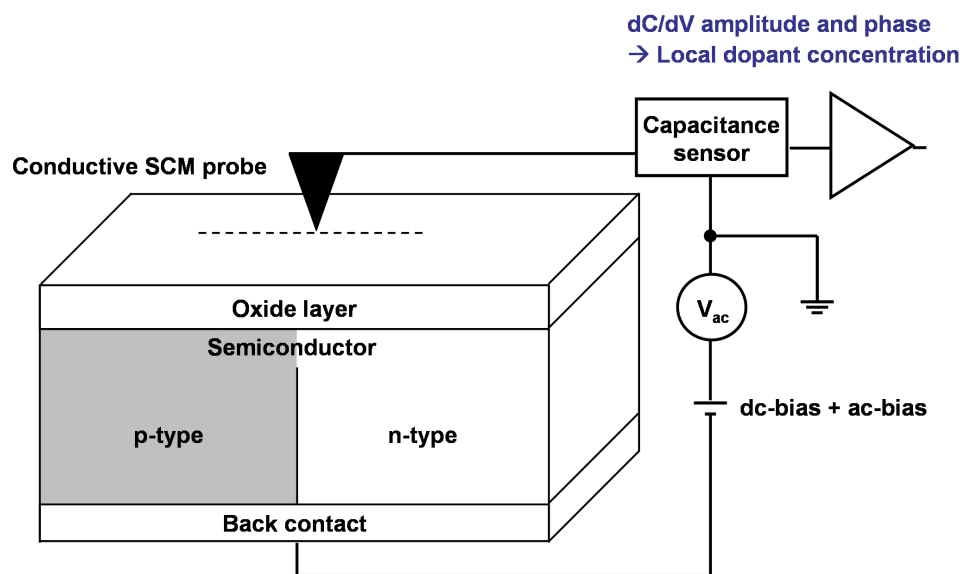


Figure 2.3: Measurement principle of scanning capacitance microscopy (SCM). When the conductive probe is in contact, a metal-oxide-semiconductor (MOS) capacitor is formed between the probe and the semiconducting sample with a thin oxide layer on top. A dc-bias and an ac-bias are applied between the cantilever and the back contact of the sample. By means of a capacitance sensor and a lock-in amplifier, relative variations in the capacitance of the formed MOS structure are detected. SCM provides a two-dimensional map of the dC/dV amplitude and phase. Adapted from Ref. [85].

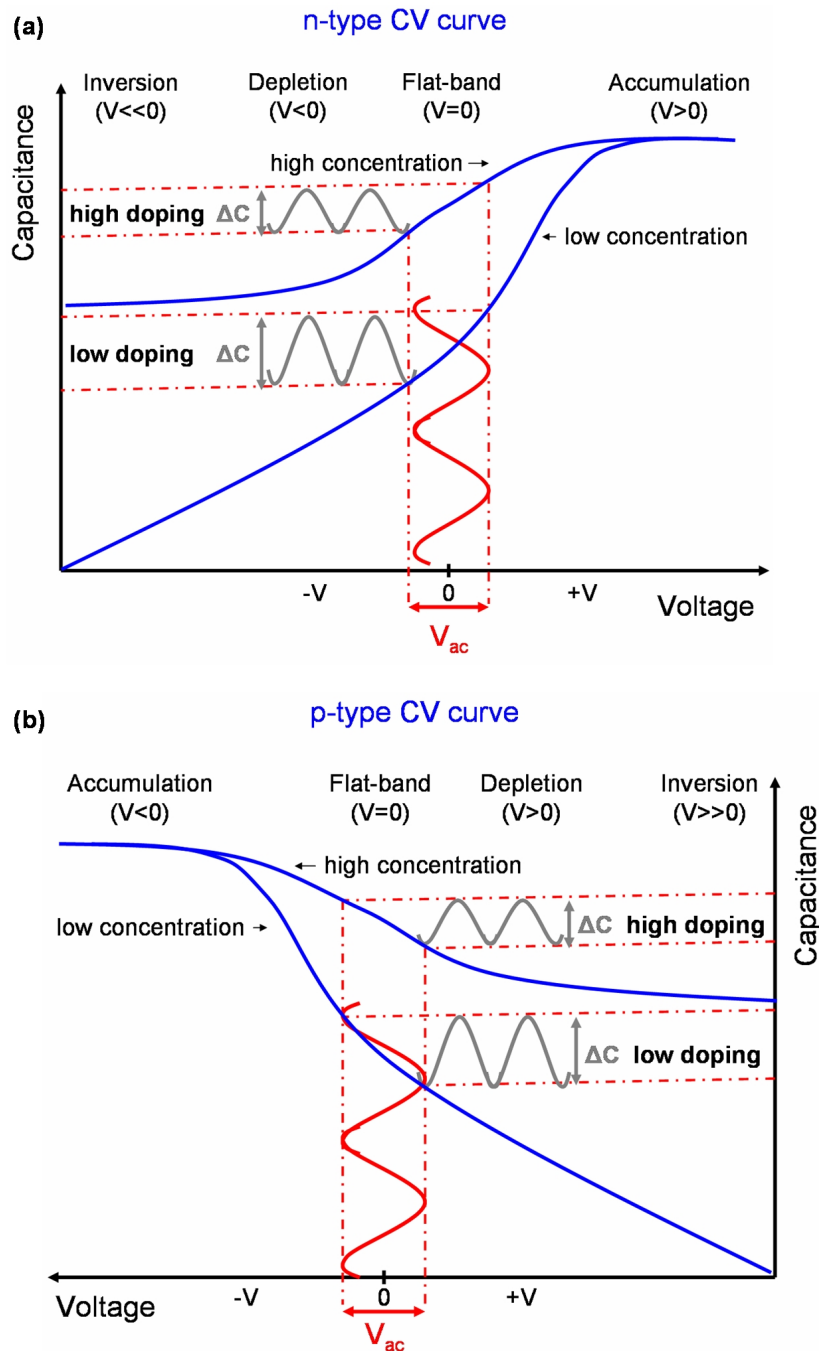


Figure 2.4: High-frequency CV curves of (a) an *n*-type and (b) a *p*-type ideal metal-oxide-semiconductor structure formed during the scanning capacitance microscopy measurement. The magnitude of the capacitance change versus the applied bias dC/dV provides information about the concentration of charge carriers. The sign of the slope of dC/dV allows a conclusion about the type of majority charge carriers. Adapted from Refs. [86, p. 10] and [87, p. 206].

changing the probe-sample capacitance. The change of the capacitance of the MOS diode is measured by means of a GHz resonant capacitance circuit.

In Fig. 2.4 the expected high-frequency CV curves of an MOS capacitor with an *n*-type [Fig. 2.4(a)] and a *p*-type [Fig. 2.4(b)] semiconductor are presented. The magnitude of the capacitance change, i.e. the amplitude of the SCM signal, provides information about the charge carrier concentration. Note that the amplitude decreases with increasing dopant concentration. The sign of the slope of dC/dV may be analysed by means of the phase of the SCM signal and allows a conclusion about the type of majority charge carriers.

In Fig. 2.5 the results of a SCM measurement across a conventional SRAM cell (Sect. 3.1.1) are presented. The surface topography is displayed in Fig. 2.5(a), while dC/dV amplitude and phase are shown in Fig. 2.5(b) and (c), respectively. The topography image has been treated with a flattening procedure. Flattening is commonly used to remove artefacts from the acquisition process. For example, it is unlikely that the sample surface is positioned perpendicular to the tip [88]. Further artefacts may be introduced by optical interference in the detection system, nonlinearity in the x - y motion of the piezoelectric scanner, and random tip jumps [88]. These artefacts may be reduced by applying polynomial or plane flattening procedures [89]. Nevertheless, it is a well-known problem that although flattening can minimize height artefacts on smooth surfaces further artefacts are introduced when images with high features are processed [90]. This effect is observed in the topography image in Fig. 2.5(a), where artefacts along the fast scan axis lead to deep artificial valleys between the higher device units. This important limitation of flattening procedures as well as the fact that artefacts like sample tilt and random tip jumps can not be identified without doubt in images of electrical signals lead to the fundamental conclusion that flattening of electrical data has to be avoided. Flattening of images of electrical data may change the contrast which prevents a correct quantitative interpretation of the measured data.

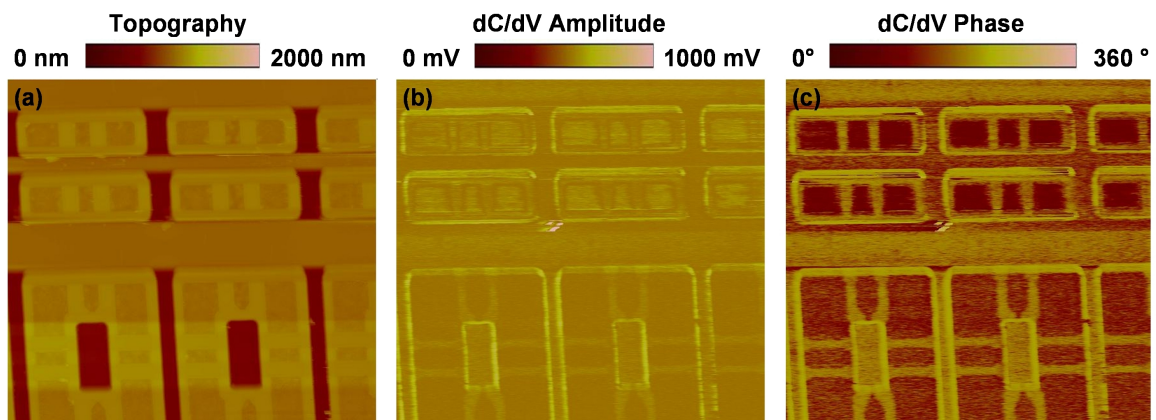


Figure 2.5: Scanning capacitance microscopy data probed on a conventional Si static random access memory cell (Sect. 3.1.1). (a) Surface topography, (b) dC/dV amplitude and (c) dC/dV phase.

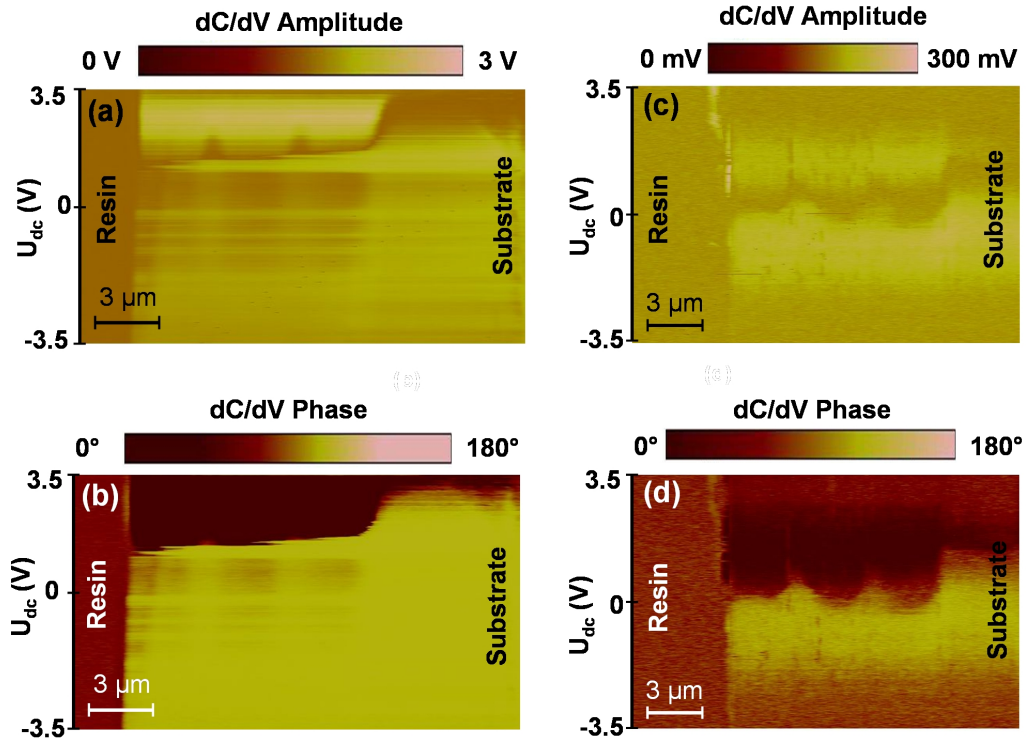


Figure 2.6: Scanning capacitance microscopy (SCM) data probed on the cross-sectionally prepared Si:B epilayer sample introduced in Sect. 3.1.2. The dC/dV amplitude and phase recorded by means of an NSG20 Au coated cantilever are plotted in (a) and (b), respectively. In (c) and (d) the dC/dV amplitude and phase probed by means of an SCM-PIC Pt/Ir coated cantilever are shown. The recorded SCM data strongly depend on the conductive probe geometry and material. (Measurements by Stephan Streit, HZDR). Adapted from Ref. [91].

Therefore, all images of electrical data, in particular the SCM data and KPFM bias data, presented in this work have *not* been treated with flattening procedures and reflect the original scan data.

The quantitative analysis of the measured SCM data is difficult. For particular aims like the quantitative dopant profiling in semiconductors, special setups have to be applied, as for example ultrahigh-precision capacitance bridges [27] which demand very time-consuming calibration procedures. Another significant disadvantage of the SCM technique is that the measured SCM signal strongly depends on probe conditions, sample preparation and dielectric film properties [32]. In the following, this problem regarding quantitative SCM is discussed by the example of SCM data probed with two different types of conductive cantilevers on a cross-sectionally prepared Si:B epilayer sample. The Si:B epilayer structure consists of three B-doped layers of $3 \mu\text{m}$ thickness with two $1 \mu\text{m}$ thick spacer layers in between. The epilayer sample is introduced in Sect. 3.1.2 and investigated in this work in detail by means of KPFM (Sect. 6.2.1).

The SCM measurements have been performed by means of a Dimension 3100 scanning probe microscope from Veeco Instruments (since 2010 Bruker Corp.). The DI 3100 system works with an ultrahigh frequency (880–1050 MHz) resonant capacitance sensor and has a sensitivity of 10^{-22} F/ $\sqrt{\text{Hz}}$ [86]. In Fig. 2.6 the results of the SCM measurement across the cross-sectionally prepared Si:B epilayer sample are presented. The SCM measurements have been carried out using a NSG20 Au coated cantilever [Fig. 2.6(a) and (b)], and a SCM-PIC Pt/Ir coated cantilever [Fig. 2.6(c) and (d)], respectively. For recording the dC/dV data, one line across the Si:B epilayer structure has been scanned repeatedly while changing the applied dc-bias U_{dc} from +3.5 V to -3.5 V in steps of 0.1 V. Strong differences occur in dependence on the probe material. The SCM amplitude probed with the NSG20 cantilever reflects only weakly the epilayer structure [Fig. 2.6(a)]. The most dominant feature is the SCM phase shift probed at a dc-bias of 1.5 V and 3.0 V across the epilayer region and the substrate region, respectively [Fig. 2.6(b)]. Using the SCM-PIC cantilever the SCM amplitude shows much more details in the epilayer region [Fig. 2.6(c)]. The SCM phase shift is observed at a dc-bias of 0 V across the epilayer region and at 1.5 V above the substrate region. It can be concluded from these measurement results that the SCM signal differs in dependence on the applied cantilever type. Therefore, the extraction of the sample contribution to the SCM signal is complicated.

The lateral resolution of SCM is limited by the measurement technique itself. At zero bias, the depletion zone which is formed during the probe-sample interaction restricts the lateral resolution to 50–100 nm [32]. This problem may be solved by new technical approaches to SCM as for example the scanning capacitance spectroscopy [92–95]. Additionally, developments have been made towards non-contact SCM techniques [96, 97].

2.4 Scanning microwave microscopy

Scanning microwave microscopy has been developed in 2008 by Agilent Technologies and was introduced in Ref. [33]. For the SMM mode a conventional AFM is combined with a vector network analyzer. The measurement principle is illustrated in Fig. 2.7. The conductive probe is scanned over the sample in contact mode. The performance network analyzer (PNA) generates a microwave signal in the GHz range which is transmitted through a matched resonant circuit to the conductive probe. The amount of reflected microwaves compared to the amount of incident microwaves is measured and depends on the mismatch between the sample impedance and the transmission line impedance, and thus on the sample properties [34]. In standard SMM the PNA amplitude and phase are mapped simultaneously with the surface topography. By means of a calibration the detected PNA amplitude and phase can be related to capacitance and dopant density values [98]. If a doping profile measurement module (DPMM) [99] is added to the SMM setup, also the dC/dV amplitude and phase can be detected [100] and compared to SCM (Sect. 2.3).

First measurements of representative test samples like conventional SRAM cells revealed that the measured SMM signal mainly depends on the sample and not on the conductive probe. In Fig. 2.8 the results of SMM measurements [98] across a SRAM cell are presented.

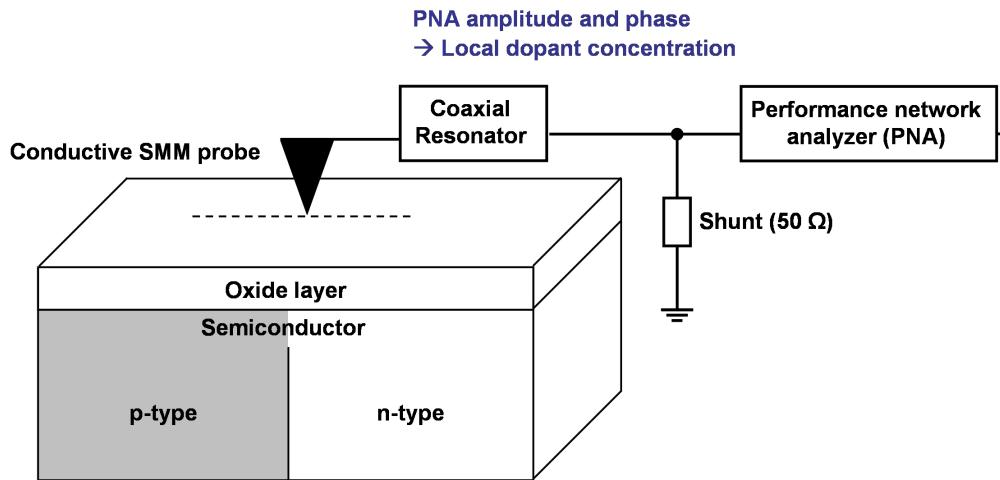


Figure 2.7: Measurement principle of scanning microwave microscopy (SMM). A performance network analyzer (PNA) generates a microwave signal in the GHz range which is transmitted through a matched resonant circuit to the conductive probe. The ratio between reflected and incident microwaves is measured. SMM provides a two-dimensional map of the PNA amplitude and phase. Adapted from Ref. [34].

This SRAM cell is comparable to the SRAM sample investigated in this work (Sect. 3.1.1), though the topographic pattern of both SRAM cells differs in particular at the edges of the device units. Surface topography, capacitance, and dC/dV signals are shown in Fig. 2.8(a), (b) and (c), respectively. The images of capacitance and dC/dV provide qualitative information about the dopant distribution. For quantitative interpretation of the SMM data a calibration procedure is required which is described in detail in Ref. [34].

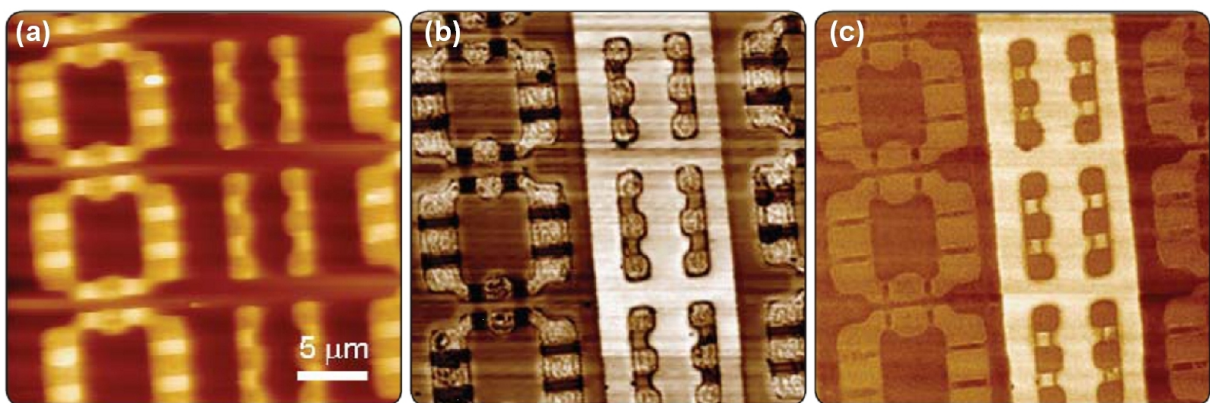


Figure 2.8: (a) Topography, (b) capacitance, and (c) dC/dV images of a Si static random access memory chip acquired with a scanning microwave microscope. The underneath n -type (bright) and p -type (dark) doped structures are clearly identified in the capacitance and the dC/dV image. From Ref. [98]. (Copyright by Agilent Technologies - Reproduced with permission.)

The sensitivity and signal-to-noise-ratio of SMM is significantly enhanced compared to conventional electrical nanometrology techniques, where the small signal-to-background ratio limits both, sensitivity and lateral resolution [33]. Thus, SMM significantly advances electrical nanometrology measurements on metals, semiconductors and insulators, compared for example to SCM (Sect. 2.3).

2.5 Electrostatic force microscopy

EFM is a non-contact dynamic SPM technique in which electrostatic forces between a conductive probe and the sample surface are detected. The measurement principle of EFM is illustrated in Fig. 2.9. During the EFM measurement the conductive cantilever vibrates at its resonance frequency f_r for detecting the surface topography. Additionally, an applied electric field oscillates at the operation frequency f_{ac} . As displayed schematically in Fig. 2.10(a), the vibration amplitude of the cantilever at f_{ac} depends on the dopant concentration in the semiconducting sample and increases with increasing electrostatic forces, i.e. with decreasing dopant concentration. Depending on the applied EFM system, the topography and the electrical signal can be detected simultaneously or one after the other.

A special measurement mode of EFM is Kelvin probe force microscopy. In KPFM the electrostatic forces acting onto the cantilever are minimized by applying an appropriate external dc-bias. The applied, appropriate dc-bias is referred to as *KPFM bias* U_K and recorded as KPFM measurement signal.

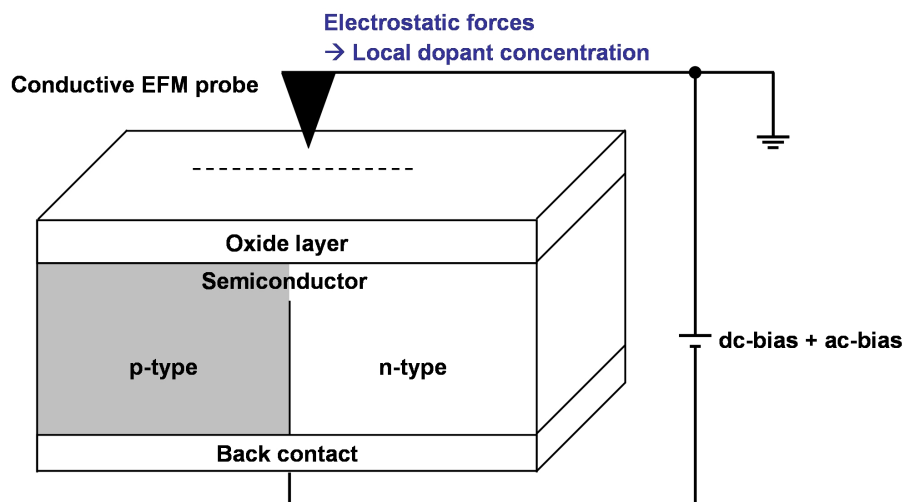


Figure 2.9: Measurement principle of electrostatic force microscopy (EFM). A dc-bias and an ac-bias are applied between the conductive probe and the back contact of the sample. The cantilever deflection due to electrostatic forces is detected. EFM provides a two-dimensional map of an electrical signal which is related to the electrostatic forces, and thus to the local dopant concentration in the semiconductor.

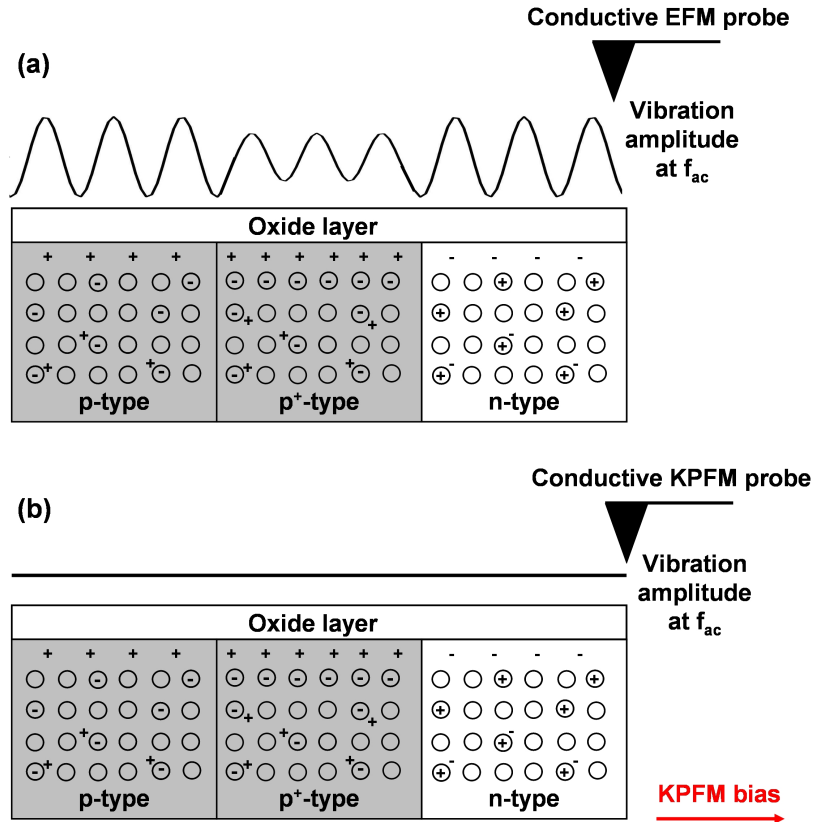


Figure 2.10: Comparison between the measurement principles of (a) electrostatic force microscopy (EFM) and (b) amplitude-modulated (AM) Kelvin probe force microscopy (KPFM). In EFM, the vibration amplitude of the conductive cantilever changes in dependence on the electrostatic forces, i.e. in dependence on the dopant concentration in locally doped semiconductors. In AM-KPFM, the dc part of the applied bias is used to nullify the vibration amplitude of the cantilever at the operation frequency f_{ac} and thus to minimize the electrostatic forces. The applied, appropriate dc-bias is recorded and referred to as the KPFM bias.

One has to distinguish between amplitude-modulated (AM) and frequency-modulated (FM) KPFM [101, p. 36]. In AM-KPFM, which is applied in the presented work and schematically shown in Fig. 2.10(b), the amplitude of the cantilever at the operation frequency f_{ac} is nullified in order to minimize the electrostatic forces acting onto the conductive cantilever. FM-KPFM is based on the fact that the gradient of the electrostatic forces modulates the resonance frequency f_r of the cantilever and causes oscillation amplitudes at the frequencies f_{ac} and $2f_{ac}$. Thus, side bands at $f_r \pm f_{ac}$ and $f_r \pm 2f_{ac}$ occur in the KPFM frequency spectrum. The KPFM bias is adjusted so that the frequency modulation of f_r and thus the oscillation amplitude of the side bands at $f_r \pm f_{ac}$ vanishes. [101, p. 36]

Since its introduction in 1991, KPFM was applied to investigate various aspects as for example the electric properties of metals [36], doped semiconductors [44, 45], and even

of insulators [54]. KPFM was also used to examine voltage drops in metal interconnects and planar resistors [102], the band bending at semiconducting surfaces [103], degradation processes in heterostructures [104], and the electronic properties of organic solar cells [55]. A new field of application of the KPFM technique is the investigation of biomolecules [56–58].

For the quantitative evaluation of the probed KPFM bias, the electrostatic forces in the cantilever-sample system and their minimization during KPFM measurements have to be understood. In this work, the focus lies on the investigation of locally doped semiconductors by means of KPFM. In the following Sect. 3.1, the investigated semiconducting samples are introduced. The technical and physical aspects of KPFM measurements on semiconductors are discussed in detail in Sect. 5.

3 Experimental details

3.1 Semiconducting samples

3.1.1 Silicon static and dynamic random access memory cells

The Si static random access memory (SRAM) and Si dynamic random access memory (DRAM) integrated circuits investigated in this work are standard SCM test samples supplied by Veeco Instruments (since 2010 Bruker Corp.).

In memory devices digital information are stored in terms of bits. For large memories, commonly the random access memory (RAM) concept is applied where memory cells are organized in a matrix structure and data can be accessed in random order. [105, p. 507] SRAM and DRAM cells are volatile RAM devices which lose the stored information when the power supply is switched off [105, p. 214].

An SRAM cell is a flip-flop circuit where each bit is stored as a voltage. One SRAM cell contains at least six MOSFETs, i.e. four enhancement-mode MOSFETs and two depletion-mode MOSFETs. Due to the working principle of SRAM cells, the stored information is retained as long as the power supply is kept switched on. [105, p. 507]

The main advantage of SRAM cells is the high-speed processing. However, SRAM cells have a large power consumption and a low accessible density. [105, p. 214]

For decreasing the unit size and the power consumption DRAM cells have been developed. A DRAM cell is a simply structured circuit combining one MOSFET and one capacitor. Charging and discharging of the capacitor is controlled by the MOSFET. The voltage level of the charged or discharged capacitor defines then the logic state of the cell. A crucial disadvantage of DRAM cells is that permanent refreshing of the stored data is necessary due to charge leakage. Refreshing is achieved by reading and writing the information every few milliseconds. [105, p. 507]

However, due to the simple structure of the DRAM unit, a high accessible density can be achieved [105, p. 214].

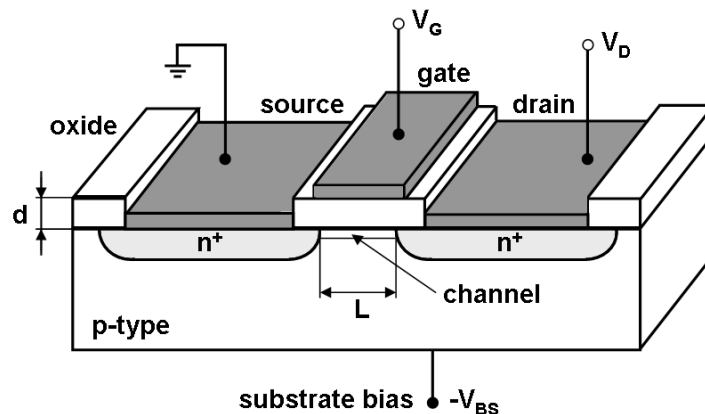


Figure 3.1: Schematic illustration of an n-MOSFET with the channel length L and the oxide thickness d . The dark grey areas are ohmic metal contacts. Adapted from Ref. [106, p. 593].

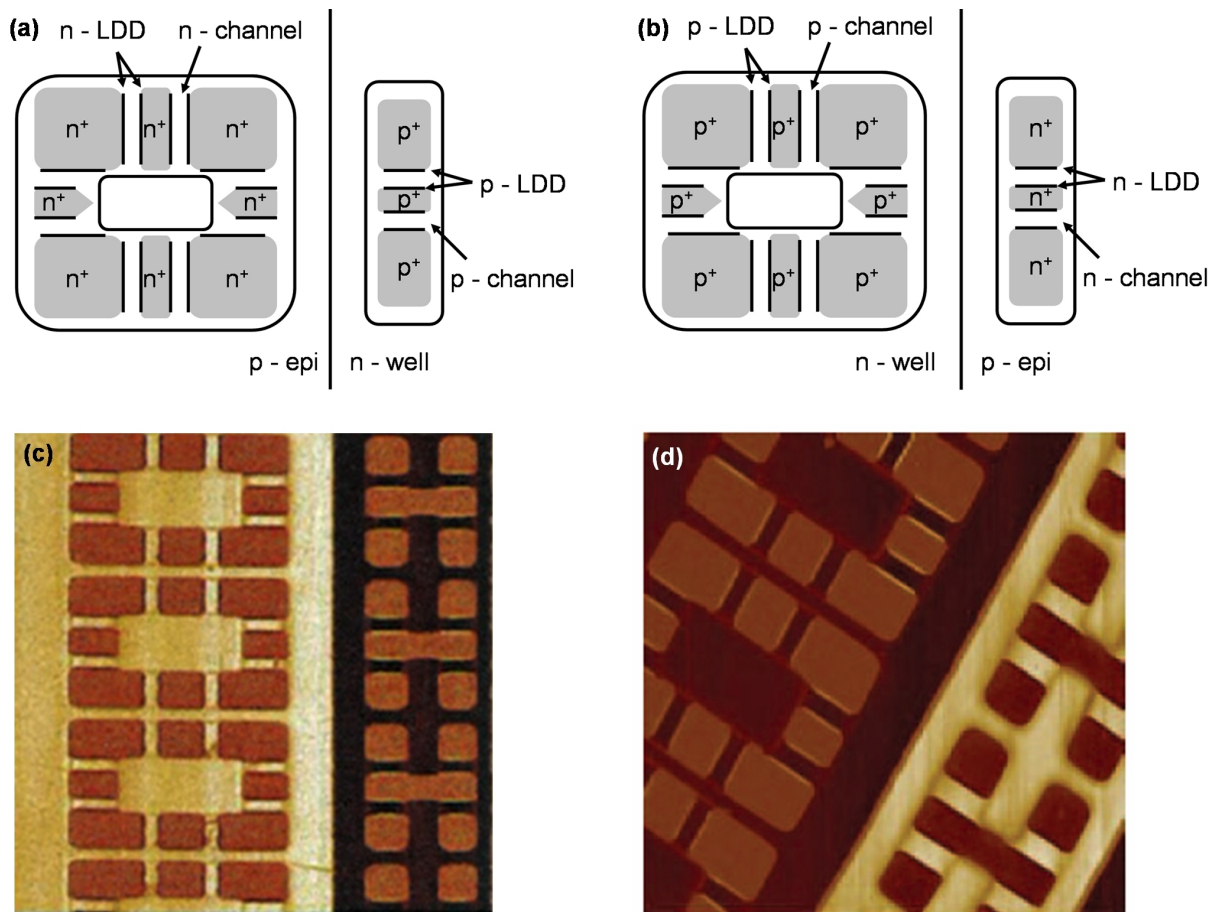


Figure 3.2: Schematic doping pattern of the (a) Si static random access memory (SRAM) and (b) Si dynamic random access memory (DRAM) cells supplied by Veeco Instruments (since 2010 Bruker Corp.) as scanning capacitance microscopy (SCM) test samples. Adapted from Refs. [107, 108]. From the SCM data images of the (c) SRAM [107] and the (d) DRAM [66] cell the type of the majority charge carriers can be identified, i.e. the n -type (dark colour) and p -type (bright colour) doped regions. (Figs. (c) and (d) ©Bruker Corp. - Reproduced with permission.)

In the following the structure and the basic working principle of MOSFETs are explained by the example of an n -MOSFET illustrated schematically in Fig. 3.1. A detailed discussion can be found in Refs. [106, p. 592f] and [87, p. 297f]. The n -MOSFET consists of two n^+ -type regions in a p -type conducting substrate, i.e. the source and the drain, with ohmic metal contacts on top. The gate diode between source and drain is a metal-oxide-semiconductor diode with the oxide thickness d . The distance between the source and the drain defines the channel length L of the n -MOSFET.

The working principle of MOSFETs is based on a current flow through the channel from source to drain which is variable by means of the gate voltage V_G . When ground or a low gate voltage is applied to the n -MOSFET, a depletion layer is present underneath the gate diode and the channel is closed. When applying a sufficiently large positive gate voltage, a surface inversion layer forms underneath the gate diode. This layer is an n -type conduct-

ing channel which enables a current flow between source and drain. By varying the gate voltage V_G the conductance of the channel can be modulated. For additional modulation of the channel conductance a voltage may be applied to the substrate contact, i.e. the back surface voltage V_{BS} . [106, p. 592f], [87, p. 297f]

For electrical nanometrology test measurements, the SRAM and DRAM cells have been step-by-step de-processed to bare Si by Veeco Instruments. The process is described in detail in Ref. [108] and summarized in the following. In a first step, reactive ion etching (O_2 , CF_4 , radio frequency 300 W) is applied to remove the passivation, metal gate electrodes, oxide and silicon layers. After this, an aluminum etching (16:1:1:1, phosphoric acid:nitric acid:acetic acid:H₂O) is carried out followed by a final HF etching (49% HF vol/vol). After de-processing, the SRAM and DRAM cells have a similar surface topography and only differ in doping pattern. The schematic doping pattern of the SRAM and DRAM cell is illustrated in Fig. 3.2(a) and (b), respectively. In Fig. 3.2(c) and (d) corresponding SCM data of the SRAM and DRAM cell from Veeco Instruments are shown. From the SCM data the type of majority charge carriers can be deduced (Sect. 2.3) and the n -type (dark colour) and p -type (bright colour) doped regions are identified.

The dopant concentration, species, ion dose, and implantation energy of the SCM test samples are summarized in Tab. 3.1. Note that the "n-channel" regions located between the n^+ -type regions are p -type conducting. The "p-channel" regions prepared between the p^+ -type regions are n -type conducting. The p-epi region is not implanted.

Table 3.1: Doping type, dopant concentration, species, ion dose, and implantation energy of the doped regions in the SCM test samples supplied from Veeco Instruments (since 2010 Bruker Corp.). Data taken from Ref. [107].

	Doping type	Dopant concentration (cm^{-3})	Dopant species	Dose (cm^{-2})	Energy (keV)
n - well	n	2×10^{17}	P^+	1.7×10^{13}	900
p - channel	n	1×10^{17}	P^+	1×10^{12}	175
p - LDD	p	3×10^{18}	BF_2^+	6×10^{13}	40
p^+	p	4×10^{19}	BF_2^+	2×10^{15}	45
p - epi	p	2×10^{16}			
n - channel	p	2×10^{17}	BF_2^+	2×10^{12}	30
n - LDD	n	5×10^{18}	P^+	6×10^{13}	40
n^+	n	2×10^{20}	As^+	4×10^{15}	100

The SRAM and DRAM cells contain *lightly doped drain* (LDD) regions which are used to extend the drain region. Thereby, high electric fields are relieved and related hot carrier effects are minimized [109]. Additionally, MOSFETs containing LDD regions offer an improved threshold voltage stability due to short-channel effects [110].

In the SRAM and DRAM cells BF_2^+ implantation is used for doping of the *p*-type regions. BF_2^+ is commonly chosen as a B dopant source due to beneficial effects of the co-implantation of fluorine. For example, after the BF_2^+ implantation the electrical activation of B is enhanced compared to the B^+ implantation [111]. Additionally, the diffusion depth of B during thermal treatment is decreased if BF_2^+ instead of B^+ is implanted [112].

The results of the KPFM measurements on the SRAM and DRAM cell are discussed in Sect. 6.1.

3.1.2 Cross-sectionally prepared silicon epilayer samples

The Si epilayer samples have been grown epitaxially at the Fraunhofer Institute for Photonic Microsystems Dresden (Fraunhofer IPMS). Two different types of Si epilayers are investigated in this work. In Fig. 3.3(a) and (b) the structure of the Si:B and the Si:P epilayer sample is illustrated, respectively.

The Si:B epilayer structure has been grown on a P-doped Si substrate. The epilayer structure consists of three B-doped layers of $3\ \mu\text{m}$ thickness with two $1\ \mu\text{m}$ thick spacer layers in between [Fig. 3.3(a)]. The Si:B epilayer sample has been investigated by means of Secondary ion mass spectrometry (SIMS) which is introduced in Sect. 3.3.1. From the SIMS results an acceptor concentration of $4.7 \times 10^{16}\ \text{cm}^{-3}$ (near-substrate Si:B layer), $8.3 \times 10^{16}\ \text{cm}^{-3}$ (central Si:B layer), and $1.2 \times 10^{17}\ \text{cm}^{-3}$ (top Si:B layer) has been determined, respectively. The donor concentration in the P-doped substrate amounts to $1.4 \times 10^{15}\ \text{cm}^{-3}$. In the spacer layers substrate conditions are expected. However, the spacer layers could not be resolved satisfyingly by the SIMS measurements. In general, the only $1\ \mu\text{m}$ thick spacer layers are strongly determined by the space charge regions forming between the spacer layers and the neighbouring Si:B layers. These space charge regions have a width of about 800 nm from the *pn* interface in the spacer layers and thus strongly overlap. The influence of those intrinsic electric fields in the Si:B epilayer sample on the KPFM measurement is discussed in detail Sect. 6.2.1.3. Quantitative dopant profiling is demonstrated in Sect. 6.2.1.1 by means of the *pn* junction between the P-doped substrate and the near-substrate B-doped epilayer.

The Si:P epilayer structure has been grown on a B-doped Si substrate and contains three P-doped layers of $3\ \mu\text{m}$ thickness with two $1\ \mu\text{m}$ thick spacer layers in between [Fig. 3.3(b)]. SIMS measurements have been performed on the Si:P epilayer sample and from the results a donor concentration of $6.5 \times 10^{15}\ \text{cm}^{-3}$ (near-substrate Si:P layer), $7.7 \times 10^{15}\ \text{cm}^{-3}$ (central Si:P layer), and $9.1 \times 10^{15}\ \text{cm}^{-3}$ (top Si:P layer) is deduced. The B-doped substrate contains an acceptor concentration of $1 \times 10^{15}\ \text{cm}^{-3}$. In the spacer layers substrate conditions are expected. Nevertheless, also in the Si:P epilayer sample the spacer layers could not

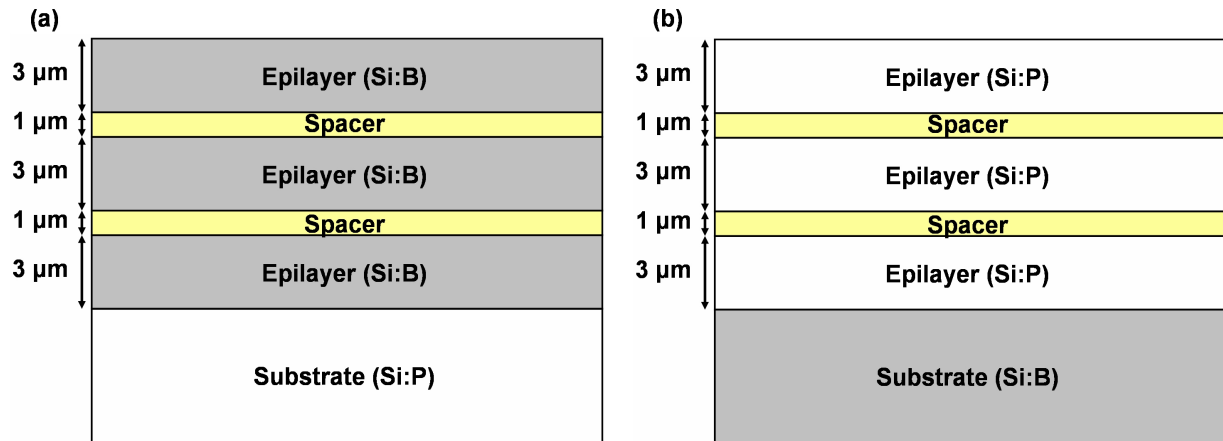


Figure 3.3: Schematic cross-sectional view of the (a) Si:B and (b) Si:P epilayer structure grown epitaxially on doped Si substrates at the Fraunhofer Institute for Photonic Microsystems Dresden.

be resolved satisfyingly by the SIMS measurements. Similar to the Si:B epilayer sample, the spacer layers in the Si:P epilayer sample are strongly determined by the space charge regions forming between the spacer layers and the neighbouring Si:P layers. In the Si:P epilayer sample, the space charge regions in the spacer layers have a width of about 850 nm from the pn interface and thus overlap. The influence of these intrinsic electric fields in the Si:P epilayer sample on the KPFM measurement is discussed in Sect. 6.2.2.2. Similar to the Si:B epilayer sample, quantitative dopant profiling is demonstrated by means of the pn junction between the B-doped substrate and the near-substrate P-doped epilayer which is presented in Sect. 6.2.2.1.

For the KPFM measurements the epilayer samples have been prepared cross-sectionally at the SGS Institut Fresenius GmbH Dresden. In a first step the Si wafers have been cut to expose the cross-section. After cleaving, the sample pieces were embedded edgewise in

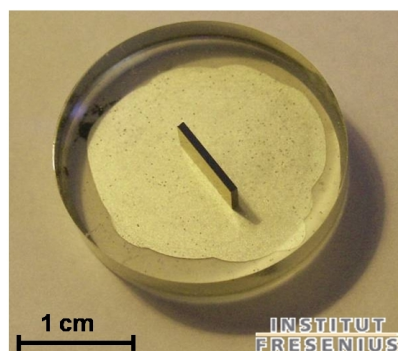


Figure 3.4: Cross-sectionally prepared Si epilayer sample embedded in epoxy resin with visible back contact. The cross-sections have been prepared at the SGS Institut Fresenius GmbH Dresden.

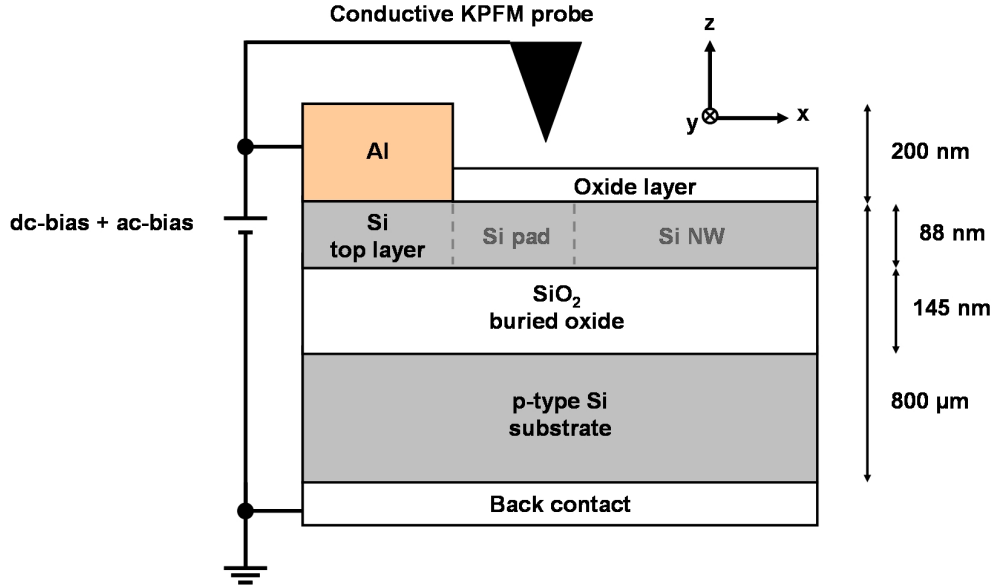


Figure 3.6: Schematic cross-sectional view of the silicon-on-insulator (SOI) structure including Si pad and horizontal Si nanowires (NWs) contacted for KPFM measurements. Note that the Si pad and the Si NWs are covered by an approximately 2 nm thick native oxide layer. To short-circuit the insulating buried oxide layer for KPFM measurements, an Al contact is deposited on top and connected with the sample back contact by means of silver conductive paint.

silicon-on-insulator (SOI) structure with a sample-specific 88 nm thick Si top layer with (001)-orientation, and a 145 nm thick SiO₂ buried oxide (BOX) layer below. In Fig. 3.6 the schematic cross-section of the SOI sample structure is shown. The Si substrate is lightly *p*-type conducting with an acceptor concentration of $1 \times 10^{15} \text{ cm}^{-3}$. As a consequence of the preparation process of the SOI structure, the Si top layer features a very low *p*-type background doping of less than $1 \times 10^{15} \text{ cm}^{-3}$. Note that the Si top layer is covered by a native oxide layer of approximately 2 nm thickness.

By means of electron-beam lithography (EBL) and reactive ion etching the Si top layer is patterned in $10 \mu\text{m}$ wide pad regions and arrays of nanowires with widths ranging from 10 nm to $2 \mu\text{m}$. In Fig. 3.7 a schematic top view of the prepared Si pad and the adjacent NW arrays is illustrated. The Si NWs have a uniform length of $65 \mu\text{m}$. The use of EBL and top-down processing provides several advantages compared to chemical vapour deposition (CVD) methods, in particular an enhanced control of the location on the sample and thus controlled alignment [113]. As a consequence, all NWs are very conform in length and width. In general, lithographically fabricated NWs are more precise and reproducible which simplifies their integration into a device architecture [113]. However, transmission electron microscopy (TEM) measurements performed in the Research Center Jülich indicate that the NWs have a slightly trapezoidal shape with the smaller side on top after processing. After transferring the structures into the Si top layer, the samples have been implanted. A photo-resist implantation mask was defined by EBL in order to protect certain segments of the patterned Si top layer against implantation. For each dopant species, implantation

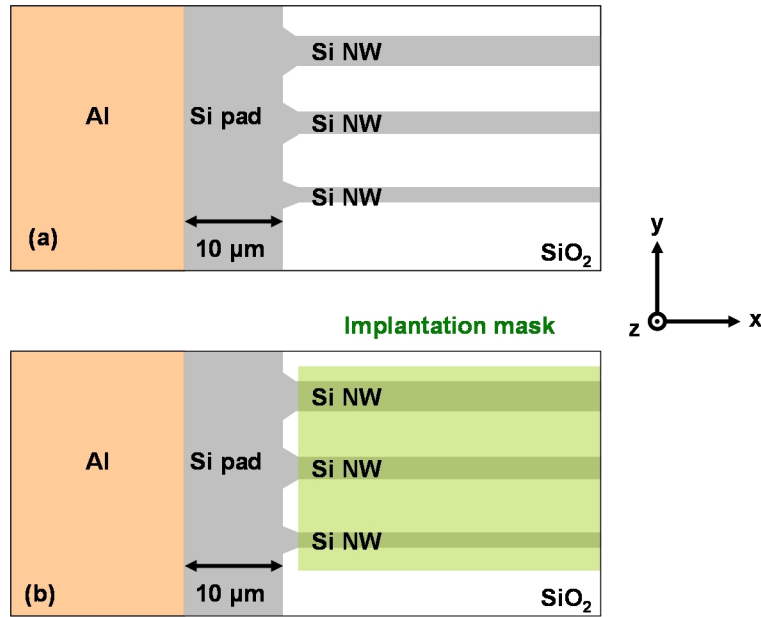


Figure 3.7: Schematic top view of the arrays of (a) implanted and (b) unimplanted horizontal Si nanowires (NWs) of different widths ranging from 10 nm to 2 μm . The implanted Si pad and the Al contact layer are illustrated schematically. Note that the Si pad and the Si NWs are covered by an approximately 2 nm thick native oxide layer.

masks have been employed to prepare implanted [Fig. 3.7(a)] and unimplanted [Fig. 3.7(b)] NWs, respectively. Note that the adjacent $10\ \mu\text{m}$ thick Si pad is always implanted.

The samples are doped by means of ion implantation of As and B at an energy 10 keV and 2.5 keV with a dose of $2 \times 10^{15}\ \text{cm}^{-2}$ and $1 \times 10^{15}\ \text{cm}^{-2}$, respectively, and an angle of incidence of 7° . Implantation conditions were chosen such that a sufficiently thick crystalline seed layer remained after the implantation in order to obtain full recrystallization of the implanted Si top layer during annealing [113]. The implantation parameters are summarized in Tab. 3.2. For a first estimation of the dopant distribution in the Si top layer after implantation, SRIM calculations (Sect. 3.3.2) have been performed. With the implantation parameters given in Tab. 3.2, the SRIM calculations reveal a Gauss distribution of As atoms with a maximum concentration of $2 \times 10^{21}\ \text{cm}^{-3}$ at a mean implantation depth of approximately 13 nm [full width half maximum (FWHM) $\cong 9$ nm]. For B-implantation a Gauss distribution of B atoms with a maximum concentration of $5 \times 10^{20}\ \text{cm}^{-3}$ at a mean implantation depth of approximately 13 nm (FWHM $\cong 15$ nm) is calculated.

After implantation, the photo-resist implantation mask has been removed wet chemically. Then the samples have been subjected to a rapid thermal annealing (RTA) for 5 sec at $1000\ ^\circ\text{C}$. Athena simulations including the applied implantation and annealing conditions have been performed in the Research Center Jülich to obtain information about the dopant distribution. With the Athena software trajectories of implanted ions can be modeled by

Table 3.2: Implantation parameters for the preparation of B-doped and As-doped nanowire arrays. Additionally, the dopant concentration and implantation depth after annealing obtained from Athena simulations performed in the Research Center Jülich are given.

Dopant species	Implantation		Athena simulations	
	Energy (kV)	Dose (cm^{-2})	Dopant concentration (cm^{-3})	Implantation depth (nm)
B	2.5	1×10^{15}	1×10^{20}	50
As	10	2×10^{15}	5×10^{20}	30

means of Monte Carlo calculations in order to determine the final distribution of stopped particles [115, p. 201ff]. Additionally, diffusion of implanted ions during thermal treatment can be calculated by means of user-specifiable models based on the concepts of *pair diffusion* and *chemical and active concentration values* [115, p. 130ff]. A detailed introduction of the Athena simulation software is given in Ref. [115].

The results of the Athena simulation are listed in Tab. 3.2. It is found that both, the *p*-type and the *n*-type NW samples, feature a box-like dopant distribution with comparable concentration of activated dopants after implantation and RTA. However, the implantation depth along *z* (Fig. 3.6) differs remarkably for As and B implantation. Note that the 88 nm thick Si top layer is implanted only in the near-surface region while deeper regions remain unimplanted. For B implantation and annealing the simulated acceptor concentration amounts to approximately $1 \times 10^{20} \text{ cm}^{-3}$ in the near-surface region of the Si top layer, i.e. to a depth of approximately 50 nm. Below 50 nm, the acceptor concentration decreases steadily to approximately $1 \times 10^{16} \text{ cm}^{-3}$ at the bottom of the Si top layer, i.e. at a depth of 88 nm. After As implantation and annealing the simulated donor concentration amounts to $5 \times 10^{20} \text{ cm}^{-3}$ which is reasonably constant to an implantation depth of approximately 30 nm. Below 30 nm, the As-concentration decreases to $1 \times 10^{14} \text{ cm}^{-3}$ at the bottom of the Si top layer at a depth of 88 nm.

For the KPFM measurements, the fabricated Si top layer has to be contacted electrically. On well-defined positions a 200 nm thick Al contact layer has been deposited as metalization via a lift-off process on the Si top layer. To short-circuit the insulating BOX layer, the deposited Al layer has been connected to the sample back contact by means of silver conductive paint. The deposited Al layer is illustrated schematically in the cross-sectional view of the SOI structure in Fig. 3.6 and in the top view in Fig. 3.7.

The results of the KPFM measurements on the Si NW samples are presented in Sect. 6.3.

3.2 Kelvin probe force microscopy setup

3.2.1 Ambient KPFM

The KPFM measurements under ambient conditions presented in this work have been performed by means of a Level-AFM from Anfatec Instruments AG. The technical details of the Level-AFM system which is shown in Fig. 3.8 are given in detail in Ref. [116]. The Level-AFM system consists of a base plate made of stone with wiring, a vibration isolation, a standard AFM body and head, and a high voltage amplifier V45C. The AFM head holds the cantilever by a spring loaded mechanism. All electronic components for the laser and the photo diode, the specialized lens and mirror system and the fine mechanics are integrated in the head. The height resolution is better than 0.2 nm, which enables the detection of atomic steps and layers. [116]

The schematic experimental setup of the Level-AFM is shown in Fig. 3.9. The Level-AFM works in an non-destructive dynamic non-contact mode. During the measurement the oscillating conductive cantilever is scanned by means of a piezo scanning device over the sample surface. A laser beam is reflected from the cantilever backside and detected in a position-sensitive photodetector. The oscillation amplitude of the cantilever at its resonance frequency $f_r = \omega_r/(2\pi)$ is influenced by short-range van der Waals forces and is therefore used to control the distance between tip and sample surface. A lock-in amplifier analyses the detector signal at the cantilever resonance frequency f_r and passes the determined amplitude value to a feedback control system that re-adjusts the tip-sample distance. The required displacement of the z-piezo is recorded as topography signal.

The Level-AFM head contains a colour-camera with a direct view onto the cantilever and an integrated illumination system consisting of two LED lamps (9000 lm white and 18000 lm green) [116]. This enables a precise positioning of the cantilever and by that the also precise choice of the measurement position. As the conductivity of semiconducting samples may be increased by illumination due to the photogeneration of charge carriers, the illumination system is switched off during the KPFM measurements. Additionally, the whole Level-AFM is operated under an opaque cover. The laser diode produces a red laser beam with a wavelength of 670 nm and a maximum power of 3 mW. The influence of the laser light on the semiconducting samples is discussed in Sect. 6.2.1 by the comparison of 1D and 2D KPFM scans on the cross-sectionally prepared Si:B epilayer sample.

For the detection of electrostatic forces a voltage U is applied to the sample backside while the cantilever is grounded during the KPFM measurements. U is given by

$$U = U_{dc} + U_{ac}e^{(2\pi i f_{ac}t + \varphi_0)} \quad (1)$$

with $\varphi_0 = -90^\circ$. As can be seen in Eq. (1) the applied voltage U consists of a dc part U_{dc} and an ac part U_{ac} which are generated by an active signal mixer [53]. The active mixer is required to keep the excitation amplitude of the ac-bias constant versus the operation frequency $f_{ac} = f_{ref} = \omega_{ref}/(2\pi)$. The applied ac-bias U_{ac} is modulated at the operation frequency f_{ac} . This modulation is necessary for the separation of electrical forces from other forces like van-de-Waals forces.

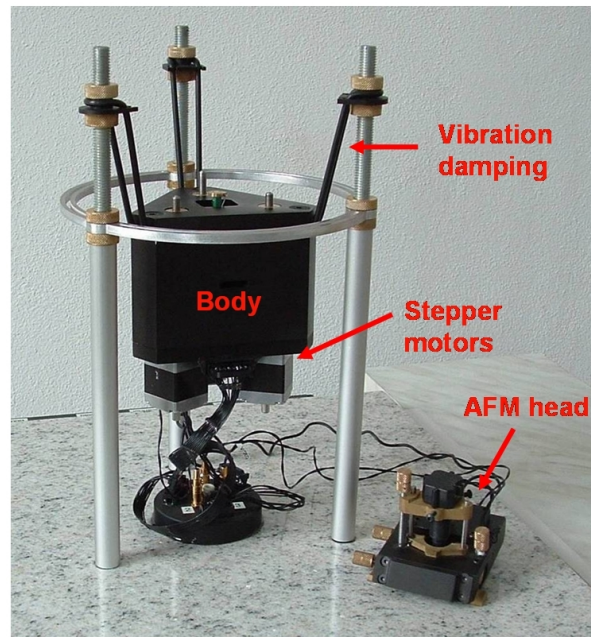


Figure 3.8: Level-AFM developed by Anfattec Instruments AG. Adapted from Ref. [117]. (Reproduced with permission from Anfattec Instruments AG.)

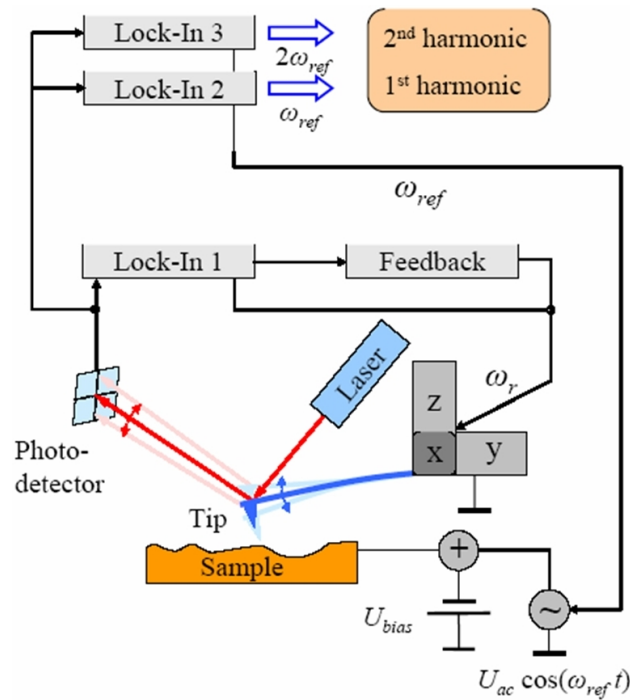


Figure 3.9: Schematic diagram of the experimental setup of the Level-AFM developed by Anfattec Instruments AG. From Ref. [118]. (Reproduced with permission from Anfattec Instruments AG.)

By using additional fully digital, integrated lock-in amplifiers (Lock-In 2 and Lock-In 3 in Fig. 3.9), the amplitudes of the 1st and 2nd harmonic of the electrical excitation can be analysed. The real part of the 1st harmonic of the KPFM signal is detected at the operation frequency f_{ac} and is used as the input signal for the digital Kelvin probe force feedback. The real part is maximized by using an autophase function. The Kelvin probe force feedback compensates the electrostatic forces between probe and sample by applying the appropriate dc-bias to the sample backside recorded as KPFM bias U_K . The Level-AFM is an amplitude-modulated KPFM system (Sect. 2.5).

Topography and all electrical KPFM signals are probed simultaneously in the Level-AFM. The operation frequency f_{ac} during the KPFM measurements is in the range of 5 kHz to 130 kHz and much smaller than the cantilever resonance frequency f_r . In this way, the detected topography and the electrical signals are independent of each other [116].

The amplitude of the non-contact oscillations used to probe the topography amounts to approximately 10 nm and is determined by the drive amplitude of typically 0.5 V. The amplitude of the non-contact oscillations used to probe electrostatic forces is nearly three orders of magnitude smaller than the amplitude of non-contact oscillations used to probe the topography, and does not exceed 20 pm. The mean probe-sample distance is approximately 30 nm. [53]

Highly doped Si cantilevers (MikroMasch NSC15/highly doped, $k = 46$ N/m) have been applied for the KPFM measurements. These probes are available with n^+ -type and with p^+ -type doping. NSC15/hd-P (n^+ -type) cantilevers feature a P-concentration of $N_D = 5 \times 10^{19}$ cm $^{-3}$, whereas NSC15/hd-B (p^+ -type) cantilevers contain B with a concentration of $N_A = 5 \times 10^{19}$ cm $^{-3}$. The NSC15/hd cantilevers have a radius of curvature of less than 10 nm. The tip height is in the range of 20 to 25 μ m, and the full tip cone angle is less than 40°. The resonance frequency f_r of the NSC15/hd cantilevers is in the range of 265 kHz to 400 kHz.

3.2.2 Ultrahigh vacuum KPFM

The comparative KPFM measurements in ultrahigh vacuum (UHV) have been carried out in the Helmholtz-Zentrum Berlin (HZB) in cooperation with PD Dr. Sascha Sadewasser. In the HZB an Omicron UHV-STM/AFM system is used for KPFM measurements. The microscope is operated in the regular non-contact detection mode. The cantilever is oscillated at its resonance frequency f_r and scanned over the sample at a constant distance of approximately 5 nm by maintaining a certain frequency shift to the free resonance frequency (FM mode, Sect. 2.5). During the KPFM measurements an opaque cover was mounted around the KPFM vacuum chamber to prevent the photogeneration of charge carriers. The UHV KPFM measurements have been performed by means of Pt-Ir coated cantilevers from Nanosensors with a resonance frequency f_r of 78 kHz. For the electrical excitation an ac-bias of 100 mV has been applied, while the operation frequency f_{ac} of 491 kHz equals the frequency of the second oscillation mode of the cantilever.

The investigated SRAM sample (Sect. 3.1.1) has been cleaned in an acetone solution before being mounted on the sample holder in the vacuum chamber. Additionally, before

performing the KPFM measurement, the SRAM sample has been heated for one hour at 155°C. The results of the UHV KPFM measurements are presented and compared to ambient KPFM results probed across the same SRAM sample in Sect. 6.1.1.4.

3.3 Complementary characterization methods

3.3.1 Secondary ion mass spectrometry

Secondary ion mass spectrometry has been carried out to obtain information about the dopant distribution in the differently doped regions of the Si epilayer samples (Sect. 3.1.2). In SIMS, primary ions are directed to the sample for sputtering atoms from the sample surface. The charge-to-mass ratio of the ionized atoms is measured. The intensity of each charge-to-mass ratio can be referred to a particular element and charge state. Comparison of the recorded values to standard data enables the correlation to the atomic concentration. [119, p. 309f]

The SIMS measurements have been performed at Qimonda Dresden GmbH und Co. OHG. The technical details are given in Ref. [120]. For detecting the positive or negative secondary ions formed from the species of interest, Cs⁺ ions with an impact energy of 15 keV and O₂⁺ ions with an impact energy of 10 keV have been used for the primary beam. Cs⁺ ions result in a negative secondary ion polarity, whereas O₂⁺ ions cause a positive secondary ion polarity. The depth resolution is in the range of 1-10 nm. The raster size was about 100 μm² with an analysed area of approximately 70 μm².

3.3.2 Stopping and range of ions in matter calculations

SRIM (*Stopping and Range of Ions in Matter*) is a software package which enables calculations of the transport of ions in matter. A detailed description is given in Ref. [121]. In this work, SRIM calculations have been applied to estimate the depth of the shallow implanted *n*⁺-type and *p*⁺-type regions in the DRAM and the SRAM cell (Sect. 3.1.1), respectively. Additionally, the dopant distribution after B- and As-implantation in the NW samples (Sect. 3.1.3) has been simulated by means of SRIM.

To estimate the implantation depth, TRIM (*TRansport of Ions in Matter*) calculations which are part of the SRIM software package have been carried out. TRIM is based on the Monte Carlo method which calculates the slowing down and scattering of energetic ions in amorphous targets, i.e. with atoms at random locations, as explained in Ref. [122]. In TRIM a large number of ion trajectories is followed individually while additionally target atom cascades are taken into account. A single implanted ion is assumed to experience binary nuclear collisions which result in an energy loss and in a change of the trajectory direction. Between the nuclear collisions the ion is supposed to suffer an inelastic, i.e. electronic, energy loss while the direction remains unchanged. As final result, the 3D distribution of the implanted ions, as well as kinetic phenomena as target damage, sputtering, and ionization may be determined by means of TRIM [121].

4 Silicon surface in ambient environment

In this work, ambient KPFM is applied to investigate differently structured, *n*- and *p*-doped Si samples. Furthermore, Si cantilevers are used for the ambient KPFM measurements (Sect. 3.2). Under ambient conditions formation of a native oxide and water adsorption on the sample and cantilever surfaces have to be taken into account.

4.1 Native oxide

The formation of a native oxide strongly depends on the surface condition of the semi-conducting samples which includes starting-materials, the preparation conditions, and the after-treatment [123]. Material and preparation steps of the investigated Si samples are described in Sect. 3.1. The influence of the after-treatment is discussed in the following.

After preparation no surface treatment has been carried out on the cross-sectionally prepared Si epilayer samples (Sect. 3.1.2) and on the Si NW samples (Sect. 3.1.3). When a clean Si surface is exposed to an ambient environment, oxygen from the ambient atmosphere breaks the Si-Si bonds and produces Si-O bonds [124]. An SiO_x transition layer forms in which x changes more or less continuously from the value $x=0$ of Si to the value $x=2$ of SiO_2 [123]. The native oxide passivates the sensitive Si surface and is inert in most solutions [125, p. 63]. The growth process of the native Si oxide is self-limited and continues at longer storage only on a logarithmic time scale [126, p. 360]. In general, a thickness of about 2 nm is commonly assumed for native oxide layers grown under ambient conditions [125, p. 93], [31, p. 94].

For reducing the relatively fast growth of the native oxide of up to 2 nm per day [126, p. 359], the clean Si surface may be treated in hydrofluoric (HF) acid solution. Note that an HF-treatment has been carried out on the conventional DRAM and SRAM cells (Sect. 3.1.1). The HF-treatment leads to an H-termination which passivates the Si surface [125, p. 63ff]. The oxide growth on HF-treated Si is divided into two different stages. During the first stage only slow growth of the oxide is observed. After this incubation period which can take several weeks the growth rate increases significantly until it reaches the self-limitation regime and grows further on a logarithmic time scale. [125, p. 63ff]

In conclusion, the native oxide is sample-specific and may change in dependence on the ambient atmosphere. The oxide layer thickness can only be estimated to be about 2 nm for the investigated samples as well as for the Si cantilevers. The basic influence of the native oxide on the KPFM measurement is discussed in Sect. 5.2.4.

4.2 Adsorption of water

Also adsorption of water molecules strongly depends on the surface conditions of the semi-conducting sample. The Si surface can be hydrophilic or hydrophobic [125, p. 70].

A hydrophilic Si surface is characterized by OH groups whereas a hydrophobic Si surface is commonly correlated with Si-H, Si-CH_x, or Si-F groups. Thus, H-terminated Si surfaces are hydrophobic, and oxide- or hydroxide-covered Si surfaces are hydrophilic. [125, p. 70] On hydrophilic Si the reported layer thickness of adsorbed water varies between 3 nm and 30 nm [127, p. 118]. On hydrophobic Si surfaces the adsorption of water is found to be much weaker and the layer thickness of the adsorbed water is in the order of only a few monolayers [128].

Note that the Si samples investigated in this work are covered by a native oxide and thus feature a hydrophilic character. The fundamental steps of water adsorption on a hydrophilic Si oxide surface are displayed in Fig. 4.1 and explained in detail in Ref. [125, p. 152]. The surface of Si oxide consists of dangling Si and O bonds [Fig. 4.1(a)]. Under medium room-humidity conditions, the surface hydroxylates and Si-OH groups form [Fig. 4.1(b)]. More water molecules adsorb [Fig. 4.1(c)] and the water layer grows in dependence on the humidity conditions. If the water layer increases to more than three monolayers, the water molecules are so-called "liquid-phase" [128], and have properties which are comparable to molecules in bulk water [Fig. 4.1(d)]. In this "liquid-phase" state, water molecules are permanently and reversibly adsorbed and desorbed [128].

Note that during long storage under ambient conditions the Si surface and thus the character of water adsorption may change. This is due to an aging of the sample surface, i.e. a loss of OH groups on hydrophilic surfaces and the appearance of associated OH groups on hydrophobic surfaces. [129]

In conclusion, similar to the native oxide, the layer thickness of the adsorbed water is sample-specific and changes in dependence on the ambient atmosphere. This also applies for the Si cantilevers. Nevertheless, the influence of the adsorbed water on the KPFM measurement can be qualitatively evaluated which is discussed in Sect. 5.2.4.

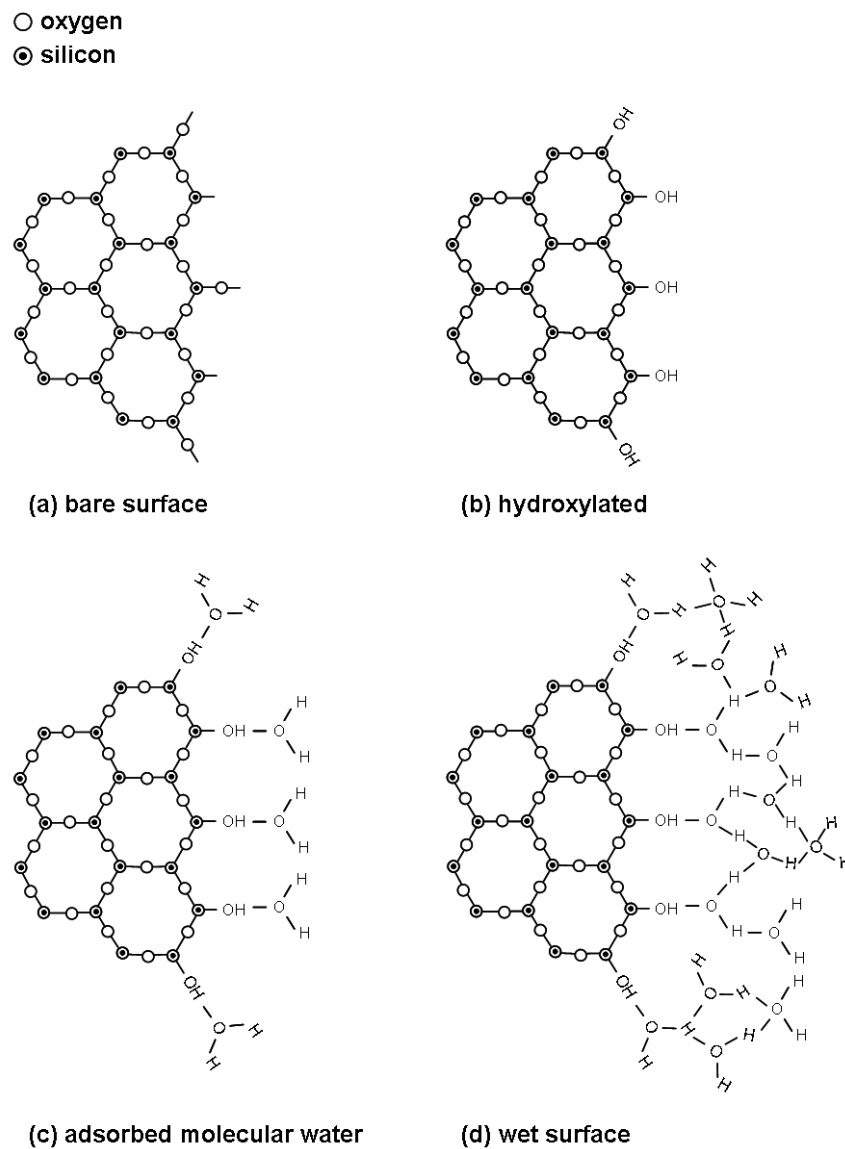


Figure 4.1: Schematic diagram showing the stepwise adsorption of water on a freshly cleaved quartz (Si oxide) surface. The (a) bare surface is (b) hydroxylated in a first step. (c) Water molecules bond directly to the Si-OH surface groups. (d) After increasing to more than three monolayers of adsorbed water, the water film shows properties like bulk water. Adapted from Ref. [125, p. 152].

5 Quantitative dopant profiling by KPFM

For quantitative dopant profiling in semiconductors the measured KPFM bias has to be evaluated with a proper physical model. In the traditional KPFM model which is discussed in Sect. 5.1 the probed KPFM bias is correlated with the contact potential difference (CPD) between the probe and the sample. In this work it is demonstrated that the CPD model is not suitable to describe the probed KPFM bias. A new KPFM model is developed which enables the quantitative correlation between the probed KPFM bias and the dopant concentration in the investigated semiconducting sample. In Sect. 5.2 it is discussed how KPFM allows the investigation of the bulk dopant concentration in semiconductors via probing the electrostatic forces from the formed surface space charge region.

5.1 Traditional KPFM model: Contact potential difference

When introducing the KPFM technique in 1991, Nonnenmacher *et al.* [36] interpreted the measured KPFM bias as the contact potential difference U_{CPD} between the sample and the probe. According to this, the KPFM bias U_K probed at a measurement position is supposed to reflect the local work function difference between the sample $\phi(\text{sample})$ and the probe $\phi(\text{probe})$. This basic relation of the CPD model is given in Eq. (2).

$$e \cdot U_K = e \cdot U_{CPD} = \phi(\text{sample}) - \phi(\text{probe}) \quad (2)$$

The work function $\phi(\text{sample})$ and $\phi(\text{probe})$ is defined as energy difference between the vacuum level E_{vac} and the respective Fermi level E_F of the sample and the probe [130, p. 15].

The CPD model is illustrated schematically in Fig. 5.1 by the example of a KPFM measurement across a semiconductor pn junction with a highly doped KPFM cantilever made of the same semiconducting material. In Fig. 5.1(a) an n^+ -type conductive KPFM probe is assumed. First, the probe is positioned above the p -type region of the semiconducting sample. In the energy band diagram the work function of the p -type sample region [$\phi(p\text{-type})$] and the work function of the n^+ -type probe [$\phi(n^+\text{-probe})$] are illustrated as green arrows. The corresponding contact potential difference [CPD($p, n^+\text{-probe}$)], i.e. the difference of both work functions, is displayed as blue arrow. In the course of the KPFM scan the probe is positioned next above the n -type region of the semiconducting sample. Again the difference between the work functions (green arrows) of the n -type sample region [$\phi(n\text{-type})$] and the n^+ -type probe [$\phi(n^+\text{-probe})$] equals the contact potential difference [CPD($n, n^+\text{-probe}$)] which is illustrated as blue arrow.

Similar to the preceding discussion of an n^+ -type probe, the CPD model for a p^+ -type KPFM probe is illustrated in Fig. 5.1(b). The resulting CPD values [CPD($p, p^+\text{-probe}$)] and [CPD($n, p^+\text{-probe}$)] are imaged as blue arrows.

Some important conclusions about the CPD model can be drawn when comparing the n^+ -type and p^+ -type conductive cantilever. In general, the CPD values are dependent on the cantilever potential. When using an n^+ -type cantilever [Fig. 5.1(a)] a large CPD

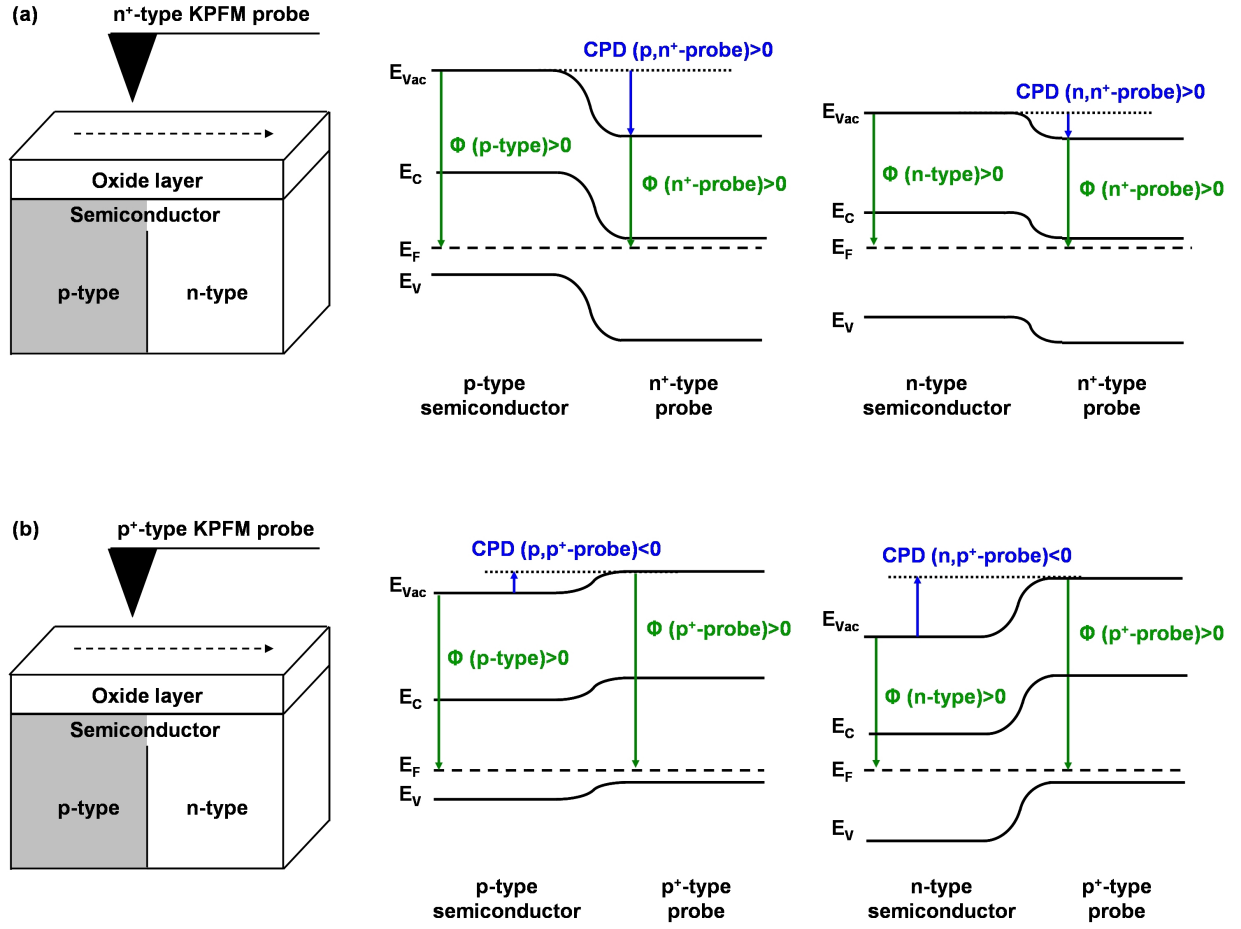


Figure 5.1: Schematic illustration of the contact potential difference (CPD) model for interpretation of the KPFM bias. A pn junction is probed with (a) an n^+ -type and (b) a p^+ -type conductive KPFM probe. The work functions of the p -type [$\phi(p\text{-type})$] and the n -type [$\phi(n\text{-type})$] sample region as well as the work function of the respective conductive probe [$\phi(n^+\text{-probe})$] and [$\phi(p^+\text{-probe})$] are imaged as green arrows in the energy band diagrams. The resulting CPD, i.e. the local work function difference between the sample region and the probe, is illustrated as blue arrow, respectively. Note that the CPD has a positive sign when probing with an n^+ -type cantilever, i.e. $[\text{CPD}(p, n^+\text{-probe})] > 0$ and $[\text{CPD}(n, n^+\text{-probe})] > 0$. When probing with a p^+ -type cantilever the CPD has a negative sign, i.e. $[\text{CPD}(p, p^+\text{-probe})] < 0$ and $[\text{CPD}(n, p^+\text{-probe})] < 0$.

is expected for the p -type sample region while a small CPD is calculated for the n -type sample region. With a p^+ -type cantilever [Fig. 5.1(b)] it is the other way around. A small CPD is expected for the p -type sample region and a large CPD is calculated for the n -type sample region. Additionally, the sign of the CPD values differs when probing with a p^+ -type cantilever compared to the n^+ -type cantilever. This aspect is illustrated in Fig. 5.2. With respect to zero on the KPFM bias scale positive values are expected to be probed with the n^+ -type cantilever. When probing with the p^+ -type cantilever the CPD values

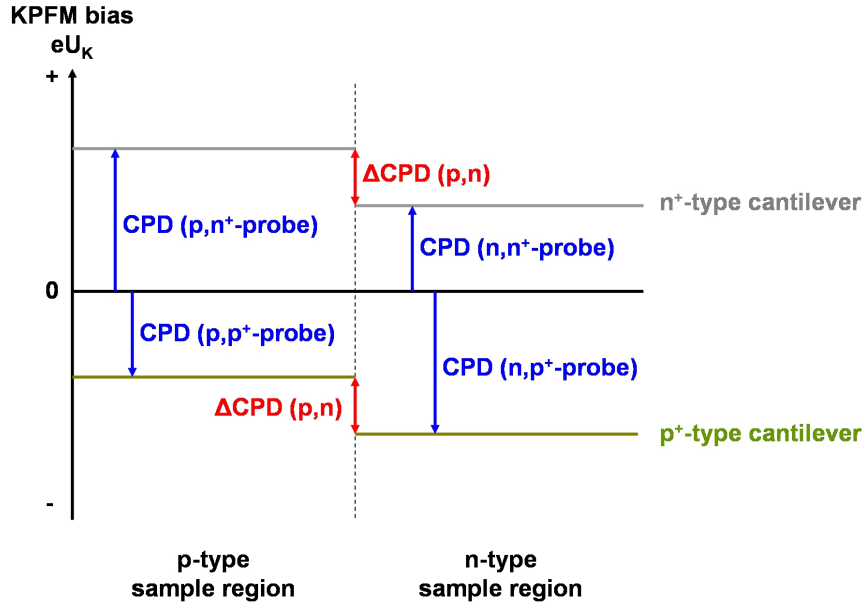


Figure 5.2: Contact potential difference (CPD) values across a pn junction in dependence on the cantilever type. Positive CPD values are expected when probing with an n^+ -type cantilever. When probing with a p^+ -type cantilever the CPD values are negative. Only the absolute value of the lateral variation of the contact potential difference $\Delta\text{CPD}(p,n)$ across the pn junction is independent of the applied cantilever type and equals the built-in potential.

are negative. This cantilever dependence is a unique property of the CPD model. Only the absolute value of the lateral variation of the contact potential difference $\Delta\text{CPD}(p,n)$ across the pn junction is independent of the applied cantilever type and equals the built-in potential [47], i.e. the Fermi energy difference between the p -type and the n -type sample region.

Since the introduction of the CPD model in 1991 [36], there have been many attempts to correlate the KPFM bias probed on semiconductors with the calculated CPD. It was shown by N. Duhayon *et al.* that a reasonably good agreement between measured and calculated lateral variation is observed for semiconducting samples with only one type of majority charge carriers as for example p -type or n -type staircase samples [44]. However, for samples containing pn junctions commonly an obvious discrepancy between the measured KPFM bias and the calculated CPD variation is observed. Respective results are given for example in Refs. [45, 47, 131]. The discrepancy usually is ascribed to the surface conditions of the investigated sample, in particular to surface states [45, 47, 131].

The partial failure of the CPD model indicates that this traditional model is not suitable to describe the KPFM bias measured on locally doped semiconductors. In the following, a physical model is developed which combines the physical properties of the semiconductor surface and bulk with the unique measurement principle of KPFM and thus enables the quantitative interpretation of the KPFM bias.

5.2 New KPFM model: Charge carrier accumulation

For a quantitative interpretation of the KPFM bias the origin of the electrostatic forces acting onto the cantilever has to be understood. Knowledge about the semiconductor surface comprising surface states and surface space charge regions, as well as about the compensation of the detected electrostatic forces during the KPFM measurement is essential. With respect to the samples investigated in this work these aspects are discussed in the following for Si.

5.2.1 Surface space charge region

5.2.1.1 Surface states

On a clean semiconductor surface localized electronic energy levels, i.e. surface states, occur due to termination of the periodic potential, to dangling bonds as well as to lattice defects. These localized electronic energy levels are commonly referred to as *intrinsic* surface states. On semiconductor surfaces under ambient conditions where chemical processes like oxidation and adsorption take place, intrinsic surface states are usually extinguished. However, formation of an oxide layer as well as adsorption of foreign atoms or molecules introduce additional localized states which are commonly referred to as *extrinsic* surface states. [132, p. 141f]

With respect to the defect nature and energetic distribution several types of surface states can be distinguished. In the following, thermally grown Si/SiO₂ is discussed which is an intensively studied structure and is regarded as well understood [133]. In Fig. 5.3 the energetic distribution of intrinsic and extrinsic surface states at the interface of thermally grown SiO₂ on Si is illustrated. The distribution of intrinsic surface states [Fig. 5.3(a)] can be divided into two groups. States occur near the band edges (U_T) due to strained Si-Si bonds, while intrinsic Si back-bonded dangling bond defects cause states symmetrically distributed around a minimum near midgap (U_M). Extrinsic surface states at the Si/SiO₂ interface [Fig. 5.3(b)] are correlated to Si atoms of lower state of oxidation, i.e. Si⁺¹ and Si⁺². The corresponding defect groups P_L and P_H form two Gaussian distributions. In general, surface states of the groups U_T , U_M , P_L and P_H are re-chargeable. [133]

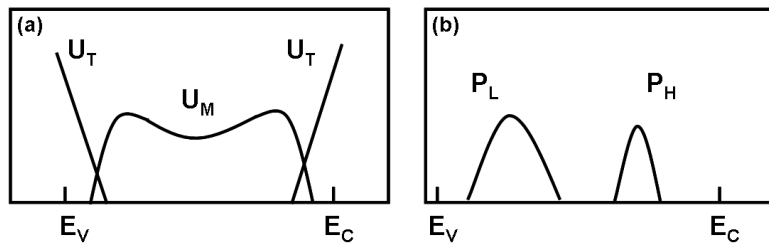


Figure 5.3: Energetic distribution of (a) intrinsic (U_T , U_M) and (b) extrinsic (P_L , P_H) surface states at the interface of thermally grown SiO₂ on Si. Adapted from [133].

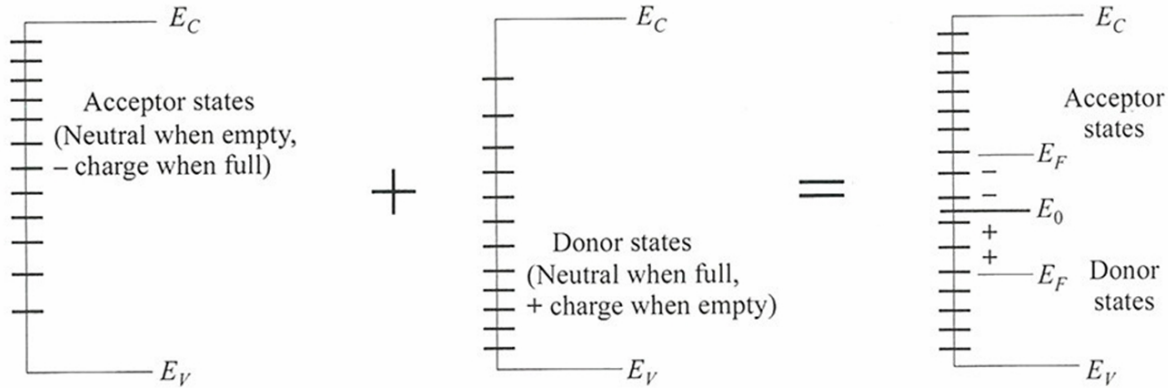


Figure 5.4: A semiconductor surface containing both acceptor-like and donor-like surface states can be described by an equivalent distribution with a neutral energy level E_0 . Above E_0 the surface states are acceptor-like while below E_0 the surface states are donor-like. The surface net charge is + (-) when the Fermi energy E_F is below (above) E_0 . From [87, p. 214]. (Courtesy of Wiley & Sons, Inc.).

In a simple model surface states are assumed to be either acceptor-like or donor-like. Complex multiple charged centers which also occur at semiconductor surfaces are normally neglected in the discussion of surface states [134, p. 167]. As explained in Ref. [87, p. 214] and schematically illustrated in Fig. 5.4 an acceptor-like surface state is neutral when empty and becomes negatively charged by accepting an electron. A donor-like surface state is neutral when full and becomes positively charged by donating an electron.

Each surface state can be either empty or occupied by an electron [134, p. 165]. In general, both types of surface states are in their most negative condition when below the Fermi level, and in their most positive condition when above the Fermi level [135]. Thus, acceptor-like surface states above the Fermi level as well as donor-like surface states below the Fermi level give no contribution to the surface net charge [136, p. 135]. The semiconductor surface which is commonly supposed to have both types of surface states can then be described by means of an equivalent distribution with a neutral energy level E_0 [87, p. 214]. Above E_0 surface states are treated as acceptor-like while below E_0 surface states are regarded as donor-like (Fig. 5.4). Thus, when the Fermi level is below (above) E_0 the surface net charge is + (-).

The position of the neutral energy level E_0 in the Si bandgap is discussed controversially in literature [137]. However, E. H. Nicollian [137] demonstrated by means of electron paramagnetic resonance measurements on radiation-induced interface traps at the Si/SiO₂ interface that the neutral energy level E_0 in Si is located in good approximation at the midgap level E_{mg} . In Eq. (3) the definition of the midgap level with respect to the conduction band minimum E_C and the valence band maximum E_V is given.

$$E_{mg} = \frac{E_C + E_V}{2} \quad (3)$$

In literature the neutral energy level E_0 in Si is also commonly correlated to the intrinsic Fermi level E_i [138]. The intrinsic Fermi level E_i is defined as

$$E_i = \frac{E_C + E_V}{2} + \frac{k_B T}{2} \ln \left(\frac{N_V}{N_C} \right). \quad (4)$$

As can be seen the second term in Eq. (4) depends on the edge density of states in the conduction band N_C and valence band N_V . A detailed discussion of N_C and N_V is given Sect. 5.2.3 where the calculation of the Fermi energy is explained. The second term in Eq. (4) additionally is a function of the thermal energy $k_B T$, i.e. the product of the Boltzmann constant k_B and the temperature T . At room temperature the second summand in Eq. (4) is much smaller than the bandgap and the intrinsic Fermi level is very close to the midgap level [105, p. 36]. Therefore, it is a common and reasonable assumption to set the intrinsic level E_i equal to the midgap level E_{mg} [139, p. 15],[140, p. 32].

It can be concluded that in Si at room temperature $E_0 \approx E_{mg} \approx E_i$. As a direct consequence surface states in Si can be treated as donor-like below E_i , i.e. in p -type Si, and as acceptor-like above E_i , i.e. in n -type Si.

5.2.1.2 Charge balance

The semiconducting samples investigated in this work are covered by a thin native oxide (Sect. 4). For a sufficiently thin oxide layer the same potential can be assumed as for the semiconductor surface [141]. In this case, the sample surface can be treated as a *free semiconductor surface* where the potential and carrier densities are not determined by the external environment of the sample. A comprehensive analytical discussion of the free semiconductor surface can be found in Ref. [141] and is summarized in the following. Note that free semiconductor surfaces can not be treated like metal-semiconductor junctions [141].

At a free semiconductor surface the occupancy of surface states is strongly correlated to interactions with free charge carriers in the semiconductor bulk. Free charge carriers from the semiconductor bulk occupy surface states. The same number of unscreened ionized immobile dopant atoms remain in the bulk forming a depletion region and generating an electric field which acts against the process of surface state occupation. This surface electric field shows in form of a surface band bending. At equilibrium, both counteracting processes are balanced and a space charge region is formed. Due to its location at the semiconductor surface, it is commonly referred to as *surface space charge region*.

The charge balance between surface state charge and surface electric field is the only constraining condition at a free semiconductor surface and determines the position of the surface Fermi energy, i.e. the Fermi level pinning at the semiconductor surface [141]. The final surface Fermi level is determined by the condition that the charge of the depletion region just balances the charge of the surface states [136, p. 135ff].

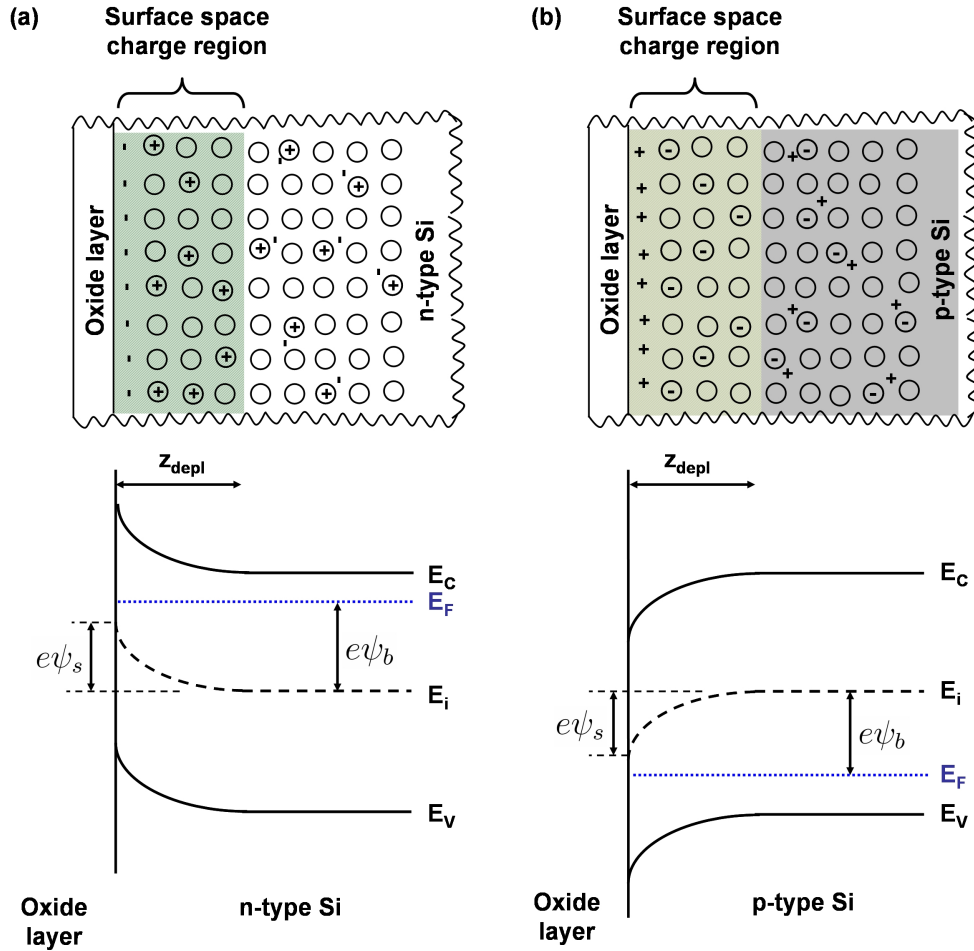


Figure 5.5: Schematic cross-sectional illustration of the surface space charge region formed in n -type and p -type Si at equilibrium. (a) In n -type Si electrons are trapped in acceptor-like surface states while the same number of positively charged ionized immobile donor atoms remains in the Si surface region. The electron depletion region is correlated with an upward band bending with respect to the bulk at the Si/Si oxide interface. (b) In p -type Si holes are trapped in donor-like surface states while the same number of negatively charged ionized immobile acceptor atoms remains in the Si surface region. The hole depletion region is correlated with a downward band bending with respect to the bulk at the Si/Si oxide interface. The width of the formed depletion region is given by the depletion length z_{depl} [Eq. (5)]. Depletion is defined by the condition $\psi_b > \psi_s > 0$ [105, p. 173ff] with the respective bulk potential ψ_b and surface potential ψ_s .

In Fig. 5.5 the surface space charge region in n -type and p -type Si at equilibrium is illustrated schematically. In n -type Si electrons from the bulk are trapped in acceptor-like surface states [Fig. 5.5(a)]. The resulting surface net charge is negative. The same number of positively charged ionized immobile dopant atoms remains in the Si surface region. The thus formed electron depletion region is correlated with an upward surface band bending with respect to the bulk as illustrated in the band diagram in the lower part of Fig. 5.5(a).

In p -type Si holes are trapped in donor-like surface states resulting in a positive surface net charge [Fig. 5.5(b)]. In the Si surface region the same number of negatively charged ionized immobile dopant atoms remains. The formation of this hole depletion region is correlated with a downward surface band bending with respect to the bulk which is shown in the lower part of Fig. 5.5(b).

The width of the formed depletion region is given by the depletion length z_{depl} [105, p. 173ff] which is illustrated schematically in Fig. 5.5. Depletion is defined by the condition $\psi_b > \psi_s > 0$ [105, p. 173ff] with the bulk potential ψ_b and the surface potential ψ_s . The upper limit of the depletion length z_{depl} can thus be estimated by means of the condition $\psi_s \cong \psi_b$, and is then given by

$$z_{depl} = \sqrt{\frac{2\epsilon_0\epsilon_r\psi_s}{eN}} \cong \sqrt{\frac{2\epsilon_0\epsilon_r\psi_b}{eN}} \quad (5)$$

with the static dielectric constant ϵ_0 , the permittivity ϵ_r , the elementary charge e and the impurity concentration N in the doped semiconductor [105, p. 173ff]. The bulk potential ψ_b is defined by the position of the bulk Fermi level E_F with respect to the bulk intrinsic Fermi level E_i . The calculation of the Fermi energy is explained in Sect. 5.2.3.

With respect to the position of the conductive cantilever above the sample, the charge distribution in the surface space charge region is asymmetric. Therefore, in the following discussion of the KPFM measurement principle the surface space charge region is also referred to as *vertical asymmetric electric dipole*. Due to the vertical asymmetric electric dipole an electrostatic force acts onto the conductive cantilever. This electrostatic force F_{el} increases with increasing size-asymmetry of the electric dipole and changes its direction above n -type and p -type regions. The latter is due to the inverse electrical structure of the vertical asymmetric electric dipole (Fig. 5.5). In n -type Si, the lines of the electrostatic force acting onto the cantilever direct perpendicularly into the sample surface due to the negative surface net charge. In p -type Si, the surface net charge is positive and the lines of the electrostatic force direct perpendicularly away from the sample surface.

Note that the formation of such a surface space charge region and the resulting electrostatic forces acting onto the cantilever are essential for successful KPFM measurements on semiconductors. Due to intrinsic surface states on clean semiconductor surfaces and additional extrinsic surface states due to oxidation and adsorption of foreign atoms under ambient atmosphere, always a surface space charge regions forms on semiconductor surfaces. The shape of the surface space charge region and thus the electrostatic forces primarily depend on the material-specific surface state distribution and on the resulting surface net charge, i.e. on the position of the neutral energy level E_0 . Therefore, the formation and properties of the surface space charge region have to be clarified for every semiconducting material for a correct understanding of the electrostatic forces and their compensation during the KPFM measurement.

5.2.2 Definition of the KPFM bias

5.2.2.1 Compensation of the electrostatic forces

During KPFM measurements the electrostatic forces acting onto the cantilever are minimized by applying the appropriate KPFM bias. As explained in the preceding Sect. 5.2.1 in semiconductors the surface space charge region causes the detected electrostatic forces. This vertical asymmetric electric dipole has to be removed in order to minimize the electrostatic forces.

In the following, the removal of the asymmetric electric dipole is discussed by the example of Si. In Fig. 5.6 the surface region of doped Si during a KPFM measurement is illustrated schematically. The thin native Si oxide is imaged as grey-blue atomic layer. The left part of Fig. 5.6 shows the vertical asymmetric electric dipole formed at the Si surface where majority charge carriers occupy surface states (animated in red) while the same number of unscreened ionized immobile dopant atoms (animated in dark-blue) remain in the Si surface region. Removal of the vertical asymmetric electric dipole is achieved by injection of majority charge carriers into the surface region of the semiconducting sample (Fig. 5.6, center). The injected majority charge carriers (animated in orange) screen the unscreened ionized immobile dopant atoms. In this way the surface electric field is removed (Sect. 5.2.1.2). The constraining condition of charge balance at the free semiconductor surface [141] is only fulfilled when the surface state charge nullifies simultaneously. The surface state charge is nullified when all donor-like surface states become neutral, i.e. full, and all acceptor-like surface states become neutral, i.e. empty. Finally, the surface space charge region, i.e. the vertical asymmetric electric dipole, is removed. The electrostatic forces F_{el} are minimized and the cantilever returns to its normal position (Fig. 5.6, right part).

In conclusion, the surface space charge region and thus the band bending shown in Fig. 5.5 is removed during the KPFM measurement by screening the unscreened ionized immobile dopant atoms with injected majority charge carriers which results in a simultaneous change of the surface state occupancy, i.e. a nullified surface state charge. This compensation procedure is part of the concept of *weak Fermi level pinning* where any change of the depletion region charge, i.e. of the unscreened ionized immobile dopant atoms, alters the position of the surface Fermi level [141].

For screening the unscreened ionized immobile dopant atoms in the surface space charge region (Fig. 5.6) majority charge carrier have to be accumulated at the Si surface. This process is also referred to as *injection of majority charge carriers into the surface region* in this work. Accumulation of electrons in n -type semiconductors is achieved by applying a dc-bias of $[E_C - E_F(n)]/e$ [87, p. 199f]. In p -type semiconductors holes are accumulated in the surface region when a dc-bias of $[E_V - E_F(p)]/e$ is applied [87, p. 199f]. As a direct consequence, the KPFM bias U_K probed across doped Si is correlated with the energy difference between Fermi level and respective band edge. This relation is illustrated in Eqs. (6) and (7) for n -type and p -type Si, respectively.

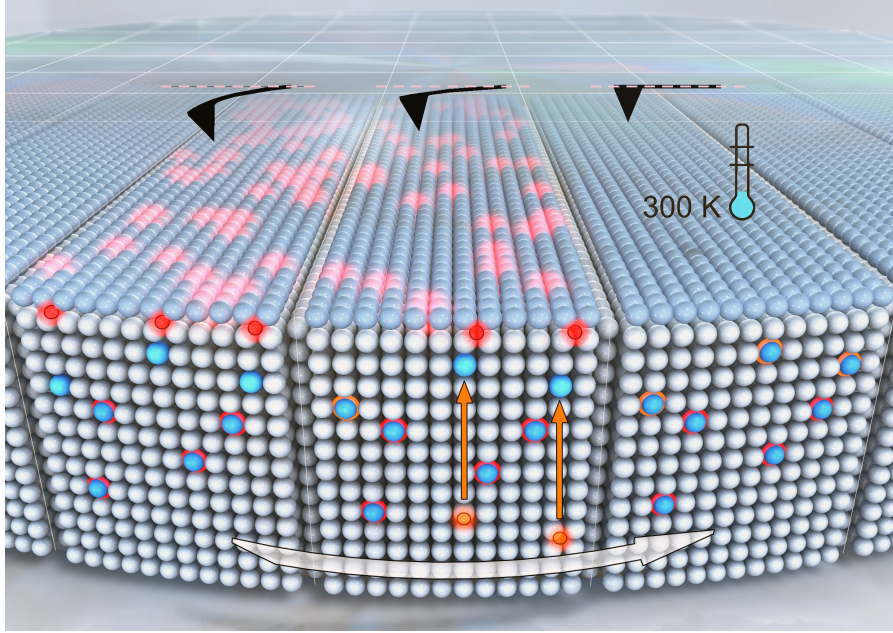


Figure 5.6: Schematic illustration of a KPFM measurement on doped Si. The thin native Si oxide is imaged as grey-blue atomic layer. Majority charge carriers occupy surface states at the Si/Si oxide interface (animated in red) while the same number of unscreened ionized immobile dopant atoms (animated in dark-blue) remain in the Si surface region. **Left:** The vertical asymmetric electric dipole causes a deflection of the probing cantilever. **Center:** By applying the appropriate KPFM bias mobile majority charge carriers are injected into the Si surface region (animated in orange) and screen the unscreened ionized immobile dopant atoms. **Right:** Finally, the vertical asymmetric electric dipole is removed. The electrostatic forces are minimized and the cantilever moves back to its normal position. (Picture and permission from Sander Münster, 3DKosmos.de).

$$e \cdot U_K(n) = E_C - E_F(n) \quad (6)$$

$$e \cdot U_K(p) = E_V - E_F(p) \quad (7)$$

In Fig. 5.7 the KPFM bias is illustrated in dependence on the position of the Fermi level E_F with respect to the intrinsic Fermi level E_i which is set to zero. In p -type Si, i.e. in the range between the valence band maximum E_V and the intrinsic Fermi level E_i , negative KPFM bias values are expected. In n -type Si, i.e. in the range between the intrinsic Fermi level E_i and the conduction band minimum E_C , the KPFM bias is expected to be positive. The absolute values of energy differences $[E_C - E_F(n)]/e$ and $[E_V - E_F(p)]/e$ are largest for intrinsic semiconductors and decrease with increasing dopant concentration. Note that due to the unique measurement principle, the measured KPFM bias is not continuous within the semiconductor bandgap but exhibits a jump at E_i .

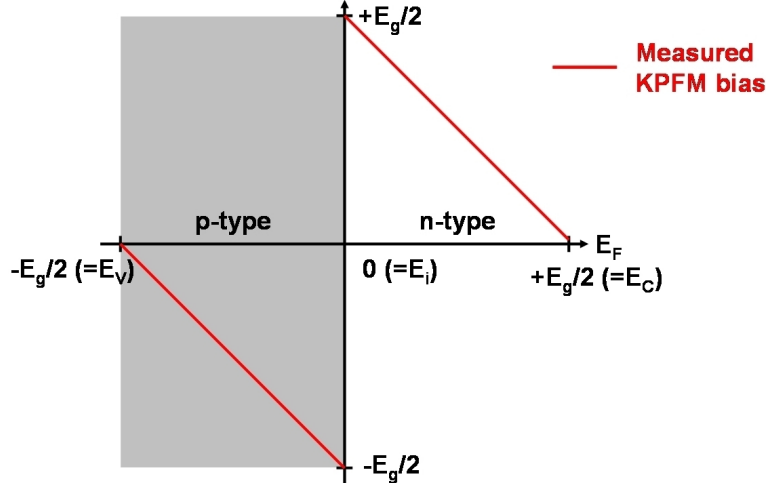


Figure 5.7: Schematic diagram of the probed KPFM bias in dependence on the position of the Fermi level E_F which is related to the doping level. Negative values are expected for p -type Si, i.e. in the range between the valence band maximum E_V and the intrinsic Fermi level E_i . In n -type Si, i.e. in the range between the intrinsic Fermi level E_i and the conduction band minimum E_C , the KPFM bias is positive. Due to the measurement principle, the KPFM bias is not continuous but features a jump at E_i .

From Eqs. (6) and (7) it follows that the KPFM bias decreases with increasing concentration of donor or acceptor ions. This reveals an important limitation of the KPFM measurement technique regarding $p^{++}n^{++}$ junctions. With increasing dopant concentration on the p -side and n -side of a pn junction, the energy differences $[E_V - E_F(p)]$ and $[E_C - E_F(n)]$ decrease until the lateral KPFM bias variation probed across the $p^{++}n^{++}$ junction approaches zero. For degenerate semiconductors where the Fermi level is located in the conduction band or in the valence band, the KPFM bias is correlated with the energy difference $[E_C - E_F(n)] = 0$ meV in n -type and $[E_V - E_F(p)] = 0$ meV in p -type regions, respectively, representing the limit of the detectable KPFM bias. Thus, no significant lateral KPFM bias variation is expected to be probed across a $p^{++}n^{++}$ junction. The same result is expected for KPFM measurements on metals where the Fermi energy is located in the conduction band. This expectation is in good agreement with results reported for example by Nonnenmacher *et al.* who found only a very small lateral KPFM bias variation when investigating palladium on gold [36, 37] or platinum on gold [36].

From the introduced new definition it can be deduced that the measured KPFM bias is *independent* of the cantilever potential. Note that this cantilever potential independence is in strong contrast to the CPD model where a KPFM bias with different sign and absolute value is expected to be probed with different cantilever types above the same doped region (Sect. 5.1). This important feature of the new KPFM model is verified in this work by means of KPFM measurements performed with different types of cantilevers on the cross-sectionally prepared Si:B epilayer sample (Sect. 3.1.2). The corresponding results are presented in Sect. 6.2.1.2.

5.2.2.2 Reclassification of CPD model results

As explained in Sect. 5.1, for semiconducting samples with only one type of majority charge carriers as for example p -type or n -type staircase samples a reasonably good agreement between probed lateral KPFM bias and calculated CPD variation is observed [44]. When probing pn junctions a discrepancy between measured KPFM bias and CPD calculation occurs [45, 47, 131]. This partial success and failure of the traditional CPD model can be explained completely within the new KPFM model. In the following, a KPFM measurement performed with an n^+ -type cantilever is discussed. KPFM measurements with a p^+ -type cantilever or other conductive KPFM cantilevers can be discussed in analogue way.

First, the example of a semiconducting sample with only one type of majority charge carriers is discussed. Without loss of generality an n -type staircase with the dopant concentrations $n_1 > n_2$ is assumed. In Fig. 5.8(a) the expected energy differences within the energy band diagram across the staircase are illustrated for both the traditional CPD model and the new KPFM model. It can be deduced from Fig. 5.8(a) that the lateral variation of the contact potential difference $\Delta CPD(n_2, n_1)$ equals the Fermi energy difference between both n -type regions. This relation is shown in Eq. (8).

$$\Delta CPD(n_2, n_1) = CPD(n_2, n^+ \text{-probe}) - CPD(n_1, n^+ \text{-probe}) = |E_F(n_2) - E_F(n_1)| \quad (8)$$

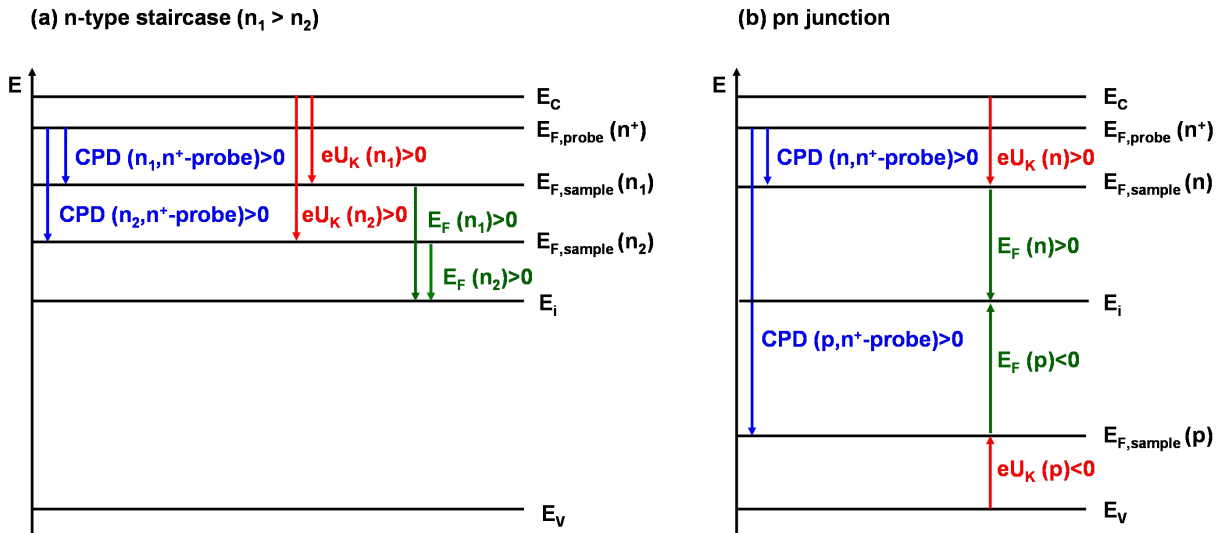


Figure 5.8: Comparison between the traditional CPD model and the new KPFM model by the example of (a) an n -type staircase with the dopant concentrations $n_1 > n_2$ and (b) a pn junction probed by means of an n^+ -type cantilever. The CPD values are illustrated as blue arrows in the band diagram, while the values predicted from the new KPFM model are imaged as red arrows. Additionally, the respective Fermi energy is marked by means of green arrows.

As can be seen in Fig. 5.8(a) also the lateral variation $e\Delta U_K(n_2, n_1)$ predicted from the new KPFBM model equals the Fermi energy difference between both n -type regions. In Eq. (9) the related definition is illustrated.

$$e \cdot \Delta U_K(n_2, n_1) = e \cdot U_K(n_2) - e \cdot U_K(n_1) = |E_F(n_2) - E_F(n_1)| \quad (9)$$

In conclusion, for a semiconducting sample with only one type of majority charge carriers both KPFBM models predict the same correct lateral variation. This explains the good agreement between probed KPFBM bias and calculated CPD for the staircase calibration sample observed by N. Duhayon *et al.* [44].

Now, both KPFBM models are compared for a pn junction. The corresponding energy band diagram is illustrated schematically in Fig. 5.8(b). The lateral variation $\Delta CPD(p, n)$ predicted from the traditional model equals the Fermi energy difference between the n -type and the p -type region, i.e. the built-in potential V_{bi} [Eq. (10)].

$$\Delta CPD(p, n) = CPD(p, n^+ \text{-probe}) - CPD(n, n^+ \text{-probe}) = |E_F(p)| + E_F(n) = V_{bi} \quad (10)$$

From Fig. 5.8(b) it is obvious that the new KPFBM model predicts a variation $e\Delta U_K(p, n)$ which amounts to the difference between bandgap energy E_g and the built-in potential of the pn junction [Eq. (11)].

$$e \cdot \Delta U_K(p, n) = |e \cdot U_K(p)| + e \cdot U_K(n) = E_g - \langle |E_F(p)| + E_F(n) \rangle = E_g - V_{bi} \quad (11)$$

It can be concluded that the traditional CPD model and the new KPFBM model predict a different lateral bias variation for pn junctions. The correlation between the CPD model and the new KPFBM model is defined in Eq. (12).

$$E_g = e \cdot \Delta U_K(p, n) + \Delta CPD(p, n) \quad (12)$$

The new KPFBM model is now applied to KPFBM bias data reported in literature. In Tab. 5.1 the KPFBM bias variations and the calculated CPD variations from measurements across Si pn junctions are summarized for each reference. As can be seen the measured KPFBM bias variation $\Delta U_K(p, n)$ differs from the calculated CPD variation $\Delta CPD(p, n)$. This discrepancy can be explained satisfyingly within the new KPFBM model by applying Eq. (12). As can be seen in Tab. 5.1, the sum of $e \cdot \Delta U_K(p, n)$ and $\Delta CPD(p, n)$ for KPFBM measurements at room temperature is in the order of the Si band gap energy of 1.124 eV at room temperature [106, p. 155] as expected from Eq. (12).

Table 5.1: KPFM bias and CPD model values of measurements across Si pn junctions as reported in literature. For each reference the measured lateral KPFM bias variation $\Delta U_K(p, n)$ is compared to the calculated CPD variation $\Delta CPD(p, n)$. As expected from Eq. (12) of the new KPFM model, the sum of $e \cdot U_K(p, n)$ and $\Delta CPD(p, n)$ is in the order of the Si band gap energy of 1.124 eV at room temperature (value taken from Ref. [106, p. 155]).

	KPFM measurement: $\Delta U_K(p, n)$ (V)	CPD model: $\Delta CPD(p, n)$ (eV)	Sum: $[e \cdot \Delta U_K(p, n) + \Delta CPD(p, n)]$ (eV)
Ref. [45]	$\cong 0.30$	$\cong 0.80$	$\cong 1.10$
Ref. [47]	$\cong 0.23$	$\cong 0.80$	$\cong 1.03$
Ref. [131]	$\cong 0.30$	$\cong 0.80$	$\cong 1.10$

In conclusion, only the new KPFM model allows the correct interpretation of the KPFM bias probed on samples with two types of majority charge carriers, i.e. on samples containing pn junctions. The partial success of the traditional CPD model above semiconducting samples with only one type of majority charge carriers is an artefact which is caused by an accidental partial agreement between both models. The failure of the CPD model shows in particular when probing pn junctions where only the new KPFM model provides a correct prediction. Therefore, in order to verify the new KPFM model, primarily pn junctions are investigated in this work.

5.2.3 Calculation of the Fermi energy

The Fermi energy E_F required for solving Eqs. (6) and (7) is calculated iteratively in dependence on the doping level. If not declared otherwise, the following equations and relations are taken from [106, pp. 149-170].

For a determination of the Fermi level position, the general charge neutrality condition for semiconductors with donor and acceptor impurities given in Eq. (13) has to be solved.

$$p + N_D^+ = n + N_A^- \quad (13)$$

N_D^+ and N_A^- is the concentration of ionized donors and acceptors, respectively. The electron density in the conduction band n and the hole density in the valence band p are given by the following integrals

$$n = \int_{E_C}^{\infty} D_e(E) f_e(E) dE, \quad (14)$$

$$p = \int_{-\infty}^{E_V} D_h(E) f_h(E) dE. \quad (15)$$

The distribution function for electrons f_e and holes f_h , namely the Fermi-Dirac distribution, is defined by

$$f_e(E) = \frac{1}{\exp\left(\frac{E-E_F}{k_B T}\right) + 1}, \quad (16)$$

$$f_h(E) = \frac{1}{\exp\left(-\frac{E-E_F}{k_B T}\right) + 1}. \quad (17)$$

The density of states in the conduction band D_e and in the valence band D_h are

$$D_e(E) = \frac{1}{2\pi^2} \left(\frac{2m_e}{\hbar^2}\right)^{3/2} (E - E_C)^{1/2}, \quad (18)$$

$$D_h(E) = \frac{1}{2\pi^2} \left(\frac{2m_h}{\hbar^2}\right)^{3/2} (E_V - E)^{1/2}, \quad (19)$$

with the effective mass of electrons m_e and holes m_h at the assumption of parabolic band edges.

The integrals in Eqs. (14) and (15) are solved by applying the Fermi integral F_n which is defined as

$$F_n(x) = \frac{2}{\sqrt{\pi}} \int_0^\infty \frac{y^n}{1 + \exp(y-x)} dy \quad (20)$$

with the restriction of $n > -1$. $F_n(x)$ is calculated by means of rational Chebyshev approximations after Cody and Thacher [142]. For bulk materials $n = 1/2$ holds true. Then the free-carrier concentrations are given by

$$n = N_C F_{1/2}\left(\frac{E_F - E_C}{k_B T}\right), \quad (21)$$

$$p = N_V F_{1/2}\left(-\frac{E_F - E_V}{k_B T}\right). \quad (22)$$

The edge density of states in the conduction band N_C and in the valence band N_V are defined as

$$N_C = 2 \left(\frac{m_e k_B T}{2\pi \hbar^2}\right)^{3/2}, \quad (23)$$

$$N_V = 2 \left(\frac{m_h k_B T}{2\pi \hbar^2}\right)^{3/2}. \quad (24)$$

Values for N_C and N_V in Si are listed in Tab. 5.2.

Table 5.2: Conduction band edge density of states N_C , valence band edge density of states N_V , and bandgap energy E_g in Si at 300 K. Values taken from Ref. [106, p. 155].

N_C (cm ⁻³)	N_V (cm ⁻³)	E_g (eV)
7.28×10^{19}	1.05×10^{19}	1.124

At sufficiently low temperatures and without photogenerated charge carriers intrinsic conduction can be neglected. In this case, no carriers in the conduction band stem from the valence band and vice versa. Thus, the number of electrons in the conduction band equals the number of ionized donors in n -type semiconductors, and the number of holes in the valence band equals the number of ionized acceptors in p -type semiconductors. The concentration of ionized donors N_D^+ and acceptors N_A^- is then given by

$$N_D^+ = \frac{N_D}{1 + \hat{g}_D \exp\left(\frac{E_F - E_D}{k_B T}\right)}, \quad (25)$$

$$N_A^- = \frac{N_A}{1 + \hat{g}_A \exp\left(-\frac{E_F - E_A}{k_B T}\right)}. \quad (26)$$

E_D and E_A are the donor and acceptor binding energies which are defined with respect to the conduction band edge E_C and the valence band edge E_V , respectively. Values of $(E_A - E_V)$ and $(E_C - E_D)$ for the investigated dopants in Si are listed in Tab. 5.3.

\hat{g}_D and \hat{g}_A is the degeneracy factor of donor and acceptor states, respectively. For donors the neutral state is degenerate since the electron of a singly charged donor can take the spin up and down state. For acceptors the charged state is degenerate. Thus, $\hat{g}_D = 2$ [106, p. 160] and $\hat{g}_A = 1/2$ [106, p. 166] have been applied for the calculation.

For the calculation and plot of the Fermi energy E_F , the position of the Fermi level of the intrinsic ($N_D^+ = N_A^- = 0$) semiconductor E_i [Eq. (4)] is set to zero on energy scale. With respect to the intrinsic level E_i the Fermi level is thus defined as $E_F(n) > 0$ and $E_F(p) < 0$ in n -type and p -type semiconductors, respectively.

Table 5.3: Acceptor binding energy $(E_A - E_V)$ and donor binding energy $(E_C - E_D)$ of the investigated dopant atoms on substitutional sites in Si. Values taken from Ref. [106, p. 157].

Si:B	Si:P	Si:As
$[E_A - E_V]$ (eV)	$[E_C - E_D]$ (eV)	$[E_C - E_D]$ (eV)
0.045	0.045	0.054

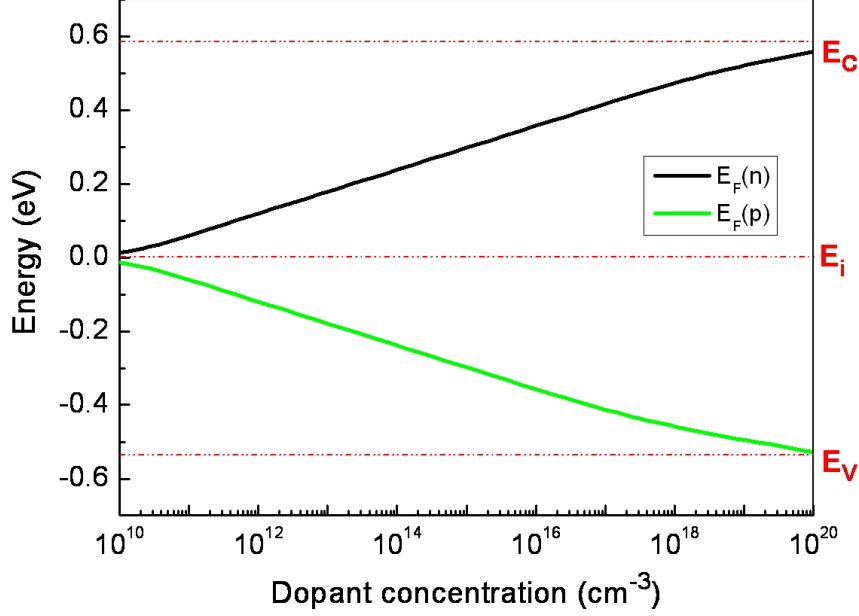


Figure 5.9: Fermi energy E_F for B and P dopants in Si calculated for 300 K and plotted in dependence on the dopant concentration. The intrinsic Fermi level E_i calculated with Eq. (4) is set to zero. The related positions of the conduction band edge E_C and valence band edge E_V are illustrated by means of dashed lines. It is assumed that E_C and E_V do not depend on the dopant concentration.

The KPFM bias data presented in this work are recorded under ambient conditions at room temperature. Therefore, the Fermi energy is calculated for 300 K. As an example, in Fig. 5.9 the Fermi energy E_F calculated for B and P dopants in Si is plotted in dependence on the dopant concentration. The intrinsic Fermi level E_i which is calculated with Eq. (4) and the related positions of the conduction band edge E_C and valence band edge E_V are illustrated by means of dashed lines. Note that it is assumed that E_C and E_V do not depend on the dopant concentration.

In the following discussion and calculations the intrinsic Fermi level E_i is set equal to the midgap level E_{mg} [Eq. (3)] which is a common and reasonable approximation [139, p. 15],[140, p. 32].

5.2.4 Potential shielding and KPFM bias offset

The applied Level-AFM from Anfatec Instruments works under ambient conditions. As explained in Sect. 4 the surface of the investigated semiconducting samples and of the highly doped Si cantilevers is oxidized. Additionally, a thin water film due to adsorption of water molecules on all surfaces has to be taken into account.

At the oxidized Si surface fixed charges, for example ionized Si^{+3} dangling-bond defects at the Si/Si oxide interface [133] and oxide trapped charges distributed within the oxide layer [87, p. 213], may occur. For the semiconducting samples investigated in this work these fixed charges can be assumed to be homogeneously distributed on the sample surface because of the homogeneous surface treatment (Sect. 3.1). Also the properties of the cantilever oxide layer are expected to be homogeneous and constant during the KPFM measurement because of the non-destructive non-contact measurement principle. In general, those fixed charges can not be neutralized by means of discharging and have to be screened against the probing cantilever by additional accumulation of charge carriers at the Si/Si oxide interface. Only then, all electrostatic forces acting onto the cantilever are minimized. This leads to a sample-specific constant contribution to the probed KPFM bias values which is referred to as *offset voltage* U_{off} and which does not depend on the dopant concentration.

Also the thin water film on the sample and cantilever surfaces may cause a constant offset voltage. Due to the applied ac-bias U_{ac} of 6 V and the operation frequency f_{ac} in the kHz range, the electric dipoles in the liquid-phase thin water film on the surface align with respect to the operation frequency. This alignment creates an additional electric dipole moment at the semiconductor surface which results in a constant contribution to the probed KPFM bias values.

Note that in contact-mode SPM techniques the water films on the sample surface and on the cantilever may touch. A liquid bridge between tip and sample is formed and capillary forces may attract the tip and drag it to the surface until they touch [143, p. 87]. This might influence the detected forces as was for example shown by Lányi *et al.* for SCM measurements [144]. In Ref. [144] the influence of the water bridge on the tip-to-surface capacitance is modeled and it is explained how the resolution and the contrast of SCM changes in dependence of the condensation of humidity.

KPFM is a non-contact SPM technique. The mean probe-sample distance amounts to approximately 30 nm, while the amplitude of the non-contact oscillation during the KPFM measurement amounts to only about 10 nm (Sect. 3.2). Thus, the distance between sample surface and probing cantilever is expected to be large enough to prevent touching water films.

A great advantage of the KPFM measurement principle is that as long as the original vertical asymmetric electric dipole of the surface space charge region is detected against potential shielding effects from the oxide layer or the thin water film, the measured lateral KPFM bias variation is correct and can be correlated quantitatively to the bulk dopant concentration via Eqs. 6 and 7. This is due the fact that the probed KPFM bias is not dependent on the explicit amplitude of the cantilever deflection, but only reflects the voltage necessary for the injection of majority charge carriers into the semiconductor surface region.

Note that if the potential shielding completely dominates the original asymmetric electric dipole, the expected KPFM bias variation between differently doped regions would

be undetectable. Therefore, very thick oxide layers and/or water films on the sample surface have to be avoided for successful KPFM measurements. Potential shielding and a strongly distorted KPFM bias values are observed for example at high vertical topographic steps on the sample surface occurring on the SRAM and DRAM cell. This observation is discussed in detail in Sect. 6.1. A solution to the restriction by potential shielding is the detection of the 2nd harmonic of the electrostatic force which is discussed in Sect. 5.2.8.

In conclusion, due to oxidized surfaces and adsorbed water, a constant offset voltage U_{off} may occur during the KPFM measurements under ambient conditions. This offset voltage U_{off} is included in the dc-bias applied from the KPFM controller. The measured KPFM bias U_K then consists of the constant voltage offset value U_{off} and the bias related to the electrical signal from the vertical asymmetric electric dipole in the semiconducting sample. This relation is summarized in Eqs. (27) and (28) for n -type and p -type regions, respectively.

$$e \cdot [U_K(n) - U_{off}] = E_C - E_F(n) \quad (27)$$

$$e \cdot [U_K(p) - U_{off}] = E_V - E_F(p) \quad (28)$$

Only the lateral variation of the KPFM bias between differently doped regions can be analysed quantitatively. The absolute value of the KPFM bias depends on the constant offset voltage U_{off} and may not be evaluated quantitatively. As a consequence, a reference value as for example the dopant concentration of the substrate is required to enable the correct correlation between the KPFM bias scale and the scale of the calculated energy differences.

In general, especially for KPFM measurements under ambient conditions the sample surface has to be prepared carefully in order to ensure that the electrostatic forces between the vertical asymmetric dipole layer and the conductive KPFM probe are detectable despite the electrostatic forces which cause the constant offset voltage. As long as the electrical KPFM signal from the asymmetric electric dipole is large enough to be detected against the shielding signal, the measured lateral KPFM bias variation is quantitatively correlated to the energy differences $[E_C - E_F(n)]$ and $[E_V - E_F(p)]$ in n -type regions and p -type regions, respectively.

5.2.5 Bias-induced band bending

An often discussed aspect in KPFM is the bias-induced band bending. When the semiconducting sample is biased, the cases accumulation, depletion and inversion of charge carriers can occur [87, p. 199f]. As a consequence, the voltage partially drops between the semiconductor surface and the bulk, which is referred to as *bias-induced band bending*.

During the KPFM measurement, an ac-bias and a dc-bias are applied to the sample (Sect. 3.2). The ac part of the applied bias is used to separate electrical forces from other

forces acting onto the conductive probe. Due to the applied ac-bias with an effective value of 6 V, the surface region of the investigated semiconducting sample experiences an alternating accumulation and depletion of majority charge carriers. As a result, an alternating, reversible ac-bias-induced surface band bending occurs which is symmetric around the zero-ac-bias case. Therefore, in the time-average the ac-bias-induced surface band bending vanishes and is *not detectable* during the KPFM measurement.

In contrast, the constant surface band bending due to the surface space charge region at the free semiconductor surface (Fig. 5.5) does not vanish in the time-average. This *detectable* constant surface band bending superimposes undisturbed with the ac-bias-induced band bending and is removed finally by applying the appropriate dc-bias, i.e. the KPFM bias.

In conclusion, ac-bias-induced band bending occurs but is not relevant for the KPFM measurement. AC-bias-induced band bending does not influence the measured lateral KPFM bias variation which is required for quantitative dopant profiling.

For the experimental investigation of the aspect of negligible ac-bias-induced band bending, ac-bias dependent KPFM measurements have been performed on the conventional SRAM cell as well as on the Si epilayer samples. The detailed results are discussed in Sect. 6. In general, it is demonstrated that the lateral KPFM bias variation probed across pn junctions is independent of the applied ac-bias for large enough values. Note that bias-induced band bending would result in an opposite change of the surface potential above n -type and p -type semiconducting regions for positive or negative biases. This effect was used for example by Nelson *et al.* to distinguish between n -type and p -type regions of patterned Si wafers by means of bias-applied phase-imaging tapping-mode AFM measurements [145]. Thus, it would be expected that the KPFM bias probed above the n -type region and above the p -type region changes oppositely to each other if bias-induced band bending plays a role. Therefore, from the fact that the lateral KPFM bias variation probed across pn junctions is independent of the ac-bias, an influence of ac-bias-induced band bending on the probed KPFM bias can be ruled out.

An additional evidence for the conclusion that ac-bias-induced band bending is not relevant in KPFM is revealed by comparing ambient and UHV KPFM measurements on the conventional SRAM cell (Sect. 6.1.1.4). Independent of the different effective ac-bias values of 6 V for ambient KPFM and only 0.1 V for UHV KPFM (Sect. 3.2), the same lateral KPFM bias variation is probed across the SRAM cell. This shows impressively that the measured lateral KPFM bias variation is not influenced by ac-bias-induced band bending.

5.2.6 Lateral resolution of KPFM

The lateral resolution is a crucial aspect when investigating samples by means of SPM techniques. It is determined by the interaction between the probing cantilever and the investigated sample. Thus, it mainly depends on the strength of the interaction forces [146, 147] and on the tip-sample volume of interaction [148]. In general, the smaller the interaction volume is, the better is also the lateral resolution.

At the applied Anfatec Level-AFM, topography and electrical signals are detected simultaneously but independent from each other. The measurement of the surface topography is based on van der Waals forces acting between atoms or molecules of the sample surface and the tip. By applying additionally an external bias to the tip-sample system, the electrostatic forces acting onto the cantilever are detected (Sect. 3.2).

The lateral resolution of both, topography and electrical signals, is limited mainly by the tip apex of the probing cantilever [146, 148, 149], and by the tip-sample distance during the scan [146, 150].

The tip apex of the probing cantilever is an important limitation factor for the lateral resolution. The tip-sample volume of interaction increases with increasing tip apex and the forces acting onto the cantilever thus represent the average over a larger sample region. Separate parts contributing laterally to the averaged detected force can not be resolved. Thus, a larger tip apex worsens the lateral resolution. The lateral resolution may be enhanced by using ultrasharp probes [151, 152].

Note that in particular at contact SPM techniques the tip apex and thus the tip-sample volume of interaction may not be constant during the scan. In contact mode SPM techniques like SSRM or SCM, the tip is scratched over the sample surface and may be deformed. The tip apex may enlarge during the scan leading to a poorer lateral resolution. Non-contact mode techniques like KPFM provide the advantage of being non-destructive regarding tip and sample. The tip-sample volume of interaction is unchanged during the scan enabling measurements with a constant lateral resolution.

The other significant factor influencing the lateral resolution is the tip-sample distance. An increased tip-sample distance enlarges the area from which forces may act onto the probe. Thus, the tip-sample volume of interaction is increased at larger tip-sample distances and the lateral resolution worsens. This phenomenon has to be taken into account when comparing ambient and UHV KPFM measurements. The mean tip-sample distance during the ambient KPFM measurements presented in this work amounts to approximately 30 nm (Sect. 3.2). At UHV KPFM the mean tip-sample distance is considerably smaller and amounts to only a few nm, i.e. to approximately 5 nm at the UHV KPFM measurements discussed in this work (Sect. 3.2). The comparably small tip-sample distance enables high-resolution UHV KPFM measurements. Only recently, Spadafora *et al.* reported a lateral resolution of 2 nm achieved by means of UHV KPFM [153]. In ambient KPFM the lateral resolution of the probed KPFM bias is limited to approximately 20 nm, as is shown in this work by the example of KPFM measurements on horizontal Si NWs (Sect. 6.3).

In general, the limitation of the lateral resolution due to both, the tip apex and the tip-sample distance, is a nm length scale effect. For example, Ono *et al.* demonstrated by comparing KPFM measurements on InAs quantum dots and simulations that a lateral averaging effect makes the probed electrical signal contrast indistinct, in particular when the size of the nanostructure is smaller than the tip apex [154]. Also the observed drop of the lateral KPFM bias variation at increased tip-sample distance due to an increased lateral averaging takes place on the lateral nm length scale [41, 155] and complicates measurements with atomic resolution [54].

In conclusion, an averaging effect influences the KPFM measurement detectably only when probing the topographic or electrical signals at a tip-sample distance [156] or with a tip apex [154] being larger compared to the dimensions of the area of interest.

The semiconducting structures investigated in this work are large compared to the tip apex of less than 10 nm and the tip-sample distance of approximately 30 nm. The Si epilayer samples as well as the DRAM and the SRAM cell are structured and doped on the μm -scale. Thus, the influence of averaging effects due to tip apex and tip-sample distance on the lateral resolution is negligible. This also holds true for the results of the horizontal Si nanowires presented in Sect. 6.3. The Si nanowires have a length of 65 μm and a width ranging between 10 nm and 2 μm (Sect. 3.1.3). However, only Si nanowires with a width larger than 100 nm have been investigated precluding averaging effects due to the tip apex and the tip-sample distance.

For KPFM measurements on semiconductors another essential influence on the lateral resolution has to be taken into account. The detection of the KPFM bias may be influenced by local intrinsic electric fields, i.e. due to doping junctions, in the investigated sample. This is due to the measurement principle of KPFM where majority charge carriers have to be injected into the semiconductor surface region in order to minimize the electrostatic forces from the surface space charge region at the measurement position. During the KPFM measurements across doping junctions, injected majority charge carriers drift within the local intrinsic electric fields. This phenomenon distorts the KPFM bias and decreases the lateral resolution of scans across the doping junction. Depending on the lateral size of the space charge region up to several hundred nanometer, intrinsic electric fields may influence the lateral resolution of the KPFM bias on a much larger scale than the tip apex or the tip-sample distance.

The influence of intrinsic electric fields regarding the KPFM measurement principle is discussed in detail in the following Sect. 5.2.7.

5.2.7 Intrinsic electric fields in locally doped semiconductors

KPFM is an electrical nanometrology technique and based on the injection of majority charge carriers into the sample surface region at the measurement position. Due to the measurement principle, local intrinsic electric fields in the sample may distort the KPFM bias measurement. In particular, pn junctions may have strong influence on the probed KPFM bias.

5.2.7.1 Investigation of pn junctions

Doping junctions in semiconductors form when regions with a different dopant concentration or dopant material are in close contact. Especially, pn junctions show unique electric properties and are essential parts of semiconductor devices. If not stated otherwise the following equations are adapted from Ref. [87, p. 80ff].

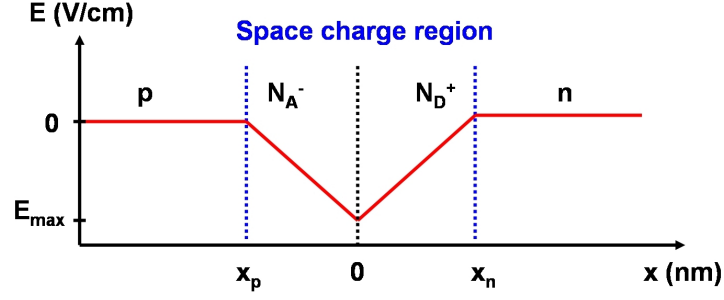


Figure 5.10: Schematic illustration of the electric field E across a pn junction in equilibrium. x_p and x_n mark the extension of the non-zero electric field on the p -side and the n -side of the pn interface, respectively. At the lateral position 0 the electric field has its maximum value E_{max} . Adapted from Ref. [106, p. 439].

At a pn interface electrons from the n -type region diffuse into the p -type region while holes from the p -type region diffuse into the n -type region. Unscreened immobile ionized dopant atoms remain on both sites of the pn interface and generate an electric field which counteracts the diffusion of charge carriers. At equilibrium, the counteracting processes are balanced and a space charge region is formed.

In Fig. 5.10 the electric field E across a pn junction in equilibrium is illustrated schematically. The width of the electric field on the p -side x_p and on the n -side x_n of the pn interface are defined, respectively, as

$$x_p = \sqrt{\frac{2\epsilon_r\epsilon_0 V_{bi}}{e} \cdot \frac{N_D}{N_A(N_D + N_A)}}, \quad (29)$$

$$x_n = \sqrt{\frac{2\epsilon_r\epsilon_0 V_{bi}}{e} \cdot \frac{N_A}{N_D(N_D + N_A)}}, \quad (30)$$

with the static dielectric constant ϵ_0 , the permittivity ϵ_r , and the donor and acceptor concentrations N_D and N_A . The built-in potential V_{bi} of the pn junction is given by

$$V_{bi} = \frac{k_B T}{e} \ln \left(\frac{N_A N_D}{n_i^2} \right) = -\frac{1}{2} E_{max} (x_p + x_n). \quad (31)$$

n_i is the intrinsic carrier concentration. The maximum electric field E_{max} in the pn junction at the position 0 in Fig. 5.10 is defined as

$$E_{max} = -\frac{e N_D x_n}{\epsilon_0 \epsilon_r} = -\frac{e N_A x_p}{\epsilon_0 \epsilon_r}. \quad (32)$$

When investigating samples with local intrinsic electric fields by means of KPFM, the unique measurement principle, i.e. the injection of majority charge carriers, has to be taken into account. An important aspect is the direction of the intrinsic electric field with

respect to the injection direction of majority charge carriers. During the presented KPFM measurements majority charge carriers are injected from the sample back contact. With respect to the direction of the intrinsic electric field, horizontal and vertical pn junctions are distinguished.

In Fig. 5.11 a horizontal pn junction is illustrated as it occurs for example in the investigated cross-sectionally prepared Si epilayer samples (Sect. 3.1.2). Majority charge carriers are injected along z -direction. When probing across the pn junction majority charge carriers are injected into the space charge region of the pn junction where they drift within the electric field along x -direction. This effect partially prevents the screening of unscreened immobile ionized dopant atoms in the vertical asymmetric electric dipole layer at the semiconductor-oxide interface. Additional majority charge carriers have to be injected for minimization of the electrostatic forces acting onto the cantilever which distorts the probed KPFM bias. This smearing out and overshoot of the KPFM bias above horizontal pn junctions is the reason for the observed discrepancy between the expected step-like potential and the probed continuous KPFM bias reported for example in Refs. [45, 47, 131, 157].

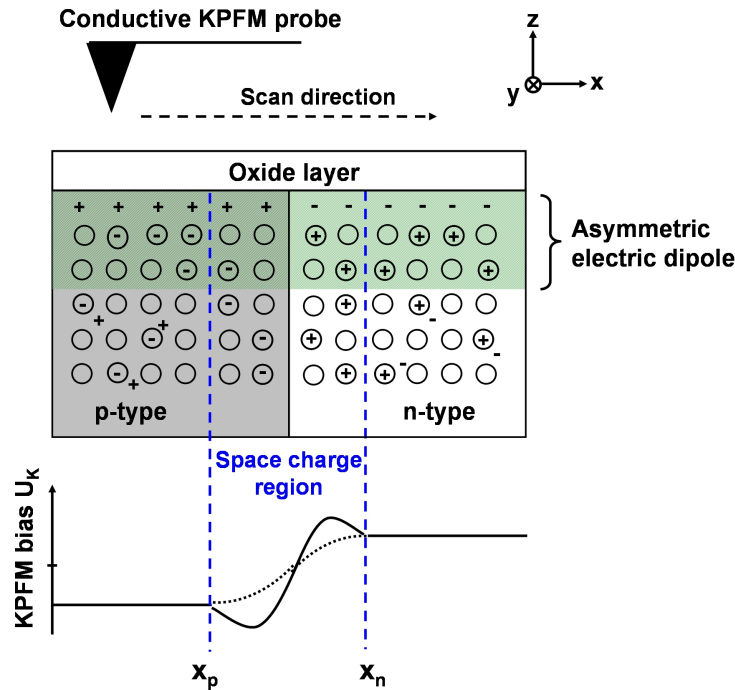


Figure 5.11: Schematic illustration of a KPFM measurement across a horizontal pn junction. Majority charge carriers are injected along z -direction into the space charge region and drift along x -direction due to the intrinsic electric field in the space charge region. The probed KPFM bias is distorted and may overshoot at the pn junction. Adapted from Ref. [158].

Vertical pn junctions occur for example in the investigated SRAM and DRAM cells (Sect. 3.1). It is observed in this work (Sect. 6.1) that these vertical pn junctions have no detectable influence on the KPFM measurement. This is ascribed to the small breakdown voltage of less than 10 V [106, p. 456, Fig. 18.46.(a)] due to the high doping level of one side of the vertical pn junctions in the SRAM and DRAM cell. Thus, the ac-bias with an effective value of 6 V and a peak voltage of ± 8.5 V applied during the KPFM measurement may cause a breakdown of the vertical pn junctions.

For investigation of the influence of intrinsic electric fields on the KPFM measurement the transport of the injected majority charge carriers has to be examined. This is possible for example by means of varying the operation frequency f_{ac} which determines the drift of charge carriers along z-direction in the sample. In the following Sect. 5.2.7.2 the technical aspects of frequency dependent KPFM measurements are discussed.

5.2.7.2 Frequency dependent KPFM

For the investigation of local intrinsic electric fields by means of the operation frequency f_{ac} all technical influences of the KPFM setup on the detected electrical signals have to be ruled out.

Mechanical and electrical in-resonance oscillations may suffer for example from parasitic coupling [159]. The Anfattec Level-AFM applied in this work uses an independent excitation of the mechanical and electrical oscillations. Therefore, the mechanical oscillations at the resonance frequency f_r (about 320 kHz) are not expected to suffer from parasitic coupling to the electrostatic oscillations at the operation frequency f_{ac} (5-130 kHz) and vice versa. In addition, an advanced offset compensation technique in dependence on the measurement frequency and geometrical tip-sample configuration is applied to reduce stray capacitances. By the use of an active signal mixer, the applied ac-bias is constant and independent of the operation frequency f_{ac} . The technical details of the Level-AFM system can be found in Ref. [53] and are summarized in Sect. 3.2.

For verification of possible technical contributions to the measured KPFM data the configuration of the detected electrical signals has to be understood. When scanning in far distance from a sample surface no electrostatic forces should be acting onto the conductive cantilever. In reality, when applying all electrical excitations a small electrical signal is detected which is referred to as *background signal*. This phenomenon was investigated and described by F. Müller *et al.* in 2009 [53]. The small background signal may be caused by interactions, i.e. crosstalk, in the electrical setup of the Level-AFM system.

For investigating the influence of the background, the electrical signal of the 1st harmonic has been recorded in retracted mode and compared to a standard measurement in close proximity to the sample surface. The background signal was recorded at a distance of 10 μm between probe and sample. In Tab. 5.4, the measured amplitude and phase values of the

Table 5.4: Amplitude and phase of the electrical signal of the 1st harmonic in standard and retracted mode probed on the conventional SRAM cell and on the cross-sectionally prepared Si:B epilayer sample in dependence on the operation frequency f_{ac} . With respect to the standard signal an in-phase background is observed on the SRAM cell while the background signal probed on the Si:B epilayer sample is out-of-phase. Adapted from Ref. [160].

Operation frequency f_{ac} (kHz)	SRAM				Epilayer			
	Standard		Background		Standard		Background	
	Amplitude (μV)	Phase ($^\circ$)	Amplitude (μV)	Phase ($^\circ$)	Amplitude (μV)	Phase ($^\circ$)	Amplitude (μV)	Phase ($^\circ$)
130	350	139	40	132	65	135	14	102
90	300	152	30	148	55	147	9	121
70	250	158	30	164	46	155	6	123
40	250	167	30	162	45	167	4	132
20	250	174	30	182	45	177	4	arbitrary
10	200	176	25	179	45	186	4	arbitrary
5	200	179	25	189	45	184	4	arbitrary

standard and the background signal probed on the conventional SRAM cell (Sect. 3.1.1) and on the cross-sectionally prepared Si:B epilayer sample (Sect. 3.1.2) are presented. In general, the frequency dependence of the adjusted phase is similar for every sample and pre-determined by the frequency response of the used lock-ins. The error of the phase adjustment for the corresponding background signal is in the range of $\pm 10\%$ for the SRAM sample and amounts to up to $\pm 20\%$ for the cross-sectionally prepared Si:B epilayer sample. The phase is better adjustable and shows a smaller error if the correspondingly detected amplitude of the standard or background signal is large. For small amplitude values the phase signal becomes unstable and a proper phase adjustment may be impossible. This was observed during the background measurement above the cross-sectionally prepared Si:B epilayer sample where the small amplitude values of the background signal cause an unstable phase between 90° and 130° for operation frequencies down to 40 kHz. Below 40 kHz the phase of the background signal shows completely arbitrary values.

As can be seen in Tab. 5.4, the background signal recorded on the SRAM cell is in-phase with respect to the corresponding standard signal for all operation frequencies. On the Si:B epilayer sample an out-of-phase background is observed. Both cases are schematically illustrated in Fig. 5.12 where the amplitude and the phase of the detected electrical signals are presented in a vector diagram. Two measurement positions 1 and 2 on the sample are assumed for proper discussion of the lateral variation of the electrical signal. In Fig. 5.12(a) the influence of an in-phase background signal as probed above the SRAM sample is discussed. In Fig. 5.12(b) an out-of-phase background signal as probed above the Si:B

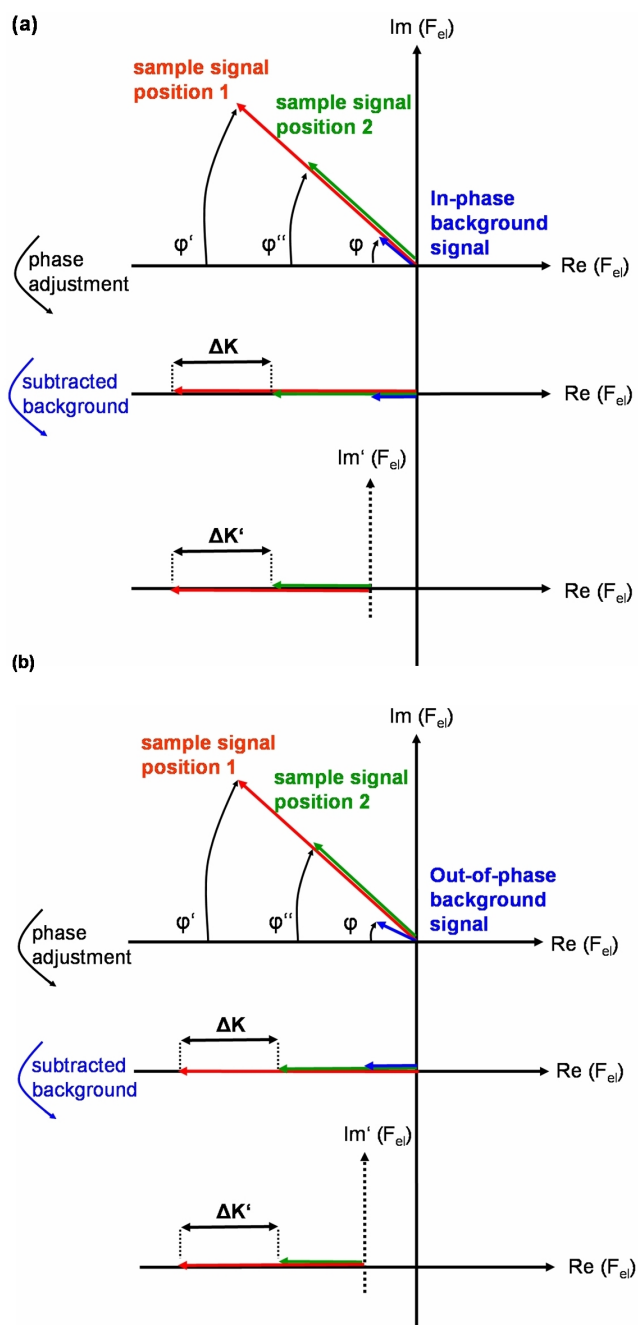


Figure 5.12: Vector diagram illustrating the electrical signal of the 1st harmonic for (a) an in-phase ($\varphi = \varphi' = \varphi''$) and (b) an out-of-phase ($\varphi \neq \varphi' = \varphi''$) background. The electrical signals probed at the measurement position 1 (red) and 2 (green) on the sample as well as the background signal (blue) are phase-adjusted to maximize the real part. The lateral variation of the electrical signal ΔK is not influenced by subtraction of an in-phase or out-of-phase background signal ($\Delta K = \Delta K'$). Adapted from Ref. [160].

epilayer sample is illustrated. The electrical signal recorded at the measurement position 1 (2) is illustrated by means of a red-coloured (green-coloured) vector in the diagrams, respectively. The background signal is imaged as blue-coloured vector. Note that due to measuring the background signal in retracted mode, a constant background amplitude and phase is assumed for the measurement positions 1 and 2. As indicated in Fig. 5.12, a phase-adjustment is performed for maximization of the real part of the electrical signal. The background signal probed in retracted mode has to be subtracted from the electrical signals probed in standard mode at the measurement positions 1 and 2. This is illustrated in the lower part of Fig. 5.12(a) and (b), respectively. It is found that the lateral variation ΔK of the electrical signal is independent of the background signal. $\Delta K = \Delta K'$ is fulfilled for both, the in-phase and the out-of-phase background.

It can be concluded that KPFM measurements performed at different operation frequencies are not influenced by technical aspects of the KPFM measurement setup. Thus, any observed frequency dependence of the probed electrical signals has to be ascribed to sample properties, i.e. to the sample-specific transport of charge carriers in the presence of local intrinsic electric fields. The results of the frequency dependent KPFM measurements on the SRAM and DRAM cell and on the epilayer samples are discussed in detail in Sect. 6.1 and 6.2, respectively.

5.2.8 Electrostatic force and higher harmonics

In the Level-AFM from Anfattec Instruments AG higher harmonics of the electrostatic force can be detected simultaneously with the 1st harmonic. Without loss of generality the electrostatic energy E between tip and sample can be written as

$$E = \frac{1}{2}CU^2. \quad (33)$$

C is the capacitance of the tip-sample system and U is the bias [Eq. (1)] applied during the KPFM measurement.

The electrostatic force F_{el} is the derivative of the electrostatic energy E with respect to the tip-sample distance z and defined as

$$F_{el} = \frac{dE}{dz} = \frac{1}{2} \frac{dC}{dz} U^2 + \frac{1}{2} C \frac{dU^2}{dz}. \quad (34)$$

The calculation of F_{el} gives a constant term F_{0el} and two time-dependent terms F_{1el} and F_{2el} .

$$F_{0el} = F_{el}(e^{0 \cdot (2\pi i f_{ac} t + \varphi_0)}) = \left(\frac{1}{2} \frac{dC}{dz} U_{dc}^2 + \frac{1}{2} C \frac{dU_{dc}^2}{dz} \right) e^{0 \cdot (2\pi i f_{ac} t + \varphi_0)} \quad (35)$$

$$F_{1el} = F_{el}(e^{1 \cdot (2\pi i f_{ac} t + \varphi_0)}) = \left(\frac{dC}{dz} U_{dc} U_{ac} + C \frac{dU_{dc}}{dz} U_{ac} + C U_{dc} \frac{dU_{ac}}{dz} \right) e^{1 \cdot (2\pi i f_{ac} t + \varphi_0)} \quad (36)$$

$$F_{2el} = F_{el}(e^{2 \cdot (2\pi i f_{ac} t + \varphi_0)}) = \left(\frac{1}{2} \frac{dC}{dz} U_{ac}^2 + \frac{1}{2} C \frac{dU_{ac}^2}{dz} \right) e^{2 \cdot (2\pi i f_{ac} t + \varphi_0)} \quad (37)$$

As was explained in Sect. 3.2 the electrical signal of the 1st harmonic F_{1el} is used as the input signal for the digital Kelvin probe force feedback. The 2nd harmonic F_{2el} depends on the capacitance of the tip-sample system C and on the applied ac-bias U_{ac} . Note that the signal of the 2nd harmonic F_{2el} does not depend on the applied dc-bias U_{dc} , i.e. on the dopant concentration dependent KPFM bias applied during the KPFM measurement in order to minimize the electrostatic forces. Thus, the 2nd harmonic is not correlated with the injection of majority charge carriers at the measurement position and is thus not influenced by local intrinsic electric fields. It is shown by the example of KPFM measurements across horizontal Si nanowires in Sect. 6.3 that F_{2el} therefore provides a better lateral resolution than the simultaneously probed KPFM bias. Additionally, the 2nd harmonic F_{2el} can also be used to investigate insulators and overcomes the strong restriction of the KPFM bias measurement. However, the quantitative interpretation of the 2nd harmonic requires extensive theoretical calculations of the capacitive and electrostatic tip-sample interaction as discussed for example in Ref. [161], and remains an open issue. The 3rd harmonic of the electrostatic force F_{3el} which also can be detected by means of the Level-AFM is proportional to the 1st harmonic F_{1el} and does not contain additional information.

6 Results

6.1 Silicon static and dynamic random access memory cells

In this section the results of KPFM measurements on the conventional SRAM and DRAM cells introduced in Sect. 3.1.1 are discussed. Quantitative dopant profiling is demonstrated successfully by use of the new KPFM model. The influence of local intrinsic electric fields is investigated by means of frequency dependent measurements. Additionally, the ac-bias dependence is discussed for the SRAM cell. In Sect. 6.1.1.4 finally the results of ambient and UHV KPFM measurements performed on the SRAM cell are compared.

6.1.1 Static random access memory cell

6.1.1.1 Quantitative dopant profiling

In the following, quantitative dopant profiling by means of the new KPFM model is discussed by the example of two different doping junctions in the conventional SRAM cell. The KPFM measurements have been carried out with an n^+ -type cantilever at an ac-bias of 6 V and an operation frequency of 130 kHz.

In Fig. 6.1 the results of the KPFM measurement across an $n^+pn^+pn^+$ junction are illustrated. The simultaneously probed surface topography and KPFM bias are presented in Fig. 6.1(a) and (b), respectively. The investigated $n^+pn^+pn^+$ junction is marked as a blue line in the KPFM bias image and in the schematic doping pattern of the SRAM cell given in Fig. 6.1(c). The KPFM bias probed along the section line is displayed in Fig. 6.1(d). A lateral KPFM bias variation of approximately 120 mV is observed between the n^+ -type regions and the p -type conducting "n-channel" regions. Above the n^+ -type region at the lateral position of around 6 μm the probed KPFM bias is larger by approximately 35 mV compared to the n^+ -type regions at 3.5 μm and 1 μm . This deviation may be caused by a surface contamination which locally distorts the electrical signal.

The n^+ -type regions are As-doped with a concentration of $2 \times 10^{20} \text{ cm}^{-3}$ while the "n-channel" regions contain B with a concentration of $2 \times 10^{17} \text{ cm}^{-3}$. The calculated energy difference between Fermi energy and respective band edge amounts to $[E_C - E_F(n)] \cong 0$ meV in the n^+ -type regions, and to $[E_V - E_F(p)] \cong -130$ meV in the "n-channel" regions. Thus, an energy difference of 130 meV is predicted by the new KPFM model. This is in good agreement with the probed lateral KPFM bias variation of 120 mV. Note that in the CPD model an energy difference of 990 meV is expected between the n^+ -type and the "n-channel" regions. A comparison between measurement and new KPFM model calculation is given in the plot in Fig. 6.1(d).

The observed small deviation of 10 mV between the measured lateral KPFM bias variation and the calculated energy difference may result from averaging over 10 scan lines as well as from minor variations of the real dopant concentrations compared to the theoretical values provided by Veeco Instruments (since 2010 Bruker Corp.). For example, a B-concentration

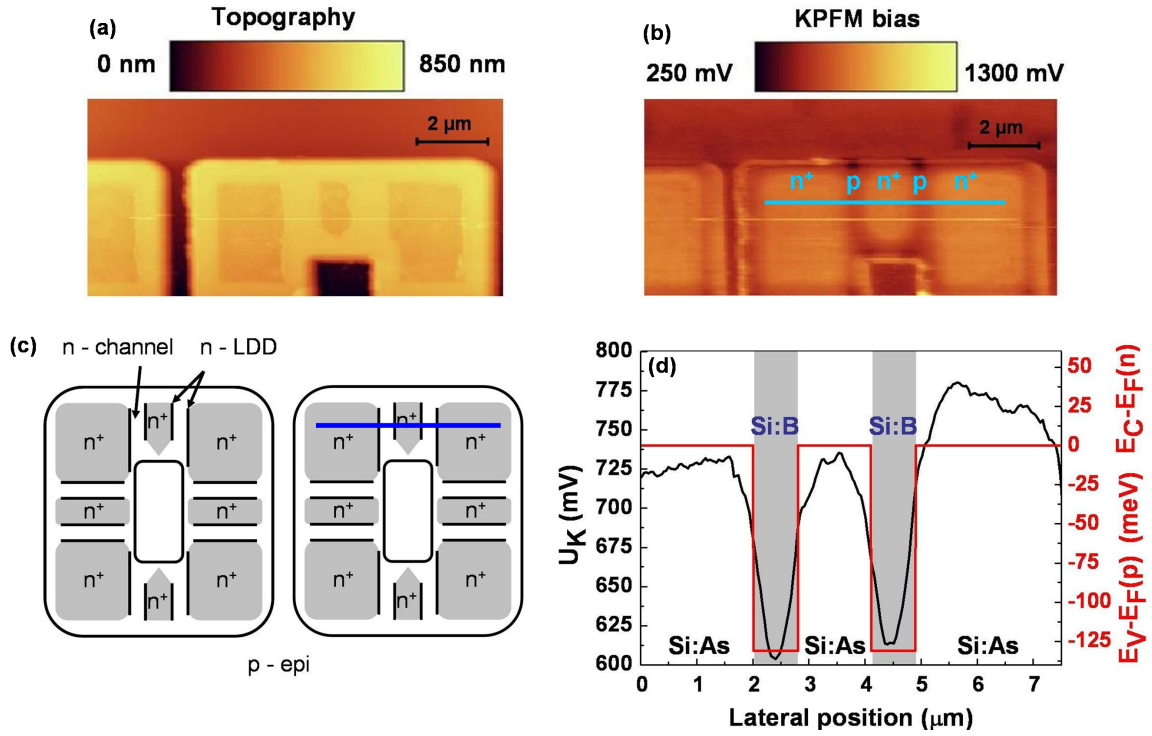


Figure 6.1: Results of the KPFM measurement across an $n^+pn^+pn^+$ junction in the SRAM cell. (a) Surface topography, (b) KPFM bias with marked investigated section line across the $n^+pn^+pn^+$ junction, (c) Schematic doping pattern of the SRAM cell with marked section line, (d) KPFM bias section line (averaged over 10 lines) compared to the calculated energy differences $[E_C - E_F(n)]$ and $[E_V - E_F(p)]$. Adapted from Ref. [162].

of $4 \times 10^{17} \text{ cm}^{-3}$ instead of the defined $2 \times 10^{17} \text{ cm}^{-3}$ in the "n-channel" region would cause a deviation of 10 meV, i.e. a calculated energy difference of 120 meV instead of 130 meV.

In Fig. 6.2 the results of the KPFM measurement across a p^+np^+ junction in the SRAM cell are presented. The simultaneously probed surface topography and KPFM bias are given in Fig. 6.2(a) and (b), respectively. The investigated p^+np^+ junction is marked as a blue line in the KPFM bias image and in the schematic doping pattern of the SRAM cell illustrated in Fig. 6.2(c). In Fig. 6.2(d) the KPFM bias probed along the section line is plotted. The KPFM bias plot features two peaks at the lateral positions $-0.5 \mu\text{m}$ and $0.5 \mu\text{m}$. These peaks which indicate a strongly distorted KPFM bias are related to the topographic step of 500 nm between the n-well region and the differently doped higher device components which can be seen in the topography image [Fig. 6.2(a)]. The KPFM bias is distorted at high vertical topographic steps due to the fact that the oxide layer and the thin water film which occur in ambient KPFM measurements are arranged vertically, too. The 500 nm thick vertical oxide layer and water film below the probing cantilever at the topographic step create a potential shielding which may dominate the electrical signal from the asymmetric electric dipole (Sect. 5.2.4). In addition, contaminations due

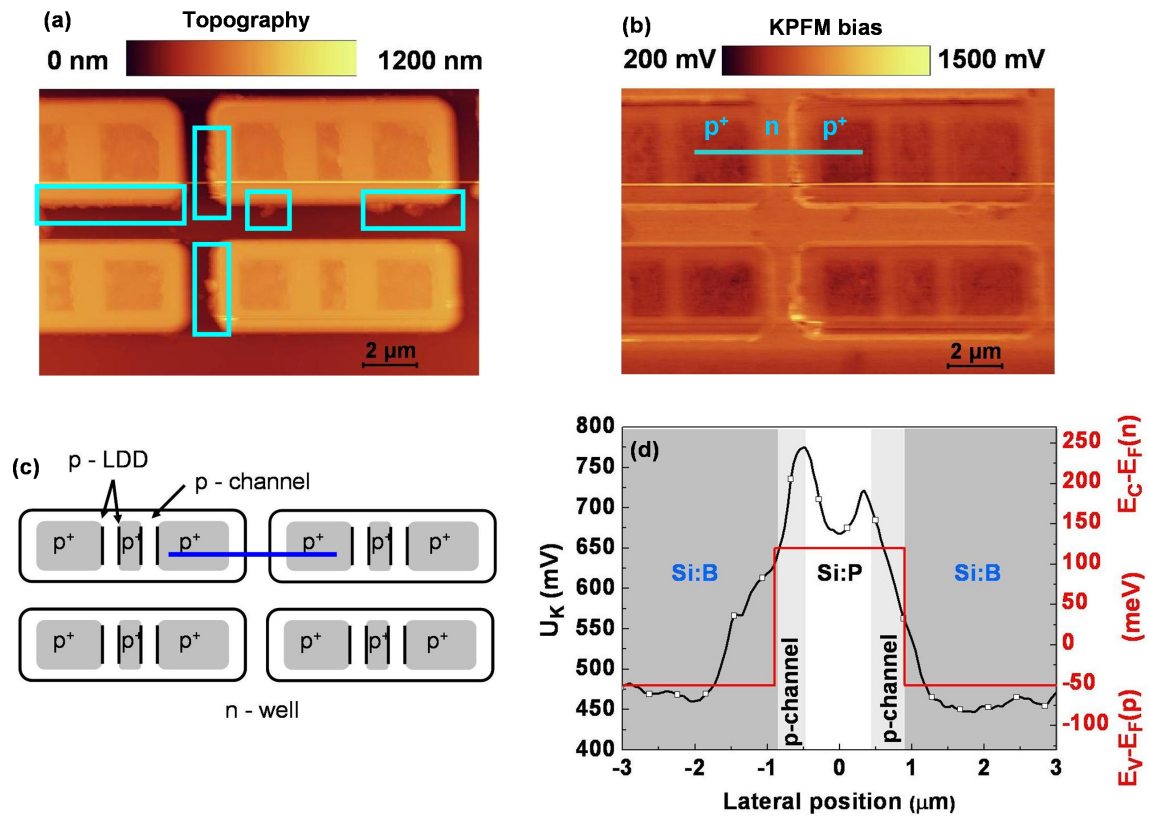


Figure 6.2: Results of the KPFM measurement across a p^+np^+ junction in the SRAM cell. (a) Surface topography with marked positions of surface contaminations at the vertical topographic steps (blue rectangles), (b) KPFM bias with marked investigated section line across the p^+np^+ junction, (c) Schematic doping pattern of the SRAM cell with marked section line, (d) KPFM bias section line (averaged over 30 lines) compared to the calculated energy differences $[E_C - E_F(n)]$ and $[E_V - E_F(p)]$.

to the exposure of the samples to environmental conditions during the ambient KPFM measurements accumulate preferentially at surface inhomogeneities such as topographic steps, wells, or scratches. The contamination in particular at the vertical topographic steps is clearly visible in the topography image where the positions are marked by means of blue rectangles [Fig. 6.2(a)].

For the analysis of the lateral KPFM bias variation across the p^+np^+ junction the central value of the n-well region at a lateral position of $0 \mu\text{m}$ and the edge values of the p^+ -type regions at the lateral positions of $-2.5 \mu\text{m}$ and $2.5 \mu\text{m}$, respectively, are chosen. These values are expected to be least influenced by the topographic step distortion. Between the chosen points a lateral KPFM bias variation of approximately 190 mV is probed.

The p^+ -type regions contain B with a concentration of $4 \times 10^{19} \text{ cm}^{-3}$. The n-well region is P-doped with a concentration of $2 \times 10^{17} \text{ cm}^{-3}$. The narrow n-type conducting "p-channel" regions adjacent to the p^+ -type regions feature a P-doping with a concentration of 1×10^{17}

cm^{-3} and thus can not be distinguished electrically from the KPFM bias probed across the n-well region. Additionally, the distortion from the vertical topographic step dominates the electrical signals probed above the "p-channel" regions and prevents a quantitative analysis. Therefore, for quantitative dopant profiling the focus lies on the p^+np^+ junction between the p^+ -type regions and the central n-well region.

The calculated energy differences amount to $[E_V - E_F(p)] \cong -50$ meV in the p^+ -type regions and to $[E_C - E_F(n)] \cong +120$ meV in the n-well region. In conclusion, for the p^+np^+ junction an energy difference of 170 meV is predicted by the new KPFM model, which is in good agreement with the probed KPFM bias variation of 190 mV. Note that in the CPD model an energy difference of 950 meV is expected between the p^+ -type regions and the n-well. The comparison between the KPFM bias section line across the p^+np^+ junction and the calculated energy differences $[E_C - E_F(n)]$ and $[E_V - E_F(p)]$ is presented in Fig. 6.2(d).

It can be concluded that the new KPFM model is suitable to quantitatively correlate the lateral KPFM bias variation with the energy difference between Fermi energy and respective band edge and thus with the local dopant concentration.

6.1.1.2 Frequency dependent KPFM measurements

For investigation of the influence of local intrinsic electric fields, frequency dependent KPFM measurements have been performed on the SRAM cell. The measurements focus on the p^+np^+ junction which was used to demonstrate quantitative dopant profiling in the preceding Sect. 6.1.1.1. The frequency dependence of the lateral KPFM bias variation across the p^+np^+ has been investigated by means of an n^+ -type and a p^+ -type cantilever. Note that the KPFM measurements with the n^+ -type and the p^+ -type cantilever have been performed on a similar p^+np^+ junction but at different measurement positions in the array of repeating doping pattern of the SRAM cell.

At first, the KPFM measurements performed with the n^+ -type cantilever are discussed. In Fig. 6.3(a) and 6.3(b) the simultaneously probed surface topography and KPFM bias recorded at 130 kHz are presented, respectively. The blue line in the KPFM bias image marks the investigated section line across the p^+np^+ junction. The p^+np^+ junction has been scanned with an operation frequency f_{ac} of 130 kHz, 90 kHz, 70 kHz, 40 kHz, 20 kHz, and 10 kHz. Note that an ac-bias of 6 V was applied during the KPFM measurements. In Fig. 6.3(c) the section lines of the frequency dependent KPFM measurements are shown. As can be seen, the KPFM bias section lines are distributed along the U_K -scale which indicates a frequency dependent offset value. For simplifying the comparison between the measured lateral KPFM bias variation and the calculated energy differences the section lines have been shifted on the U_K -scale to reach overlay of the spectra which is shown in Fig. 6.3(d). From the overlay of the spectra it can be concluded that for all operation frequencies the same lateral KPFM bias variation of approximately 190 mV is observed

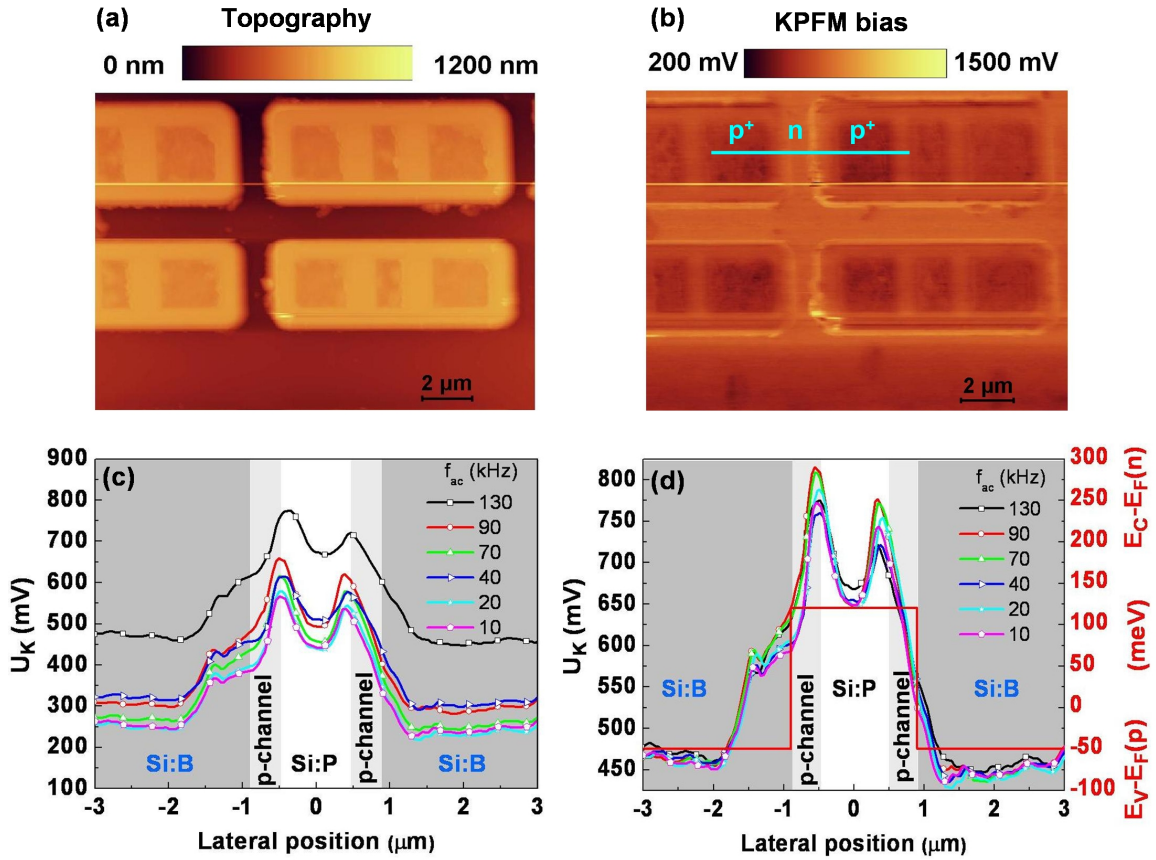


Figure 6.3: Results of the frequency dependent KPFM measurement across the p^+np^+ junction in the SRAM cell performed with an n^+ -type cantilever. (a) Surface topography, (b) KPFM bias probed at 130 kHz with marked investigated section line, (c) Section lines (averaged over 30 lines) of scans with 130 kHz, 90 kHz, 70 kHz, 40 kHz, 20 kHz and 10 kHz, (d) Shifted section lines compared to the calculated energy differences $[E_C - E_F(n)]$ and $[E_V - E_F(p)]$. Adapted from Ref. [160].

between the p^+ -type regions and the n-well region. The lateral KPFM bias variation is in good agreement with the calculated energy difference of 170 meV for the p^+np^+ junction (Sect. 6.1.1.1). Note that the frequency dependent KPFM bias offset does not influence the lateral KPFM bias variation.

The frequency dependent KPFM measurements across the p^+np^+ junction have been repeated with a p^+ -type cantilever. In Fig. 6.4(a) and (b) the surface topography and KPFM bias simultaneously probed at an operation frequency of 130 kHz are illustrated. The p^+np^+ junction has been scanned with operation frequencies of 130 kHz, 90 kHz, 70 kHz, 40 kHz, 20 kHz, and 10 kHz at an ac-bias of 6 V. The KPFM bias section lines are given in Fig. 6.4(c). Similar to the measurement with the n^+ -type cantilever the KPFM bias section lines are distributed along the U_K -scale indicating the frequency dependence of the offset value. The section lines are shifted on the U_K -scale in Fig. 6.4(d) to reach overlay

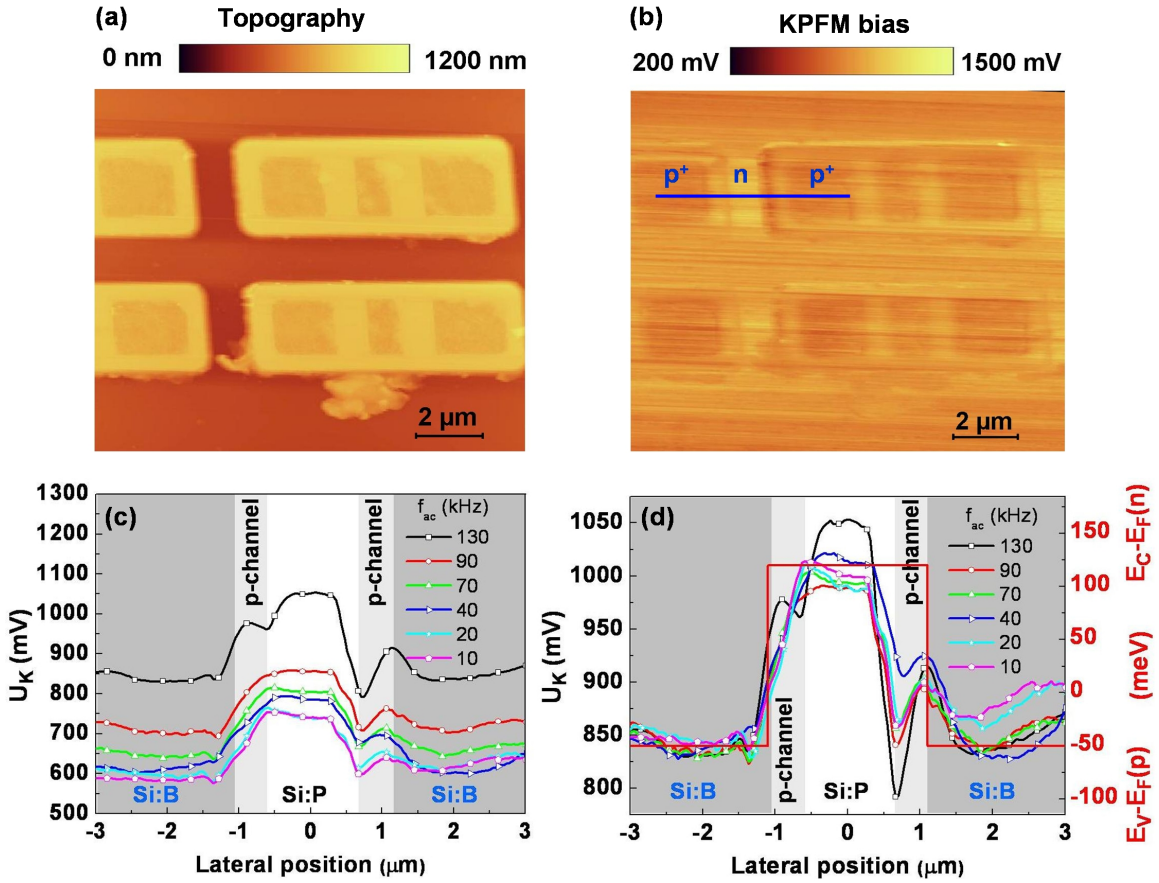


Figure 6.4: Results of the frequency dependent KPFM measurement across the p^+np^+ junction in the SRAM cell performed with a p^+ -type cantilever. (a) Surface topography, (b) KPFM bias probed at 130 kHz with marked investigated section line, (c) Section lines (averaged over 30 lines) of scans with 130 kHz, 90 kHz, 70 kHz, 40 kHz, 20 kHz and 10 kHz, (d) Shifted section lines compared to the calculated energy differences $[E_C - E_F(n)]$ and $[E_V - E_F(p)]$. Adapted from Ref. [160].

of the spectra for the comparison between the measured lateral KPFM bias variation and the calculated energy differences. As can be seen in Fig. 6.4(d) for all applied operation frequencies a lateral KPFM bias variation of approximately 170 mV is probed between the p^+ -type regions and the n-well region which is in good agreement with the calculated energy difference of 170 meV predicted from the new KPFM model (Sect. 6.1.1.1). The slightly increased KPFM bias variation for 130 kHz as well as the deviating KPFM bias values probed with 10 kHz (pink) and 20 kHz (turquoise) at the lateral position of approximately $2.5 \mu\text{m}$ [Fig. 6.4(d)] are caused by spurious lines which occur in the recorded KPFM bias image and which influence the KPFM bias average over 30 scan lines. However, in the topography at the vertical topographic step at the investigated p^+np^+ junction almost no contamination is observed [Fig. 6.4(a)] and the probed KPFM bias shows less distortion at the lateral positions $-0.5 \mu\text{m}$ and $0.5 \mu\text{m}$.

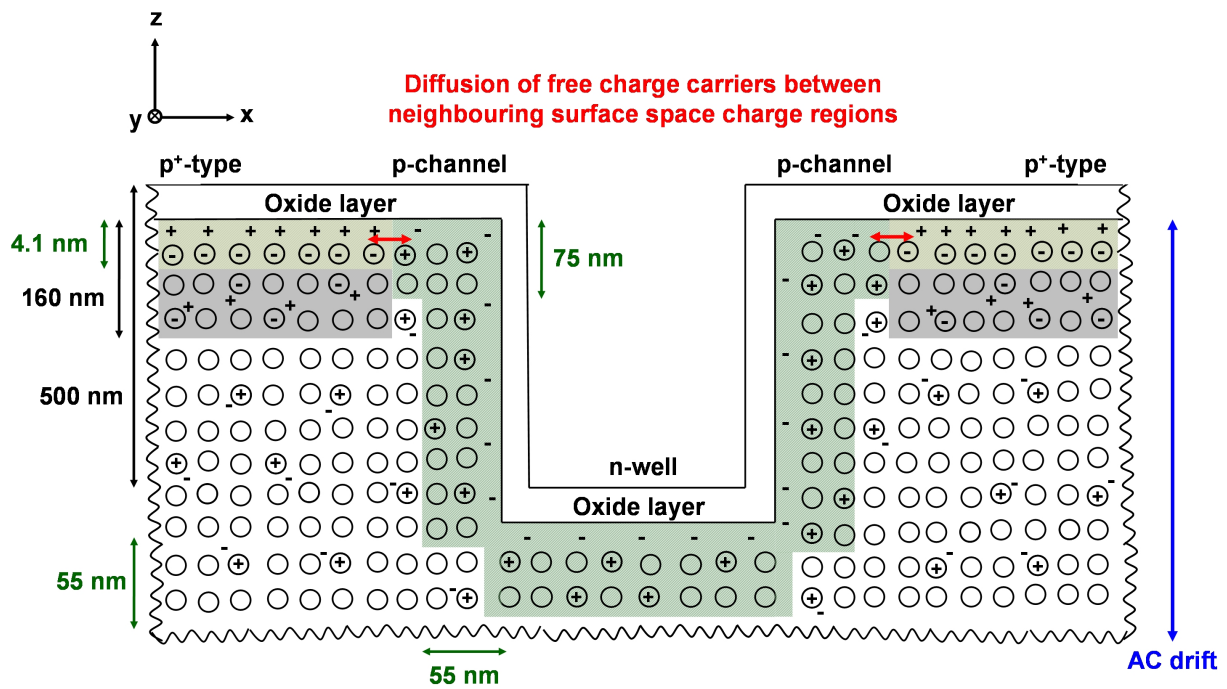


Figure 6.5: Schematic cross-sectional illustration of the surface region of the SRAM cell with shallow p^+ -type regions, n -type conducting "p-channel" regions, and the n-well region. The maximum thickness of the surface space charge region (green) amounts to 4.1 nm in the p^+ -type regions, to 55 nm in the n-well and to 75 nm in the "p-channel" regions. The diffusion between neighbouring surface space charge regions along x (red) and the ac-drift along z (blue) are indicated.

It can be concluded that within the investigated range the lateral KPFM bias variation probed across the p^+np^+ junction is independent of the applied operation frequency f_{ac} .

For understanding this very promising result the KPFM measurement principle has to be discussed with respect to the structure of the SRAM cell. The surface region of the SRAM cell is illustrated schematically as cross-section in Fig. 6.5. SRIM calculations (Sect. 3.3.2) using the implantation details provided by Veeco Instruments (Sect. 3.1.1) have been performed for an estimation of the thickness of the shallow implanted p^+ -type regions. A Gauss distribution of B atoms with a mean implantation depth of approximately 160 nm (FWHM \cong 100 nm) is found. Note that the SRIM calculations do not include an annealing treatment which may be part of the fabrication process of the SRAM cell and which may lead to a more box-like dopant distribution with increased depth as was observed after implantation and annealing of the NW samples (Sect. 3.1.3).

Due to the small thickness of the p^+ -type regions, primarily vertical pn junctions form between the p^+ -type and the n -type conducting regions (Sect. 5.2.7.1). The space charge region at the pn junctions is not illustrated in Fig. 6.5.

The maximum thickness of the surface space charge regions is estimated by means of Eq. (5) and amounts to 4.1 nm in the p^+ -type regions, to 55 nm in the n-well and to 75 nm in the "p-channel" regions. Note that also along the edges at the vertical topographic step an asymmetric electric dipole forms as shown schematically in Fig. 6.5. Injected majority charge carriers are expected to drift along x-direction within the thus formed horizontal electric field (Sect. 5.2.7.1) which distorts the KPFM bias probed above this region. However, due to the topographic step near this measurement position a possible influence on the probed KPFM bias can not be distinguished satisfyingly from the step distortion.

During the KPFM measurements an ac-bias is applied to the sample via the back contact. The resulting ac-drift in z-direction (Fig. 6.5) causes an alternating accumulation and depletion of majority charge carriers in the surface region of the investigated SRAM sample. For minimizing the electrostatic force acting onto the cantilever, majority charge carriers are injected into the sample surface region at the measurement position by additionally applying the appropriate KPFM bias. These injected majority charge carriers screen the unscreened immobile ionized dopant atoms and thus remove the vertical asymmetric electric dipole at the measurement position. Note that the probed lateral KPFM bias variation can only be correlated quantitatively to the local dopant concentration via Eqs. (6) and (7) if the asymmetric electric dipole is removed exclusively by majority charge carriers injected via the applied KPFM bias.

In samples containing regions with opposite type of majority charge carriers the applied ac-bias causes a lateral gradient in the charge carrier concentration. This is due to the fact that accumulated charge carriers are of majority type in some regions but of minority type in oppositely doped regions. As a result, charge carriers diffuse between neighbouring doped regions. In particular the diffusion between neighbouring surface space charge regions may have strong influence on the measurement of the KPFM bias. If charge carriers from a neighbouring surface space charge region diffuse into the surface space charge region at the measurement position during the KPFM scan, they may partially remove the asymmetric electric dipole and thus distort the probed KPFM bias. From the structure of the SRAM cell shown in Fig. 6.5 it can be deduced that only between the p^+ -type regions and the adjacent narrow "p-channel" regions neighbouring surface space charge regions form where diffusion of charge carriers may occur. Thus, the central n-well region is expected not to be influenced by diffusion of charge carriers.

In the following, drift and diffusion of charge carriers in the SRAM cell are discussed for the largest and the smallest applied operation frequency, i.e. for 130 kHz and for 10 kHz. First of all, the ac-drift due to the applied ac-bias with an effective value of 6 V is estimated. The applied ac-bias oscillates between the positive and negative peak voltage ± 8.5 V resulting in a similarly oscillating electric field in the 1 mm thick SRAM cell. The time-dependent values of the electric field have been used to calculate the time-dependent ac-drift velocity $v_{ac-drift}$ at 300 K by means of Eq. (9) in Ref. [163], namely

$$v_{ac-drift} = v_m \frac{E/E_c}{[1 + (E/E_c)^\beta]^{1/\beta}}. \quad (38)$$

Table 6.1: Fitting parameters for the electric field and temperature dependence of the electron drift velocity $v_{ac-drift}$ calculated by means of Eq. (38) with the temperature T in degrees Kelvin. Adapted from Ref. [163].

v_m (cm/s)	E_c (V/cm)	β
$1.53 \times 10^9 \times T^{-0.87}$	$1.01 \times T^{1.55}$	$2.57 \times 10^{-2} \times T^{0.66}$

Note that Eq. (38) describes the drift velocity of electrons and holes in pure silicon but is in reasonable agreement with the drift velocity in doped semiconductors with small to medium dopant concentration. This aspect is discussed in more detail below in this section. For simplicity, $v_{ac-drift}$ has been calculated only for electrons. The corresponding fitting parameters used in Eq. (38) are given in Tab. 6.1. Transport of holes can be discussed in analogue way.

In Fig. 6.6 $v_{ac-drift}$ of electrons in the SRAM cell is plotted for the operation frequencies 130 kHz and 10 kHz. The calculated ac-drift velocity $v_{ac-drift}$ corresponds to an electron mobility of about 1530 cm²/Vs.

Note that diffusion of charge carriers between neighbouring regions starts to play a role when the diffusion velocity v_{diff} is larger than the ac-drift velocity $v_{ac-drift}$. The diffusion velocity v_{diff} is given by the quotient of the diffusion coefficient D and the diffusion length L [164]. In Si the diffusion coefficient of electrons and holes amounts to ≤ 36 cm²/s and ≤ 12 cm²/s, respectively (Ioffe database, www.ioffe.ru). The diffusion length L typically is in the order of several hundred micrometer (Ioffe database, www.ioffe.ru). From these values a diffusion velocity v_{diff} in the order of 1×10^3 cm/s can be estimated for Si. This estimated value is used in the following discussion and indicated as red line in Fig. 6.6.

In Fig. 6.6(a) the ac-drift velocity $v_{ac-drift}$ is plotted for one period T_{ac} of the 10 kHz oscillation, i.e. for 10^{-4} s. The maximum ac-drift velocity amounts to 1.3×10^5 cm/s. For an estimation of the time period in which $v_{ac-drift} < v_{diff}$ is fulfilled, the calculated data are plotted on a smaller time-scale in Fig. 6.6(b). The time periods with $v_{ac-drift} < v_{diff}$ are summarized in Tab. 6.2. Note that during one period T_{ac} of the ac-oscillation for electrons twice the condition $v_{ac-drift} < v_{diff}$ is fulfilled. Accumulation of holes via the applied ac-bias is related to negative ac-drift velocities in Fig. 6.6 and can be discussed in similar way.

For 130 kHz, the time period in which $v_{ac-drift} < v_{diff}$ is fulfilled amounts to 9×10^{-9} s. At 10 kHz this time period is enhanced by approximately one order of magnitude and amounts to 1.2×10^{-7} s. Note that these time periods are much smaller than the period T_{ac} of the ac-oscillation which amounts to 7.7×10^{-6} s for 130 kHz and to 1.0×10^{-4} s for 10 kHz. During the estimated time periods charge carriers may diffuse with a range of 90 nm and 1200 nm, respectively (Tab. 6.2). The estimated diffusion ranges show that at large operation frequencies diffusion of charge carriers between the neighbouring surface space charge regions of the p^+ -type regions and the adjacent narrow "p-channel" regions only takes place on a small lateral scale. Due to the large scan range as well as due to the distorting topographic step near this measurement position, the very small distorted

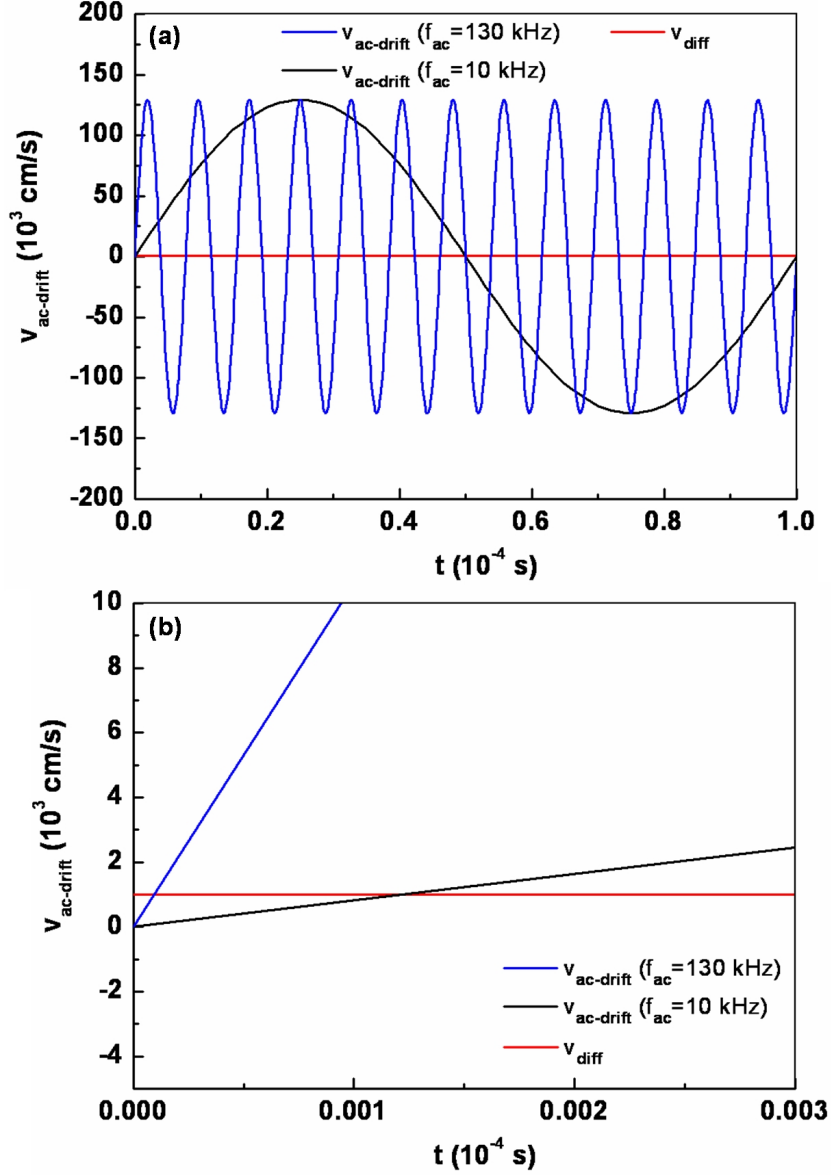


Figure 6.6: AC-drift velocity in the SRAM cell calculated for electrons by means of Eq. (38) for the operation frequencies 130 kHz and 10 kHz at an effective ac-bias of 6 V. Plot over (a) 1×10^{-4} s corresponding to a period T_{ac} of the 10 kHz-oscillation and (b) 3×10^{-7} s for investigation of the time period in which $v_{ac-drift} < v_{diff}$ is fulfilled. The constant diffusion velocity v_{diff} of 1×10^3 cm/s is indicated as a red line.

region of only 90 nm width for measurements at 130 kHz is not resolved laterally and electrically. With decreasing operation frequency the diffusion range increases up to 1200 nm at 10 kHz and a possible distortion of the probed KPFM bias in the p^+ -type regions could be detected. However, the specific structure of the SRAM cell has to be included in the discussion. The interface between the neighbouring surface space charge regions

Table 6.2: Diffusion in the SRAM cell. Time period in which the condition $v_{ac-drift} < v_{diff}$ is fulfilled for the operation frequencies 130 kHz and 10 kHz. Additionally, the diffusion range of charge carriers in the respective time period is given.

Operation frequency f_{ac} (kHz)	Time period of $v_{ac-drift} < v_{diff}$ (s)	Diffusion range (nm)
130	9×10^{-9}	90
10	1.2×10^{-7}	1200

of the p^+ -type regions and the adjacent narrow "p-channel" regions is smaller than 4.1 nm. Thus, only a small amount of charge carriers may diffuse between the neighbouring surface space charge regions of the p^+ -type and the "p-channel" regions. Additionally, the dopant concentration in the p^+ -type regions is comparably large which results in a negligible contribution of diffusing charge carriers to the removal of the vertical asymmetric electric dipole.

In conclusion, the asymmetric electric dipole in the surface region of the discussed p^+ -type regions and the n-well is removed at all operation frequencies mainly by majority charge carriers injected via the applied KPFM bias. The probed lateral KPFM bias variation is thus independent of the operation frequency and remains quantitatively correlated with the local dopant concentration via Eqs. (6) and (7) even at small operation frequencies.

Note that the presented estimation of ac-drift and diffusion in the SRAM cell is only a very simple approximation of the complex dynamic transport phenomena in locally structured and doped semiconducting samples during the KPFM measurement. The applied Eq. (38) describes the electron drift velocity in pure silicon. It can be deduced from Ref. [163] that the electron drift velocity calculated by means of Eq. (38) is in very good agreement with the electron drift velocity in semiconductors with small to medium dopant concentration, i.e. to about $1 \times 10^{16} \text{ cm}^{-3}$, and in reasonable agreement for dopant concentrations to about $1 \times 10^{17} \text{ cm}^{-3}$. Therefore, Eq. (38) is regarded as reasonable approximation for the description of the SRAM cell with the large low doped n-well region and the only shallow implanted highly p^+ -type regions. The DRAM cell (Sect. 3.1.1) and the cross-sectionally prepared Si epilayer samples (Sect. 3.1.2) with the mainly low-doped regions are discussed in similar way. As pointed out in Ref. [163] in reality the ac-drift velocity depends on the charge carrier type, the charge carrier mobilities and on the local impurity concentration of the doped regions. Additionally, the ac-drift velocity is influenced by sample-specific vertical and horizontal intrinsic electric fields due to the formed space charge regions at pn junctions as well as at the sample surface, which further complicates a quantitative discussion. Also the diffusion velocity depends on the specific structure of the investigated region of the semiconducting sample and the related charge carrier properties. Therefore, for an exact study of the complex dynamic transport phenomena in locally structured and

doped semiconducting samples like the SRAM cell comprehensive calculations including the sample-specific structure and the local doping-dependent properties of charge carriers as well as an detailed analysis of charge carrier transport between the differently doped regions are recommended. Nevertheless, the presented rough estimation provides a first overview over the order of magnitude of drift and diffusion and allows with respect to the sample structure simple conclusions about the influence on the KPFM measurement.

The frequency independence of the lateral KPFM bias probed on the SRAM cell is evidence for an import aspect of the new KPFM model. As discussed in 5.2.4 the new KPFM model predicts that the probed KPFM bias is independent of the explicit oscillation amplitude of the cantilever, i.e. of the amplitude of the electrical signal of the 1st harmonic. In Tab. 5.4 (Sect. 5.2.7.2), it can be seen that the amplitude of the 1st harmonic decreases with decreasing operation frequency. However, the lateral KPFM bias variation probed across the p^+np^+ junction is constant for all applied operation frequencies. This is due to the fact that the KPFM bias only reflects the voltage necessary for the injection of majority charge carriers into the semiconductor surface region and is independent of the amplitude of the 1st harmonic signal used as input for the Kelvin probe force feedback.

6.1.1.3 AC-bias dependent KPFM measurements

For verification of the negligible influence of bias-induced band bending which was discussed in Sect. 5.2.5, ac-bias dependent KPFM measurements have been performed on the SRAM cell. The measurements have been carried out with an n^+ -type cantilever. An operation frequency of 130 kHz has been applied during the ac-bias dependent KPFM measurements.

The p^+np^+ junction which was used to demonstrate quantitative dopant profiling (Sect. 6.1.1.1) was investigated in dependence on the ac-bias. The KPFM bias section lines recorded at ac-biases with the effective values of 6 V, 5 V, 4 V, and 3 V are presented in Fig. 6.7. As can be seen, the same lateral KPFM bias variation is probed for all applied ac-biases. Note that a non-negligible bias-induced band bending should show in an opposite change of the KPFM bias values probed above n -type and p -type semiconducting regions for positive or negative biases [145]. Due to the ac-bias an alternating positive and negative voltage is applied to the p^+ -type and the n -type regions. When decreasing the effective ac-bias values also the peak value of the ac-bias decreases. It would be expected that with decreasing positive and negative ac-bias peak value the KPFM bias probed above the p^+ -type regions changes oppositely to the value probed above the n -type regions. Thus, the lateral KPFM bias variation should change with decreasing ac-bias. Such effect is not observed during the ac-bias dependent KPFM measurements. This result shows that ac-bias-induced band bending may occur but has no influence on the KPFM measurements.

Another important aspect regarding ac-bias dependent KPFM measurements is that at decreasing ac-bias the maximum value of the ac-drift velocity decreases. This leads to

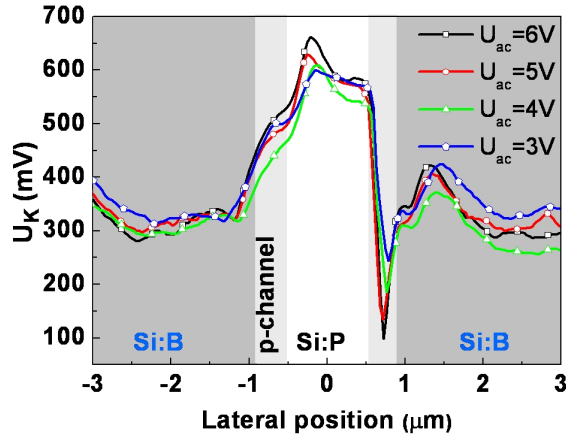


Figure 6.7: Results of the ac-bias dependent KPFM measurement on the SRAM cell performed with an n^+ -type cantilever. Section lines (averaged over 20 lines) of the KPFM bias probed across the p^+np^+ junction of the SRAM cell in dependence on the effective ac-bias U_{ac} . The section lines have been shifted on the U_K -scale to reach overlay of the spectra.

an enhancement of the time period in which the diffusion velocity v_{diff} is larger than the ac-drift velocity $v_{ac-drift}$. Similar to the discussion of the frequency dependent KPFM measurements performed on the SRAM cell (Sect. 6.1.1.2), the ac-drift velocity has been calculated in dependence on the applied ac-bias for the operation frequency f_{ac} of 130 kHz by means of Eq. (38) for electrons. The calculated ac-drift velocity $v_{ac-drift}$ is related to an electron mobility of about $1530 \text{ cm}^2/\text{Vs}$. The ac-bias dependent ac-drift velocities $v_{ac-drift}$ are plotted in Fig. 6.8, where also the typical diffusion velocity in the order of $v_{diff} = 1 \times 10^3 \text{ cm/s}$ in Si (Sect. 6.1.1.2) is indicated as red line. The time periods in which the condition $v_{ac-drift} < v_{diff}$ is fulfilled are estimated from Fig. 6.8(b). The values are listed in Tab. 6.3, where additionally the correlated diffusion range is given.

Table 6.3: Diffusion in the SRAM cell. Time period in which the condition $v_{ac-drift} < v_{diff}$ is fulfilled in dependence on the applied ac-bias. Additionally, the diffusion range of charge carriers in the respective time period is given.

Effective ac-bias U_{ac} (V)	AC-bias peak (V)	Time period of $v_{ac-drift} < v_{diff}$ (s)	Diffusion range (nm)
6	± 8.5	0.9×10^{-8}	90
5	± 7.1	1.1×10^{-8}	110
4	± 5.7	1.4×10^{-8}	140
3	± 4.2	1.8×10^{-8}	180

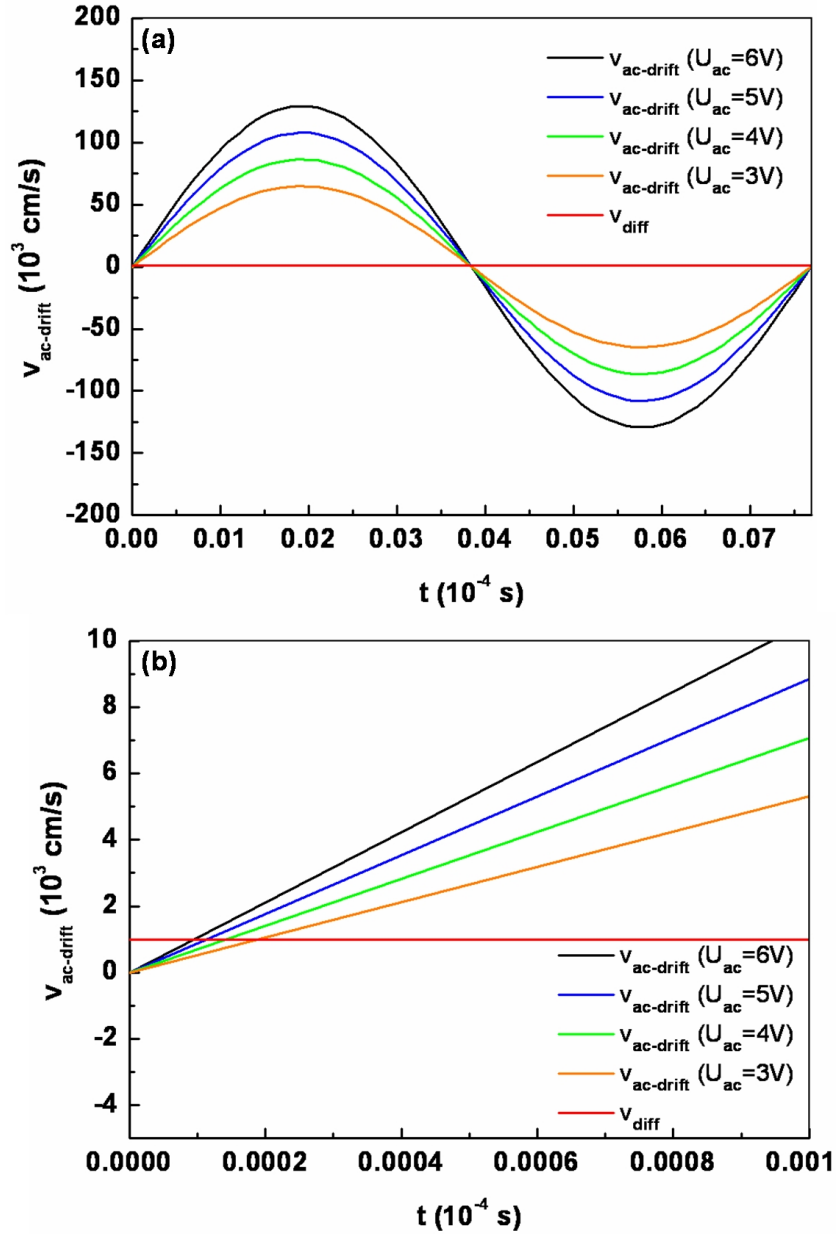


Figure 6.8: AC-drift velocity in the SRAM cell calculated for electrons by means of Eq. (38) for the effective ac-bias values 6V, 5V, 4V and 3V at the operation frequency f_{ac} of 130 kHz. Plot over (a) 7.7×10^{-6} s corresponding to a period T_{ac} of the 130 kHz-oscillation and (b) 1×10^{-7} s for estimation of the time period in which $v_{ac-drift} < v_{diff}$ is fulfilled. The constant diffusion velocity v_{diff} of 1×10^3 cm/s is indicated as a red line.

It is found that for all applied ac-biases the diffusion range is smaller than 200 nm. Therefore, the probed lateral KPFM bias may be distorted by diffusion of charge carriers between the neighbouring surface space charge regions of the p^+ -type regions and the adjacent narrow "p-channel" regions (Fig. 6.5) only on a small lateral scale. The expected distortion is

not detectable due to the large scan range and due to the distorting topographic step near this measurement position. It can be concluded that the contribution of diffusion between the neighbouring surface space charge regions is negligible for all applied ac-biases.

The vertical asymmetric electric dipole at the surface of the p^+ -type and the n-well region is removed mainly by majority charge carriers injected via the applied KPFM bias which thus remains quantitatively correlated with the local dopant concentration via Eqs. (6) and (7) even at small ac-biases.

6.1.1.4 Comparison between UHV and ambient KPFM

In comparison to the results obtained by means of ambient KPFM, the SRAM cell has also been investigated with UHV KPFM at the Helmholtz-Zentrum Berlin. The conventional SRAM cell has been chosen for the comparative measurements because the lateral KPFM bias variation probed during the ambient KPFM measurements does not depend on the operation frequency (Sect. 6.1.1.2) or on the applied ac-bias (Sect. 6.1.1.3) which are different for the UHV and the ambient KPFM system (Sect. 3.2).

The ambient and UHV KPFM measurements have been performed across the $n^+pn^+pn^+$ junction, which was used to demonstrate quantitative dopant profiling in Sect. 6.1.1.1 (Fig. 6.1). For direct comparison, the results of the ambient KPFM measurement from Fig. 6.1 are illustrated again together with the UHV KPFM results in Fig. 6.9. The schematic doping pattern of the SRAM cell is illustrated in Fig. 6.9(a), where also the investigated section line across the $n^+pn^+pn^+$ junction is marked as a blue line.

The results of the ambient KPFM measurements are illustrated in the left part of Fig. 6.9. The simultaneously recorded surface topography and KPFM bias are given in Fig. 6.9(b) and (c), respectively. The investigated section line across the $n^+pn^+pn^+$ junction is marked as a blue line in the KPFM bias image. The KPFM bias section line probed across the $n^+pn^+pn^+$ junction is plotted and compared to the calculated energy differences $[E_C - E_F(n)]$ and $[E_V - E_F(p)]$ in Fig. 6.9(d). A lateral KPFM bias variation of approximately 120 mV is probed between the n^+ -type and the "n-channel" regions at the ambient KPFM measurements which is in good agreement with the calculated energy difference of 130 meV [Fig. 6.9(d)]. As discussed in Sect. 6.1.1.1, the CPD model predicts an energy difference of 990 meV between the n^+ -type and the "n-channel" regions.

The results of the UHV KPFM measurements are shown in the right part of Fig. 6.9. Also in the UHV KPFM setup the surface topography [Fig. 6.9(e)] and the KPFM bias [Fig. 6.9(f)] are probed simultaneously. The investigated section line across the $n^+pn^+pn^+$ junction is marked as a blue line in the KPFM bias image [Fig. 6.9(f)]. The KPFM bias probed along the section line is compared to the calculated energy differences $[E_C - E_F(n)]$ and $[E_V - E_F(p)]$ in Fig. 6.9(g). Note that zero on the U_K -scale of the UHV measurements is defined by a calibration procedure performed before the UHV KPFM measurements which includes the applied cantilever. A lateral KPFM bias variation of about 160 mV is probed between the n^+ -type and the "n-channel" regions in the UHV KPFM measurement. This is in reasonable agreement with the calculated energy difference of 130 meV.

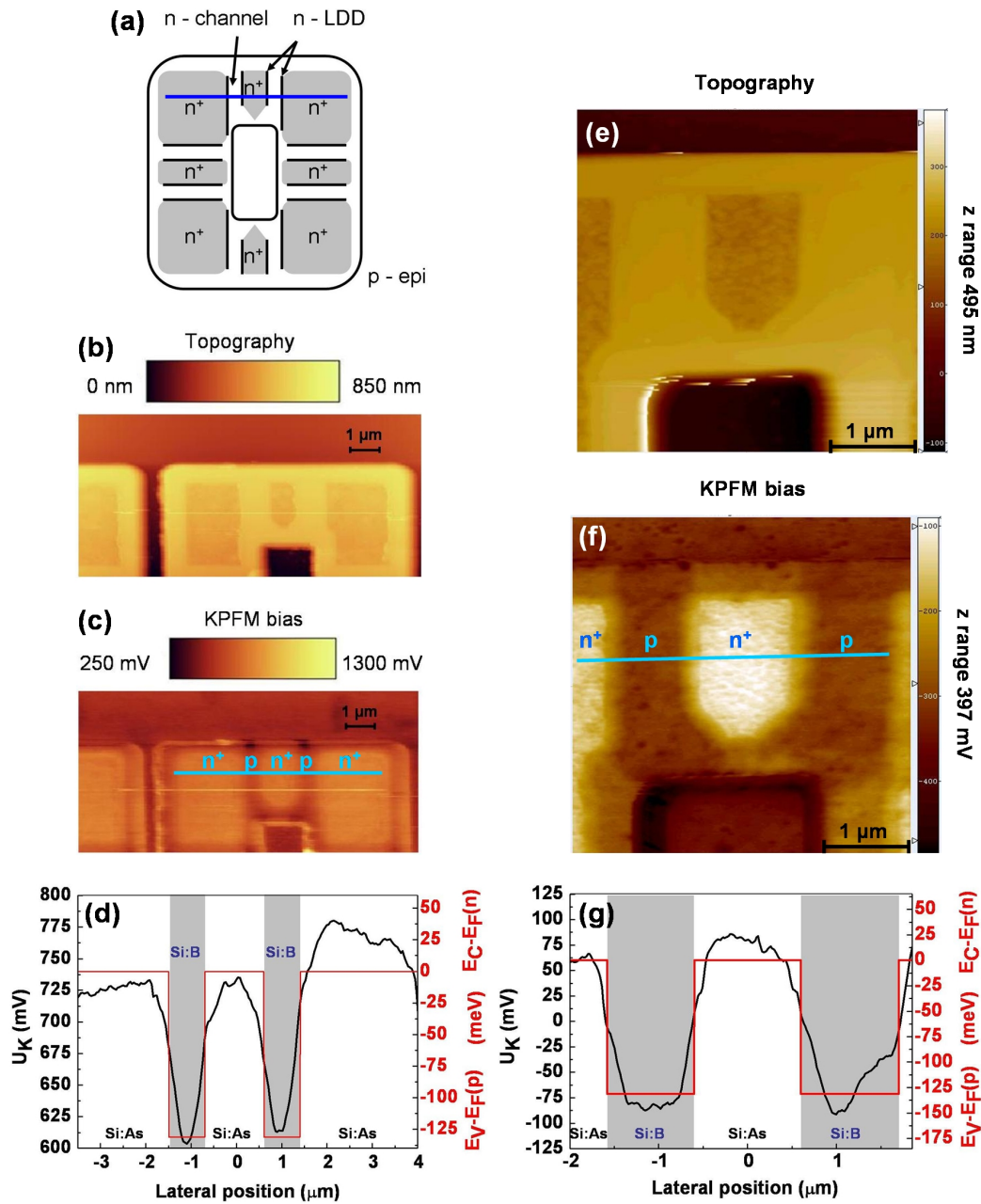


Figure 6.9: Comparison between ambient and UHV KPFM measurements performed across the $n^+pn^+pn^+$ junction in the SRAM cell. (a) Schematic doping pattern with marked section line, (b) ambient surface topography, (c) ambient KPFM bias with marked section line, (d) ambient KPFM bias section line (averaged over 10 scan lines) compared to the calculated energy differences $[E_C - E_F(n)]$ and $[E_V - E_F(p)]$, (e) UHV surface topography, (f) UHV KPFM bias with marked section line, (g) UHV KPFM bias section line (averaged over 10 scan lines) compared to the calculated energy differences $[E_C - E_F(n)]$ and $[E_V - E_F(p)]$.

Some important conclusions can be drawn from the presented comparison between ambient and UHV KPFM measurements.

First of all, almost the same lateral KPFM bias variation is probed across the investigated $n^+pn^+pn^+$ junction at the ambient and the UHV KPFM measurements. Note that the lateral KPFM bias variation is independent of the applied cantilever, i.e. n^+ -type conductive NSC15 Si cantilevers from MikroMasch for ambient and Pt-Ir coated cantilevers from Nanosensors for UHV KPFM measurements (Sect. 3.2). The lateral KPFM bias variation probed during the ambient and the UHV KPFM measurements can be explained satisfyingly with the energy differences between Fermi energy and respective band edge [$E_C - E_F(n)$] and [$E_V - E_F(p)$], i.e. with the new KPFM model. The small deviation of the lateral KPFM bias variation between ambient and UHV KPFM may on the one hand result from minor differences between the real dopant concentration and the values provided from Veeco Instruments (Sect. 3.1.1). The ambient and UHV KPFM measurements have been performed on the same SRAM sample and on a similar $n^+pn^+pn^+$ junction, but not on the very same local position in the array of repeating doping pattern. For example, a B-concentration of $8 \times 10^{16} \text{ cm}^{-3}$ instead of the defined $2 \times 10^{17} \text{ cm}^{-3}$ in the "n-channel" region would result in a calculated energy difference of 160 meV instead of 130 meV. On the other hand, the small deviation between ambient and UHV measurements may result from the averaging due to the larger tip-sample distance in ambient KPFM (Sect. 5.2.6). Another important aspect is the much higher lateral resolution of UHV KPFM. The narrow n-LDD regions [Fig. 6.9(a)] containing P with a concentration of $5 \times 10^{18} \text{ cm}^{-3}$, which are expected at the lateral positions of approximately $-1.5 \mu\text{m}$, $-0.6 \mu\text{m}$, $0.6 \mu\text{m}$, and $1.5 \mu\text{m}$ in Fig. 6.9(d), are not resolved in ambient KPFM. However, those narrow n-LDD regions can be weakly resolved as approximately 200 nm broad, differently coloured surrounding of the central n^+ -region in the UHV KPFM bias image [Fig. 6.9(f)]. The UHV KPFM bias section line probed across the $n^+pn^+pn^+$ shows a continuous characteristic in which the n-LDD regions appear as weakly pronounced saddle points at the lateral positions of approximately $-1.6 \mu\text{m}$, $-0.6 \mu\text{m}$, $0.6 \mu\text{m}$ and $1.6 \mu\text{m}$ [Fig. 6.9(g)]. Therefore, it can be concluded that UHV KPFM provides a much better lateral resolution than ambient KPFM and is recommended for electrical investigations of nanostructures.

The third fundamental conclusion concerns the negligible influence of ac-bias-induced band bending (Sect. 5.2.5). The ambient KPFM measurements have been performed with an effective ac-bias of 6 V. In UHV KPFM only 0.1 V ac-bias are applied. However, independent of the different ac-bias almost the same lateral KPFM bias variation is probed in ambient and UHV KPFM. Thus, ac-bias-induced band bending may occur during the KPFM measurement but has no influence on the probed lateral KPFM bias variation.

The final important remark concerns the KPFM offset bias due to potential shielding (Sect. 5.2.4). The ambient KPFM measurements have been performed on the untreated sample surface featuring a native oxide as well as adsorbed water (Sect. 4). For reducing surface contaminations and the thin water film, the SRAM sample has been cleaned with acetone and heated for one hour at 155°C before the UHV KPFM measurements (Sect. 3.2.2). Only the contribution of the native oxide layer on the SRAM cell is expected to be similar during the ambient and UHV KPFM measurements. Therefore, the KPFM

offset bias differs during the ambient and UHV KPFM measurements. However, independent of the surface treatment almost the same lateral KPFM bias variation is probed in ambient and UHV KPFM measurements. It can be concluded that independent of the surface condition in ambient and UHV KPFM the probed lateral KPFM bias variation may be used for quantitative dopant profiling. This holds true as long as the signal from the asymmetric electric dipole is not completely dominated by potential shielding (Sect. 5.2.4).

Although a comparison between ambient and UHV KPFM measurements has been performed only for one of the semiconducting samples discussed in this work, i.e. the conventional SRAM cell, the observed agreement of the lateral KPFM bias variation for both measurement types is promising. Further comparative measurements are recommended. Nevertheless, these first results show that ambient KPFM as well as UHV KPFM are suitable for the quantitative investigation of the dopant concentration in semiconductors.

6.1.2 Dynamic random access memory cell

6.1.2.1 Quantitative dopant profiling

For verification of the results of the KPFM measurements performed on the conventional SRAM cell discussed in the preceding Sect. 6.1.1, additionally a conventional DRAM cell (Sect. 3.1.1) has been investigated. The KPFM measurements have been carried out with an n^+ -type cantilever at an ac-bias of 6 V and an operation frequency of 130 kHz.

In Fig. 6.10 the results of the KPFM measurement on the DRAM cell are presented. The doping pattern of the DRAM cell is illustrated schematically in Fig. 6.10(a). In Fig. 6.10(b) and (c) the simultaneously probed surface topography and KPFM bias are presented, respectively. Two different doping junctions in the DRAM cell have been investigated. The section lines are marked in the doping pattern in Fig. 6.10(a) as well as in the KPFM bias image in Fig. 6.10(c). One section line has been chosen across the pn junction in y -direction (blue line). The KPFM bias probed along this section line is plotted in Fig. 6.10(d). A lateral KPFM bias variation of approximately 300 mV is probed across the pn junction. The second investigated section line is across the n^+pn^+ in x -direction (green line). In Fig. 6.10(e) the corresponding KPFM bias section line is plotted. As can be seen, a lateral KPFM bias variation of approximately 200 mV is observed for the n^+pn^+ junction. Both section lines cross in the p -epi region which is indicated by means of the blue point in Fig. 6.10.

The p -epi region contains B with a concentration of $2 \times 10^{16} \text{ cm}^{-3}$. The corresponding energy difference between Fermi energy and valence band maximum amounts to $[E_V - E_F(p)] \cong -190 \text{ meV}$. The n -well region is P -doped with a concentration of $2 \times 10^{17} \text{ cm}^{-3}$ related to the energy difference $[E_C - E_F(n)] \cong +120 \text{ meV}$. The n^+ -type regions contain As with a concentration of $2 \times 10^{20} \text{ cm}^{-3}$ resulting in an energy difference of $[E_C - E_F(n)] \cong 0 \text{ meV}$. Adjacent to the n^+ -type regions narrow p -type conducting "n-channel" regions are implanted. These regions contain B with a concentration of $2 \times 10^{17} \text{ cm}^{-3}$. The resulting energy difference amounts to $[E_V - E_F(p)] \cong -130 \text{ meV}$. Similar to the p^+np^+ junction in

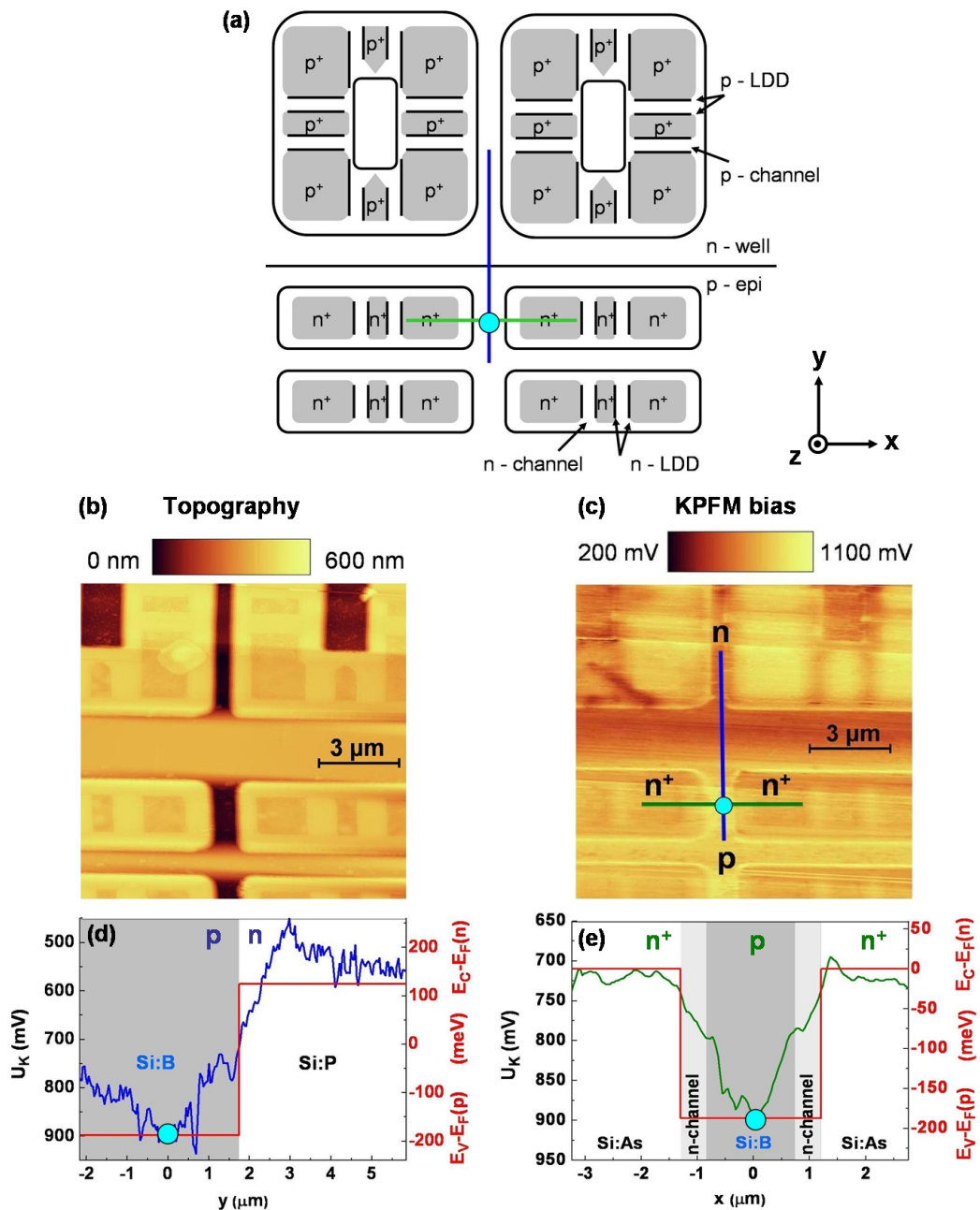


Figure 6.10: Results of the KPFM measurement on the DRAM cell. (a) Doping pattern of the DRAM cell with marked section lines across a *pn* junction in *y*-direction (blue) and an *n⁺pn⁺* junction in *x*-direction (green), (b) Surface topography, (c) KPFM bias with marked section lines. The KPFM bias section lines (averaged over 10 lines) probed (d) across the *pn* junction and (e) across the *n⁺pn⁺* junction are compared to the calculated energy differences $[E_C - E_F(n)]$ and $[E_V - E_F(p)]$. The crossing of both section lines in the p-epi region is indicated by the blue point. Adapted from Ref. [165].

the SRAM cell (Sect. 6.1.1.1), the narrow "n-channel" regions can not be discussed quantitatively due to distortion from the vertical topographic step between the p-epi region and the differently doped higher device components in the DRAM cell. However, in the KPFM bias section line probed across the n^+pn^+ junction a slight change of slope at the lateral positions $-1 \mu\text{m}$ and $1 \mu\text{m}$ occurs [Fig. 6.10(e)] which indicates the position of the "n-channel" regions.

From the new model calculation it can be concluded that for the pn junction in y-direction a calculated energy difference of 310 meV is predicted which is in good agreement with the probed lateral KPFM bias variation of approximately 300 mV. Note that the expected CPD difference for the pn junction amounts to 810 meV. The comparison between measurement and new KPFM model calculation for the pn junction is given in the plot in Fig. 6.10(d). For the n^+pn^+ junction in x-direction the calculated energy difference amounts to 190 meV. This is in good agreement to the probed lateral KPFM bias variation of approximately 200 mV. In the CPD model an energy difference of 930 meV is expected for the n^+pn^+ junction. Measurement and new model calculation for the n^+pn^+ junction are compared in Fig. 6.10(e).

It can be concluded that the lateral KPFM bias variation probed across the two doping junctions can be satisfyingly explained within the new KPFM model.

The presented results of the KPFM measurement across the two doping junctions in the DRAM cell reveal another important aspect regarding the different predictions from the traditional CPD model and the new KPFM model. In the CPD model a larger KPFM bias variation is expected to be probed across the n^+pn^+ junction than across the pn junction, i.e. $930 \text{ meV} > 810 \text{ meV}$. Additionally, the calculated lateral CPD variation $\Delta\text{CPD}(p,n)$ reflects the built-in potential of the doping junctions (Sect. 5.1) and is thus larger than half the bandgap energy in Si, i.e. larger than 560 meV.

Both predictions of the traditional CPD model are not in agreement with the results of the KPFM measurement. The lateral KPFM bias variation probed across the n^+pn^+ junction is smaller than the variation probed across the pn junction, i.e. $200 \text{ mV} < 300 \text{ mV}$. Besides, the probed lateral KPFM bias variation of both doping junctions is smaller than half the bandgap energy, i.e. smaller than 560 meV. Both observations can only be explained within the new KPFM model presented in this work (Sect. 5.2).

6.1.2.2 Frequency dependent KPFM measurements

Frequency dependent KPFM measurements have been performed on the n^+pn^+ junction in the DRAM cell which was used to demonstrate quantitative dopant profiling in the preceding Sect. 6.1.2.1. The frequency dependent KPFM measurements have been carried out by means of an n^+ -type cantilever at an ac-bias of 6 V.

The n^+pn^+ junction has been probed at the two operation frequencies 130 kHz and 30 kHz. The corresponding KPFM bias section lines are displayed in Fig. 6.11. In agreement

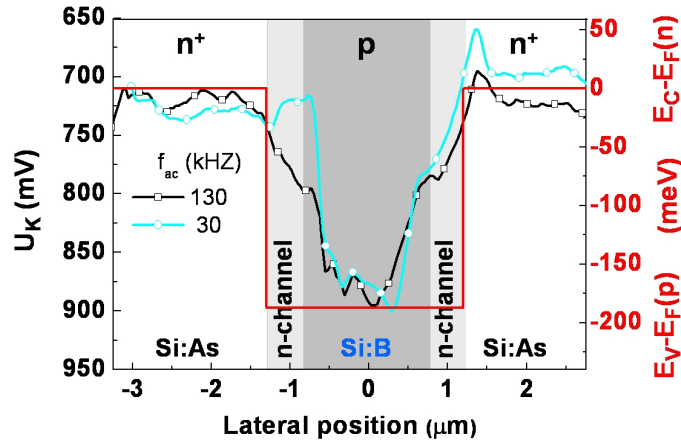


Figure 6.11: Results of the frequency dependent KPFM measurement across the n^+pn^+ junction in the DRAM cell performed with an n^+ -type cantilever. Section lines (averaged over 10 scan lines) of scans with 130 kHz and 30 kHz. The section lines are shifted on the U_K -scale to reach overlay of the spectra and are compared to the calculated energy differences $[E_C - E_F(n)]$ and $[E_V - E_F(p)]$.

with the results observed on the SRAM cell, the lateral KPFM bias variation probed between the n^+ -type regions and the central p -epi region in the DRAM cell is independent of the applied operation frequency. For both operation frequencies a lateral KPFM bias variation of approximately 200 mV is probed which is in good agreement with the new model calculation of 190 meV (Sect. 6.1.2.1).

The observed frequency independence indicates that the contribution of diffusing charge carriers between neighbouring surface space charge regions is negligible. Similar to the SRAM cell (Sect. 6.1.1.2) in the following discussion the focus lies on diffusion between the neighbouring surface space charge regions of the shallow n^+ -type and the adjacent "n-channel" regions is discussed. The asymmetric electric dipole at the investigated measurement positions is removed mainly by majority charge carriers injected via the applied KPFM bias which thus remains quantitatively correlated with the local dopant concentration. For verification of this conclusion, the time period in which diffusion between neighbouring surface space charge regions dominates the ac-drift is estimated in the following for the 1 mm thick DRAM cell.

The surface region of the DRAM cell is illustrated schematically in Fig. 6.12. Similar to the SRAM cell primarily vertical pn junctions occur between the n^+ -type regions and the p -type regions. The thickness of the n^+ -type regions has been estimated by means of SRIM calculations (Sect. 3.3.2) using the implantation details provided by Veeco Instruments (Sect. 3.1.1). A Gauss distribution of As atoms with a mean implantation depth of approximately 70 nm ($\text{FWHM} \cong 50$ nm) is calculated. Note that the SRIM calculations do not include an annealing treatment which may be part of the fabrication process of the DRAM cell and which may lead to a more box-like dopant distribution with increased depth as observed after implantation and annealing of the NW samples (Sect. 3.1.3).

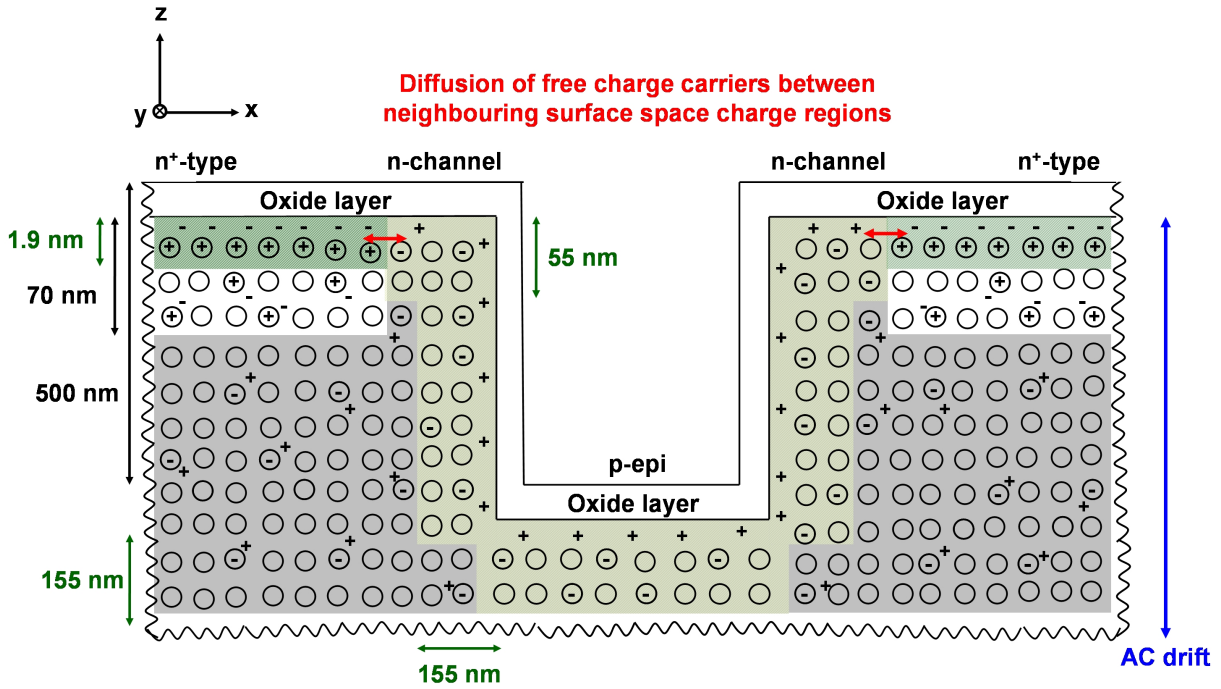


Figure 6.12: Schematic cross-sectional illustration of the surface region of the DRAM cell with shallow n^+ -type regions, p -type conducting "n-channel" regions, and the p -epi region. The maximum thickness of the surface space charge region (green) amounts to 1.9 nm in the n^+ -type regions, to 155 nm in the p -epi and to 55 nm in the "n-channel" regions. The diffusion between neighbouring surface space charge regions along x (red) and the ac-drift along z (blue) are indicated.

The maximum thickness of the surface space charge regions has been estimated by means of Eq. (5) and amounts to 1.9 nm in the n^+ -type regions, to 155 nm in the p -epi and to 55 nm in the "n-channel" regions. As discussed for the SRAM cell, the horizontal asymmetric electric dipoles which are expected to form at the vertical topographic steps of the DRAM cell (Fig. 6.12) can not be distinguished laterally and electrically from the distortion due to the surface step near this measurement position.

For an estimation of the time period in which diffusion dominates the ac-drift, the ac-drift velocity of electrons has been calculated for 130 kHz and 30 kHz at an effective ac-bias of 6 V by means Eq. (38). Similar to the discussion of the frequency dependent KPFM measurements performed on the SRAM cell (Sect. 6.1.1.2) the calculated ac-drift velocity in the DRAM cell is compared to the typical diffusion velocity v_{diff} in Si which is in the order of 1×10^3 cm/s. The time periods in which the condition $v_{ac-drift} < v_{diff}$ is fulfilled are estimated from the calculated data. In Tab. 6.4 the time periods and the respective diffusion ranges are listed.

It can be concluded from this rough estimation that for 130 kHz and 30 kHz the diffusion range amounts to 90 nm and 400 nm, respectively. Thus, compared to the large scan range a possible distortion of the probed KPFM bias due to the contribution of diffusing charge

Table 6.4: Diffusion in the DRAM cell. Time period in which the condition $v_{ac-drift} < v_{diff}$ is fulfilled for the operation frequencies 130 kHz and 30 kHz. Additionally, the diffusion range of charge carriers in the respective time period is given.

Operation frequency f_{ac} (kHz)	Time period of $v_{ac-drift} < v_{diff}$ (s)	Diffusion range (nm)
130	0.9×10^{-8}	90
30	4×10^{-8}	400

carriers between the shallow n^+ -type and the adjacent "n-channel" regions to the removal of the asymmetric electric dipole only occurs in a small region and can not be distinguished satisfyingly from the distortion due to the topographic step near this measurement position. Additionally, the interface of the neighbouring surface space charge regions of the shallow n^+ -type and the adjacent "n-channel" regions is even smaller in the DRAM cell than in the SRAM cell and amounts to only 1.9 nm. Therefore, a much smaller amount of charge carriers is expected to diffuse between both neighbouring surface space charge regions. It can be concluded that the asymmetric electric dipole in the surface region of the discussed n^+ -type regions and the central p-epi region is removed at all operation frequencies mainly by majority charge carriers injected via the applied KPFM bias. The probed lateral KPFM bias variation is thus independent of the operation frequency and remains quantitatively correlated with the local dopant concentration via Eqs. (6) and (7).

6.2 Cross-sectionally prepared silicon epilayer samples

In this section the results of KPFM measurements on the cross-sectionally prepared Si epilayer samples introduced in Sect. 3.1.2 are presented. Quantitative dopant profiling by means of the new KPFM model is demonstrated on the Si:B and on the Si:P epilayer sample. The influence of local intrinsic electric fields is discussed by use of frequency dependent KPFM measurements. Additionally, ac-bias dependent KPFM measurements have been performed on the epilayer samples and are discussed in this section.

6.2.1 Si:B epilayer sample

6.2.1.1 Quantitative dopant profiling

For verification of the new KPFM model, the doping profile in the Si:B epilayer sample has been determined by means of SIMS measurements (Sect. 3.3.1). As explained in Sect. 3.1.2, in order to avoid the influence of local intrinsic electric fields due to overlapping space charge regions in the narrow spacer regions, the focus lies on the pn junction between the P-doped substrate and the near-substrate B-doped epilayer.

In Fig. 6.13 the SIMS data recorded across the pn junction between the P-doped substrate and the near-substrate B-doped epilayer are presented. As can be seen, the abrupt doping junction expected at the lateral position of $0 \mu\text{m}$ is distorted by an exponential decline of the B-concentration in the P-doped substrate. This observation is ascribed to SIMS artefacts which are induced for example by ion beam mixing [166] and an additional forward recoil process, i.e. the "knock-on" effect [167] during the sputtering. The knock-on effect is known to produce a measured doping profile which extends much deeper into the substrate than is actually there [168], and increases with increasing depth of the investigated structure from the sample surface [169]. The examined pn junction between P-doped substrate and near-substrate B-doped epilayer is located in a depth of $11 \mu\text{m}$ from the epilayer sample surface resulting in a large influence of sputtering artefacts and thus in a decreased quality of the SIMS data. As a consequence in the P-doped substrate an artificial B-concentration appears in the SIMS data which is even larger than the P-concentration. Nevertheless, a P-concentration of approximately $1.4 \times 10^{15} \text{ cm}^{-3}$ can be deduced for the substrate, while a B-concentration of about $4.7 \times 10^{16} \text{ cm}^{-3}$ in the near-substrate epilayer can be extracted from the SIMS data.

The Si:B epilayer sample has been prepared cross-sectionally after the SIMS measurements (Sect. 3.1.2). This enables KPFM measurements across the thus horizontally arranged differently doped layers of the Si:B epilayer structure. In agreement with the SIMS measurement, the KPFM measurements focus on the horizontal pn junction between the P-doped substrate and the near-substrate B-doped epilayer.

The KPFM measurements have been carried out with an n^+ -type cantilever at an applied ac-bias of 6 V and an operation frequency of 130 kHz. The results of the KPFM measurement are presented in Fig. 6.14. The simultaneously probed surface topography and KPFM bias are given in Fig. 6.14(a) and (b), respectively. In Fig. 6.14(c) a KPFM bias

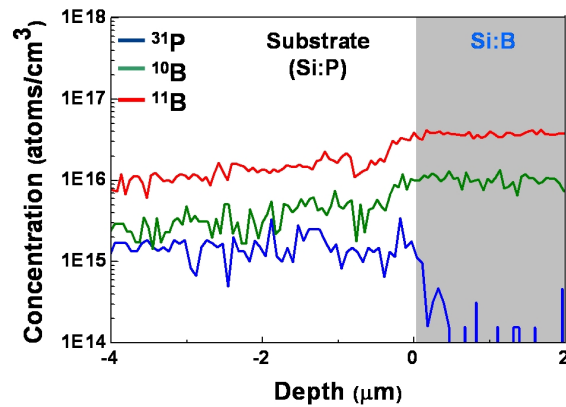


Figure 6.13: Secondary ion mass spectrometry data recorded across the pn junction between the P-doped substrate and the near-substrate B-doped epilayer in the Si:B epilayer sample.

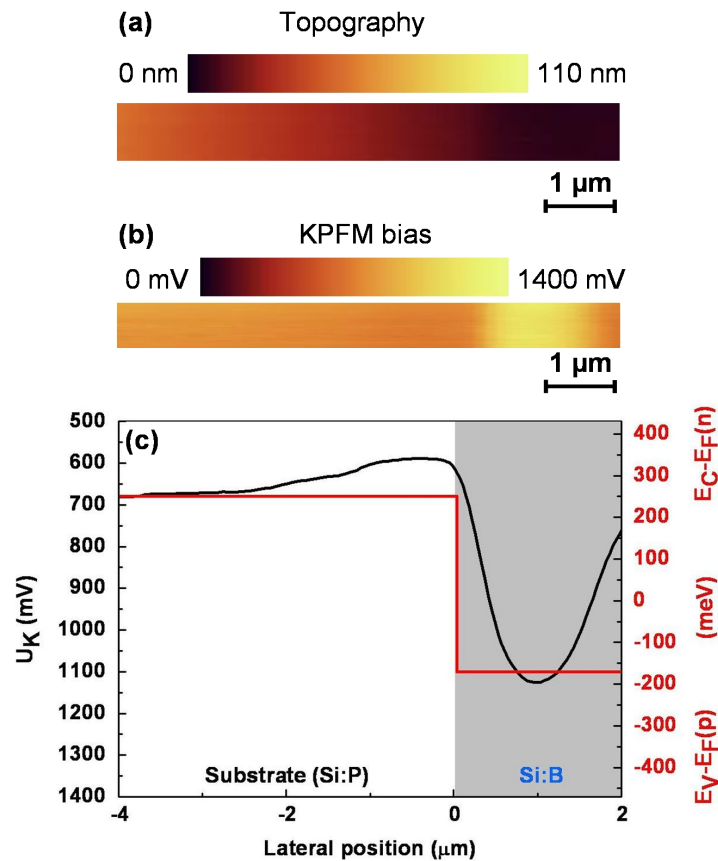


Figure 6.14: Results of the KPFM measurement across the pn junction between the P-doped substrate and the near-substrate B-doped epilayer in the Si:B epilayer sample. (a) Surface topography, (b) KPFM bias, (c) KPFM bias section line (averaged over 20 lines) compared to the calculated energy differences $[E_C - E_F(n)]$ and $[E_V - E_F(p)]$. Adapted from Ref. [158].

section line averaged over 20 scan lines probed across the P-doped substrate and the near-substrate B-doped epilayer is plotted. As can be seen, the KPFM bias probed between the lateral positions of about $-2 \mu\text{m}$ to $0 \mu\text{m}$ is distorted. This is ascribed to the space charge region of the horizontal pn junction. The width of the space charge region amounts to approximately 800 nm in the P-doped substrate and to about only 20 nm in the B-doped epilayer. As explained in Sect. 5.2.7.1, injected majority charge carriers drift within the electric field of the space charge region which partially prevents the screening of unscreened ionized dopant atoms in the vertical asymmetric electric dipole at the measurement position. This leads to a distortion, i.e. to an overshoot of the KPFM bias probed across horizontal pn junctions. Due to the much larger width of the space charge region on the side of the P-doped substrate, there the largest distortion of the KPFM bias is observed. However, the KPFM bias values probed in large enough distance from the space charge region of the horizontal pn junction can be used for a quantitative analysis. It can be concluded that a lateral KPFM bias variation of approximately 430 mV is probed between the lateral positions of $-3 \mu\text{m}$ above the P-doped substrate and of $1 \mu\text{m}$ above the B-doped epilayer. The probed lateral KPFM bias variation is compared to the new model calculation in Fig. 6.14(c). The energy difference between Fermi energy and respective band edge amounts to $[E_C - E_F(n)] \cong +250 \text{ meV}$ in the P-doped substrate and to $[E_V - E_F(p)] \cong -170 \text{ meV}$ in the B-doped epilayer. Thus, the new KPFM model predicts an energy difference of 420 meV. This is in good agreement with the probed lateral KPFM bias variation of 430 mV. Note that the CPD model predicts an energy difference of 700 meV.

6.2.1.2 Independence of the cantilever potential

As discussed in Sect. 5.2.2, a major aspect of the new KPFM model is the independence of the cantilever potential. For verification of this aspect, KPFM measurements with different cantilever types have been performed on the cross-sectionally prepared Si:B epilayer sample. In Fig. 6.15(a) the KPFM bias section lines probed with an n^+ -type cantilever and with a p^+ -type cantilever are presented. As can be seen, both section lines show the same lateral KPFM bias variation across the epilayer structure and are only shifted slightly on the U_K -scale. This is ascribed to a slightly different offset (Sect. 5.2.4).

The KPFM bias probed above the spacer layers is expected to be distorted by intrinsic electric fields due to space charge regions forming between the spacer layers and the neighbouring B-doped layers which was discussed in Sect. 3.1.2. These space charge regions have a width of about 800 nm from the respective pn interface in the $1 \mu\text{m}$ thick spacer layers and thus strongly overlap. Therefore, in the following discussion it is focused on the pn junction between P-doped substrate and near-substrate B-doped epilayer which was also used to demonstrate quantitative dopant profiling in the preceding Sect. 6.2.1.1. The results of the cantilever dependent KPFM measurements on this pn junction are shown in Fig. 6.15(b). The KPFM bias section lines in Fig. 6.15(b) are shifted with respect to $[E_C - E_F(n)] = [E_V - E_F(p)] = 0 \text{ meV}$ to reach overlay of both spectra for comparison to the energy differences predicted from the traditional CPD model and the new KPFM

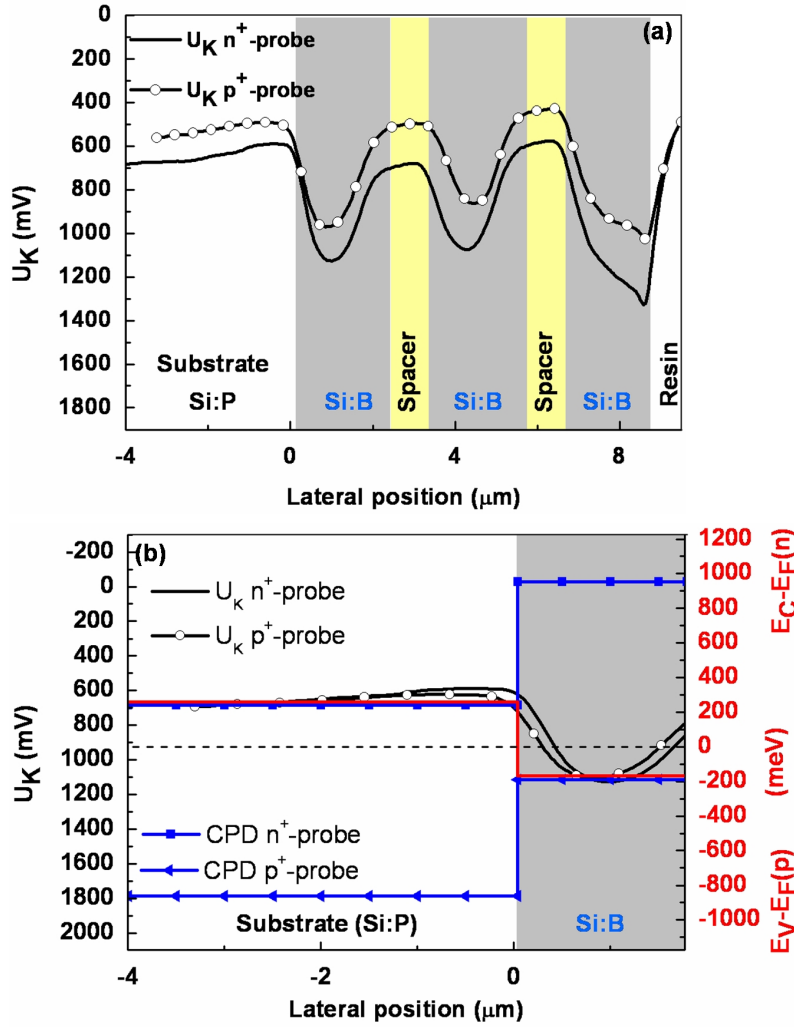


Figure 6.15: Results of the KPFM measurements on the cross-sectionally prepared Si:B epilayer sample performed with an n^+ -type and a p^+ -type cantilever. KPFM bias section lines (averaged over 20 scan lines) probed across (a) the whole Si:B epilayer structure and (b) with focus on the pn junction between P-doped substrate and the near-substrate B-doped epilayer. The KPFM bias section lines in (b) are shifted with respect to $[E_C - E_F(n)] = [E_V - E_F(p)] = 0$ meV to reach overlay of both spectra for comparison to the energy differences predicted from the traditional CPD model and the new KPFM model.

model. For both cantilever types a lateral KPFM bias variation of approximately 430 mV is probed which is in good agreement with the new model calculation of $[E_C - E_F(n)] \cong +250$ meV in the P-doped substrate and to $[E_V - E_F(p)] \cong -170$ meV in the B-doped epilayer.

For comparison, the traditional CPD model calculation is plotted for the n^+ -type and the p^+ -type cantilever with respect to the energy scale in Fig. 6.15(b). As was illustrated in Fig. 5.2 and explained in Sect. 5.1, positive CPD values are calculated for the n^+ -type

cantilever while the p^+ -type cantilever results in negative CPD values. In particular, the CPD values expected for the n^+ -type cantilever amount to $[\text{CPD}(n,n^+\text{-probe})]= +250$ meV in the P-doped substrate and to $[\text{CPD}(p,n^+\text{-probe})]= +950$ meV in the B-doped epilayer. The CPD values for the p^+ -type cantilever amount to $[\text{CPD}(n,p^+\text{-probe})]= -870$ meV in the P-doped substrate and to $[\text{CPD}(p,p^+\text{-probe})]= -170$ meV in the B-doped epilayer. The absolute value of the lateral variation of the contact potential difference $\Delta\text{CPD}(p,n)$ equals the built-in potential of the pn junction and amounts to 700 meV for both cantilever types. It can be concluded from the comparison given in Fig. 6.15(b) that neither the absolute energy difference of 700 meV predicted from the CPD model nor the dependence on the cantilever potential is in agreement with the probed KPFM bias. The lateral KPFM bias variation probed across the pn junction is independent of the applied cantilever type which can only be explained within the new KPFM model (Sect. 5.2.2).

6.2.1.3 Frequency dependent KPFM measurements

For investigation of the influence of intrinsic electric fields in the cross-sectionally prepared Si:B epilayer sample, KPFM measurements in dependence on the operation frequency f_{ac} have been performed. An ac-bias of 6 V has been applied during the frequency dependent KPFM measurements. In Fig. 6.16 the results of the frequency dependent KPFM measurements are presented. The Si:B epilayer sample has been scanned with an n^+ -type and a p^+ -type cantilever. Additionally, scans in 1D and 2D mode have been performed with each cantilever type. In 1D mode the cantilever is scanned repeatedly across the same line, while in 2D mode the cantilever is moved laterally for a line-wise scan of a certain measurement area.

As can be seen in Fig. 6.16 the probed lateral KPFM bias variation changes in dependence on the operation frequency. Note that this result is in strong contrast to the SRAM and DRAM cells where a frequency independent lateral KPFM bias variation was observed (Sects. 6.1.1.2 and 6.1.2.2). In the Si:B epilayer sample it is found that the lateral KPFM bias variation between the differently doped layers decreases with decreasing operation frequency. Finally, the same KPFM bias, i.e. the substrate value, is probed across the whole epilayer structure. This effect is strongest for the central B-doped epilayer at approximately $4 \mu\text{m}$ and weakest for the near-resin B-doped epilayer at approximately $8 \mu\text{m}$.

Note that the strong KPFM bias peak at approximately $8.5 \mu\text{m}$ remains detectable even at small operation frequencies. The strongly distorted KPFM bias at this measurement position is ascribed to the sample structure. As shown schematically in Fig. 6.17 a native oxide layer has to be considered at the original surface of the wafer. After cross-sectional preparation, the original wafer surface with the asymmetric electric dipole and the native oxide layer is arranged vertically. As explained in detail for the vertical topographic steps of the SRAM cell (Sect. 6.1.1.1), a thick vertical oxide may strongly distort the KPFM bias. The maximum thickness of the horizontal asymmetric electric dipole amounts to only about 70 nm in the near-resin B-doped epilayer and can not be distinguished from the distortion due to the vertical oxide layer.

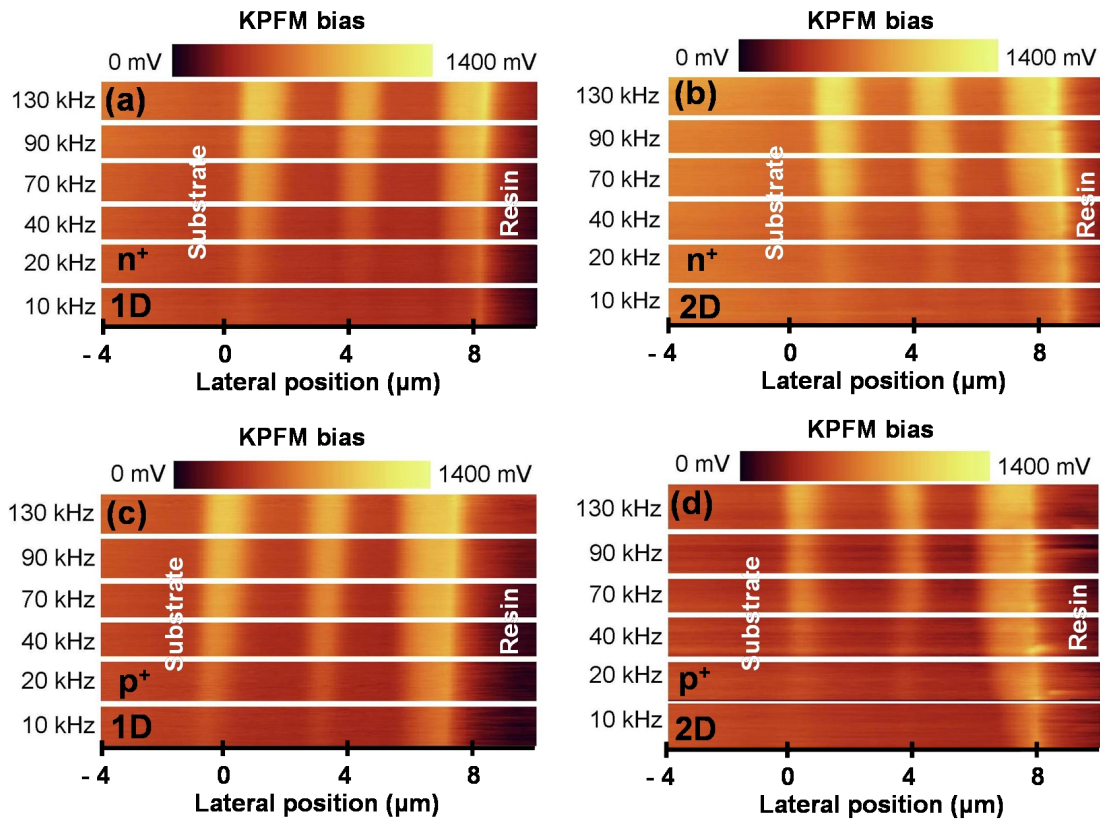


Figure 6.16: Results of the frequency dependent KPFM measurement on the cross-sectionally prepared Si:B epilayer sample performed with an n^+ -type and a p^+ -type cantilever. The KPFM bias of scans with 130 kHz, 90 kHz, 70 kHz, 40 kHz, 20 kHz and 10 kHz is shown for (a) an n^+ -type cantilever in 1D mode, (b) an n^+ -type cantilever in 2D mode, (c) a p^+ -type cantilever in 1D mode, and (d) a p^+ -type cantilever in 2D mode. Adapted from Ref. [160].

For the detailed discussion of the observed frequency dependence of the KPFM bias probed across the Si:B epilayer sample, section lines from the results presented in Fig. 6.16 are plotted in Fig. 6.18. The small difference between the KPFM bias section lines along the lateral position in Fig. 6.18 is ascribed to the different measurement position during the KPFM scans.

Three major conclusions can be deduced from the results illustrated in Fig. 6.18.

First of all, the lateral KPFM bias variation is saturated and maximal for large operation frequencies. This aspect can be seen in Fig. 6.18(a), where the KPFM bias section lines probed with a p^+ -type cantilever at 130 kHz and 90 kHz are illustrated. It is obvious that for 130 kHz and 90 kHz the lateral KPFM bias variation does not depend on the operation frequency and the probed lateral KPFM bias variation may be used for quantitative dopant profiling.

The second important aspect is the different frequency dependence for scans in 1D and 2D mode as illustrated in 6.18(b). As can be seen, the lateral KPFM bias variation

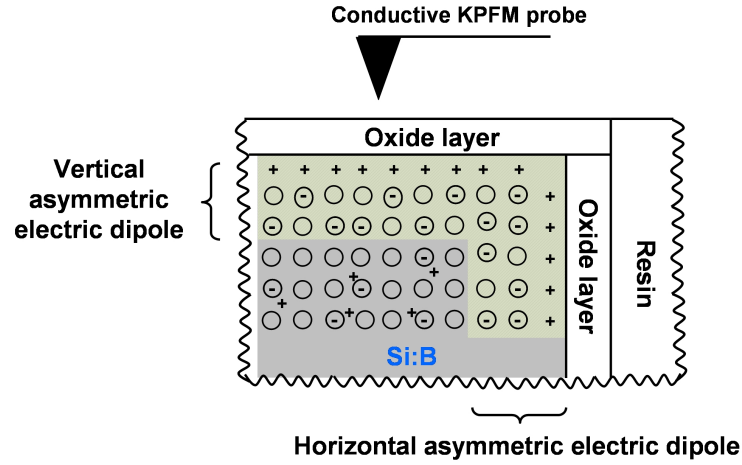


Figure 6.17: Schematic illustration of the interface between the wafer and the surrounding resin in the cross-sectionally prepared Si:B epilayer sample. Additional to the vertical asymmetric electric dipole formed at the cross-section surface, a horizontal asymmetric electric dipole is formed at the interface between wafer and resin, i.e. at the original wafer surface. Adapted from Ref. [160].

probed in 2D mode shows a much stronger frequency dependence. Already at 70 kHz a significant difference between the 1D and 2D scan lateral KPFM bias variation occurs. At the operation frequency of 10 kHz a small lateral KPFM bias variation is detected between the differently doped regions in the 1D scan. The 2D scan at 10 kHz reveals only the peak at approximately $8.5 \mu\text{m}$, i.e. at the interface between wafer and resin.

The final remark concerns the frequency dependence with respect to the applied cantilever. As can be seen in Fig. 6.18(c) the same decrease of the lateral KPFM bias variation is observed for the n^+ -type and the p^+ -type cantilever. It can be deduced that the frequency dependence of the lateral KPFM bias variation probed across the Si:B epilayer structure is independent of the applied cantilever type.

In general, it can be concluded from Fig. 6.18 that the observed frequency dependence of the lateral KPFM bias variation is independent of the cantilever material, reproducible and sample-specific.

For a final overview over the frequency dependence, the unshifted KPFM bias section lines of the 1D scan performed with the p^+ -type cantilever presented in Fig. 6.16(c) are shown in Fig. 6.19. In Fig. 6.19(a) the KPFM bias section lines probed across the whole Si:B epilayer are given. Note that the epilayer structure appears smaller in the KPFM bias scans than the expected value of $11 \mu\text{m}$ (Sect. 3.1.2). This is ascribed to a deviation of the scaling factor in the piezo calibration for large scan ranges. In Fig. 6.19(b) the focus lies on the pn junction between the P-doped substrate and the B-doped near-substrate epilayer which was used to demonstrate quantitative dopant profiling in Sect. 6.2.1.1.

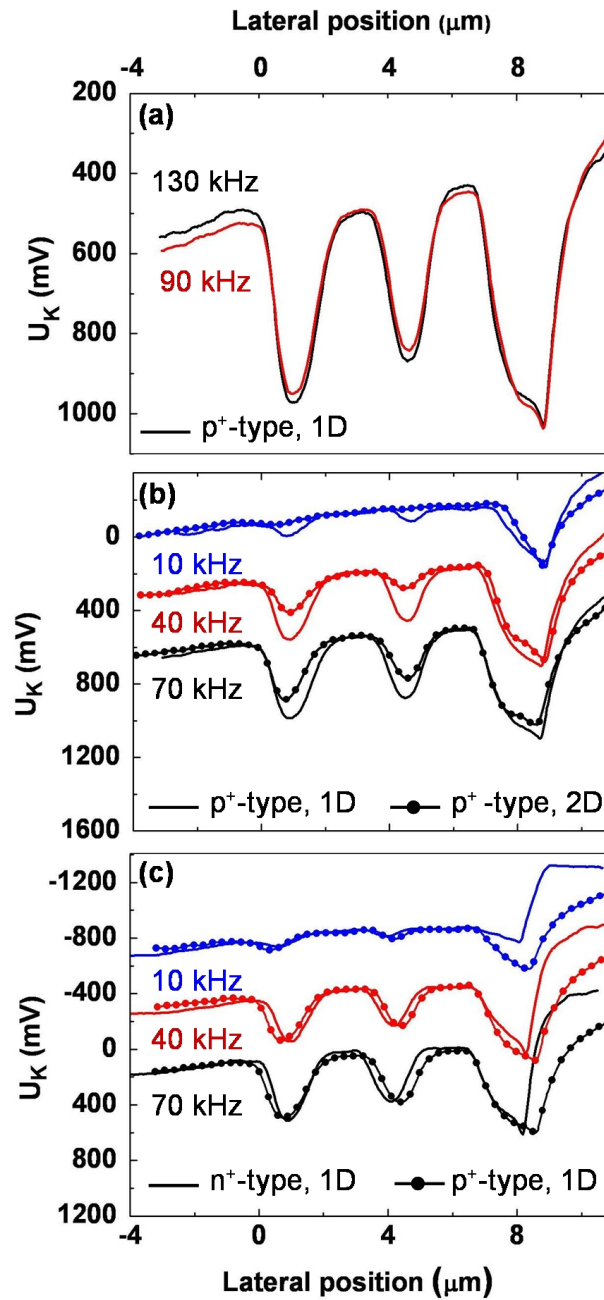


Figure 6.18: KPFM bias section lines of the frequency dependent KPFM measurements across the Si:B epilayer sample presented in Fig. 6.16. The section lines are shifted on the U_K -scale to reach overlay of the spectra. (a) KPFM bias section lines probed in 1D mode at 130 kHz and 90 kHz with a p^+ -type cantilever, (b) Comparison of the lateral KPFM bias variation of KPFM scans in 1D and 2D mode probed with a p^+ -type cantilever at 70 kHz, 40 kHz and 10 kHz, (c) Comparison of the lateral KPFM bias variation of KPFM scans in 1D mode probed with an n^+ -type and a p^+ -type cantilever at 70 kHz, 40 kHz and 10 kHz. Adapted from Ref. [160].

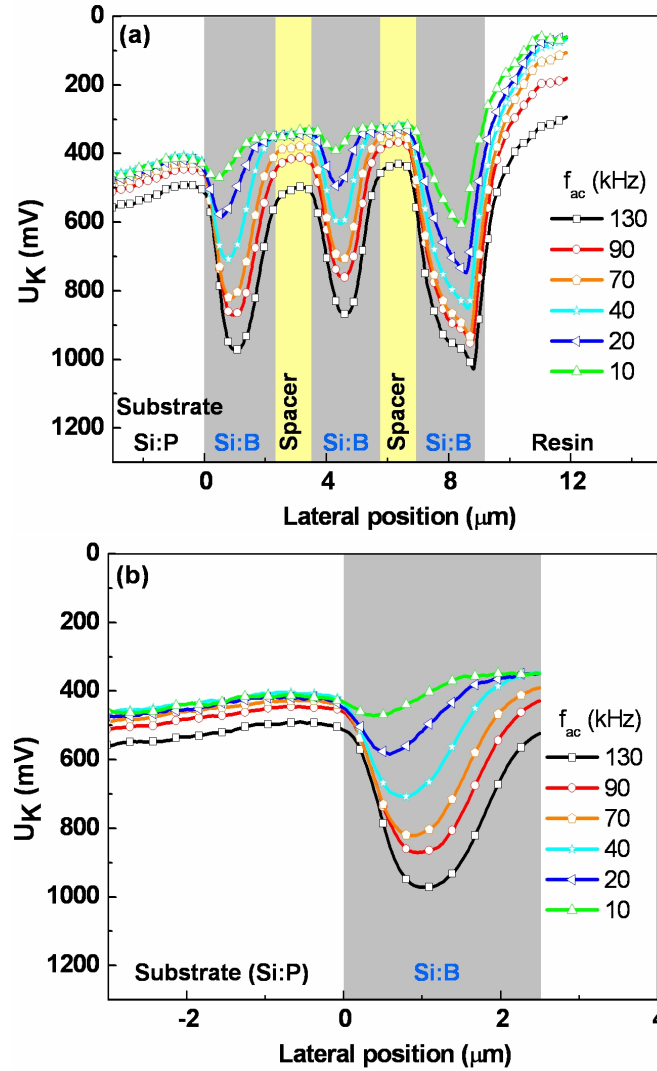


Figure 6.19: KPFM bias section lines of the frequency dependent 1D KPFM scan performed with a p^+ -type cantilever presented in Fig. 6.16(c). Unshifted KPFM bias section lines probed (a) across the whole Si:B epilayer structure, and (b) across the pn junction between P-doped substrate and B-doped near-substrate epilayer. Adapted from Ref. [160].

The observed sample-specific frequency dependence of the lateral KPFM bias variation probed across the Si:B epilayer is related with the KPFM measurement principle and the sample-specific drift and diffusion of charge carriers. The surface region of the cross-sectionally prepared Si:B epilayer sample with focus on the horizontal pn junction between P-doped substrate and the near-substrate B-doped epilayer is illustrated schematically in Fig. 6.20.

The maximum thickness of the surface space charge regions has been estimated by means of Eq. (5) and amounts to 535 nm in the substrate and to 105 nm in the B-doped epilayer. Note that the interface between neighbouring surface space charge regions in the Si:B

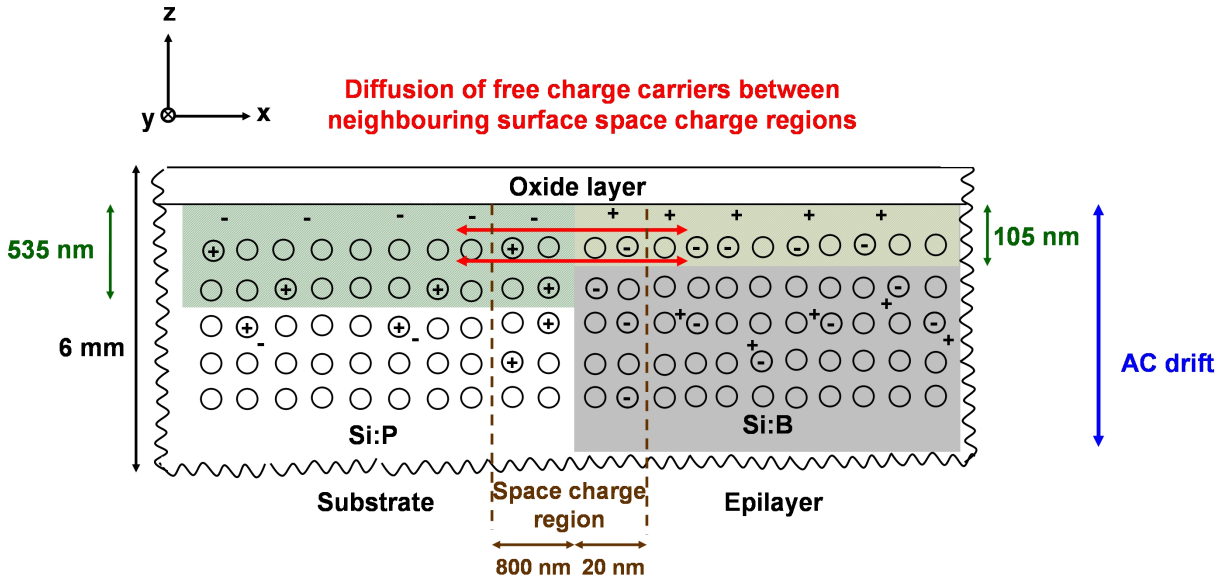


Figure 6.20: Schematic cross-sectional illustration of the surface region of the cross-sectionally prepared Si:B epilayer sample with focus on the P-doped substrate and the near-substrate B-doped epilayer. The maximum thickness of the surface space charge region (green) amounts to 535 nm in the substrate and to 105 nm in the epilayer. The diffusion between neighbouring surface space charge regions along x (red) and the ac-drift along z (blue) are indicated.

epilayer is thus much larger than in the SRAM and DRAM cell.

In contrast to the conventional SRAM and DRAM cells with mainly vertical pn junctions (Sect. 6.1), the cross-sectionally prepared Si:B epilayer sample contains differently doped regions with horizontal pn junctions in between (Fig. 6.20). Note that the horizontal pn junctions in the cross-sectionally prepared Si:B epilayer sample run from the top to the bottom of the 6 mm thick sample.

Similar to the simple approximation discussed for the SRAM cell in Sect. 6.1.1.2, in the following ac-drift and diffusion are estimated for the cross-sectionally prepared Si:B epilayer sample. The ac-drift velocity has been calculated for 130 kHz and 10 kHz at an effective ac-bias of 6 V by means of Eq. (38) for electrons and is plotted in Fig. 6.21. The calculated ac-drift velocity $v_{ac-drift}$ corresponds to an electron mobility of about $1530 \text{ cm}^2/\text{Vs}$. The diffusion velocity which is typically in the order of $v_{diff} = 1 \times 10^3 \text{ cm/s}$ in Si (Sect. 6.1.1.2) is indicated as red line. Note that the maximum ac-drift velocity amounts to $2.2 \times 10^4 \text{ cm/s}$ and is thus almost one order of magnitude smaller than in the SRAM and DRAM cell (Sects. 6.1.1.2 and 6.1.2.2). This is due to the much larger sample thickness of 6 mm of the cross-sectionally prepared Si:B epilayer compared to the only 1 mm thick SRAM and DRAM samples. The smaller maximum ac-drift velocity results in an enhanced time period in which the diffusion velocity is larger than the ac-drift velocity. From the plot of the ac-drift velocity $v_{ac-drift}$ on the small time scale in Fig. 6.21(b) the time periods in which the condition $v_{ac-drift} < v_{diff}$ is fulfilled are estimated. The time periods are

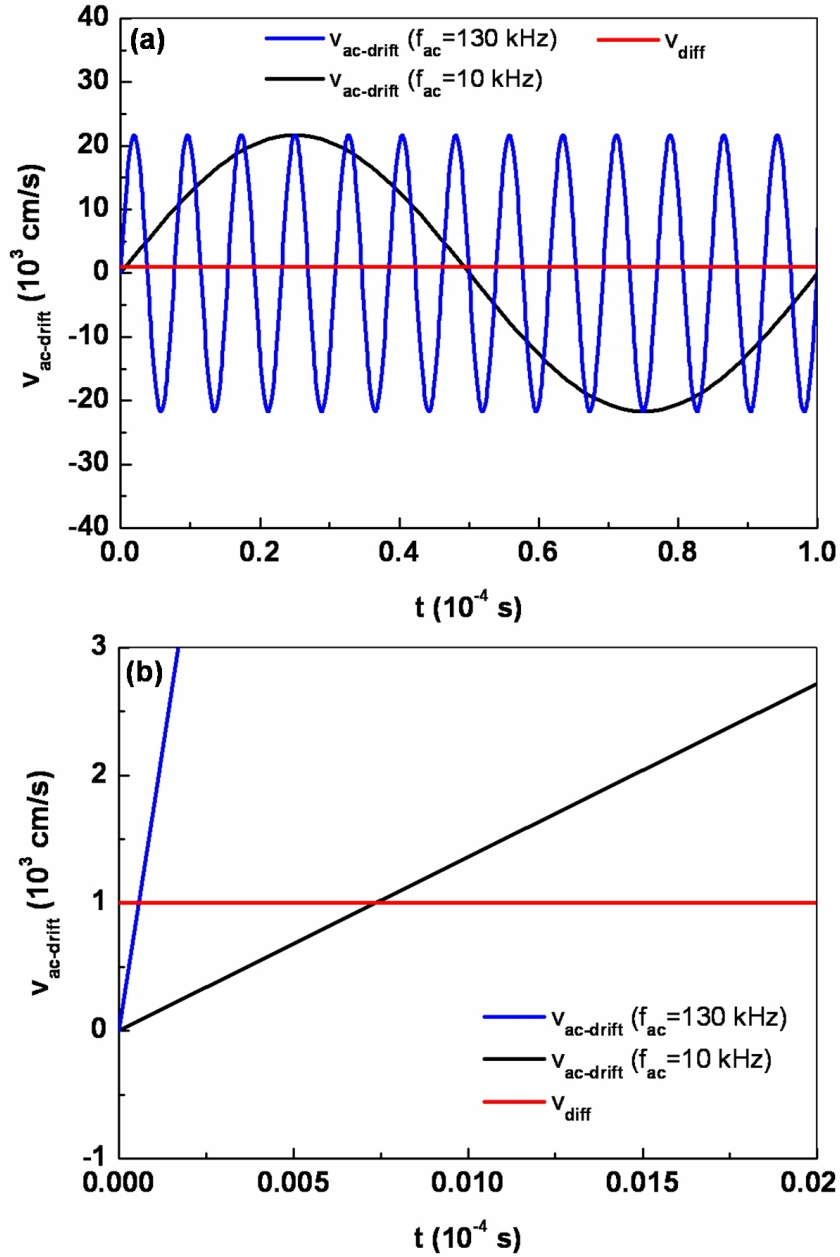


Figure 6.21: AC-drift velocity in the cross-sectionally prepared Si:B epilayer sample calculated for electrons by means of Eq. (38) for the operation frequencies 130 kHz and 10 kHz at an effective ac-bias of 6 V. Plot over (a) 1×10^{-4} s corresponding to a period T_{ac} of the 10 kHz-oscillation and (b) 2×10^{-6} s for investigation of the time period in which $v_{ac-drift} < v_{diff}$ is fulfilled. The constant diffusion velocity v_{diff} of 1×10^3 cm/s is indicated as a red line.

listed in Tab. 6.5, where also the calculated diffusion range is given. The diffusion range amounts to 600 nm at an operation frequency of 130 kHz and to 7400 nm at 10 kHz.

Table 6.5: Diffusion in the cross-sectionally prepared Si:B epilayer sample. Time period in which the condition $v_{ac-drift} < v_{diff}$ is fulfilled for the operation frequencies 130 kHz and 10 kHz. Additionally, the diffusion range of charge carriers in the respective time period is given.

Operation frequency f_{ac} (kHz)	Time period of $v_{ac-drift} < v_{diff}$ (s)	Diffusion range (nm)
130	0.6×10^{-7}	600
10	7.4×10^{-7}	7400

The discussed rough estimation of ac-drift and diffusion enables conclusions about the observed frequency dependence of the lateral KPFM bias variation probed across the S:B epilayer sample. With respect to the sample structure given in Fig. 6.20 it can be concluded that at an operation frequency of 130 kHz, diffusion of charge carriers between neighbouring surface space charge regions only locally distorts the KPFM bias measurement. On the n -side of the investigated pn junction, i.e. in the P-doped substrate, the diffusion range of 600 nm is smaller than the space charge region with a width of 800 nm where injected charge carriers always drift along x-direction. Thus, for 130 kHz no detectable influence of diffusing charge carriers is expected on the n -side. On the p-side of the pn junction, i.e. in the B-doped epilayer, charge carriers from the neighbouring surface space charge region of the P-doped substrate are expected to diffuse about 600 nm into the surface space charge region of the B-doped epilayer. The B-doped epilayer has a width of $3 \mu\text{m}$. Therefore, only the KPFM bias probed above the central part of the B-doped epilayer is expected not to be influenced by diffusion of charge carriers. For 130 kHz, the lateral KPFM bias variation probed between the center of the B-doped epilayer and the P-doped substrate in a suitable distance from the pn interface is not distorted by charge carrier diffusion and can thus be correlated with the local dopant concentration via Eqs. (6) and (7).

However, with decreasing operation frequency, the diffusion time and range increases. For 10 kHz a diffusion range of 7400 nm is estimated. Charge carriers are able to diffuse into neighbouring surface space charge regions, in particular into the center of the $3 \mu\text{m}$ thick near-substrate B-doped epilayer, and partially remove the vertical asymmetric electric dipole. The KPFM measurement is strongly distorted and a much smaller lateral KPFM bias variation is probed compared to the value at 130 kHz.

It can be concluded that the lateral KPFM bias variation probed across the Si:B epilayer sample decreases with decreasing operation frequency f_{ac} due to the fact that the unscreened immobile ionized dopant atoms in the surface space charge regions are partially screened by charge carriers diffusing from and into neighbouring surface space charge regions along x-direction (Fig. 6.20). As a consequence, at smaller operation frequencies a decreased lateral KPFM bias variation is measured which can not be related quantitatively with the local dopant concentration via Eqs. (6) and (7).

As discussed in Sect. 6.1.1.2 the presented estimation of ac-drift and diffusion is only a very simple approximation of the complex dynamic transport phenomena in semiconducting samples during the KPFM measurement. However, the presented calculations allow simple conclusions about the order of magnitude of ac-drift and diffusion and provide a possible explanation for the frequency dependence observed in the Si:B epilayer samples in contrast to the frequency independence observed in the SRAM and the DRAM cell.

The observed different frequency dependence of the KPFM bias probed in 1D and 2D mode possibly result from the laser illumination during the KPFM measurement. In 1D mode, the cantilever is scanned repeatedly across the same line which is thus permanently shadowed by the cantilever. Only charge carriers accumulated via the applied ac-bias may diffuse between neighbouring surface space charge regions in the time periods in which the condition $v_{ac-drift} < v_{diff}$ is fulfilled and partially remove the vertical asymmetric electric dipole. In 2D mode, the cantilever is moved laterally for a line-wise scan of the measurement area and thus scans above regions which have not been shadowed by the cantilever. Those sample regions suffer illumination from the red laser diode which causes photogeneration of charge carriers. The photogenerated charge carriers also may diffuse between neighbouring surface space charge regions along x-direction in the Si:B epilayer sample. Thus, in 2D mode the asymmetric electric dipole is removed at small operation frequencies by diffusing charge carriers accumulated via the applied ac-bias as well as by photogenerated charge carriers. Therefore, the influence of charge carrier diffusion between neighbouring surface space charge regions and thus the distortion of the probed KPFM bias at smaller operation frequencies is enhanced in 2D mode compared to 1D mode scans.

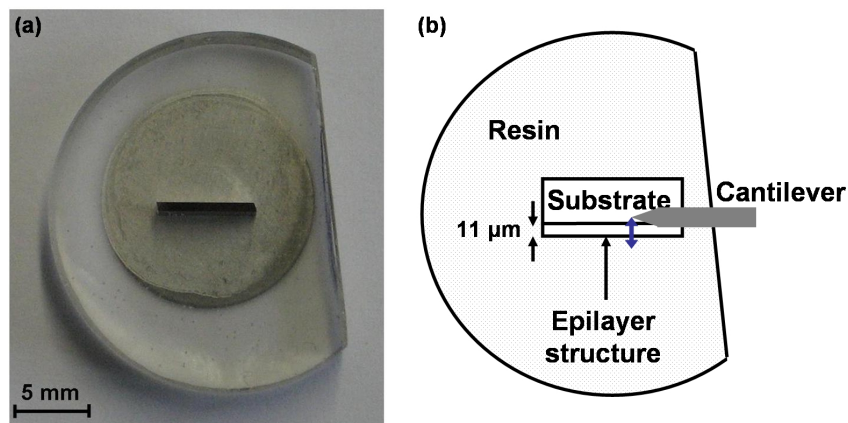


Figure 6.22: Cantilever position above the cross-sectionally prepared Si:B epilayer sample during the KPFM measurement. (a) Picture of the cross-sectionally prepared Si:B sample embedded in resin. Part of the resin has been cut for fitting the sample into the KPFM setup. (b) Schematic illustration of the cantilever position partially covering the substrate region and the surrounding resin during the KPFM measurement. The scan line across the epilayer structure is illustrated as blue arrow.

It was observed that the KPFM bias probed at small operation frequencies shifts towards the substrate value. This is due to the fact that in the substrate region of the Si:B epilayer sample, diffusion of charge carriers has less influence on the probed KPFM bias. At increasing distance to the neighbouring substrate-near B-doped epilayer the number of charge carriers which reach and partially remove the vertical asymmetric electric dipole at the measurement position decreases. In large distance from the pn junction the KPFM bias probed on the P-doped substrate is not influenced by diffusing charge carriers and remains correlated with the local dopant concentration even for small operation frequencies. Therefore, at smaller operation frequencies the substrate starts to play an important role. It has to be kept in mind that the cantilever covers a huge part of the P-doped substrate region during the KPFM measurement across the Si:B epilayer sample as shown schematically in Fig. 6.22. If due to diffusion of charge carriers between neighbouring surface space charge regions along x-direction at small operation frequencies the vertical asymmetric electric dipole in the 11 μm long epilayer structure is almost removed all over the time, only the contribution of the P-doped substrate region to electrostatic forces determines the measured KPFM signal. In this case, the KPFM bias across the whole Si:B epilayer sample equals the substrate value.

In general, for sample structures where the accessible operation frequency is not large enough to exclude the change of the vertical asymmetric electric dipole at the measurement position by diffusing charge carriers between neighbouring surface space charge regions, quantitative dopant profiling by means of Eqs. (6) and (7) is not possible. As long as the vertical asymmetric electric dipole in the surface region is removed by additional charge carriers, the probed KPFM bias can not be related with the local dopant concentration. It is of utmost importance to investigate the sample-specific intrinsic electric fields and related drift and diffusion of charge carriers for any sample before attempting a quantitative interpretation of the measured KPFM bias. For the Si:B epilayer sample operation frequencies larger than 90 kHz [Fig. 6.18(a)] have to be applied in order to ensure a negligible contribution of diffusion of injected charge carriers along x-direction between neighbouring surface space charge regions.

6.2.1.4 AC-bias dependent KPFM measurements

In addition to the frequency dependent KPFM measurements discussed in the preceding Sect. 6.2.1.3, the dependence on the ac-bias has been investigated for the cross-sectionally prepared Si:B epilayer sample. An operation frequency of 130 kHz has been applied during the ac-bias dependent KPFM measurements performed with an n^+ -type cantilever.

In Fig. 6.23(a) the section lines of the KPFM bias recorded at ac-biases with the effective values of 6 V, 5 V, 4 V and 3 V are presented. For discussion of the ac-bias dependence the focus lies on the pn junction between P-doped substrate and B-doped near-substrate epilayer which is shown in Fig. 6.23(b). As can be seen, the lateral KPFM bias variation

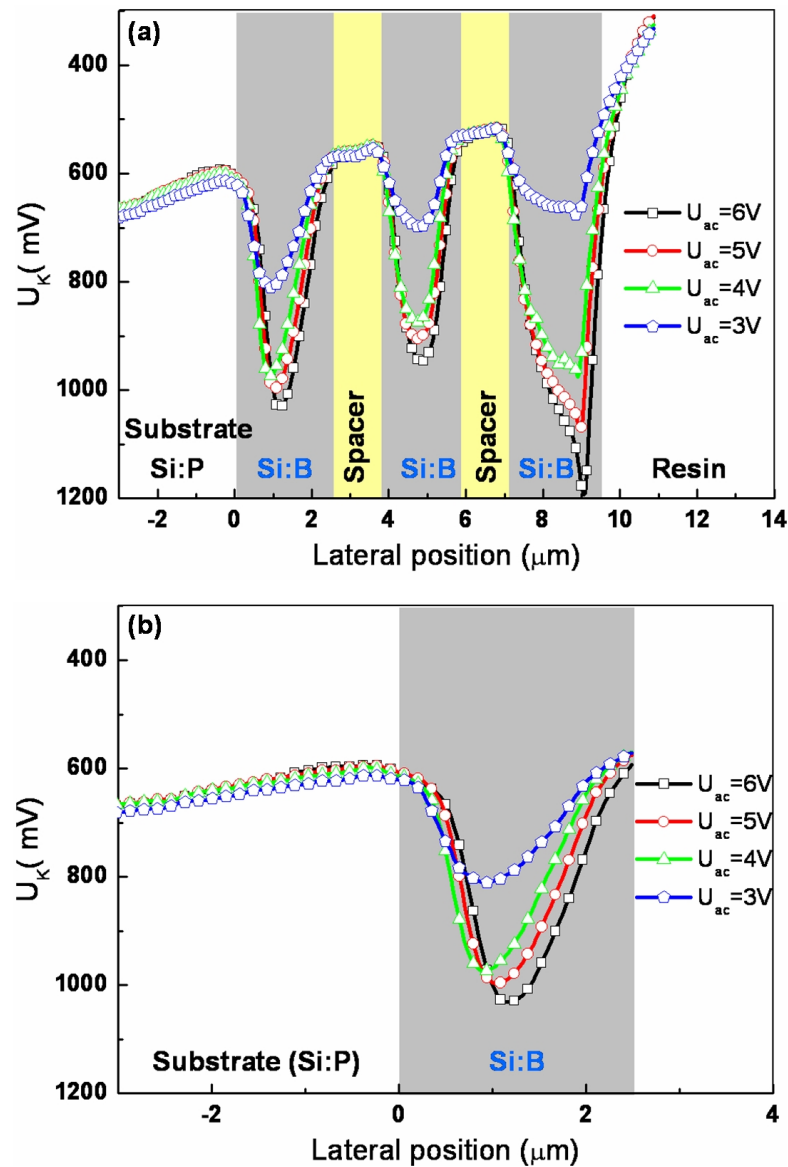


Figure 6.23: Results of the ac-bias dependent 1D KPFM measurement on the cross-sectionally prepared Si:B epilayer sample performed with an n^+ -type cantilever. KPFM bias section lines (averaged over 20 lines) probed (a) across the whole Si:B epilayer structure, and (b) across the pn junction between the P-doped substrate and the B-doped near-substrate epilayer. The section lines are shifted on the U_K -scale to reach overlay of the spectra.

decreases only slightly for the ac-biases of 6 V, 5 V and 4 V. However, for an ac-bias of 3 V a much smaller lateral KPFM bias variation is probed. Note that this observation can not be ascribed to an ac-bias-induced band bending (Sect. 5.2.4). This is due to the fact that for the same measurement parameters no ac-bias dependence was observed for the SRAM cell (Sect. 6.1.1.3).

The reason for the observed ac-bias dependence of the lateral KPFM bias variation probed across the Si:B epilayer sample is an increasing influence of diffusing charge carriers between neighbouring surface space charge regions at decreasing ac-bias. Similar to the discussion of the frequency dependence of the Si:B epilayer sample in the preceding Sect. 6.2.1.3, ac-drift and diffusion are estimated in the following for the different applied ac-biases.

The ac-drift velocity has been calculated in dependence on the applied ac-bias for the operation frequency f_{ac} of 130 kHz by means of Eq. (38) for electrons and is plotted in Fig. 6.24. The calculated ac-drift velocity $v_{ac-drift}$ is related with an electron mobility of about $1530 \text{ cm}^2/\text{Vs}$. The typical diffusion velocity in the order of $v_{diff} = 1 \times 10^3 \text{ cm/s}$ in Si (Sect. 6.1.1.2) is indicated as red line. From the plot on a smaller time scale in Fig. 6.24(b) the time periods in which the condition $v_{ac-drift} < v_{diff}$ is fulfilled are estimated. The values are listed in Tab. 6.6 where also the correlated diffusion range is given. As can be seen, the diffusion range increases with decreasing ac-bias. For ac-biases of 6 V and 5 V the range amounts to 600 nm and 700 nm, which is still smaller than the width of the space charge region in the P-doped regions of the Si:B epilayer sample and not large enough to enable charge carrier diffusion to the center of the near-substrate B-doped epilayer. For these ac-biases the center of the $3 \mu\text{m}$ thick B-doped epilayer is expected not to be influenced by charge carriers diffusing from the P-doped substrate. Thus, the KPFM bias probed above the center of the B-doped epilayer is related to the local dopant concentration. When further decreasing the ac-bias, the diffusion time and thus the diffusion range increases and amounts to more than $1 \mu\text{m}$ at 3 V (Tab. 6.6). Charge carriers are able to diffuse into neighbouring surface space charge regions, in particular almost into the center of the $3 \mu\text{m}$ thick near-substrate B-doped epilayer, and partially remove the vertical asymmetric electric dipole. The lateral KPFM bias variation probed between the center of the B-doped epilayer and the P-doped substrate in suitable distance from the pn interface can not be related quantitatively to the local dopant concentration via Eqs. (6) and (7).

In conclusion, the observed ac-bias dependence can not be ascribed to ac-bias-induced band bending but is caused by diffusion of charge carriers between neighbouring surface

Table 6.6: Diffusion in the cross-sectionally prepared Si:B epilayer sample. Time period in which the condition $v_{ac-drift} < v_{diff}$ is fulfilled in dependence on the applied ac-bias. Additionally, the diffusion range of charge carriers in the respective time period is given.

Effective ac-bias U_{ac} (V)	AC-bias peak (V)	Time period of $v_{ac-drift} < v_{diff}$ (s)	Diffusion range (nm)
6	± 8.5	0.6×10^{-7}	600
5	± 7.1	0.7×10^{-7}	700
4	± 5.7	0.9×10^{-7}	900
3	± 4.2	1.1×10^{-7}	1100

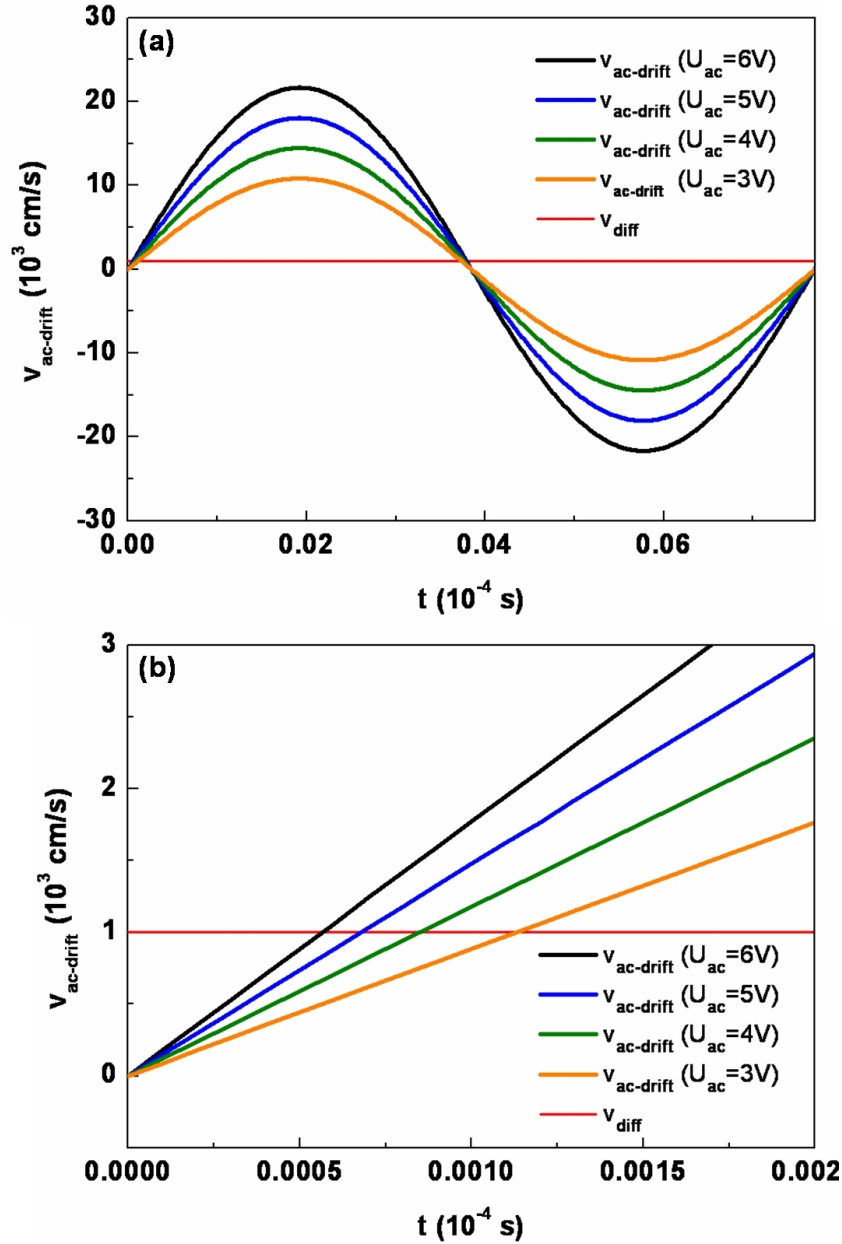


Figure 6.24: AC-drift velocity in the cross-sectionally prepared Si:B epilayer sample calculated for electrons by means of Eq. (38) for the effective ac-bias values 6V, 5V, 4V and 3V at the operation frequency f_{ac} of 130 kHz. Plot over (a) 7.7×10^{-6} s corresponding to a period T_{ac} of the 130 kHz-oscillation and (b) 2×10^{-7} s for estimation of the time period in which $v_{ac-drift} < v_{diff}$ is fulfilled. The constant diffusion velocity v_{diff} of 1×10^3 cm/s is indicated as a red line.

space charge regions. A large enough ac-bias, i.e. $U_{ac} > 3V$, has to be applied in order to minimize the influence of diffusion of charge carriers and thus to ensure the quantitative correlation between the probed KPFM bias and the local dopant concentration.

6.2.2 Si:P epilayer sample

6.2.2.1 Quantitative dopant profiling

For verification of the results of the KPFM measurements on the cross-sectional Si:B epilayer sample, additionally a Si:P epilayer with inverse doping profile (Sect. 3.1.2) has been investigated. The measurements focus on the pn junction between the B-doped substrate and the near-substrate P-doped epilayer in order to avoid the influence of local intrinsic electric fields due to overlapping space charge regions in the narrow spacer regions (Sect. 3.1.2).

In Fig. 6.25 results of a SIMS measurement across the B-doped substrate and the near-substrate P-doped epilayer are presented. A discrete drop of the P-concentration is observed at the lateral position of the abrupt pn junction at $0 \mu\text{m}$. This indicates a smaller influence of sputtering artefacts which strongly distorted the SIMS data of the inversely doped Si:B epilayer sample discussed in Sect. 6.2.1.1. From the SIMS results shown in Fig. 6.25 a B-concentration of about $1.0 \times 10^{15} \text{ cm}^{-3}$ can be deduced for the substrate. The substrate-near epilayer contains P with a concentration of approximately $6.5 \times 10^{15} \text{ cm}^{-3}$.

After the SIMS measurements the Si:P epilayer sample has been prepared cross-sectionally for KPFM. The KPFM measurements have been carried out with an n^+ -type cantilever at an ac-bias of 6 V and an operation frequency of 130 kHz. The results of the KPFM measurements across the pn junction between the B-doped substrate and the near-substrate P-doped epilayer are illustrated in Fig. 6.26. In Fig. 6.26(a) and (b) the simultaneously probed surface topography and KPFM bias are given. The KPFM bias section line across the horizontal pn junction averaged over 20 lines is plotted in Fig. 6.26(c). Between the B-doped substrate and the P-doped epilayer a lateral KPFM bias variation of approximately 510 mV is probed. The measured KPFM bias variation is compared to the new model calculation in Fig. 6.26(c).

The energy difference between Fermi energy and respective band edge amounts to $[E_C - E_F(n)] \cong +210 \text{ meV}$ in the P-doped epilayer and to $[E_V - E_F(p)] \cong -260 \text{ meV}$ in the B-doped substrate. In conclusion, an energy difference of 470 meV is predicted from the new KPFM model which is in reasonable agreement with the probed lateral KPFM bias variation of 510 mV. Note that the CPD model predicts an energy difference of 650 meV.

As explained for the Si:B epilayer sample in Sect. 6.2.1.1, the distortion of the probed KPFM bias at the lateral position of -3μ to $0 \mu\text{m}$ can be ascribed to drift of injected majority charge carriers within the intrinsic electric field of the space charge region of the horizontal pn junction.

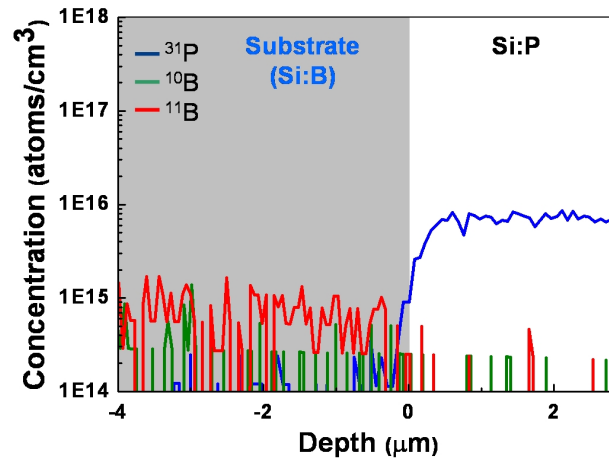


Figure 6.25: Secondary ion mass spectrometry data recorded across the pn junction between the B-doped substrate and the near-substrate P-doped epilayer in the Si:P epilayer sample.

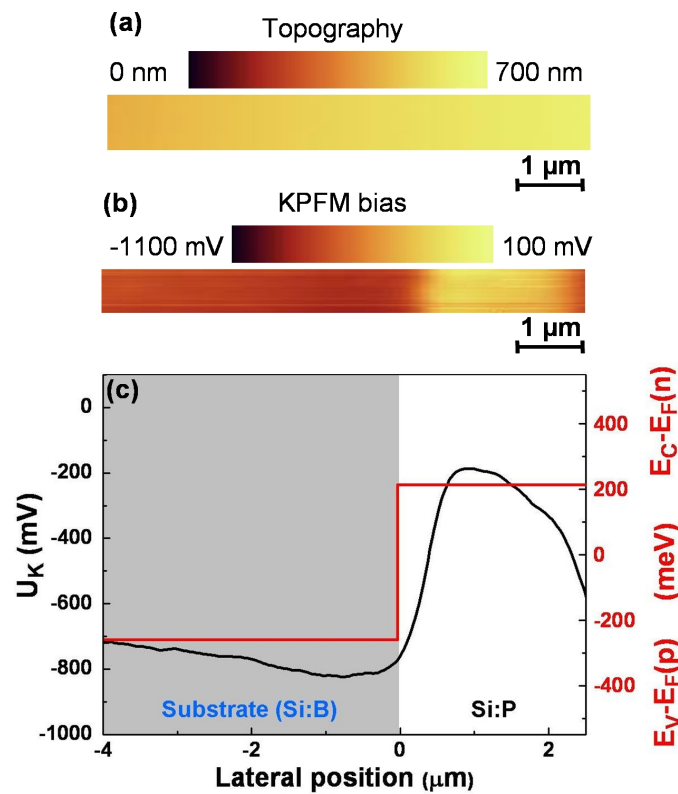


Figure 6.26: Results of the KPFM measurement across the pn junction between the B-doped substrate and the near-substrate P-doped epilayer in the Si:P epilayer sample. (a) Surface topography, (b) KPFM bias, (c) KPFM bias section line (averaged over 20 lines) compared to the calculated energy differences $[E_C - E_F(n)]$ and $[E_V - E_F(p)]$. Adapted from Ref. [158].

6.2.2.2 Frequency dependent KPFM measurements

Similar to the frequency dependent KPFM measurements performed on the Si:B epilayer (Sect. 6.2.1.3) the Si:P epilayer sample has been examined at decreasing operation frequency. The KPFM bias was recorded at the operation frequencies f_{ac} 130 kHz, 90 kHz, 70 kHz, 40 kHz, 20 kHz, 10 kHz, and 5 kHz at an ac-bias of 6 V. The results of the KPFM measurement across the whole Si:P epilayer structure are presented in Fig. 6.27(a) while in Fig. 6.27(b) the focus lies on the pn junction between B-doped substrate and near-substrate P-doped epilayer which was used to demonstrate quantitative dopant profiling in the preceding Sect. 6.2.2.1.

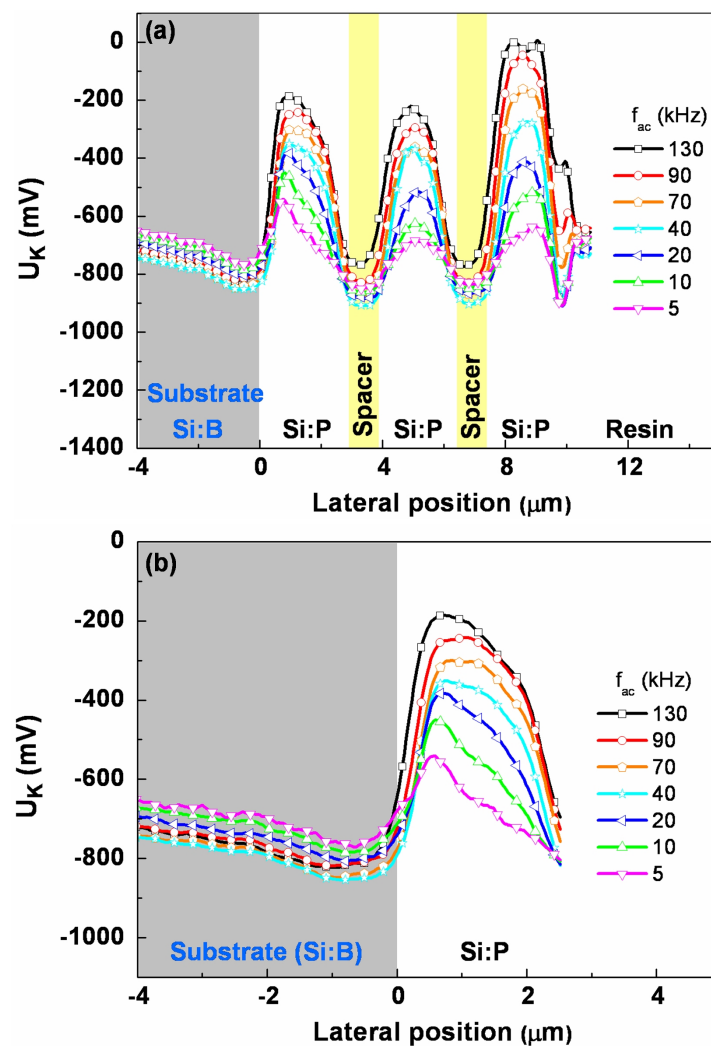


Figure 6.27: KPFM bias section lines of the frequency dependent 1D KPFM scan performed with a p^+ -type cantilever. Unshifted KPFM bias section lines probed (a) across the whole Si:P epilayer structure, and (b) across the pn junction between B-doped substrate and P-doped near-substrate epilayer.

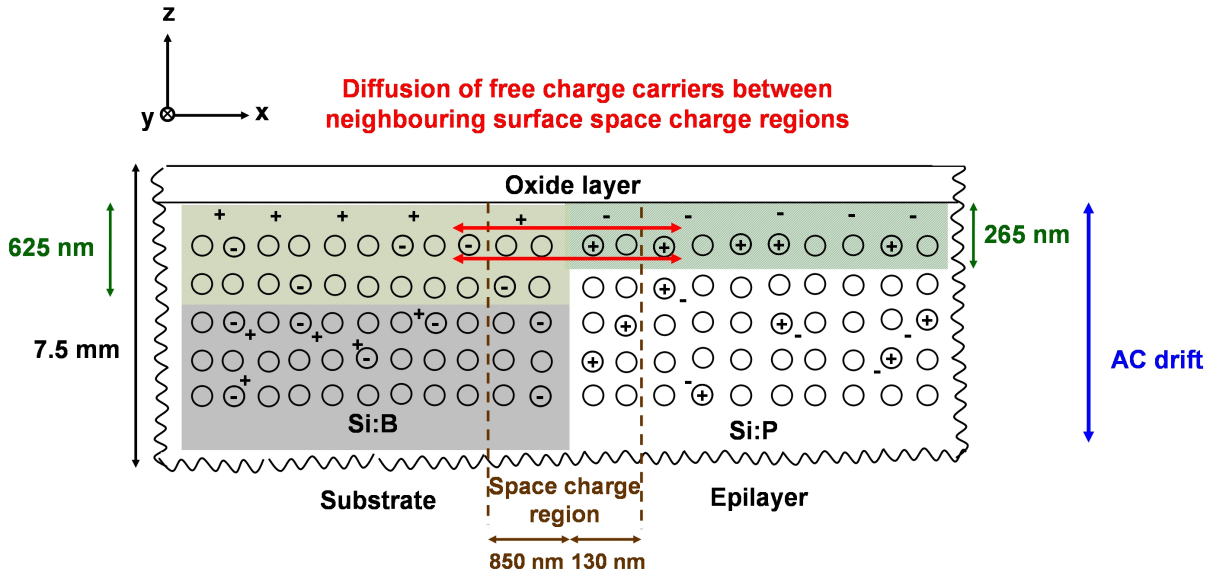


Figure 6.28: Schematic cross-sectional illustration of the surface region of the cross-sectionally prepared Si:P epilayer sample with focus on the B-doped substrate and the near-substrate P-doped epilayer. The maximum thickness of the surface space charge region (green) amounts to 625 nm in the substrate and to 265 nm in the epilayer. The diffusion between neighbouring surface space charge regions along x (red) and the ac-drift along z (blue) are indicated.

The observed frequency dependence of the lateral KPFM bias variation is in agreement with the results of the Si:B epilayer sample. The probed lateral KPFM bias variation between the differently doped regions of the Si:P epilayer sample decreases with decreasing operation frequency. Additionally, with decreasing operation frequency the KPFM bias values shift towards the substrate value.

Similar to the Si:B epilayer sample, the frequency dependence of the lateral KPFM bias variation probed across the Si:P epilayer sample is ascribed to an increasing contribution of diffusing charge carriers between neighbouring surface space charge regions. The surface region of the cross-sectionally prepared Si:P epilayer sample with focus on the horizontal pn junction between B-doped substrate and the near-substrate P-doped epilayer is illustrated schematically in Fig. 6.28. Similar to the Si:B epilayer sample, only horizontal pn junctions occur in the 7.5 mm thick cross-sectionally prepared Si:P epilayer sample.

The maximum thickness of the surface space charge regions has been estimated by means of Eq. (5) and amounts to 625 nm in the substrate and to 265 nm in the P-doped epilayer. Note that the interface between neighbouring surface space charge regions in the Si:P epilayer is even larger than in the Si:B epilayer (Sect. 6.2.1.3).

For an estimation of the time period in which diffusion between neighbouring surface space charge regions dominates the ac-drift, the ac-drift velocity of electrons has been calculated for 130 kHz and 10 kHz at an effective ac-bias of 6 V by means of Eq. (38). The maximum

Table 6.7: Diffusion in the cross-sectionally prepared Si:P epilayer sample. Time period in which the condition $v_{ac-drift} < v_{diff}$ is fulfilled for the operation frequencies 130 kHz and 10 kHz. Additionally, the diffusion range of charge carriers in the respective time period is given.

Operation frequency f_{ac} (kHz)	Time period of $v_{ac-drift} < v_{diff}$ (s)	Diffusion range (nm)
130	0.7×10^{-7}	700
10	9.2×10^{-7}	9200

ac-drift velocity amounts to $1.8 \times 10^4 \text{ cm}^{-3} \text{ cm/s}$ and is smaller than the maximum ac-drift velocity in the thinner Si:B epilayer sample. The calculated ac-drift velocity $v_{ac-drift}$ has been compared to the typical diffusion velocity in the order of $v_{diff} = 1 \times 10^3 \text{ cm/s}$ in Si (Sect. 6.1.1.2) for an estimation of the time periods in which $v_{ac-drift} < v_{diff}$ is fulfilled. In Tab. 6.7 the time periods and the corresponding diffusion ranges are listed. The diffusion range amounts to 700 nm for 130 kHz and is increased by about one order of magnitude to 9200 nm for 10 kHz. From this rough estimation it can be concluded that for small operation frequencies charge carriers diffuse into neighbouring surface space charge regions and partially remove the asymmetric electric dipole on a large lateral scale. The KPFM bias is distorted and can not be related quantitatively to the local dopant concentration via Eqs. (6) and (7). For quantitative KPFM measurements it is therefore essential to apply a large enough operation frequency, i.e. 130 kHz in the Si:P epilayer sample, to disable diffusion of charge carriers in particular into the central part of the $3 \mu\text{m}$ thick P-doped epilayer.

The observed shift of the KPFM bias towards the substrate value for small operation frequencies is ascribed to the increased contribution of the electrical signal from the substrate when the vertical asymmetric electric dipole in the $11 \mu\text{m}$ long Si:P epilayer structure is partially removed by charge carriers diffusing between neighbouring surface space charge regions. In this case, the KPFM bias probed above the epilayer structure reflects the substrate value [Fig. 6.27].

6.2.2.3 AC-bias dependent KPFM measurements

For the investigation of bias-induced band bending (Sect. 5.2.5), ac-bias dependent KPFM measurements comparable to the measurements carried out on the Si:B epilayer sample (Sect. 6.2.1.4) have been performed on the Si:P epilayer sample. For the KPFM measurements an n^+ -type cantilever and an operation frequency of 130 kHz have been applied.

The results of the ac-bias dependent KPFM measurements on the Si:P epilayer sample are presented in Fig. 6.29. In Fig. 6.29(a) the section lines of the KPFM bias recorded across the whole Si:P epilayer structure at ac-biases with the effective values of 6 V, 5 V, 4 V and 3 V are shown. For discussion of the ac-bias dependence the focus lies on the pn

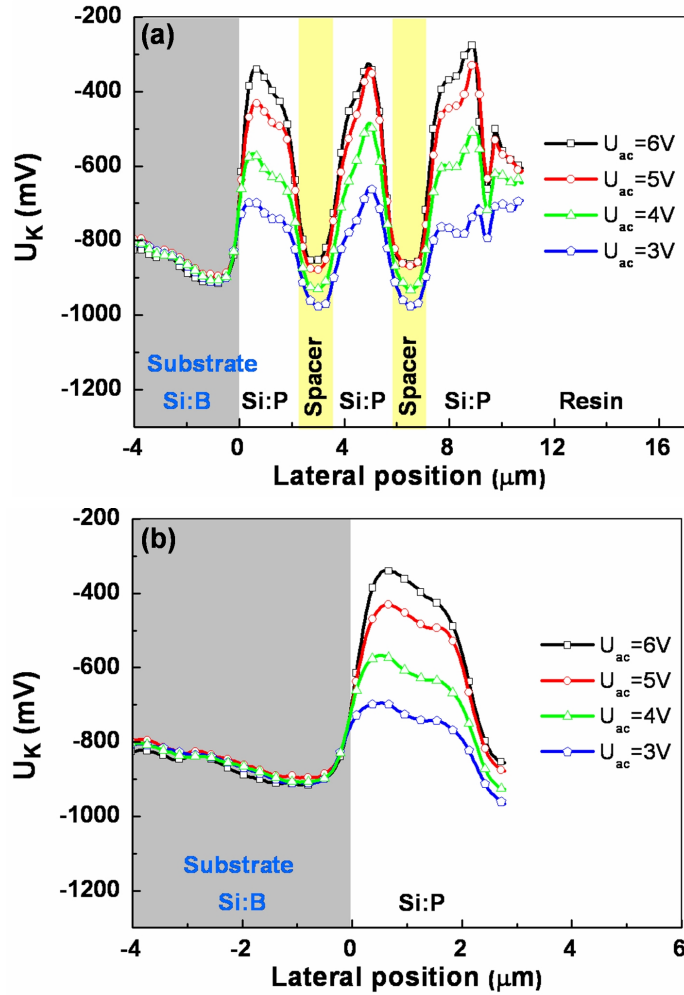


Figure 6.29: Results of the ac-bias dependent 1D KPFM measurement on the cross-sectionally prepared Si:P epilayer sample performed with an n^+ -type cantilever. KPFM bias section lines (averaged over 20 lines) probed (a) across the whole Si:P epilayer structure, and (b) across the pn junction between B-doped substrate and P-doped near-substrate epilayer. The section lines are shifted on the U_K -scale to reach overlay of the spectra.

junction between B-doped substrate and P-doped near-substrate epilayer in Fig. 6.29(b). As can be seen, the probed lateral KPFM bias variation decreases with decreasing ac-bias. Note that this observation can not be ascribed to an ac-bias-induced band bending (Sect. 5.2.4) due to the fact that for the same measurement parameters no ac-bias dependence was observed for the SRAM cell (Sect. 6.1.1.3).

The observed ac-bias dependence of the lateral KPFM bias variation probed across the Si:P epilayer sample has to be ascribed to an increasing influence of diffusion of charge carriers between neighbouring surface space charge regions at decreasing ac-bias. In the following the contributions of ac-drift and diffusion are estimated.

Table 6.8: Diffusion in the cross-sectionally prepared Si:P epilayer sample. Time period in which the condition $v_{ac-drift} < v_{diff}$ is fulfilled in dependence on the applied ac-bias. Additionally, the diffusion range of charge carriers in the respective time period is given.

Effective ac-bias U_{ac} (V)	AC-bias peak (V)	Time period of $v_{ac-drift} < v_{diff}$ (s)	Diffusion range (nm)
6	± 8.5	0.7×10^{-7}	700
5	± 7.1	0.9×10^{-7}	900
4	± 5.7	1.1×10^{-7}	1100
3	± 4.2	1.4×10^{-7}	1400

The ac-drift velocity has been calculated in dependence on the applied ac-bias for the operation frequency f_{ac} of 130 kHz by means of Eq. (38) for electrons and compared to the typical diffusion velocity in the order of $v_{diff} = 1 \times 10^3$ cm/s in Si (Sect. 6.1.1.2). The time periods in which the condition $v_{ac-drift} < v_{diff}$ is fulfilled are listed in Tab. 6.8 where also the correlated diffusion ranges are given. As can be seen, the diffusion range increases with decreasing ac-bias. For an ac-bias of 6 V the diffusion range amounts to 700 nm, while for 3 V the diffusion range is increased to 1400 nm.

It can be concluded that for 6 V KPFM bias probed above the center of the 3 μm thick P-doped epilayer is not distorted by charge carriers diffusing from neighbouring surface space charge regions. The KPFM bias probed above the center of the P-doped epilayer is thus correlated with the local dopant concentration via Eqs. (6) and (7). Also in the B-doped substrate in a suitable distance from the pn interface no detectable influence of charge carriers diffusing from the P-doped epilayer is expected. However, at an ac-bias of 3 V charge carriers from neighbouring surface space charge regions are able to diffuse to the center of the 3 μm thick P-doped epilayer and thus distort the KPFM bias measurement on a large scale. The vertical asymmetric electric dipoles in the 11 μm long S:P epilayer structure are removed partially by charge carriers diffusing from and into neighbouring surface space charge regions, and the probed lateral KPFM bias variation can not be quantitatively correlated with the local dopant concentrations via Eqs. (6) and (7).

In conclusion, the observed ac-bias dependence of the lateral KPFM bias variation probed across the Si:P epilayer sample can not be ascribed to ac-bias-induced band bending. The distortion is caused by diffusion of charge carriers from and into neighbouring surface space charge regions and the partial removal of the vertical asymmetric electric dipole. A large enough ac-bias, i.e. $U_{ac} > 5$ V in the Si:P epilayer sample, has to be applied to prevent diffusion of charge carriers and thus to ensure the quantitative correlation between the probed KPFM bias and the local dopant concentration.

6.3 Horizontal silicon nanowires

In this section the results of KPFM measurements performed on horizontal Si NW arrays introduced in Sect. 3.1.3 are presented. Horizontal Si NWs are a starting point for gate-all-around MOSFETs. The main focus of the investigations lies on the homogeneity of the dopant distribution and on the shape of the Si NWs which both are essential requirements for GAA MOSFET devices.

The KPFM measurements have been carried out by means of an n^+ -type cantilever. During the measurements an ac-bias of 6 V and an operation frequency of 130 kHz have been applied.

6.3.1 Dopant distribution

6.3.1.1 Implanted silicon nanowires

First, the NW samples are discussed in which both the Si pad and the NWs are implanted. The results of the KPFM measurements performed on the B-implanted sample are illustrated in Fig. 6.30. In Fig. 6.30(a) and (b) the simultaneously probed surface topography and KPFM bias are presented. The investigated section line along the Si pad and one Si NW is illustrated as a blue line in the KPFM bias image. The corresponding KPFM bias section line is plotted in Fig. 6.30(c). The implanted Si pad and NW contain B with a concentration of $1 \times 10^{20} \text{ cm}^{-3}$ which was deduced from the Athena simulations presented in Sect. 3.1.3. The corresponding calculated energy difference between Fermi level and valence band maximum amounts to $[E_V - E_F(p)] \cong -30 \text{ meV}$. The comparison between the measured KPFM bias and the new model calculation is shown in Fig. 6.30(c).

From the sample preparation the same dopant concentration and thus also the same KPFM bias is expected to be probed across the Si pad and the NWs. However, a steadily increasing KPFM bias is observed along the investigated section line. As can be seen in Fig. 6.30(c) the KPFM bias increases by about 80 mV between the measurement position above the Si pad at $-4 \mu\text{m}$ and above the Si NW at $7 \mu\text{m}$.

The same characteristic of the KPFM bias is observed at the As-implanted NW sample. In Fig. 6.31 the results of the KPFM measurement on the As-implanted Si pad and one NW are illustrated. The simultaneously probed surface topography and KPFM bias are shown in Fig. 6.31(a) and (b). In the surface topography and the KPFM bias image a contamination is observed on the SiO_2 near the edge of the Si pad. This contamination is ascribed to the preparation process and identified as remains of photoresist. The investigated section line across the Si pad the NW which is marked as a blue line in the KPFM bias image is not expected to be influenced by the contamination. The KPFM bias probed along the section line is plotted in Fig. 6.31(c). The As-concentration deduced from Athena simulations (Sect. 3.1.3) amounts to $5 \times 10^{20} \text{ cm}^{-3}$ and is related to the energy difference $[E_C - E_F(n)] \cong 0 \text{ meV}$. In Fig. 6.31(c) the comparison between the measured KPFM bias and the calculated energy difference is given.

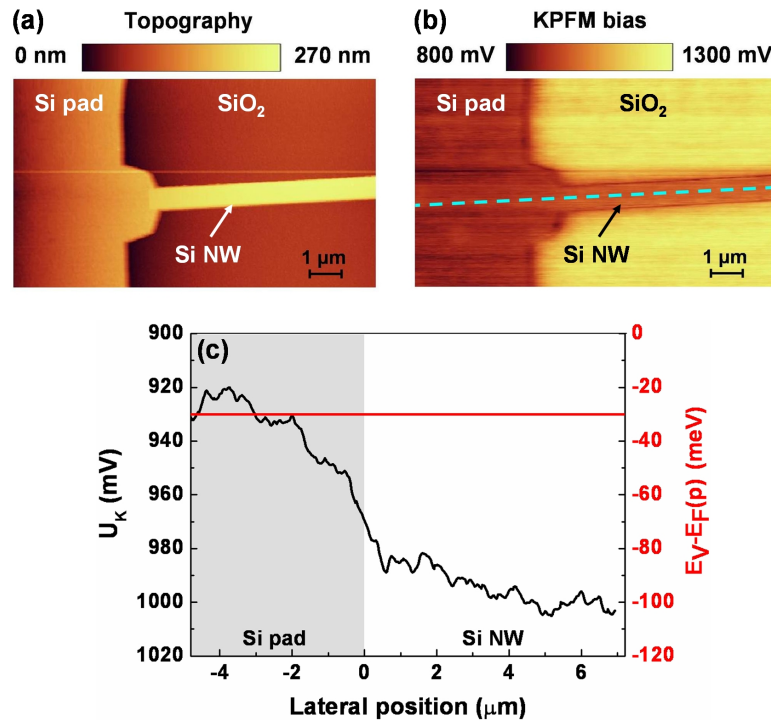


Figure 6.30: Results of the KPFM measurement on the sample with B-implanted pad and nanowires (NWs). (a) Surface topography, (b) KPFM bias with marked investigated section line, (c) KPFM bias section line (averaged over 10 lines) compared to the calculated energy difference $[E_V - E_F(p)]$.

As can be seen in Fig. 6.31(c) the KPFM bias increases by about 60 mV between the measurement position above the Si pad at $-3 \mu\text{m}$ and above the Si NW at $7 \mu\text{m}$.

The observed increase of the KPFM bias probed above the B-implanted and As-implanted NWs indicates a decreasing dopant concentration. For example, the deviation of 80 mV in the B-implanted NW compared to the Si pad indicates a decrease of the dopant concentration from $1 \times 10^{20} \text{ cm}^{-3}$ to $6 \times 10^{17} \text{ cm}^{-3}$. The deviation of 60 mV in the As-implanted sample between Si pad and NW indicates a decrease of the As-concentration from $5 \times 10^{20} \text{ cm}^{-3}$ to $5 \times 10^{18} \text{ cm}^{-3}$. However, the influence of the KPFM measurement principle has to be considered carefully before aiming for a quantitative interpretation of the probed KPFM bias. In particular, the transport of majority charge carriers injected via the applied KPFM bias in the SOI structure has to be taken into account. As explained in Sect. 3.1.3, the NW samples fabricated from the SOI structure are electrically contacted via the Al layer deposited on the Si top layer. Thus, injected majority charge carriers have to be transported horizontally through the Si top layer to reach the respective measurement position in the Si pad and the NWs. During this horizontal transport the injected majority charge carriers experience an additional vertical deflection between top and bottom of the Si top layer. This is due to the fact that the 88 nm thick Si top layer is implanted only in the

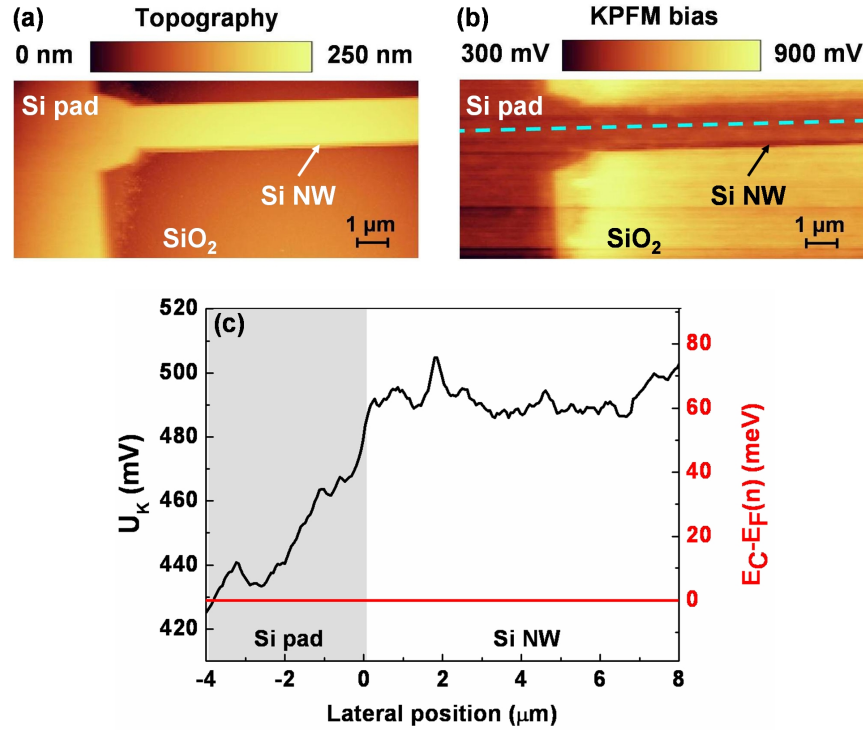


Figure 6.31: Results of the KPFM measurement on the sample with As-implanted pad and nanowires (NWs). (a) Surface topography, (b) KPFM bias with marked investigated section line, (c) KPFM bias section line (averaged over 10 lines) compared to the calculated energy difference $[E_C - E_F(n)]$.

near-surface region. The implantation depth deduced from Athena simulations amounts to about 50 nm in the B-implanted sample and to about 30 nm in the As-implanted sample (Sect. 3.1.3). In deeper regions of the Si top layer the dopant concentration is decreased by several orders of magnitude and amounts to about $1 \times 10^{16} \text{ cm}^{-3}$ at the bottom of the B-doped Si top layer and to about $1 \times 10^{14} \text{ cm}^{-3}$ at the bottom of the As-doped Si top layer. The gradient of the dopant concentration along the depth of the Si top layer results in a vertical deflection of injected majority charge carriers. The distorting contribution of the vertical deflection increases with increasing transport path length, i.e. with increasing distance between the Al contact and the measurement position. Therefore, the KPFM bias probed along the section lines above the Si pad and the NWs increases steadily. The resulting lateral KPFM bias variation can not be correlated quantitatively with a decrease of the dopant concentration.

It can be concluded that the application of KPFM for verification of the homogeneity of the dopant concentration in the Si NWs is limited by the measurement principle. The horizontal transport of majority charge carriers to the measurement position is distorted due to the implantation profile of the SOI structure which prevents a quantitative interpretation of the probed KPFM bias.

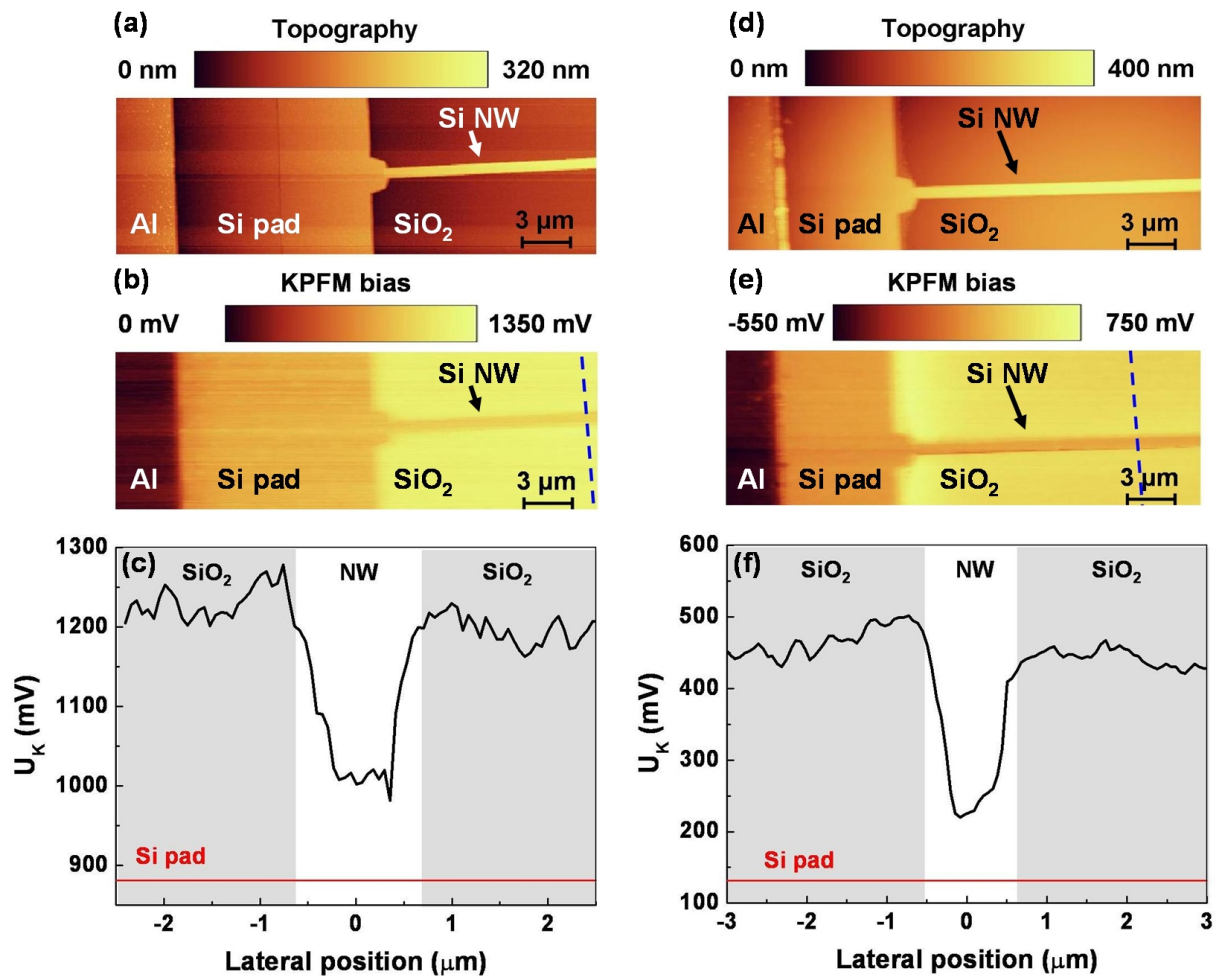


Figure 6.32: Results of the KPFM measurements on (a,b,c) B-implanted and (d,e,f) As-implanted horizontal nanowires (NWs) with focus on the doping profile along the NW width. (a,d) Surface topography, (b,e) KPFM bias with marked investigated section line at the same distance from the Al contact, (c,f) KPFM bias section lines (averaged over 10 lines).

In addition to the discussed investigation of the doping profile along the implanted Si pad and NWs, the dopant distribution along the NW width has been examined. In Fig. 6.32 the results of the KPFM measurements on the B-implanted [Fig. 6.32(a,b,c)] and the As-implanted sample [Fig. 6.32(d,e,f)] are presented. With respect to the distorting contribution due to vertical deflection of majority charge carriers between top and bottom of the Si top layer, the investigated section lines along the NW width have been chosen in the same distance of about 12 μm from the Si pad and thus of about 22 μm from the Al contact. The KPFM bias section lines across the B-implanted and the As-implanted NW which are marked as a blue line in the respective KPFM bias image are plotted in Fig. 6.32(c) and (f), respectively. In the plots, the KPFM bias value of the Si pad is indicated by means of a red line. The KPFM bias probed across the B-implanted and

the As-implanted NW is increased by about 100 mV compared to the Si pad value. This observation indicates that for the same distance between measurement position and Al contact, injected majority charge carriers experience nearly the same vertical deflection due to the dopant concentration gradient in the B-implanted and in the As-implanted Si top layer.

The KPFM bias probed along the NW width is reasonably constant and amounts to about 1000 mV for the B-implanted NW [Fig. 6.32(c)] and to about 220 mV for the As-implanted NW [Fig. 6.32(f)]. Thus, a reasonably constant dopant concentration along the NW width is deduced. However, the lateral resolution of the presented KPFM images is limited due to the large scan range of 30 μm . For a detailed investigation of the doping profile along the NW width KPFM measurements with a much smaller scan range are recommended.

Note that KPFM is sensitive to the surface space charge region. The maximum thickness of the asymmetric electric dipole layer amounts to only 2.6 nm in the B-implanted and 1.2 nm in the As-implanted Si top layer estimated by means of Eq. (5). KPFM provides no quantitative information about the dopant distribution within the 88 nm thick Si top layer.

6.3.1.2 Unimplanted silicon nanowires

In comparison to the implanted NWs, samples with unimplanted NWs featuring only the background doping have been investigated. In these samples, the Si pad has been implanted with B or As, respectively, while the horizontal NWs have been shadowed by means of a mask during the implantation (Sect. 3.1.3).

The results of the KPFM measurements on the B-implanted sample are presented in Fig. 6.33. The simultaneously probed surface topography and KPFM bias are shown in Fig. 6.33(a) and (b). The investigated section line along the B-implanted Si pad and the unimplanted NW is marked as a blue line in the KPFM bias image. In Fig. 6.33(c) the KPFM bias probed along the section line is plotted. As can be seen in the plot, a lateral KPFM bias variation of approximately 590 meV is probed between the Si pad and the NW.

Similar to the samples with implanted NWs, the Si pad contains B with a concentration of $1 \times 10^{20} \text{ cm}^{-3}$. The related calculated energy difference amounts to $[E_V - E_F(p)] \cong -30 \text{ meV}$. From the preparation process of the SOI structure (Sect. 3.1.3) and the probed lateral KPFM bias variation it can be deduced that the unimplanted NWs contain a very low p -type background doping and can be considered as almost intrinsic. Therefore, the energy difference between Fermi energy and valence band maximum in the NW is set to $[E_V - E_F(p)] \cong -560 \text{ meV}$. The comparison between the measured KPFM bias and the calculated energy differences is given in Fig. 6.33(c).

The KPFM bias probed above the implanted Si pad slightly increases by about 50 mV between the lateral positions of -4 μm to -1 μm . This is ascribed to the vertical deflection of injected majority charge carriers caused by the gradient of the dopant concentration between top and bottom of the Si top layer (Sect. 3.1.3). Note that the KPFM bias

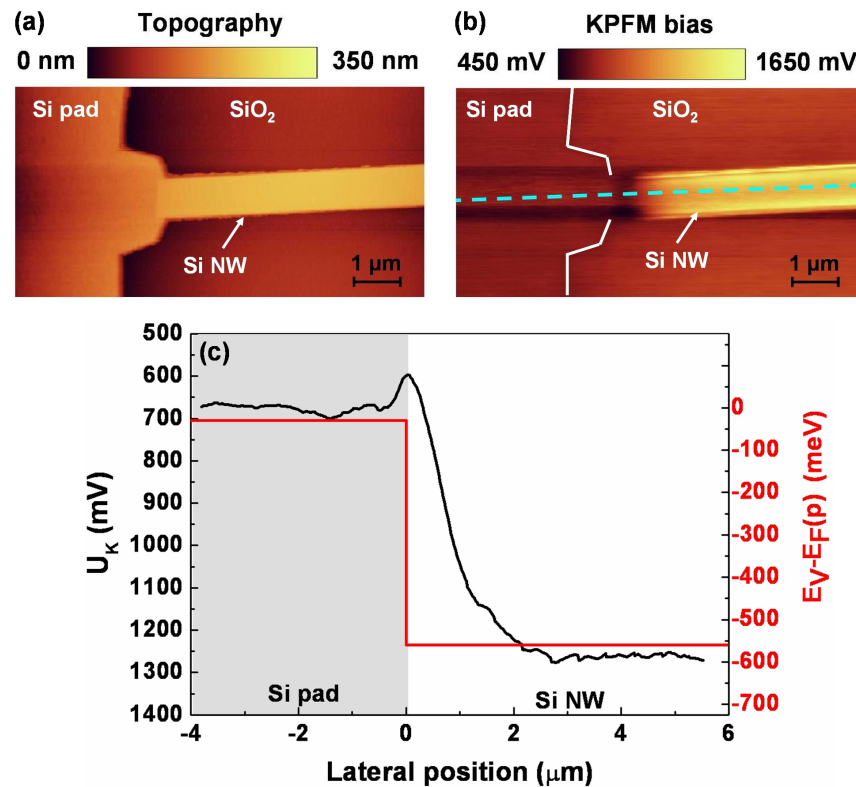


Figure 6.33: Results of the KPFM measurement on the sample with B-implanted pad and unimplanted nanowires (NWs). (a) Surface topography, (b) KPFM bias with marked investigated section line. The interface between Si pad and SiO₂ is illustrated as white line in the KPFM bias image. (c) KPFM bias section line (averaged over 10 lines) compared to the calculated energy difference $[E_V - E_F(p)]$.

probed across the unimplanted NW at the lateral positions between 3 μm and 6 μm is reasonably constant. This is due to the fact that in the unimplanted NW the horizontal transport of majority charge carriers to the measurement position is not interfered by a vertical deflection.

In Fig. 6.34 the results of the KPFM measurement on the As-implanted sample are illustrated. The surface topography and KPFM bias simultaneously probed across the As-implanted Si pad and the unimplanted NW are shown in Fig. 6.34(a) and (b). A contamination by large particles, i.e. remains of photoresist, is observed at the edge of the Si pad. This contamination also distorts the KPFM bias probed above the junction between the Si pad and the Si NW. The investigated KPFM bias section line across the Si pad and the NW is marked as a blue line in the KPFM bias image and plotted in Fig. 6.34(c). The small peak at the lateral position of approximately 0 μm is ascribed to the contaminating particles. As can be seen in Fig. 6.34(c) a lateral KPFM bias variation of approximately 1300 mV is probed between the Si pad and the NW.

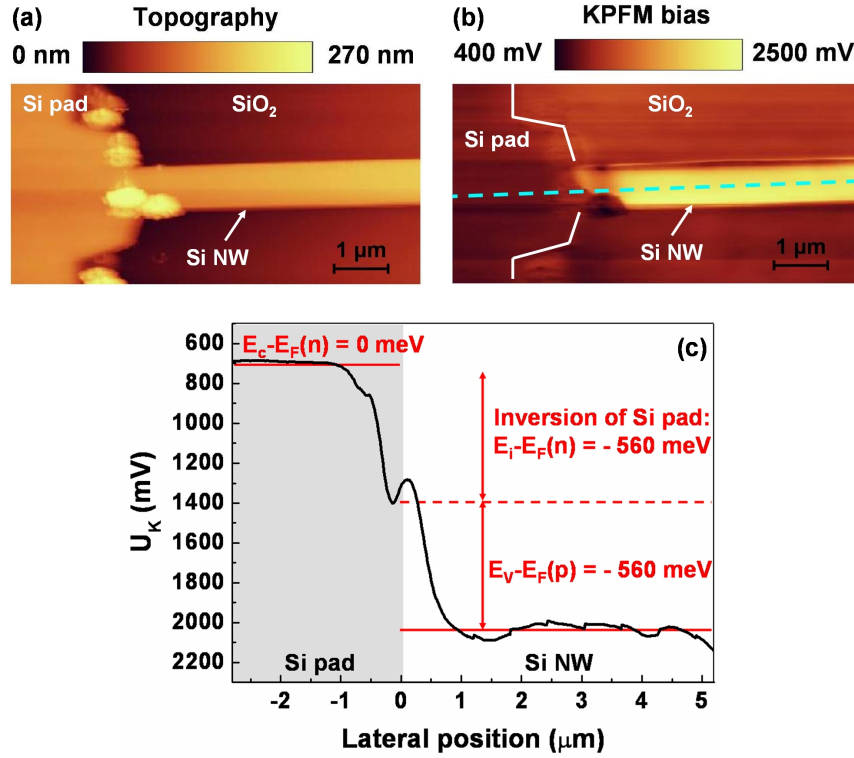


Figure 6.34: Results of the KPFM measurement on the sample with As-implanted pad and unimplanted nanowires (NWs). (a) Surface topography, (b) KPFM bias with marked investigated section line. The interface between Si pad and SiO₂ is illustrated as white line in the KPFM bias image. (c) KPFM bias section line (averaged over 10 lines) compared to the contributions necessary for inversion of the Si pad [$E_i - E_F(n)$], and for accumulation of holes in the NW [$E_V - E_F(p)$].

The Si pad is As-implanted and contains a concentration of $5 \times 10^{20} \text{ cm}^{-3}$ related to $[E_C - E_F(n)] \cong 0 \text{ meV}$. The calculated energy difference of the unimplanted NW with the almost intrinsic very low p -type background doping is set to $[E_V - E_F(p)] \cong -560 \text{ meV}$. Thus, an energy difference of 560 meV is expected for the KPFM measurement across the As-implanted Si pad and the unimplanted NW which is in disagreement with the probed lateral KPFM bias variation of approximately 1300 mV. Note that also the traditional CPD model predicts an energy difference of 560 meV.

The discrepancy between calculation and measurement can be understood as a result of the measurement principle, i.e. the transport of majority charge carriers to the measurement position, which results in an additional contribution to the probed lateral KPFM bias variation.

The KPFM bias probed above the As-doped Si pad is related to the removal of the asymmetric electric dipole by means of majority charge carriers, i.e. electrons, injected horizontally via the Al contact. Thus, the KPFM bias probed above the Si pad is related to the energy difference $[E_C - E_F(n)] \cong 0 \text{ meV}$ as illustrated in Fig. 6.34(c).

When probing above the unimplanted NW, holes have to be transported to the measurement position passing the As-doped Si pad. To enable this transport and to avoid recombination of holes in the n -type Si pad, the Si pad has to be inverted. For inversion a bias related to the energy difference between the Fermi energy of the As-implanted Si pad and the intrinsic Fermi level E_i has to be applied. Thus, the inversion bias amounts to $[E_i - E_F(n)] \cong -560$ meV. When the inversion bias is applied, the transport of holes from the Al contact to the measurement position in the NW is possible. For accumulation of holes and the removal of the vertical asymmetric electric dipole in the unimplanted NW additionally $[E_V - E_F(p)] \cong -560$ meV has to be applied.

Thus, the KPFM bias probed above the unimplanted NW in the As-implanted sample reflects the sum of the bias required for inversion of the Si pad and the bias required for accumulation of holes at the measurement position in the NW, i.e. to 1120 mV. The two contributions are illustrated in Fig. 6.34(c). With the additional contribution due to inversion of the Si pad the lateral KPFM bias variation probed between the Si pad and the NW can be understood.

Note that this additional contribution occurs in the As-implanted sample (Fig. 6.34) but not in the B-implanted sample (Fig. 6.33). This is due to the fact that in the B-implanted sample holes can be transported from the Al contact through the p^+ -type Si pad into the unimplanted NWs without difficulties. Therefore, no additional contribution to the probed KPFM bias has to be taken into account. In the As-implanted sample transport of holes into the unimplanted NWs is prevented by the n^+ -type Si pad which has thus to be inverted first resulting in the additional contribution to the probed KPFM bias.

It can be concluded that transport of majority charge carriers to a measurement position is an essential aspect of the KPFM measurement and can result in additional contributions to the KPFM bias. Therefore, it is recommended to investigate the transport path of majority charge carriers within samples before aiming for quantitative interpretation of the probed KPFM bias. On the other hand, the unique KPFM measurement principle may be used to investigate the transport of charge carriers in semiconducting samples.

A second interesting phenomenon related to the KPFM measurement principle is observed at the investigation of the unimplanted Si NWs. In contrast to the implanted NWs, the KPFM bias probed along the width of unimplanted NWs reveals a strong difference between NW center and NW edges. In Fig. 6.35 the results of the KPFM measurements on the B-implanted [Fig. 6.35(a,b,c)] and the As-implanted [Fig. 6.35(d,e,f)] sample with focus on the doping profile along the NW width are presented. The investigated section lines in the B-implanted and the As-implanted NW are marked as a blue line in the respective KPFM bias image and plotted in Fig. 6.35(c) and (f), respectively. In the plots, the KPFM bias probed across the implanted Si pad is indicated by means of a red line. The investigated section lines have a distance of approximately $5 \mu\text{m}$ to the Si pad and thus a distance of about $15 \mu\text{m}$ to the Al contact. As can be seen in the plotted KPFM bias section lines, a much larger KPFM bias is probed at the NW edges compared to the NW center. Additionally, the smaller the width of the NWs, the smaller is also the lateral

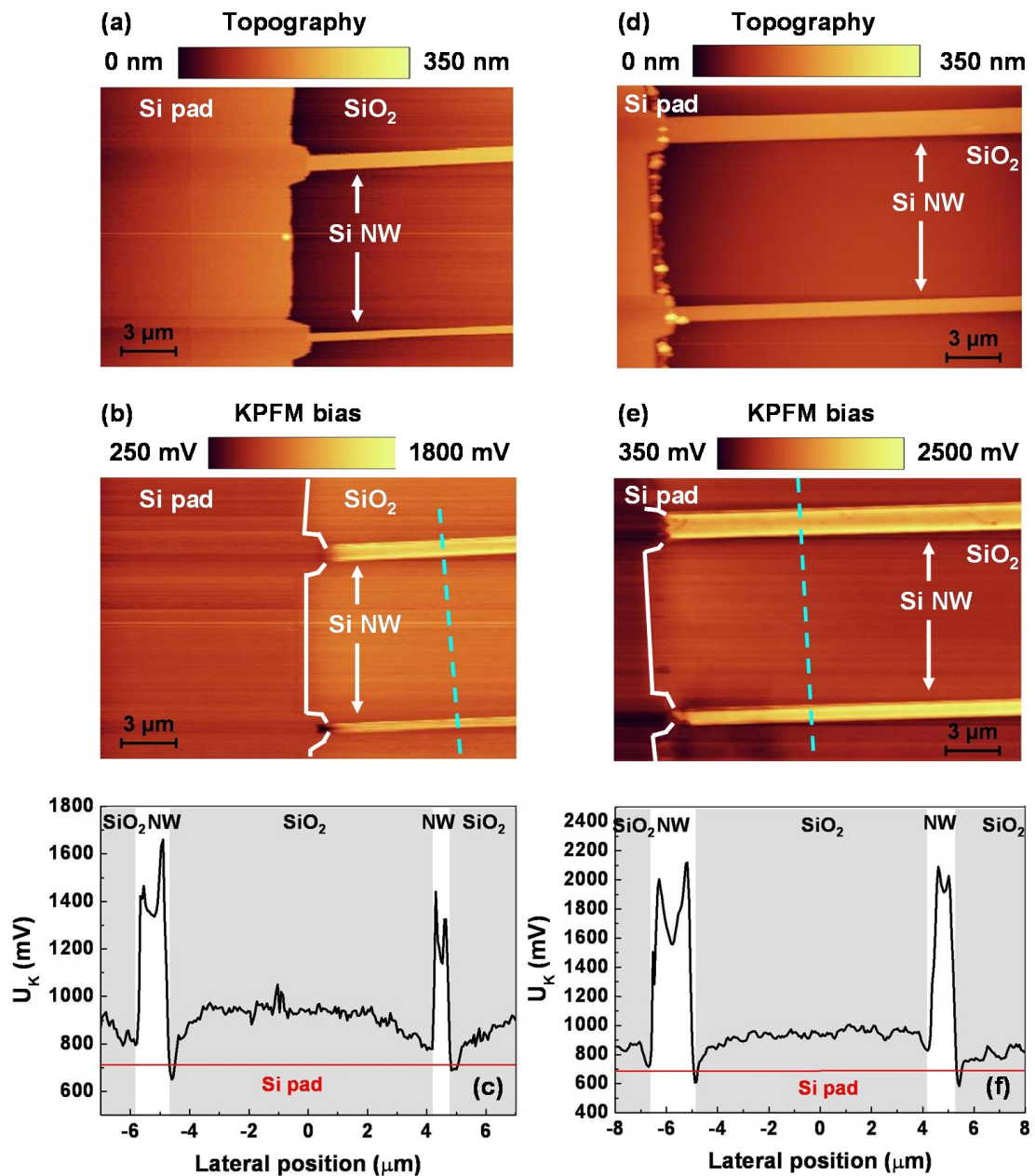


Figure 6.35: Results of the KPFM measurements on samples with (a,b,c) B-implanted and (d,e,f) As-implanted Si pad but unimplanted horizontal nanowires (NWs) with focus on the doping profile along the NW width. (a,d) Surface topography, (b,e) KPFM bias with marked investigated section line. The interface between Si pad and SiO₂ is illustrated as white line in the KPFM bias images. (c,f) KPFM bias section lines (averaged over 10 lines).

KPFM bias variation probed between NW edge and NW center.

Note that this observation is restricted to the unimplanted NWs which feature an almost intrinsic very low p -type doping. It has to be kept in mind that also at the vertical side walls

of the NWs a surface space charge region forms. With decreasing dopant concentration the width of the asymmetric electric dipole formed at the horizontal and vertical NW surface increases. In the unimplanted NWs the thickness of the asymmetric electric dipole [Eq. (5)] is much larger than 2000 nm. With respect to the size of the NWs, i.e. the thickness of 88 nm and the maximum width of 2 μm it can be concluded that all free majority charge carriers, i.e. holes, are trapped in surface states while in the NW center only unscreened ionized immobile acceptor atoms remain. Majority charge carriers injected via the applied KPFM bias are expected to drift within the thus formed electric field which distorts the KPFM measurement. The distortion is largest near the position of the maximum of electric field, i.e. near the NW side walls. Therefore, with decreasing width of the NWs an increasing distortion of the KPFM measurement due to drift of majority charge carriers is expected. This expectation is verified by the investigation of unimplanted NWs with different width. At the B-implanted Si pad with the unimplanted NWs [Fig. 6.35(c)] the lateral KPFM bias variation between NW center and the NW edge amounts to approximately 350 mV for the broader NW at the lateral position of about -5.5 μm , and is decreased to about 200 mV for the thinner NW at about 4.5 μm . At the As-implanted Si pad and the unimplanted NWs [Fig. 6.35(f)] the width dependence of the lateral KPFM bias variation is even more pronounced. A lateral KPFM bias variation of 500 mV is probed between the NW center and the NW edges for the broader NW at the lateral position of about -6 μm , while a lateral KPFM bias variation of only 100 mV is detected at the thinner NW at about 5 μm .

The observed width-dependent lateral KPFM bias variation between NW center and edge may be the reason for the observed deviation of 180 mV between the expected energy difference of 1120 meV and the measured lateral KPFM bias variation of 1300 mV in the As-implanted sample (Fig. 6.34). Note that the corresponding section line has been averaged over 10 scan lines and thus includes the smaller KPFM bias probed above the NW center as well as the larger KPFM bias probed above the NW walls.

In conclusion, the results of KPFM measurements performed on nanostructures have to be evaluated carefully since the measurement principle of injection of majority charge carriers as well as the shape and size of bulk and surface space charge regions in nanostructures may have strong influence on the KPFM measurement and thus may disable the quantitative discussion of the probed KPFM bias.

6.3.2 Shape of the silicon nanowires

With respect to the application in GAA MOSFET devices, NWs with a well-defined shape are required. For investigation of this aspect, the horizontal Si NWs have been probed on a small lateral scale. In Fig. 6.36(a) and (b) the surface topography and KPFM bias probed in an overview scan above an As-implanted sample with unimplanted NWs are shown. The blue squares mark the position of a zoom-in scan with a smaller scan range applied for the detailed investigation of the NW side walls. The results of the zoom-in scan are shown in Fig. 6.37. The simultaneously probed surface topography and KPFM

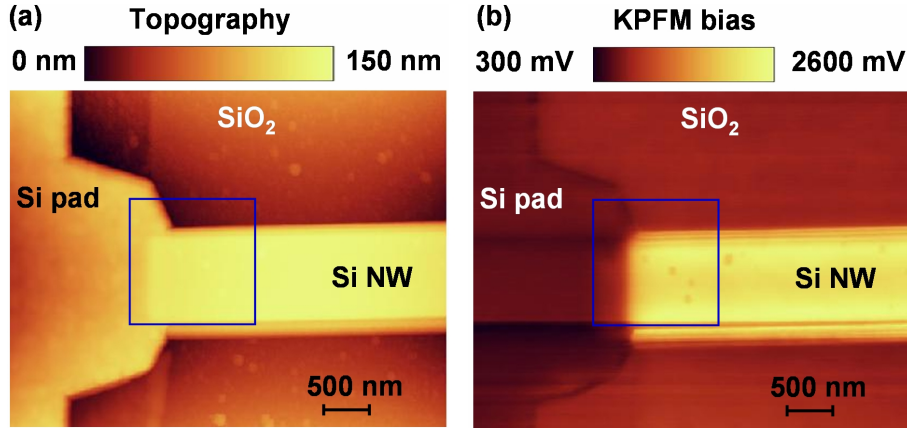


Figure 6.36: Results of the KPFM measurement on a sample with As-implanted pad and unimplanted nanowires (NWs) with focus on the NW side walls. (a) Surface topography, (b) KPFM bias. The blue squares mark the position of the zoom-in scan with a smaller scan range discussed in Fig. 6.37.

bias are illustrated in Fig. 6.37(a) and (b). In the images small contaminations on top of the Si NW are observed which are identified as remains of the photoresist from the NW preparation. With exception of the four photoresist particles, the RMS surface roughness of the Si NW amounts to 0.1 nm. This promising result is evidence for the high quality of the NW preparation process described in Sect. 3.1.3.

However, a closer investigation of the vertical side wall of the NW reveals a shape inhomogeneity. In the surface topography [Fig. 6.37(a)] and KPFM bias [Fig. 6.37(b)] image a terrace-like form of the side wall is observed. The blue lines in the images mark the chosen section line across the NW side wall. In Fig. 6.37(d) and (e) the topography and the KPFM bias section line is plotted, respectively. From the plots it can be deduced that the terrace-like side walls consists of mainly two terraces of about 50 nm width between the NW surface and the SiO₂. The two terraces are located at about 10 nm and 30 nm below the top level of the Si NW.

Note that the terraces are more pronounced in the KPFM bias image than in the image of surface topography, revealing the strong electrostatic forces at the NW side walls. Therefore, NWs with an inhomogeneous shape are not suitable for the application in GAA MOSFET devices, and optimization of the preparation process is required.

As can be deduced from the measured KPFM bias in Fig. 6.37(b) the lateral resolution of the KPFM bias probed under ambient conditions amounts to about 20 nm. For a comparison, the electrical signal of the simultaneously probed 2nd harmonic of the electrostatic force [Eq. (37)] is presented in Fig. 6.37(c) with the corresponding section line plotted in Fig. 6.37(f). As explained in Sect. 5.2.8, the 2nd harmonic does not depend on the applied dc-bias, i.e. on the dopant concentration dependent KPFM bias applied during the KPFM measurement. Therefore the 2nd harmonic is not correlated with the injection of majority charge carriers at the measurement position and is thus not influenced by local intrinsic

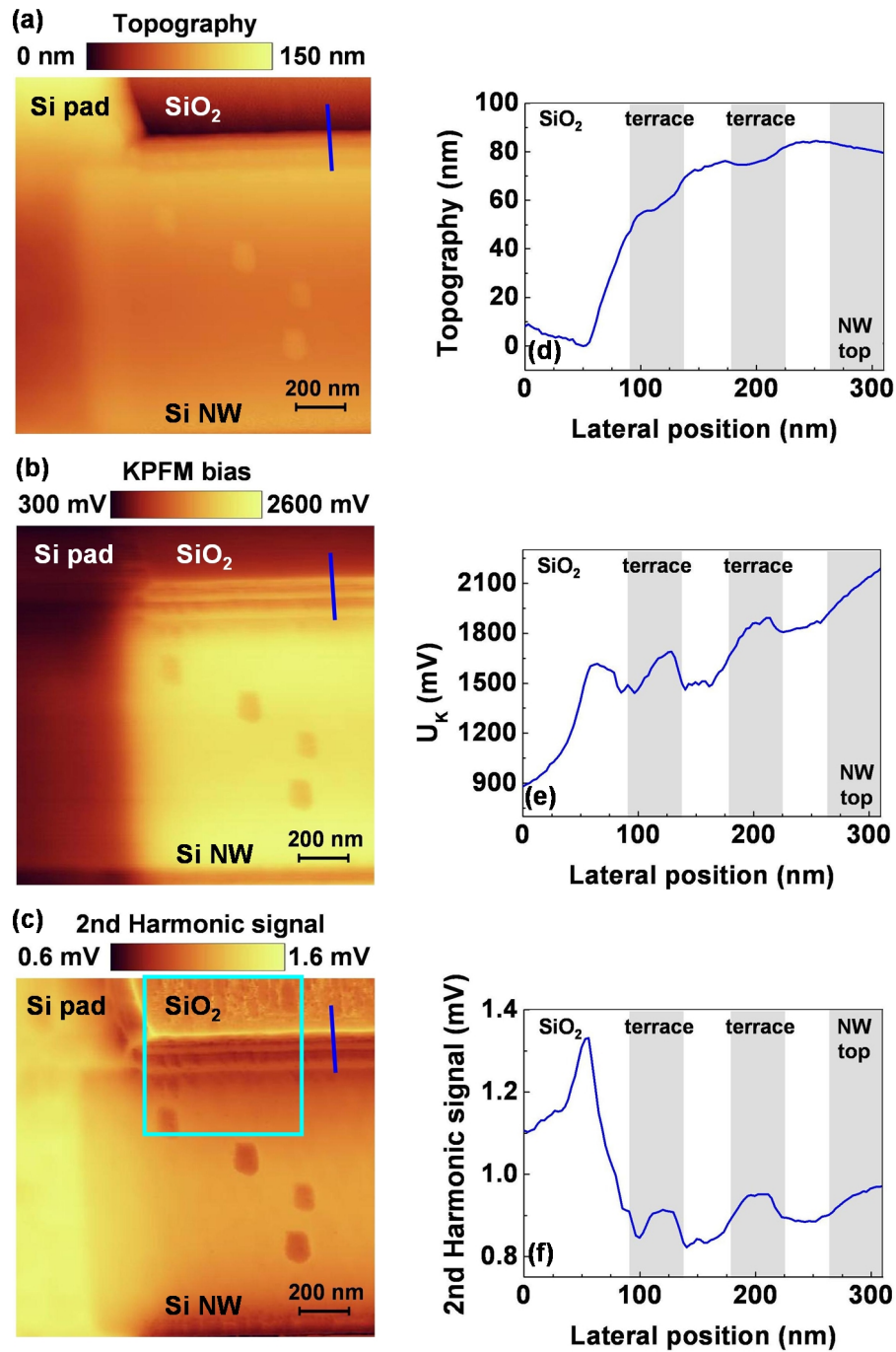


Figure 6.37: Results of the zoom-in scan on the unimplanted nanowire (NW) at the position marked in Fig. 6.36. (a) Surface topography, (b) KPFM bias, (c) 2nd harmonic signal. The investigated section lines are marked as a blue line in the respective image and plotted in (d), (e) and (f), respectively. The blue square in (c) marks the position of the zoom-in image presented in Fig. 6.38.

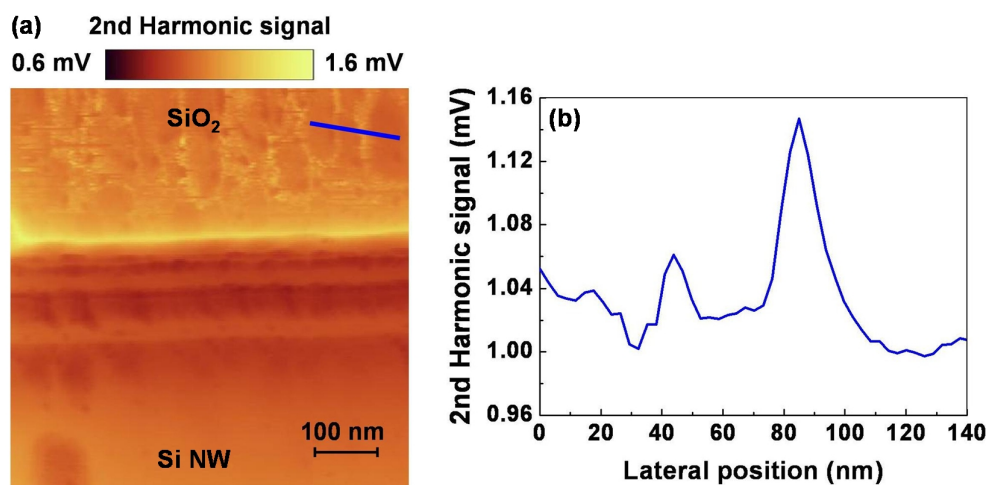


Figure 6.38: Zoom-in image of the 2nd harmonic signal from the position marked as blue square in Fig. 6.37(c). (a) 2nd harmonic signal with marked section line across the SiO₂, (b) 2nd harmonic signal probed along the section line (averaged over 10 lines).

electric fields. As a consequence the signal of the 2nd harmonic provides a much better lateral resolution and can also be used to investigate insulating materials as for example the SiO₂ adjacent to the NWs. In Fig. 6.38(a) a zoom-in image of the 2nd harmonic signal probed above the position marked as blue square in Fig. 6.37(c) is presented. The zoom-in image provides highly detailed information about the insulating SiO₂. A section line across the SiO₂ which is marked as blue line in the zoom-in image in Fig. 6.38(a) is plotted in Fig. 6.38(b). From the plot, the lateral resolution of the 2nd harmonic signal can be determined to be in the sub-10 nm range. This most promising result shows that the measurement of the 2nd harmonic could help to overcome the restriction of the KPFM bias, which is not suitable to investigate insulators and which has a lateral resolution of only about 20 nm in ambient KPFM. However, the quantitative interpretation of the 2nd harmonic signal requires extensive theoretical calculations of the capacitive and electrostatic tip-sample interaction and remains an open issue so far.

7 Conclusions

In the presented work, Kelvin probe force microscopy (KPFM) has been applied for the investigation of differently structured, *n*- and *p*-type doped silicon. The high potential of KPFM as a non-destructive, quantitative electrical nanometrology technique has been pointed out. The technical facets of the KPFM measurement technique as well as the physical aspects required for the correct interpretation of the KPFM bias probed on semiconductors have been discussed. Facing the demands of today's semiconductor industry the presented work focused on the aspect of quantitative dopant profiling. A new KPFM model was developed which enables the quantitative correlation between the probed KPFM bias and the local dopant concentration in the investigated semiconductor. Additionally, it was demonstrated that transport of charge carriers in the investigated sample is a crucial aspect of the unique measurement technique and has to be taken into account when aiming for a quantitative evaluation of the probed KPFM bias.

7.1 Quantitative dopant profiling

For a correct interpretation of the measured KPFM bias, understanding of the measurement principle and the influence of the specific sample structure is essential. In this work it was discussed how KPFM allows the investigation of the bulk dopant concentration in semiconductors via probing the electrostatic forces from the formed surface space charge region. A new KPFM model was introduced which defines the measured KPFM bias as the voltage required to accumulate majority charge carriers in the surface region of the investigated silicon samples in order to remove the vertical asymmetric electric dipole. Quantitative dopant profiling has been successfully demonstrated by KPFM measurements on conventional SRAM and DRAM cells and on cross-sectionally prepared Si epilayer samples. Important predictions from the new KPFM model as for example the independence of the cantilever potential have been successfully verified.

With respect to the applied ambient Level-AFM from Anfatec Instruments AG, the properties of a semiconductor surface exposed to ambient environment have been discussed. It was shown that a quantitative analysis of the probed lateral KPFM bias variation is possible despite of the sample-specific contribution of an oxide layer and adsorbed water. However, in particular for KPFM measurements under ambient conditions the sample surface has to be prepared carefully in order to ensure that the electrical KPFM signal from the asymmetric electric dipole is large enough to be detected against the potential shielding signal. A comparative UHV KPFM measurement has been performed on the conventional SRAM cell for verification of the results obtained in ambient KPFM. It was shown that the lateral KPFM bias variation probed under ambient and under UHV conditions is in good agreement and can be explained satisfyingly within the presented new KPFM model.

A major aspect of the KPFM measurement principle is transport of majority charge carriers in the investigated sample from the contact to the measurement position. Within the new

KPFM model the influence of intrinsic electric fields in particular due to vertical and horizontal pn junctions and due to surface space charge regions has been discussed. A simple approximation of the complex dynamic transport phenomena in semiconducting samples during the KPFM measurement enabled an estimation of drift and diffusion in the differently structured and doped Si samples. It was discussed that diffusion of charge carriers between neighbouring surface space charge regions may have strong influence on the KPFM measurement. The contribution of diffusion was shown to be dependent on the specific sample structure, i.e. on the location and direction of intrinsic electric fields, as well as on the chosen measurement parameters, i.e. on the applied operation frequency f_{ac} and the ac-bias U_{ac} . It has been pointed out in this work that a large enough operation frequency and ac-bias have to be applied to enable quantitative dopant profiling in samples containing neighbouring regions with opposite type of majority charge carriers. On the other hand, KPFM measurements performed at small operation frequencies or small ac-biases may be used in particular for the investigation of transport of charge carriers in doped semiconductors with intrinsic electric fields.

The importance of knowledge about the transport of charge carriers in the investigated sample has been demonstrated by the example of KPFM measurements on horizontal Si nanowire arrays fabricated from a SOI structure. The KPFM bias probed across the Si NW samples could only be explained including the transport of the horizontally injected majority charge carriers and the properties of sample-specific intrinsic electric fields.

7.2 Lateral resolution

Due to the permanent down-scaling of semiconductor devices an electrical nanometrology technique with a lateral resolution in the sub-10 nm range is required. In the presented work it has been shown that the lateral resolution of the KPFM bias probed under ambient conditions is limited to approximately 20 nm. It was pointed out by the example of the measurements performed on the SRAM cell that UHV KPFM enables scans with an improved lateral resolution. As an additional example, a lateral resolution of 2 nm achieved in UHV KPFM has been reported only recently [153]. Therefore, for the electrical investigations of nanostructures UHV KPFM is recommended.

However, an important conclusion of the presented work is that the measurement principle of the KPFM bias itself limits the lateral resolution for semiconducting samples containing doping junctions. Injected majority charge carriers drift within electric fields of space charge regions formed at doping junctions which distorts the KPFM measurement. This strong limitation to the lateral resolution is restricted to the measurement of the KPFM bias. By the example of KPFM measurements performed on the horizontal Si NW samples it was demonstrated that simultaneously detected electrical KPFM signals as for example the 2nd harmonic allow to overcome the limitation of the KPFM bias measurement. The electrical signal correlated with the 2nd harmonic of the electrostatic force provides a lateral resolution below 10 nm and is not influenced by local intrinsic electric fields in the sample. However, the quantitative interpretation of the higher harmonic signals detected by means of KPFM remains an open issue.

7.3 Future challenges

The KPFM measurements presented in this work have been restricted to semiconducting samples, i.e. to differently structured, n - and p -type doped silicon. However, it is expected that for any material system a correct description of the electrostatic forces acting onto the cantilever and their minimization during the KPFM measurement will allow to quantitatively correlate the measured KPFM bias with the electrical properties of the investigated sample. The achieved quantitative understanding of the KPFM bias probed on doped silicon could be used for example as a starting point for investigations on biosensors which are often based on semiconducting nanostructures [170, 171]. KPFM could be applied in particular for locating and manipulating biomolecules on doped semiconductors.

Due to the possibility of the simultaneous detection of higher harmonics of the electrostatic force, KPFM may be applied to all material systems, even to thick insulators which represent a restriction for KPFM bias measurements. Additionally, the quantitative analysis of higher harmonics of the electrostatic force is expected to provide extended insight into the physics of the investigated materials. To approach this challenge, it is suggested to compare higher harmonic KPFM signals probed on simple test structures to theoretical calculations of the capacitive and electrostatic tip-sample interactions. Such investigations are one issue of the cooperation between the Helmholtz-Zentrum Dresden-Rossendorf e.V. and Anfatec Instruments AG in the framework of a recently started project (project number: SAB-59948/245).

List of Figures

2.1	Measurement principle of scanning spreading resistance microscopy. Adapted from Ref. [60].	5
2.2	Measurement principle of conductive atomic force microscopy. Adapted from Ref. [67].	6
2.3	Measurement principle of scanning capacitance microscopy. Adapted from Ref. [85].	7
2.4	High-frequency CV curves of an <i>n</i> -type and a <i>p</i> -type ideal metal-oxide-semiconductor structure formed during the scanning capacitance microscopy measurement. Adapted from Refs. [86] and [87].	8
2.5	Scanning capacitance microscopy data probed on a conventional Si static random access memory cell.	9
2.6	Scanning capacitance microscopy data probed on a cross-sectionally prepared Si:B epilayer sample. Adapted from Ref. [91].	10
2.7	Measurement principle of scanning microwave microscopy. Adapted from Ref. [34].	12
2.8	Topography, capacitance, and dC/dV images of a Si static random access memory chip acquired with a scanning microwave microscope. From Ref. [98].	12
2.9	Measurement principle of electrostatic force microscopy.	13
2.10	Comparison between the measurement principles of electrostatic force microscopy and amplitude-modulated Kelvin probe force microscopy.	14
3.1	Schematic illustration of an n-MOSFET. Adapted from Ref. [106].	16
3.2	Doping pattern and corresponding scanning capacitance microscopy data of the Si static and dynamic random access memory cells supplied by Veeco Instruments (since 2010 Bruker Corp.).	17
3.3	Cross-sectional view of the Si:B and Si:P epilayer structure grown epitaxially on doped Si substrates at the Fraunhofer Institute for Photonic Microsystems Dresden.	20
3.4	Cross-sectionally prepared Si epilayer sample embedded in epoxy resin.	20
3.5	Schematic view of a Si gate-all-around MOSFET. From Ref. [114].	21
3.6	Schematic cross-sectional view of the silicon-on-insulator structure.	22
3.7	Schematic top view of the arrays of implanted and unimplanted horizontal Si nanowires.	23
3.8	Level-AFM developed by Anfatec Instruments AG. Adapted from Ref. [117].	26

3.9	Schematic diagram of the experimental setup of the Level-AFM developed by Anfatec Instruments AG. From Ref. [118].	26
4.1	Schematic diagram showing the stepwise adsorption of water on a freshly cleaved quartz (Si oxide) surface. Adapted from Ref. [125]. . .	31
5.1	Schematic illustration of the contact potential difference model for interpretation of the KPFM bias.	33
5.2	Contact potential difference values across a pn junction in dependence on the cantilever type.	34
5.3	Energetic distribution of intrinsic and extrinsic surface states at the interface of thermally grown SiO_2 on Si. Adapted from [133].	35
5.4	Description of a semiconductor surface containing both acceptor-like and donor-like surface states by an equivalent distribution with a neutral energy level. From [87].	36
5.5	Schematic cross-sectional illustration of the surface space charge region formed in n -type and p -type Si at equilibrium.	38
5.6	Schematic illustration of a KPFM measurement on doped Si. (Picture and permission from Sander Münster, 3DKosmos.de).	41
5.7	Schematic diagram of the probed KPFM bias in dependence on the position of the Fermi level.	42
5.8	Comparison between the traditional CPD model and the new KPFM model by the example of an n -type staircase and a pn junction probed by means of an n^+ -type cantilever.	43
5.9	Fermi energy for B and P dopants in Si plotted in dependence on the dopant concentration.	48
5.10	Schematic illustration of the electric field across a pn junction in equilibrium. Adapted from Ref. [106].	54
5.11	Schematic illustration of a KPFM measurement across a horizontal pn junction. Adapted from Ref. [158].	55
5.12	Vector diagram illustrating the electrical signal of the 1st harmonic for an in-phase and an out-of-phase background. Adapted from Ref. [160].	58
6.1	Results of the KPFM measurement across an $n^+pn^+pn^+$ junction in the SRAM cell. Adapted from Ref. [162].	62
6.2	Results of the KPFM measurement across a p^+np^+ junction in the SRAM cell.	63
6.3	Results of the frequency dependent KPFM measurement across the p^+np^+ junction in the SRAM cell performed with an n^+ -type cantilever. Adapted from Ref. [160].	65

6.4	Results of the frequency dependent KPFM measurement across the p^+np^+ junction in the SRAM cell performed with a p^+ -type cantilever. Adapted from Ref. [160].	66
6.5	Schematic cross-sectional illustration of the surface region of the SRAM cell with indicated diffusion between neighbouring surface space charge regions along x and ac-drift along z.	67
6.6	Frequency dependent ac-drift velocity in the SRAM cell.	70
6.7	Results of the ac-bias dependent KPFM measurement on the SRAM cell performed with an n^+ -type cantilever.	73
6.8	AC-bias dependent ac-drift velocity in the SRAM cell.	74
6.9	Comparison between ambient and UHV KPFM measurements performed on the SRAM cell.	76
6.10	Results of the KPFM measurement across a pn junction and an n^+pn^+ junction in the DRAM cell. Adapted from Ref. [165].	79
6.11	Results of the frequency dependent KPFM measurement across the n^+pn^+ junction in the DRAM cell performed with a n^+ -type cantilever.	81
6.12	Schematic cross-sectional illustration of the surface region of the DRAM cell with indicated diffusion between neighbouring surface space charge regions along x and ac-drift along z.	82
6.13	Secondary ion mass spectrometry data recorded on the Si:B epilayer sample.	85
6.14	Results of the KPFM measurement across the pn junction in the Si:B epilayer sample. Adapted from Ref. [158].	85
6.15	Results of the KPFM measurements on the cross-sectionally prepared Si:B epilayer sample performed with an n^+ -type and a p^+ -type cantilever.	87
6.16	Results of the frequency dependent KPFM measurement on the cross-sectionally prepared Si:B epilayer sample in 1D and 2D mode performed with an n^+ -type and a p^+ -type cantilever. Adapted from Ref. [160].	89
6.17	Schematic illustration of the interface between the Si:B epilayer wafer and the surrounding resin in the cross-sectionally prepared sample. Adapted from Ref. [160].	90
6.18	KPFM bias section lines of the frequency dependent KPFM measurements across the Si:B epilayer sample presented in Fig. 6.16. Adapted from Ref. [160].	91

6.19	KPFM bias section lines of the frequency dependent KPFM measurements across the Si:B epilayer sample with focus on the pn junction between P-doped substrate and B-doped near-substrate epilayer. Adapted from Ref. [160].	92
6.20	Schematic cross-sectional illustration of the surface region of the cross-sectionally prepared Si:B epilayer sample with indicated diffusion between neighbouring surface space charge regions along x and ac-drift along z.	93
6.21	Frequency dependent ac-drift velocity in the cross-sectionally prepared Si:B epilayer sample.	94
6.22	Schematic illustration of the cantilever position above the cross-sectionally prepared Si:B epilayer sample during the KPFM measurement.	96
6.23	Results of the ac-bias dependent KPFM measurement on the cross-sectionally prepared Si:B epilayer sample performed with an n^+ -type cantilever.	98
6.24	AC-bias dependent ac-drift velocity in the cross-sectionally prepared Si:B epilayer sample.	100
6.25	Secondary ion mass spectrometry data recorded on the Si:P epilayer sample.	102
6.26	Results of the KPFM measurement across the pn junction in the Si:P epilayer sample. Adapted from Ref. [158].	102
6.27	KPFM bias section lines of the frequency dependent KPFM measurements across the Si:P epilayer sample with focus on the pn junction between B-doped substrate and P-doped near-substrate epilayer.	103
6.28	Schematic cross-sectional illustration of the surface region of the cross-sectionally prepared Si:P epilayer sample with indicated diffusion between neighbouring surface space charge regions along x and ac-drift along z.	104
6.29	Results of the ac-bias dependent KPFM measurement on the cross-sectionally prepared Si:P epilayer sample performed with an n^+ -type cantilever.	106
6.30	Results of the KPFM measurement on the sample with B-implanted pad and nanowires.	109
6.31	Results of the KPFM measurement on the sample with As-implanted pad and nanowires.	110
6.32	Results of the KPFM measurements on B-implanted and As-implanted horizontal nanowires with focus on the doping profile along the nanowire width.	111

6.33	Results of the KPFM measurement on the sample with B-implanted pad and unimplanted nanowires.	113
6.34	Results of the KPFM measurement on the sample with As-implanted pad and unimplanted nanowires.	114
6.35	Results of the KPFM measurements on B-implanted and As-implanted Si pad but unimplanted horizontal nanowires with focus on the doping profile along the nanowire width.	116
6.36	Results of the KPFM measurement on a sample with As-implanted pad and unimplanted nanowires with focus on the NW side walls. . .	118
6.37	Results of the zoom-in scan on the unimplanted nanowire at the position marked in Fig. 6.36.	119
6.38	Zoom-in image of the 2nd harmonic signal from the position marked as blue square in Fig. 6.37(c).	120

List of Tables

3.1	Doping type, dopant concentration, species, ion dose, and implantation energy of the doped regions in the SCM test samples supplied from Veeco Instruments (since 2010 Bruker Corp.). Data taken from Ref. [107].	18
3.2	Implantation parameters for the preparation of B-doped and As-doped nanowire arrays, and respective dopant concentration and implantation depth after annealing obtained from Athena simulations.	24
5.1	KPFM bias and CPD model values of measurements across Si <i>pn</i> junctions as reported in literature.	45
5.2	Conduction band edge density of states, valence band edge density of states, and bandgap energy in Si at 300 K. Values taken from Ref. [106].	47
5.3	Acceptor binding energy and donor binding energy of the investigated dopant atoms on substitutional sites in Si. Values taken from Ref. [106].	47
5.4	Amplitude and phase of the electrical signal of the 1st harmonic in standard and retracted mode probed on the conventional SRAM cell and on the cross-sectionally prepared Si:B epilayer sample in dependence on the operation frequency. Adapted from Ref. [160].	57
6.1	Fitting parameters for the electric field and temperature dependence of the electron drift velocity. Adapted from Ref. [163].	69
6.2	Diffusion time period and diffusion range of charge carriers in the SRAM cell in dependence on the operation frequency.	71
6.3	Diffusion time period and diffusion range of charge carriers in the SRAM cell in dependence on the ac-bias.	73
6.4	Diffusion time period and diffusion range of charge carriers in the DRAM cell in dependence on the operation frequency.	83
6.5	Diffusion time period and diffusion range of charge carriers in the cross-sectionally prepared Si:B epilayer sample in dependence on the operation frequency.	95
6.6	Diffusion time period and diffusion range of charge carriers in the cross-sectionally prepared Si:B epilayer sample in dependence on the ac-bias.	99
6.7	Diffusion time period and diffusion range of charge carriers in the cross-sectionally prepared Si:P epilayer sample in dependence on the operation frequency.	105
6.8	Diffusion time period and diffusion range of charge carriers in the cross-sectionally prepared Si:P epilayer sample in dependence on the ac-bias.	107

References

- [1] W. B. Shockley. *Circuit element utilizing semiconductor material*. US patent 2.569.347 (1948).
- [2] V. Sverdlov, E. Ungersboeck, H. Kosina, and S. Selberherr. Current transport models for nanoscale semiconductor devices. *Mat. Sci. Engin. R*, **58**:228–270 (2008).
- [3] Z. Ren, S. Hegde, B. Doris, P. Oldiges, T. Kanarsky, O. Dokumaci, R. Roy, M. Jeong, E. C. Jones, and H.-S. P. Wong. An experimental study on transport issues and electrostatics of ultrathin body SOI pMOSFETs. *IEEE Electron Device Letters*, **23**:609–611 (2002).
- [4] W.-K. Yeh, W.-H. Wang, Y.-K. Fang, M.-C. Chen, and F.-L. Yang. Hot-carrier-induced degradation for partially depleted SOI 0.25–0.1 μm CMOSFET with 2-nm thin gate oxide. *IEEE Transactions on Electron Devices*, **49**:2157–2162 (2002).
- [5] H. Wakabayashi, T. Ezaki, S. Sakamoto, H. Kawaura, N. Ikarashi, N. Ikezawa, M. Narihiro, Y. Ochiai, T. Ikezawa, K. Takeuchi, T. Yamamoto, M. Hane, and T. Mogami. Characteristics and modeling of sub-10-nm planar bulk CMOS devices fabricated by lateral source/drain junction control. *IEEE Transactions on Electron Devices*, **53**:1961–1970 (2006).
- [6] S. C. Rustagi, N. Singh, Y. F. Lim, G. Zhang, S. Wang, G. Q. Lo, N. Balasubramanian, and D.-L. Kwong. Low-temperature transport characteristics and quantum-confinement effects in gate-all-around Si-nanowire n-MOSFET. *IEEE Electron Device Letters*, **28**:909–912 (2007).
- [7] A. Pecchia, L. Salamandra, L. Latessa, B. Aradi, T. Frauenheim, and A. Di Carlo. Atomistic modeling of gate-all-around Si-nanowire field-effect transistors. *IEEE Transaction on Electron Devices*, **54**:3159–3167 (2007).
- [8] Z. Kang, L. Zhang, R. Wang, and R. Huang. Investigations on the physical limitation and electrostatic improvement of a gate-all-around silicon nanowire transistor with Schottky barrier source/drain. *Semicond. Sci. Technol.*, **24**:105001 (2009).
- [9] K. Rogdakis, S. Poli, E. Bano, K. Zekentes, and M. G. Pala. Phonon- and surface-roughness-limited mobility of gate-all-around 3C-SiC and Si nanowire FETs. *Nanotechnology*, **20**:295202 (2009).
- [10] J.-T. Sheu, P.-C. Huang, T.-S. Sheu, C.-C. Chen, and L.-A. Chen. Characteristics of gate-all-around twin poly-Si nanowire thin-film transistors. *IEEE Electron Device Letters*, **30**:139–141 (2009).

-
- [11] K.D. Buddharaju, N. Singh, S. C. Rustagi, S. H. G. Teo, G. Q. Lo, N. Balasubramanian, and D. L. Kwong. Si-nanowire CMOS inverter logic fabricated using gate-all-around (GAA) devices and top-down approach. *Solid-State Electronics*, **52**:1312–1317 (2008).
- [12] J. Fu, Y. Jiang, N. Singh, C. X. Zhu, G. Q. Lo, and D. L. Kwong. Polycrystalline Si nanowire SONOS nonvolatile memory cell fabricated on a gate-all-around (GAA) channel architecture. *IEEE Electron Device Letters*, **30**:246–249 (2009).
- [13] S. Sato, H. Kamimura, H. Arai, K. Kakushima, P. Ahmet, K. Ohmori, K. Yamada, and H. Iwai. Electrical characterization of Si nanowire field-effect transistors with semi gate-around structure suitable for integration. *Solid-State Electronics*, **54**:925–928 (2010).
- [14] H. Yoshioka, N. Morioka, J. Suda, and T. Kimoto. Mobility oscillation by one-dimensional quantum confinement in Si-nanowire metal-oxide-semiconductor field effect transistors. *J. Appl. Phys.*, **106**:034312 (2009).
- [15] X.-W. Jiang, H.-X. Deng, S.-S. Li, J.-W. Luo, and L.-W. Wang. Quantum mechanical simulation of nanosized metal-oxide-semiconductor field-effect transistor using empirical pseudopotentials: A comparison for charge density occupation methods. *J. Appl. Phys.*, **106**:084510 (2009).
- [16] Z. Ren. *Nanoscale MOSFETs: Physics, simulation and design*. PhD thesis, Purdue University, West Lafayette, IN, USA, (2001).
- [17] C. C. Williams. Two-dimensional dopant profiling by scanning capacitance microscopy. *Annu. Rev. Mater. Sci.*, **29**:471–504 (1999).
- [18] F. Giannazzo, D. Goghero, V. Raineri, S. Mirabella, and F. Priolo. Scanning capacitance microscopy on ultranarrow doping profiles in Si. *Appl. Phys. Lett.*, **83**:2659–2661 (2003).
- [19] F. Giannazzo, V. Raineri, A. La Magna, S. Mirabella, G. Impellizzeri, A. M. Piro, F. Priolo, E. Napolitani, and S. F. Liotta. Carrier distribution in quantum nanostructures by scanning capacitance microscopy. *J. Appl. Phys.*, **97**:014302 (2005).
- [20] L. Zhang, K. Ohuchi, K. Adachi, K. Ishimaru, M. Takayanagi, and A. Nishiyama. High-resolution characterization of ultrashallow junctions by measuring in vacuum with scanning spreading resistance microscopy. *Appl. Phys. Lett.*, **90**:192103 (2007).
- [21] L. Zhang, H. Tanimoto, K. Adachi, and A. Nishiyama. 1-nm spatial resolution in carrier profiling of ultrashallow junctions by scanning spreading resistance microscopy. *IEEE Electron Device Letters*, **29**:799–801 (2008).

- [22] P. De Wolf, W. Vandervorst, H. Smith, and N. Khalil. Comparison of two-dimensional carrier profiles in metal-oxide-semiconductor field-effect transistor structures obtained with scanning spreading resistance microscopy and inverse modeling. *J. Vac. Sci. Technol. B*, **18**:540–544 (2000).
- [23] K. Smaali, M. Troyon, A. El Hdiy, M. Molinari, G. Saint-Girons, and G. Patriarche. Imaging the electric properties of InAs/InP(001) quantum dots capped with a thin InP layer by conductive atomic force microscopy: Evidence of memory effect. *Appl. Phys. Lett.*, **89**:112115 (2006).
- [24] M. Porti, M. Avidano, M. Nafria, X. Aymerich, J. Carreras, and B. Garrido. Conduction mechanism and charge storage in Si-nanocrystals metal-oxide-semiconductor memory devices studied with conducting atomic force microscopy. *J. Appl. Phys.*, **98**:056101 (2005).
- [25] M. Porti, M. Avidano, M. Nafria, X. Aymerich, J. Carreras, O. Jambois, and B. Garrido. Nanoscale electrical characterization of Si-nc based memory metal-oxide-semiconductor devices. *J. Appl. Phys.*, **101**:064509 (2007).
- [26] J. R. Matey and J. Blanc. Scanning capacitance microscopy. *J. Appl. Phys.*, **57**:1437–1444 (1985).
- [27] W. Brezna, M. Schramboeck, A. Lugstein, S. Harasek, H. Enichlmair, E. Bertagnolli, E. Gornik, and J. Smoliner. Quantitative scanning capacitance spectroscopy. *Appl. Phys. Lett.*, **83**:4253–4255 (2003).
- [28] J. J. Kopanski, J. F. Marchiando, and J. R. Lowney. Scanning capacitance microscopy applied to two-dimensional dopant profiling of semiconductors. *Mat. Sci. Engin. B*, **44**:46–51 (1997).
- [29] W. Vandervorst, T. Clarysse, P. De Wolf, L. Hellemans, J. Snauwaert, V. Privitera, and V. Raineri. On the determination of two-dimensional carrier distributions. *Nuclear Instruments and Methods in Physics Research B*, **96**:123–132 (1995).
- [30] R. G. Mazur and D. H. Dickey. A spreading resistance technique for resistivity measurements on silicon. *Journal of the Electrochemical Society*, **113**:255–259 (1966).
- [31] P. De Wolf. *Two-dimensional carrier profiling of semiconductor structures with nanometer resolution*. PhD thesis, Katholieke Universiteit Leuven, Belgium, (1998).
- [32] G. Benstetter, R. Biberger, and D. Liu. A review of advanced scanning probe microscope analysis of functional films and semiconductor devices. *Thin Solid Films*, **517**:5100–5105 (2009).
- [33] W. Han. *Introduction to scanning microwave microscopy mode*. Agilent Technologies, Application note 5989-8881EN Rev A, (2008).

- [34] J. Smoliner, H. P. Huber, M. Hochleitner, M. Moertelmaier, and F. Kienberger. Scanning microwave microscopy/spectroscopy on metal-oxide-semiconductor systems. *J. Appl. Phys.*, **108**:064315 (2010).
- [35] William Thomson Lord Kelvin. Contact electricity of metals. *The London, Ediburgh, and Dublin Philosophical Magazin and Journal of Science*, **46**:82–120 (1898).
- [36] M. Nonnenmacher, M. P. O’Boyle, and H. K. Wickramasinghe. Kelvin probe force microscopy. *Appl. Phys. Lett.*, **58**:2921–2923 (1991).
- [37] M. Nonnenmacher, M. O’Boyle, and H. K. Wickramasinghe. Surface investigations with a Kelvin probe force microscope. *Ultramicroscopy*, **42-44**:268–273 (1992).
- [38] C. Loppacher, U. Zerweck, and L. M. Eng. Kelvin probe force microscopy of alkali chloride thin films on Au(111). *Nanotechnology*, **15**:S9–S13 (2004).
- [39] U. Zerweck, C. Loppacher, T. Otto, S. Grafström, and L. M. Eng. Accuracy and resolution limits of Kelvin probe force microscopy. *Phys. Rev. B*, **71**:125424 (2005).
- [40] T. Glatzel, D. F. Marrón, T. Schedel-Niedrig, S. Sadewasser, and M. C. Lux-Steiner. CuGaSe₂ solar cell cross section studied by Kelvin probe force microscopy in ultrahigh vacuum. *Appl. Phys. Lett.*, **81**:2017–2019 (2002).
- [41] Y. Rosenwaks, R. Shikler, T. Glatzel, and S. Sadewasser. Kelvin probe force microscopy of semiconductor surface defects. *Phys. Rev. B*, **70**:085320 (2004).
- [42] T. Glatzel, S. Sadewasser, R. Shikler, Y. Rosenwaks, and M. C. Lux-Steiner. Kelvin probe microscopy on III-V semiconductors: the effect of surface defects on the local work function. *Mat. Sci. Engin. B*, **102**:138–142 (2003).
- [43] R. Shikler, F. Fried, T. Meoded, and Y. Rosenwaks. Measuring minority-carrier diffusion length using a Kelvin probe force microscope. *Phys. Rev. B*, **61**:11041–11046 (2000).
- [44] N. Duhayon, P. Eyben, M. Fouchier, T. Clarysse, W. Vandervorst, D. Alvarez, S. Schoemann, M. Ciappa, M. Stangoni, W. Fichtner, P. Formanek, M. Kittler, V. Raineri, F. Giannazzo, D. Goghero, Y. Rosenwaks, R. Shikler, S. Saraf, S. Sadewasser, N. Barreau, T. Glatzel, M. Verheijen, S. A. M. Mentink, M. von Sprekelsen, T. Maltezopoulos, R. Wiesendanger, and L. Hellemanns. Assessing the performance of two-dimensional dopant profiling techniques. *J. Vac. Sci. Technol. B*, **22**:385–393 (2004).
- [45] A. K. Henning, T. Hochwitz, J. Slinkman, J. Never, S. Hoffmann, P. Kaszuba, and C. Daghljan. Two-dimensional surface dopant profiling in silicon using scanning Kelvin probe microscopy. *J. Appl. Phys.*, **77**:1888–1896 (1995).

- [46] M. Ligowski, D. Moraru, M. Anwar, T. Mizuno, R. Jablonski, and M. Tabe. Observation of individual dopants in a thin silicon layer by low temperature Kelvin probe force microscope. *Appl. Phys. Lett.*, **93**:142101 (2008).
- [47] B.-Y. Tsui, C.-M. Hsieh, P.-C. Su, S.-D. Tzeng, and S. Gwo. Two-dimensional carrier profiling by Kelvin probe force microscopy. *Jap. J. Appl. Phys.*, **47**:4448–4453 (2008).
- [48] M. Tanimoto and O. Vatel. Kelvin probe force microscopy for characterization of semiconductor devices and processes. *J. Vac. Sci. Technol. B*, **14**:1547–1551 (1996).
- [49] A. Doukkali, S. Ledain, C. Guasch, and J. Bonnet. Surface potential mapping of biased pn junction with Kelvin probe force microscopy: application to cross-section devices. *Appl. Surf. Sci.*, **235**:507–512 (2004).
- [50] G. H. Buh, H. J. Chung, C. K. Kim, J. H. Yi, I. T. Yoon, and Y. Kuk. Imaging of a silicon pn junction under applied bias with scanning capacitance microscopy and Kelvin probe force microscopy. *Appl. Phys. Lett.*, **77**:106–108 (2000).
- [51] H. O. Jacobs, P. Leuchtmann, O. J. Homan, and A. Stemmer. Resolution and contrast in Kelvin probe force microscopy. *J. Appl. Phys.*, **84**:1168–1173 (1998).
- [52] A. Liscio, V. Palermo, K. Müllen, and P. Samori. Tip-sample interactions in Kelvin probe force microscopy: Quantitative measurement of the local surface potential. *J. Phys. Chem. C*, **112**:17368–17377 (2008).
- [53] F. Müller and A.-D. Müller. Frequency dependent Kelvin probe force microscopy on silicon surfaces. *J. Vac. Sci. Technol. B*, **27**:969–974 (2009).
- [54] F. Bocquet, L. Nony, C. Loppacher, and T. Glatzel. Analytical approach to the local contact potential difference on (001) ionic surfaces: Implications for Kelvin probe force microscopy. *Phys. Rev. B*, **78**:035410 (2008).
- [55] V. Palermo, S. Morelli, M. Palma, C. Simpson, F. Nolde, A. Herrmann, K. Müllen, and P. Samori. Nanoscale structural and electronic properties of ultrathin blends of two polyaromatic molecules: A Kelvin probe force microscopy investigation. *ChemPhysChem*, **7**:847–853 (2006).
- [56] A. K. Sinensky and A. M. Belcher. Label-free and high-resolution protein/DNA nanoarray analysis using Kelvin probe force microscopy. *Nature Nanotechnology*, **2**:653–659 (2007).
- [57] P. Gao and Y. Cai. Label-free detection of the aptamer binding on protein patterns using Kelvin probe force microscopy (KPFM). *Anal. Bioanal. Chem.*, **394**:207–214 (2009).

- [58] E. Mikamo-Satoh, F. Yamada, A. Takagi, T. Matsumoto, and T. Kawai. Electrostatic force microscopy: imaging DNA and protein polarizations one by one. *Nanotechnology*, **20**:145102 (2009).
- [59] P. De Wolf, T. Clarysse, W. Vandervorst, J. Snauwaert, and L. Hellemans. One- and two-dimensional carrier profiling in semiconductors by nanospreading resistance profiling. *J. Vac. Sci. Technol. B*, **14**:380–385 (1996).
- [60] P. Eyben, M. Xu, N. Duhayon, T. Clarysse, S. Callewaert, and W. Vandervorst. Scanning spreading resistance microscopy and spectroscopy for routine and quantitative two-dimensional carrier profiling. *J. Vac. Sci. Technol. B*, **20**:471–478 (2002).
- [61] M. V. Stangoni. *Scanning probe techniques for dopant profile characterization*. PhD thesis, Swiss Federal Institute Of Technology Zürich, Switzerland, (2005).
- [62] T. Hantschel, P. Niedermann, T. Trenkler, and W. Vandervorst. Highly conductive diamond probes for scanning spreading resistance microscopy. *Appl. Phys. Lett.*, **76**:1603–1605 (2000).
- [63] P. De Wolf, T. Clarysse, W. Vandervorst, and L. Hellemans. Low weight spreading resistance profiling of ultrashallow dopant profiles. *J. Vac. Sci. Technol. B*, **16**:401–405 (1998).
- [64] P. Eyben, T. Janssens, and W. Vandervorst. Scanning spreading resistance microscopy (SSRM) 2D carrier profiling for ultra-shallow junction characterization in deep-submicron technologies. *Mat. Sci. Engin. B*, **124-125**:45–53 (2005).
- [65] X. Ou, P. D. Kanungo, R. Kögler, P. Werner, U. Gösele, W. Skorupa, and X. Wang. Carrier profiling of individual Si nanowires by scanning spreading resistance microscopy. *Nano Letters*, **10**:171–175 (2010).
- [66] *Electrical characterization with scanning probe microscopes*. Bruker Nano Surfaces, Application note AN79, Rev A0, (2004).
- [67] *A practical guide to SPM - Scanning probe microscopy*. Veeco Instruments Inc., (2005).
- [68] A. Olbrich, B. Ebersberger, and C. Boit. Nanoscale electrical characterization of thin oxides with conducting atomic force microscopy. *36th Annual IEEE International Reliability Physics Symposium, Reno, Nevada*, pages 163–168 (1998).
- [69] W. Frammelsberger, G. Benstetter, T. Schweinboeck, R. Stamp, and J. Kiely. Advanced analysis of thin and ultrathin SiO₂ films and SiO₂/Si interfaces with combined atomic force microscopy methods. *Proceedings of 29th International Symposium for Testing and Failure Analysis, 2-6 November, Santa Clara, California*, pages 406–412 (2003).

- [70] M. Porti, M. Nafria, X. Aymerich, A. Olbrich, and B. Ebersberger. Nanometer-scale electrical characterization of stressed ultrathin SiO₂ films using conducting atomic force microscopy. *Appl. Phys. Lett.*, **78**:4181–4183 (2001).
- [71] P. Fiorenza, R. Lo Nigro, V. Raineri, S. Lombardo, R. G. Toro, G. Malandrino, and I. L. Fragalà. Breakdown kinetics of Pr₂O₃ films by conductive-atomic force microscopy. *Appl. Phys. Lett.*, **87**:231913 (2005).
- [72] M. Lanza, M. Porti, M. Nafria, G. Benstetter, W. Frammelsberger, H. Ranzinger, E. Lodermeier, and G. Jaschke. Influence of the manufacturing process on the electrical properties of thin (<4nm) Hafnium based high-k stacks observed with CAFM. *Microelectronics Reliability*, **47**:1424–1428 (2007).
- [73] S. Gsell, M. Schreck, G. Benstetter, E. Lodermeier, and B. Stritzker. Combined AFM-SEM study of the diamond nucleation layer on Ir(001). *Diamond & Related Materials*, **16**:665–670 (2007).
- [74] D. Liu, G. Benstetter, and W. Frammelsberger. The effect of the surface layer of tetrahedral amorphous carbon films on their tribological and electron emission properties investigated by atomic force microscopy. *Appl. Phys. Lett.*, **82**:3898–3900 (2003).
- [75] A. A. Pomarico, D. Huang, J. Dickinson, A. A. Baski, R. Cingolani, H. Morkoc, and R. Molnar. Current mapping of GaN films by conductive atomic force microscopy. *Appl. Phys. Lett.*, **82**:1890–1892 (2003).
- [76] L. S. C. Pingree, M. C. Hersam, M. M. Kern, B. J. Scott, and T. J. Marks. Spatially-resolved electroluminescence of operating organic light-emitting diodes using conductive atomic force microscopy. *Appl. Phys. Lett.*, **85**:344–346 (2004).
- [77] H.-N. Lin, H.-L. Lin, S.-S. Wang, L.-S. Yu, G.-Y. Perng, S.-A. Chen, and S.-H. Chen. Nanoscale charge transport in an electroluminescent polymer investigated by conducting atomic force microscopy. *Appl. Phys. Lett.*, **81**:2572–2574 (2002).
- [78] Z. G. Sun, H. Kuramochi, H. Akinaga, H. H. Yu, and E. D. Gu. Conductive atomic force microscopy study of silica nanotrench structure. *Appl. Phys. Lett.*, **90**:042106 (2007).
- [79] S. Banerjee, M. A. Salem, and S. Oda. Conducting-tip atomic force microscopy for injection and probing of localized charges in silicon nanocrystals. *Appl. Phys. Lett.*, **83**:3788–3790 (2003).
- [80] M. Yamauchi, T. Inoshita, and H. Sakaki. Electronic structure of nanometer-scale quantum dots created by a conductive atomic force microscope tip in resonant tunneling structures. *Appl. Phys. Lett.*, **74**:1582–1584 (1999).

- [81] H. R. Moutinho, R. G. Dhere, C.-S. Jiang, M. M. Al-Jassim, and L. L. Kazmerski. Electrical properties of CdTe/CdS solar cells investigated with conductive atomic force microscopy. *Thin Solid Films*, **514**:150–155 (2006).
- [82] G. Benstetter, P. Breitschopf, W. Frammelsberger, H. Ranzinger, P. Reislhuber, and T. Schweinboeck. AFM-based scanning capacitance techniques for deep sub-micron semiconductor failure analysis. *Microelectronics Reliability*, **44**:1615–1619 (2004).
- [83] P. De Wolf, R. Stephenson, T. Trenkler, T. Clarysse, T. Hantschel, and W. Vandervorst. Status and review of two-dimensional carrier and dopant profiling using scanning probe microscopy. *J. Vac. Sci. Technol. B*, **18**:361–368 (2000).
- [84] P. De Wolf, E. Brazel, and A. Erickson. Electrical characterization of semiconductor materials and devices using scanning probe microscopy. *Materials Science in Semiconductor Processing*, **4**:71–76 (2001).
- [85] J. J. Kopanski, J. F. Marchiando, and J. R. Lowney. Scanning capacitance microscopy measurements and modeling: Progress towards dopant profiling of silicon. *J. Vac. Sci. Technol. B*, **14**:242–247 (1996).
- [86] *Application modules: Dimension and MultiMode Manual*. Veeco Instruments Inc., (2003).
- [87] S. M. Sze and Kwok K. Ng. *Physics of semiconductor devices, 3rd Edition*. John Wiley & Sons, Inc., Hoboken, New Jersey, (2007).
- [88] J. D. Kiely and D. A. Bonnell. Quantification of topographic structure by scanning probe microscopy. *J. Vac. Sci. Technol. B*, **15**:1483–1493 (1997).
- [89] F. Kienberger, V. P. Pastushenko, G. Kada, T. Puntheeranurak, L. Chtcheglova, C. Riethmueller, C. Rankl, A. Ebner, and P. Hinterdorfer. Improving the contrast of topographical AFM images by a simple averaging filter. *Ultramicroscopy*, **106**:822–828 (2006).
- [90] A. Méndez-Vilas, M. L. González-Martín, and M. J. Nuevo. Optical interference artifacts in contact atomic force microscopy images. *Ultramicroscopy*, **92**:243–250 (2002).
- [91] C. Baumgart, S. Streit, M. Helm, and H. Schmidt. Quantitative electrical nanometrology - Kelvin probe force microscopy measurements on semiconductors. *Imaging&Microscopy GIT-Verlag (www.imaging-git.com)*, (2009).
- [92] H. Edwards, R. McGlothlin, R. San Martin, E. U, M. Gribelyuk, R. Mahaffy, C. K. Shih, R. S. List, and V. A. Ukraintsev. Scanning capacitance spectroscopy: An analytical technique for pn-junction delineation in Si devices. *Appl. Phys. Lett.*, **72**:698–700 (1998).

- [93] J. Isenbart, A. Born, and R. Wiesendanger. The physical principles of scanning capacitance spectroscopy. *Appl. Phys. A*, **72**:S243–S251 (2001).
- [94] W. Brezna, S. Harasek, A. Lugstein, T. Leitner, H. Hoffmann, E. Bertagnolli, and J. Smoliner. Mapping of local oxide properties by quantitative scanning capacitance spectroscopy. *J. Appl. Phys.*, **97**:093701 (2005).
- [95] W. Brezna, T. Roch, G. Strasser, and J. Smoliner. Quantitative scanning capacitance spectroscopy on GaAs and InAs quantum dots. *Semicond. Sci. Technol.*, **20**:903–907 (2005).
- [96] J. J. Kopanski and S. Mayo. Intermittent-contact scanning capacitance microscope for lithographic overlay measurement. *Appl. Phys. Lett.*, **72**:2469–2471 (1998).
- [97] R. Biberger, G. Benstetter, T. Schweinboeck, P. Breitschopf, and H. Goebel. Intermittent-contact scanning capacitance microscopy versus contact mode SCM applied to 2D dopant profiling. *Microelectronics Reliability*, **48**:1339–1342 (2008).
- [98] *Scanning microwave microscopy (SMM) mode - highly sensitive imaging mode for complex, calibrated electrical and spatial measurements*. Agilent Technologies, Data Sheet 5989-8817EN, (2008).
- [99] R. Debroucke, J.-F. Larchanche, D. Theron, D. Ducatteau, H. Tanbakuchi, and C. Gaquiere. Sub-femto-Farad MOS varactor characterization tools. *Proceedings of 40th European Microwave Conference, 28-30 September 2010, Paris, France*, pages 783–786 (2010).
- [100] H. Tanbakuchi. The challenges of the nanoscale material and device characterization. *Proceedings of International Microwave Symposium, 23-28 May 2010, Anaheim, California, USA*, (2010).
- [101] U. Zerweck-Trogisch. *Auflösungsvermögen und Genauigkeit der Kelvinsonden-Rasterkraftmikroskopie und deren Anwendung an molekularen Systemen*. PhD thesis, Technical University Dresden, Germany, (2007).
- [102] I. Karpov, R. W. Belcher, and J. H. Linn. Electric force microscopy as a probe of active and passive elements of integrated circuits. *Appl. Surf. Sci.*, **125**:332–338 (1998).
- [103] C. Sommerhalter, T. W. Matthes, T. Glatzel, A. Jäger-Waldau, and M. C. Lux-Steiner. High-sensitivity quantitative Kelvin probe microscopy by noncontact ultra-high-vacuum atomic force microscopy. *Appl. Phys. Lett.*, **75**:286–288 (1999).
- [104] W. Bergbauer, T. Lutz, W. Frammelsberger, and G. Benstetter. Kelvin probe force microscopy - An appropriate tool for the electrical characterisation of LED heterostructures. *Microelectronics Reliability*, **46**:1736–1740 (2006).

- [105] S. M. Sze. *Semiconductor devices - Physics and technology, 2nd Edition*. John Wiley & Sons, Inc., (2002).
- [106] M. Grundmann. *The physics of semiconductors - An introduction including devices and nanophysics*. Springer-Verlag Berlin Heidelberg, (2006).
- [107] The SCM test sample. *Bruker Nano Surfaces, Data sheet for SCM test sample*.
- [108] M. W. Nelson, P. G. Schroeder, R. Schlaf, and B. A. Parkinson. Two-dimensional dopant profiling of an integrated circuit using bias-applied phase-imaging tapping mode atomic force microscopy. *Electrochemical and Solid-State Letters*, **2**:475–477 (1999).
- [109] Y. Taur. MOSFET channel length: Extraction and interpretation. *IEEE Transaction on Electron Devices*, **47**:160–170 (2000).
- [110] Z.-H. Liu, C. Hu, J.-H. Huang, T.-Y. Chan, M.-C. Jeng, P. K. Ko, and Y. C. Cheng. Threshold voltage model for deep-submicrometer MOSFETs. *IEEE Transaction on Electron Devices*, **40**:86–95 (1993).
- [111] J. A. Sharp, R. M. Gwilliam, B. J. Sealy, C. Jeynes, J. J. Hamilton, and K. J. Kirkby. Comparison of elemental boron and boron halide implants into silicon. *Nuclear Instruments and Methods in Physics Research B*, **237**:93–97 (2005).
- [112] A. Dusch, J. Marcon, K. Masmoudi, F. Olivié, M. Benzohra, K. Ketata, and M. Ketata. Modeling of the transient enhanced diffusion of boron implanted into preamorphized silicon: the case of BF_2^+ implantation. *Mat. Sci. Engin. B*, **80**:65–67 (2001).
- [113] S. Habicht. *Strained and unstrained Si-nanowire array MOSFETs: Fabrication and physical analysis*. PhD thesis, RWTH Aachen University, Germany, (2011).
- [114] M. Bescond, N. Cavassilas, and M. Lannoo. Effective-mass approach for n-type semiconductor nanowire MOSFETs arbitrarily oriented. *Nanotechnology*, **18**:255201 (2007).
- [115] *Athena - User's Manual*. Silvaco Inc., (2011).
- [116] F. Müller and A.-D. Müller. *Anfatec Level-AFM Manual*. Anfatec Instruments AG, (2008).
- [117] *Scanning probe microscopy and digital signal analysis*. Anfatec Instruments AG, Anfatec measurement science catalogue version 1b (2008).
- [118] F. Müller and A.-D. Müller. *eLockIn 204 Manual*. Anfatec Instruments AG, (2007).
- [119] Ed. A. Anders. *Handbook of plasma immersion ion implantation and deposition*. John Wiley & Sons, Inc., (2000).

- [120] Secondary ion mass spectrometry. *Fraunhofer-Center Nanoelectronic Technologies Dresden, Germany, Product information.*
- [121] J. F. Ziegler, J. P. Biersack, and U. Littmark. *The stopping and range of ions in matter.* Pergamon Press, (1985).
- [122] J. P. Biersack and L. G. Haggmark. A Monte Carlo computer program for the transport of energetic ions in amorphous targets. *Nucl. Instr. and Meth.*, **174**:257–269 (1980).
- [123] K. Hübner. Structure and properties of the Si-SiO₂ interregion. *Lecture Notes in Physics*, **175**:221–229 (1983).
- [124] M. Morita, T. Ohmi, E. Hasegawa, M. Kawakami, and M. Ohwada. Growth of native oxide on a silicon surface. *J. Appl. Phys.*, **68**:1272–1281 (1990).
- [125] X. G. Zhang. *Electrochemistry of silicon and its oxide.* Kluwer Academic / Plenum Publishers, New York, (2001).
- [126] J. Dabrowski and H.-J. Müssig. *Silicon surfaces and formation of interfaces.* World Scientific Publishing Co. Pte. Ltd., (2000).
- [127] S. Metz. *Analytik von Kontaminationen auf Siliciumoberflächen - Möglichkeiten und Grenzen des VPD-Verfahrens.* PhD thesis, Johann Wolfgang Goethe-Universität, Frankfurt am Main, Germany, (2004).
- [128] T. Takahagi, H. Sakaue, and S. Shingubara. Adsorbed water on a silicon wafer surface exposed to atmosphere. *Jap. J. Appl. Phys.*, **40**:6198–6201 (2001).
- [129] M. Grundner and H. Jacob. Investigations on hydrophilic and hydrophobic silicon (100) wafer surfaces by X-ray photoelectron and high-resolution electron energy loss-spectroscopy. *Appl. Phys. A*, **39**:73–82 (1986).
- [130] W. Mönch. *Semiconductor surfaces and interfaces, 3rd Edition.* Springer-Verlag Berlin Heidelberg, (2010).
- [131] S. Saraf, M. Molotskii, and Y. Rosenwaks. Local measurement of surface states energy distribution in semiconductors using Kelvin probe force microscope. *Appl. Phys. Lett.*, **86**:172104 (2005).
- [132] Eds. D. A. King and D. P. Woodruff. *The chemical physics of solid surfaces and heterogeneous catalysis, Vol. 3, Chemisorption Systems, Part B.* Elsevier Science Publishers B. V., (1984).
- [133] H. Angermann, T. Dittrich, and H. Flietner. Investigation of native-oxide growth on HF-treated Si(III) surfaces by measuring the surface-state distribution. *Appl. Phys. A*, **59**:193–197 (1994).

- [134] Eds. C. G. Scott and C. E. Reed. *Surface physics of phosphors and semiconductors*. Academic Press Inc. (London) LTD., (1975).
- [135] L. M. Terman. An investigation of surface states at a silicon/silicon oxide interface employing metal-oxide-silicon diodes. *Solid-State Electronics*, **5**:285–299 (1962).
- [136] A. Many, Y. Goldstein, and N. B. Grover. *Semiconductor surfaces*. North-Holland Publishing Company - Amsterdam, (1965).
- [137] E. H. Nicollian. Electrical characterization of defects created in the Si-SiO₂ system by ionizing radiation. *J. Electron. Mat.*, **21**:721–729 (1992).
- [138] Y. D. Hong and Y. T. Yeow. Modeling the effects of interface traps on scanning capacitance microscopy dC/dV measurement. *Proceedings of Conference on Optoelectronic and Microelectronic Materials and Devices COMMAD 2004, 8-10 December, Brisbane, Australia*, (2005).
- [139] K. F. Brennan. *Introduction to semiconductor devices - For computing and telecommunications applications*. Cambridge University Press, New York, (2010).
- [140] H. F. Wolf. *Silicon semiconductor data*. Pergamon Press, (1969).
- [141] R. B. Darling. Defect-state occupation, Fermi-level pinning, and illumination effects on free semiconductor surfaces. *Phys. Rev. B*, **43**:4071–4083 (1991).
- [142] W. J. Cody and H. C. Thatcher Jr. Rational Chebyshev approximations for Fermi-Dirac integrals of orders $-\frac{1}{2}$, $\frac{1}{2}$ and $\frac{3}{2}$. *Math. Comput.*, **21**:30–40 (1966).
- [143] M. Jenke. *Micro- and nano-electrostatic force fields: Generation, 3-dimensional measurement using a novel AFM method and applications*. PhD thesis, École Polytechnique Fédérale de Lausanne, Switzerland, (2008).
- [144] S. Lányi. Effect of adsorbed water on the resolution of scanning capacitance microscopes. *Surf. Interface Anal.*, **27**:348–353 (1999).
- [145] M. W. Nelson, P. G. Schroeder, R. Schlaf, B. A. Parkinson, C. W. Almgren, and A. N. Erickson. Spatially resolved dopant profiling of patterned Si wafers by bias-applied phase-imaging tapping-mode atomic force microscopy. *Appl. Phys. Lett.*, **74**:1421–1423 (1999).
- [146] R. García and R. Pérez. Dynamic atomic force microscopy methods. *Surface Science Reports*, **47**:197–301 (2002).
- [147] Y. Seo and W. Jhe. Atomic force microscopy and spectroscopy. *Rep. Prog. Phys.*, **71**:016101 (2008).

- [148] T. R. Albrecht, S. Akamine, T. E. Carver, and C. F. Quate. Microfabrication of cantilever styli for the atomic force microscope. *J. Vac. Sci. Technol. A*, **8**:3386–3396 (1990).
- [149] O. Douherét, S. Bonsels, and S. Anand. Determination of spatial resolution in atomic-force-microscopy-based electrical characterization techniques using quantum well structures. *J. Vac. Sci. Technol. B*, **23**:61–65 (2005).
- [150] H. O. Jacobs, H. F. Knapp, S. Müller, and A. Stemmer. Surface potential mapping: A qualitative material contrast in SPM. *Ultramicroscopy*, **69**:39–49 (1997).
- [151] M. Kitazawa and A. Toda. Fabrication of sharp tetrahedral probes with platinum coating. *Jap. J. Appl. Phys.*, **41**:4928–4931 (2002).
- [152] M. Komiyama, S. Ohkubo, K. Tazawa, K. Tsujimichi, A. Hirotani, M. Kubo, and A. Miyamoto. Effects of atomic arrangement at tip apex and tip-sample distance on atomic force microscopy images: A simulation study. *Jap. J. Appl. Phys.*, **35**:2318–2325 (1996).
- [153] E. J. Spadafora, R. Demadrille, B. Ratier, and Grévin. Imaging the carrier photo-generation in nanoscale phase segregated organic heterojunctions by Kelvin probe force microscopy. *Nano Letters*, **10**:3337–3342 (2010).
- [154] S. Ono and T. Takahashi. Lateral averaging effects on surface potential measurements on InAs dots studied by Kelvin probe force microscopy. *Jap. J. Appl. Phys.*, **43**:4639–4642 (2004).
- [155] C. Leendertz, F. Streicher, M. C. Lux-Steiner, and S. Sadewasser. Evaluation of Kelvin probe force microscopy for imaging grain boundaries in chalcopyrite thin films. *Appl. Phys. Lett.*, **89**:113120 (2006).
- [156] T. Glatzel, L. Zimmerli, S. Koch, B. Such, S. Kawai, and E. Meyer. Determination of effective tip geometries in Kelvin probe force microscopy on thin insulating films on metals. *Nanotechnology*, **20**:264016 (2009).
- [157] T. Hochwitz, A. K. Henning, C. Levey, C. Daghljan, and J. Slinkman. Capacitive effects on quantitative dopant profiling with scanned electrostatic force microscopes. *J. Vac. Sci. Technol. B*, **14**:457–462 (1996).
- [158] C. Baumgart, M. Helm, and H. Schmidt. Quantitative dopant profiling in semiconductors: A Kelvin probe force microscopy model. *Phys. Rev. B*, **80**:085305 (2009).
- [159] H. Diesinger, D. Deresmes, J.-P. Nys, and T. Mélin. Kelvin force microscopy at the second cantilever resonance: An out-of-vacuum crosstalk compensation setup. *Ultramicroscopy*, **108**:773–781 (2008).

- [160] C. Baumgart, A.-D. Müller, F. Müller, and H. Schmidt. Kelvin probe force microscopy in the presence of intrinsic local electric fields. *Phys. Stat. Sol. A*, **208**:777–789 (2011).
- [161] M. Lucchesi, G. Privitera, M. Labardi, D. Prevosto, S. Capaccioli, and P. Pingue. Electrostatic force microscopy and potentiometry of realistic nanostructured systems. *J. Appl. Phys.*, **105**:054301 (2009).
- [162] C. Baumgart, S. Zhou, M. Helm, and H. Schmidt. Raster-Kelvinkraft-Mikroskopie zur quantitativen Dotierprofilierung an dotiertem Silizium und Mn-implantiertem Germanium. *Analytik News (www.analytik-news.de)*, (2010).
- [163] C. Jacoboni, C. Canali, G. Ottaviani, and A. A. Quaranta. A Review of some charge transport properties of silicon. *Solid-State Electronics*, **20**:77–89 (1977).
- [164] A. Morales-Acevedo and G. Santana. Surface recombination velocity in silicon substrates determined from light beam induced current measurements. *25th PVSC; May 13-17, Washington, D.C.*, pages 553–556 (1996).
- [165] C. Baumgart, M. Helm, and H. Schmidt. Quantitative Kelvin probe force microscopy. *Mater. Res. Soc. Symp. Proc.*, **1232**:0007–02 (2010).
- [166] B. Kalkofen, M. Lisker, and E. P. Burte. Phosphorus diffusion into silicon after vapour phase surface adsorption of phosphine. *Mat. Sci. Engin. B*, **124-125**:288–292 (2005).
- [167] S. Hofmann. Sputter depth profile analysis of interfaces. *Rep. Prog. Phys.*, **61**:827–888 (1998).
- [168] Y. S. Suh, M. S. Carroll, R. A. Levy, M. A. Sahiner, G. Bisognin, and C. A. King. Modeling of boron and phosphorus implantation into (100) germanium. *IEEE Transactions on Electron Devices*, **52**:91–98 (2005).
- [169] S. Heikman, S. Keller, T. Mates, S. P. DenBaars, and U. K. Mishra. Growth and characteristics of Fe-doped GaN. *Journal of Crystal Growth*, **248**:513–517 (2003).
- [170] Y.-C. C. Liu, N. Rieben, L. Iversen, B. S. Sorensen, J. Park, J. Nygard, and K. L. Martinez. Specific and reversible immobilization of histidine-tagged proteins on functionalized silicon nanowires. *Nanotechnology*, **21**:245105 (2010).
- [171] R. J. Martin-Palma, M. Manso, and V. Torres-Costa. Optical biosensors based on semiconductor nanostructures. *Sensors*, **9**:5149–5172 (2009).

Publications during PhD study

Scientific Publications

1. *C. Baumgart*, A.-D. Müller, F. Müller, and H. Schmidt, Higher harmonic functions of the electrostatic force detected by Kelvin probe force microscopy, *Phys. Rev. B.*, in preparation, (2012).
2. *C. Baumgart*, S. Habicht, S. Feste, M. Helm, and H. Schmidt, Transport of charge carriers in horizontal Si nanowires during Kelvin probe force microscopy measurements, *Nano Letters*, in preparation, (2012).
3. S. Prucnal, S. Facsko, *C. Baumgart*, H. Schmidt, M. O. Liedke, L. Rebohle, A. Shalimov, H. Reuther, A. Kanjilal, A. Mücklich, M. Helm, J. Zuk, and W. Skorupa, n-InAs nanopylramids fully integrated into silicon, *Nano Letters*, **11**:2814-2818 (2011).
4. *C. Baumgart*, A.-D. Müller, F. Müller, and H. Schmidt, Kelvin probe force microscopy in the presence of intrinsic local electric fields, *Phys. Stat. Sol. (a)*, **208**:777-789 (2011), **Editor's Choice + Back cover in Issue April 2011**.
5. T. Naydenova, P. Atanasov, M. Koleva, N. Nedialkov, J. Perriere, D. Defourneau, H. Fukuoka, M. Obara, *C. Baumgart*, S. Zhou and H. Schmidt, Influence of vanadium concentration on the microstructure and magnetic properties of V-doped ZnO thin films, *Thin Solid Films*, **518**:5505-5508 (2010).
6. S. Zhou, D. Bürger, A. Mücklich, *C. Baumgart*, W. Skorupa, C. Timm, P. Oesterlin, M. Helm, and H. Schmidt, Hysteresis in the magnetotransport of manganese-doped germanium: Evidence for carrier-mediated ferromagnetism, *Phys. Rev. B*, **81**:165204 (2010).
7. *C. Baumgart*, S. Zhou, M. Helm, and H. Schmidt, **Invited article**: Raster-Kelvinkraft-Mikroskopie zur quantitativen Dotierprofilierung an dotiertem Silizium und Mn-implantiertem Germanium, *Analytik News* (www.analytik-news.de), (2010).
8. *C. Baumgart*, M. Helm, and H. Schmidt, Quantitative Kelvin probe force microscopy, *Mater. Res. Soc. Symp. Proc.*, **1232**:OO07-02, Materials Research Society (2010).
9. *C. Baumgart*, S. Streit, M. Helm, and H. Schmidt, **Invited article**: Quantitative electrical nanometrology - Kelvin probe force microscopy measurements on semiconductors, *Imaging&Microscopy GIT-Verlag* (www.imaging-git.com), (2009).
10. *C. Baumgart*, and H. Schmidt, Mikroskopische Aufnahmen neu gedeutet - Revolution in der Raster-Kelvin-Mikroskopie?, *GIT Labor-Fachzeitschrift*, **53**:680-681 (2009).
11. *C. Baumgart*, Kelvin probe digs deep, *TRAC Trends In Analytical Chemistry* **28**:VI (2009).

12. *C. Baumgart*, M. Helm, and H. Schmidt, Quantitative dopant profiling in semiconductors: A Kelvin probe force microscopy model, *Phys. Rev. B*, **80**:085305 (2009); Virtual Journal of Nanoscale Science & Technology (www.vjnano.org), August 24 (2009).

Conference Presentations

1. *C. Baumgart*, S. Habicht, S. Feste, M. Helm, and H. Schmidt, Kelvin probe force microscopy imaging on locally doped silicon nanowires, **Poster 18**, Subtherm 2011, Dresden, Germany, October 25-27, (2011), **Poster Award**.
2. *C. Baumgart*, A.-D. Müller, F. Müller, M. Helm, and H. Schmidt, Kelvin probe force microscopy on doped semiconductor nanostructures with local, carrier-depleted space charge regions, **Talk HL 19.8**, DPG Spring Meeting, Dresden, Germany, March 13-18, (2011).
3. *C. Baumgart*, A.-D. Müller, F. Müller, M. Helm, and H. Schmidt, Quantitative Kelvin probe force microscopy imaging on locally doped semiconductors, **Talk We-am-F-C4**, X International Conference on Nanostructured Materials, Rome, Italy, September 13-17, (2010).
4. *C. Baumgart*, A.-D. Müller, F. Müller, M. Helm, and H. Schmidt, Quantitative Kelvin probe force microscopy on semiconductors, **Invited Talk, 2**. Wissenschaftliches Seminar des Dresdner Fraunhofer-Clusters Nanoanalytik, Dresden, Germany, August 5, (2010).
5. *C. Baumgart*, A.-D. Müller, F. Müller, M. Helm, and H. Schmidt, Quantitative Kelvin probe force microscopy on semiconductors under ambient conditions, **Talk Analytics II**, Nanofair, Dresden, Germany, July 6-7, (2010).
6. *C. Baumgart*, Quantitative KPFM Measurements on Silicon Nanowire Structures, **Talk**, Workshop FZD/FZJ: Silicon Nanowire Structures, Dresden, Germany, April 04, (2010).
7. *C. Baumgart*, A.-D. Müller, F. Müller, M. Helm, and H. Schmidt, Quantitative Kelvin probe force microscopy imaging on locally doped Si, **Talk ID95**, Nanocoatings, Dresden, Germany & **Chairwoman** of the Session Characterization 1, March 28-31, (2010).
8. *C. Baumgart*, A.-D. Müller, F. Müller, M. Helm, and H. Schmidt, Quantitative Kelvin probe force microscopy imaging on locally doped Si, **Poster O 60.12**, DPG Spring Meeting, Regensburg, Germany, March 21-26, (2010).
9. *C. Baumgart*, M. Helm, H. Schmidt, Frequency dependent Kelvin probe force microscopy on locally doped Si, **Poster OO 7.2**, MRS Fall Meeting, Boston MA, USA, November 30th - December 4th, (2009).

-
10. *C. Baumgart*, S. Jaensch, M. Helm, and H. Schmidt, Kelvin probe force and scanning capacitance microscopy on MOS structures, **Poster HL 48.88**, DPG Spring Meeting, Dresden, Germany, March 22-27, (2009).
 11. *C. Baumgart*, A.-D. Müller, F. Müller, M. Helm, A. Möller, and H. Schmidt, Kelvin probe force microscopy imaging of cross-sections of Si multilayer structures, **Talk HL 14.2**, DPG Spring Meeting, Dresden, Germany, March 22-27, (2009).

Acknowledgements

I want to thank all people, who contributed to succeeding this work. Especially, I am much obliged to a number of people for scientific, practical, theoretical, experimental and last but not least moral support:

- Prof. Dr. M. Helm, Prof. Dr. J. Fassbender and Prof. Dr. W. Möller for the opportunity to work in the Institute for Ion Beam Physics and Materials Research of the Helmholtz-Zentrum Dresden-Rossendorf.
- Dr. H. Schmidt for engaged supervision.
- Prof. Dr. A. Kolitsch for funding of the Anfatec Level-AFM in 01/08.
- The FWIM-team and the Nanospintronics group for a very cooperative and pleasant working atmosphere.
- Dr. A.-D. Müller and Dr. F. Müller from Anfatec Instruments AG for reliable technical support and helpful discussions on technical aspects of the KPFM measurement technique.
- Dr. S. Habicht and Dr. S. Feste from the Research Center Jülich for fruitful cooperation and scientific discussions on nanowires.
- PD Dr. S. Sadewasser from the Helmholtz Zentrum Berlin for UHV KPFM measurements and scientific discussions.
- Dr. A. Möller, K. Göhler, M. Hänisch and P. Pelzing from SGS Institut Fresenius GmbH Dresden for cross-sectional sample preparation and for encouraging our research on quantitative dopant profiling in semiconductors.
- H. Hortenbach from Qimonda Dresden for SIMS measurements.
- Dr. M. Fenner from Agilent Technologies for encouraging our research.
- To Antje for being a best friend.
- To my family.

Erklärung

Hiermit versichere ich, dass ich die vorliegende Arbeit

Quantitative dopant profiling in semiconductors: A new approach to Kelvin probe force microscopy

ohne unzulässige Hilfe Dritter und nur unter Benutzung der angegebenen Hilfsmittel angefertigt habe. Die aus fremden Quellen direkt oder indirekt übernommenen Gedanken sind als solche kenntlich gemacht. Die Arbeit wurde weder im Inland noch im Ausland in gleicher oder ähnlicher Form einer anderen Prüfungsbehörde vorgelegt.

Die vorliegende Arbeit wurde am Institut für Ionenstrahlphysik und Materialforschung des Helmholtz-Zentrums Dresden-Rossendorf unter der wissenschaftlichen Betreuung von Herrn Prof. Dr. Manfred Helm und Frau Dr. Heidemarie Schmidt angefertigt. Die Promotionsordnung der Fakultät für Mathematik und Naturwissenschaften der Technischen Universität Dresden erkenne ich an.

Dresden, den 23.11.2011

Christine Baumgart